Master Thesis Report

An experimental study into accuracy of novel techniques in Power Curve verification

H. J. Wessels

Delft University of Technology

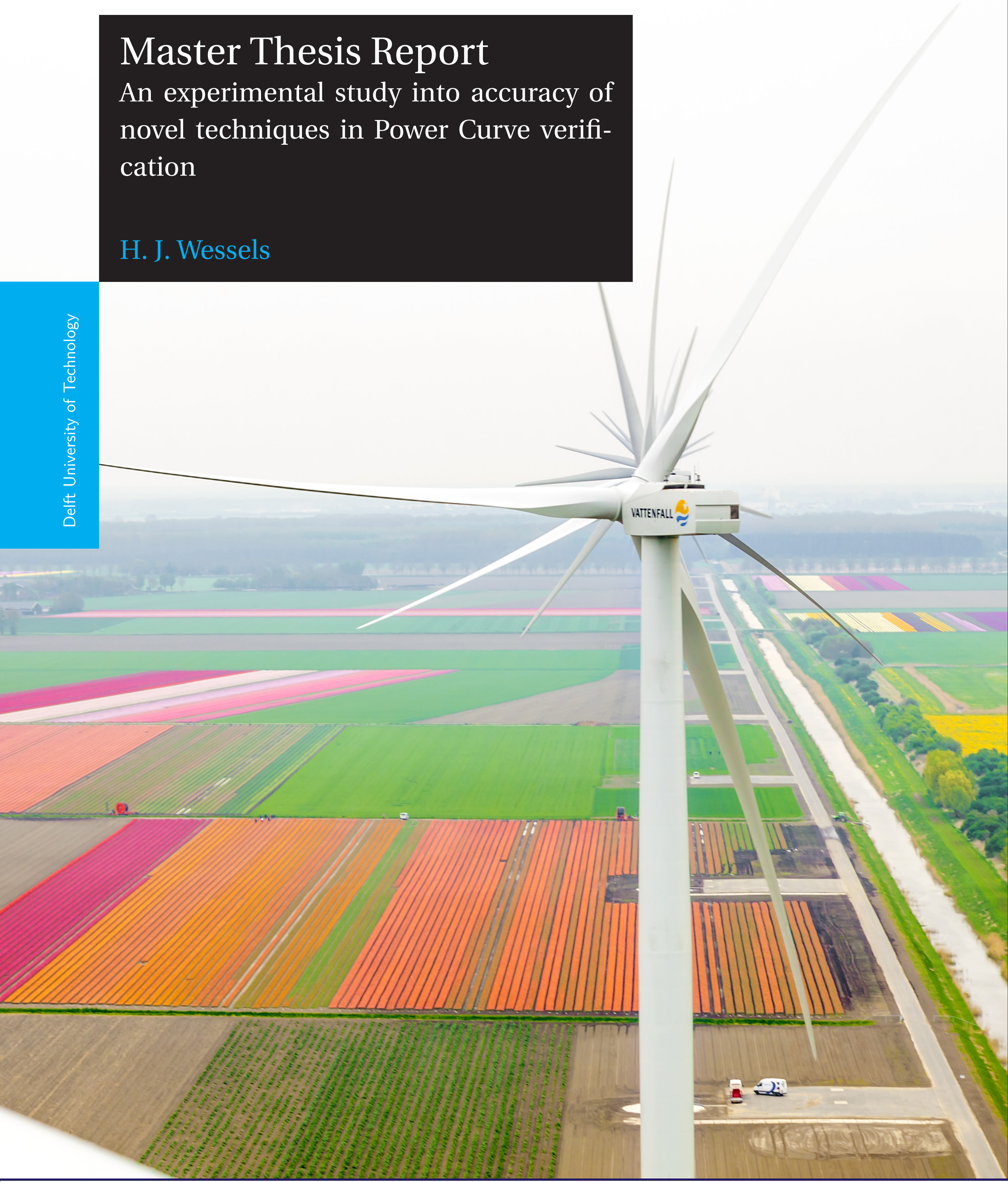

Delft University of Technology

Challenge the future

Cover photo: Wind park Prinses Alexia made by Jorrit Lousberg on 06/05/2013.

Master Thesis Report

An experimental study into accuracy of novel techniques in Power Curve verification

by

H. J. Wessels

in partial fulfillment of the requirements for the degree of

Master of Science
in Sustainable Energy Technology

at the Delft University of Technology,
to be defended publicly on December 16, 2015 at 10:00.

Student number: 1372327
Project duration: February 1, 2015 – December 16, 2015
Supervisor: Dr. ir. W.A.A.M. Bierbooms
Thesis committee: Dr. ir. W.A.A.M. Bierbooms, TU Delft
Prof. Dr. G.J.W. van Bussel, TU Delft
Drs. J.P. Coelingh, Nuon/Vattenfall
Dr. ir. M. Snellen, TU Delft

An electronic version of this thesis is available at http://repository.tudelft.nl/.

Delft
University of
Technology

ABSTRACT

The EU goals to decrease wind energy prices are driving the wind energy industry to give more attention to monitoring and improving turbine performance. Meanwhile, as turbines grow bigger and more are placed offshore, performance monitoring costs are increasing, making it more interesting to consider novel devices to measure turbine performance. The purpose of this study was to investigate the applicability of these devices in power performance monitoring and evaluating the potential gains which can be achieved.

A comparative study of the measurement accuracies was performed of the nacelle-based Lidar (WindIris) and a spinner anemometer (iSpins) against an IEC-compliant met-mast. Accuracies of both devices in measuring wind speeds, yaw misalignment and power curves were found to be comparable to a met-mast and therefore could be worthy replacements of met-masts for power performance measurements in the future. The impact of non-ideal wind conditions, like yaw misalignment, turbulence and wind shear, on power performance was also investigated using both experimental and Bladed simulated results. No conclusive results were found on the relationship between yaw misalignment and performance loss. The ideal yaw error was found to increase with increasing wind shear, caused by higher angles of attack in the top of the rotor area. The direct impact of turbulence intensity and wind shear on power curves was found to be wind speed dependent and not that significant on overall energy production. Finally, combining the knowledge acquired about yaw misalignment and device accuracies, a financial feasibility study was performed to evaluate future implementation of the novel devices for yaw misalignment correction. Since no conclusive evidence was presented that correcting for yaw misalignment could increase power performance significantly, current implementation of such a correction campaign is not recommended. If a deliberate yaw misalignment campaign were to be performed, however, the impact of yaw misalignment on turbine performance should be quantifiable and expectations are that implementation of novel devices should be financially feasible.

ACKNOWLEDGMENTS

As the journey comes closer to an end, it is time to look back and salute the people I met and who made the journey possible.

First of all, I would like to express my sincere gratitude to Jan Coelingh for giving me the opportunity to perform my thesis in collaboration with Vattenfall. Also, your guidance and time taken to brainstorm with me about the continuation of my research was very valuable and much appreciated. A great word of thanks to my Wind Resource colleagues at Nuon: Jorn, Stathis, Stefan, and Henrik, your help and advice kept me going in my research while your jokes and laughter made me feel welcome from the first day I joined Vattenfall.

Many thanks also to Wim Bierbooms for guiding me through the process of research and always being able to point me in the right scientific directions when necessary. I thank you for your patience and good ideas during our regular meetings, which has lifted this research to a higher level.

Thanks to my fellow graduates in room 5.12 at the Wind Energy department for being such good sparring partners. Thanks to your openness yet critical stance, interesting discussions occurred causing time to fly by. Wishing you all the best in your future careers and hoping to meet again soon in the wind energy sector.

Last but not least, I thank my family (Jan, Beppie, Peter, Matthijs and Hanna) for the their love and support, as well as my girlfriend, Britt, for coping with me even though at times I was not the most cheerful of souls due to my thesis. Also a big thank you to my friends in Delft and abroad for being a part of the journey and making it worthwhile!

Rik Wessels
Delft, December 2015

CONTENTS

Abstract iii

Acknowledgments v

List of Acronyms and Symbols xi

List of Figures xiii

List of Tables xvi

1 Introduction 1

2 Research objectives 3
2.1 Research opportunity . . . 3
2.2 Research questions . . . 3

3 Theoretical background 5
3.1 IEC standards on Power performance measurements . . . 5
3.1.1 Preparation for performance test . . . 5
3.1.2 Measurement devices . . . 6
3.1.3 Measurement procedure . . . 6
3.1.4 Analysis procedure . . . 7
3.2 Measurement techniques . . . 8
3.2.1 Lidar . . . 8
3.2.2 Spinner anemometers . . . 10
3.3 Yaw Misalignment . . . 13
3.3.1 Effect of wind shear on ideal yaw error . . . 13

4 Literature review 15
4.1 Measurement devices . . . 15
4.2 Yaw Misalignment . . . 17
4.3 Outer envelope conditions . . . 18

5 Research Setup 21
5.1 Site description . . . 21
5.1.1 Wind park Prinses Alexia . . . 21
5.1.2 Wind park Norrekaer Enge . . . 23
5.2 Research Methodology . . . 26
5.3 Analysis tools . . . 28
5.3.1 Matlab Computations . . . 28
5.3.2 Bladed Simulations . . . 28

6 Data Validation 31
6.1 Prinses Alexia Campaign . . . 31
6.2 Norrekaer Enge Campaigns . . . 32
6.2.1 Lidar Validation . . . 33
6.2.2 Spinner Anemometer Validation . . . 36

7 Exercise of Power Curve Verification 41
7.1 Power performance tests . . . 41
7.1.1 Power Curves . . . 41
7.1.2 Annual Energy Production . . . 41
7.1.3 Performance loss factors . . . 42
7.2 Complete park comparison . . . 46

8 Accuracy of novel devices **49**
- 8.1 Nacelle-based Lidar against met-mast . . . 49
  - 8.1.1 Wind speed comparison . . . 50
  - 8.1.2 Yaw misalignment comparison . . . 50
  - 8.1.3 Turbulence intensity comparison . . . 53
  - 8.1.4 PC verification applicability . . . 54
  - 8.1.5 Other possibilities for Lidar . . . 56
- 8.2 Spinner Anemometer against met-mast. . . . 56
  - 8.2.1 Wind speed comparison . . . 56
  - 8.2.2 Wind direction comparison . . . 57
  - 8.2.3 Yaw misalignment comparison . . . 57
  - 8.2.4 Turbulence intensity comparison . . . 59
  - 8.2.5 PC verification applicability . . . 60
- 8.3 Direct comparison Lidar against Spinner Anemometer . . . 61

9 The Behavior of Yaw Misalignment **65**
- 9.1 Effect of Yaw Misalignment on turbine . . . 65
  - 9.1.1 Bladed Simulations . . . 65
  - 9.1.2 Applying Boorsma's method on Prinses Alexia data . . . 66
- 9.2 Effect of WS on ideal yaw error . . . 69
  - 9.2.1 Bladed simulations . . . 69
  - 9.2.2 Boorsma method with WS bins . . . 69

10 Outer Envelope Conditions **75**
- 10.1 Conditions during campaign . . . 75
- 10.2 Effect of Wind Shear . . . 76
  - 10.2.1 Results with Bladed simulations . . . 76
  - 10.2.2 Results based on measurements . . . 77
- 10.3 Effect of Turbulence Intensity . . . 79

11 Financial Feasibility Study **83**
- 11.1 Analysis method . . . 83
  - 11.1.1 Assumptions . . . 83
  - 11.1.2 Method . . . 84
- 11.2 Analysis results . . . 85
  - 11.2.1 Costs . . . 85
  - 11.2.2 Benefits . . . 87
  - 11.2.3 Results . . . 88
  - 11.2.4 Business case discussion . . . 89
- 11.3 Conclusions. . . . 90

12 Conclusions and Recommendations **93**
- 12.1 Reflection on Research Goals . . . 93
- 12.2 Final Remarks. . . . 95
- 12.3 Recommendations for Future Research . . . 95

Bibliography **97**

A Wind speed distribution **101**
- A.1 Least Squares Estimation . . . 101
- A.2 European Wind Atlas Method . . . 101
- A.3 Matlab scripts. . . . 103

B Density Correction **105**
- B.1 Proposed solution. . . . 105
- B.2 Implementation . . . 105

C Wind direction and YM simulations **107**

D Accounting for heterogeneity **109**
D.1 Quantification of heterogeneity in Lidar measurements 109
D.1.1 Alternative approaches 110
D.2 Proposal of heterogeneity measurement campaign 111

E Proposal Fast YM influence test **113**
E.1 Introduction 113
E.2 The analysis method 113
E.3 How does this method make the measurement period shorter? 114

F Simulations of YM campaign using side-by-side method **115**

G Bladed simulations **119**
G.1 Setting wind conditions 119
G.2 Power production loading 120
G.3 Post processing 120

H Performance heatplots wind park Prinses Alexia **123**

LIST OF ACRONYMS AND SYMBOLS

LIST OF ACRONYMS

ABL	Atmospheric Boundary Layer
AEP	Annual Energy Production
CNR	Carrier-to-Noise Ratio
COE	Cost of Electricity
HAWT	Horizontal Axis Wind Turbine
HWS	Horizontal Wind Speed
IEC	International Electrotechnical Commission
IRR	Internal Rate of Return
LAWINE	Lidar Applications for Wind Farm Efficiency
Lidar	Light Detection and Ranging
LOS	Line-of-Sight
NPV	Net Present Value
PBT	Payback Time
PC	Power Curve
PCV	Power Curve Verification
PCWG	Power Curve Working Group
PIF	Performance Improvement Factor
RWS	Radial Wind Speed
Scada	Supervisory control and data acquisition
Sodar	Sonic Detection and Ranging
TI	Turbulence Intensity
WACC	Weighted Average Cost of Capital
WAM	Wind Atlas Method
WS	Wind Shear
WTG	Wind Turbine Generator
YM	Yaw Misalignment

LIST OF SYMBOLS

a	Induction factor [-]
A	Weibull scale parameter
A_r	Rotor swept area $[m^2]$
B_{10min}	10min averaged air pressure[Pa]
B_w	Vapour pressure [Pa]
C_p	Power coefficient [-]
C_t	Net cash flow in year t [€]
D	Rotor diameter [m]

$\mathbf{E}$	Power density [W/m^2]
f	Doppler frequency shift [Hz]
$\mathbf{G}$	Gearbox ratio [-]
$\mathbf{k}$	Weibull shape parameter
k_1, k_2	Spinner anemometer calibration constants
$\mathbf{N}$	Number of data points [-]
$\mathbf{P}$	Produced power [W]
Q_d^{opt}	Generator torque [Nm]
$\mathbf{r}$	Discount rate [%]
$\mathbf{R}$	Rotor radius [m]
R^2	Coefficient of Determination [-]
R_0	Gas constants of dry air (287,05 J/(kgK))
R_w	Gas constants of dry air (461,5 J/(kgK))
T_{10min}	10min averaged air temperature[K]
U_0	Rotor incoming wind speed [m/s]
U_{hor}	Rotor incoming wind speed [m/s]
$\mathbf{V}$	Wind speed [m/s]
$\hat{x}_{YM}$	Change in inflow angle due to YM [deg]
z_M	Lidar measurement height [m]
α	Lidar opening angle [°]
α_d	Lidar disturbed sector width [°]
β_{lidar}	Lidar pre-tilt angle [°]
γ	Lidar relative wind direction/YM [°]
δ	Turbine shaft tilt angle [°]
θ	Azimuth position of flow stagnation point [°]
κ	Relative humiditiy [-]
λ	Tip speed ratio $[-]$
λ_{lid}	Lidar signal wavelength $[\mu m]$
ρ_0	Standard sea level air density (1.225 kg/m^3)
ρ_{10min}	10min averaged air density [kg/m^3]
σ	Measurement accuracy [°]
ϕ	Rotor azimuth position measured by spinner anemometer [°]
ω	Rotor speed [rad/s]

LIST OF FIGURES

3.1 Requirements to distance and allowed measurement sectors due to wake of a turbine on the met-mast.[1] . . . 6
3.2 Graphical overview of calculation method of wind vector (V) using a two beam Lidar[6] . . . 8
3.3 Measurement distance and height of nacelle-based Lidar given the tilt angle and the height of the Lidar optical head[6]. . . . 10
3.4 Graphical layout of the spinner anemometer system [8] . . . 11
3.5 Sinusoidal variations becoming visible in the sonic anemometer wind speed measurements as the turbine is influenced by YM. The index 'c' indicates data has had an internal calibration.[11] 11
3.6 Definition of coordinate systems and variables applicable to the turbine-stalled spinner anemometers. . . . 12
3.7 Effect of wind shear on YM at top of rotor plane looking from above. . . . 14
3.8 Effect of wind shear on YM at bottom of rotor plane looking from above. . . . 14

4.1 Effects of yawed inflow and wind shear on angle of attack, relative airfoil velocity, blade root moment, axial velocity and velocity measured by Lidar, respectively.[18] . . . 16

5.1 Graphical description of wind park Prinses Alexia . . . 22
5.2 Wind conditions at wind park Prinses Alexia for the period of February - October 2015. . . . 23
5.3 Geographical description of wind park Norrekaer Enge . . . 24
5.4 Wind conditions at wind park Norrekaer Enge over the period October 2014 till April 2015. . . . 25
5.5 Plots of electric power resulting from Bladed power production loading simulations at different wind speeds. . . . 29
5.6 Wind profiles specified by different wind shear exponents . . . 29

6.1 Met-mast and nacelle anemometer readings at Prinses Alexia compared to each other for time-logging validation. Each data log is a 10-minute average value. . . . 32
6.2 Prinses Alexia: Ratio of two met-mast anemometer readings at 98m per wind direction . . . 32
6.3 Prinses Alexia: Filtered and unfiltered nacelle anemometer against met-mast readings . . . 33
6.4 Wind speed validation of Lidar measurements against a met-mast. Each data log is a 10-minute average value. . . . 34
6.5 Analysis of the wind sectors as measured by Lidar at different ranges. . . . 35
6.6 CNR values of LOS0 against the HWS availability before and after the mentioned filters have been applied. . . . 35
6.7 CNR signal of both LOSs at different measurement ranges. Each data log is a 10-minute average value. . . . 36
6.8 Validation of temperature readings of spinner anemometers against an IEC-compliant met-mast. Each data log is a 10-minute average value. . . . 37
6.9 Validation of air density readings of spinner anemometers against an IEC-compliant met-mast. Each data log is a 10-minute average value. . . . 37
6.10 Validation of YM readings of spinner anemometer against the wind direction as measured by met-mast. . . . 38
6.11 Validation of independent active power readings by Romowind against Vattenfall Scada system. 38
6.12 Validation of rotor speed readings by Romowind against Vattenfall Scada system. . . . 39
6.13 Histogram of rotor speed difference between spinner anemometer and Scada system. . . . 39

7.1 Binned power curves for turbines R01 and R02 compared to reference PC . . . 42
7.2 Annual Energy Productions predicted using several wind speed distributions . . . 42
7.3 YM measurements for turbines R01 and R02 using the adjacent met-mast . . . 43
7.4 Histogram of the energy loss due to the absolute 10-minute average YM using the cos^2-rule. . . 44

7.5 Average pitch angles of turbines R01 and R02 plotted against wind speed . . . 44
7.6 Comparison of generator torque of R01 and R02 against wind speed . . . 45
7.7 Comparison of rotor and generator speeds of R01 and R02 . . . 45
7.8 Measured power coefficient of turbines R01 and R02 against tip speed ratio. . . . 46
7.9 Heatmap displaying power performance of all turbines at Prinses Alexia from February-August 2015. . . . 47

8.1 Post-calibration corrected tilt and roll readings as measured by the inclinometer installed on the Lidar. . . . 50
8.2 Correlation between met-mast and Lidar wind speed readings measured at 2.5D in front of Turbine 4. . . . 51
8.3 Histogram of Lidar YM measurements at different ranges. . . . 51
8.4 Comparison of Lidar YM measurements at 80m and YM calculations using met-mast and Scada data . . . 52
8.5 Comparison of YM simulations for the Wind Iris Lidar . . . 53
8.6 Correlation between met-mast and Lidar standard deviation measurements at turbine 4 and their binned averages. . . . 54
8.7 Distribution of met-mast and Lidar TI measurements at turbine 4 and the correlation between them. . . . 54
8.8 Binned power curves measured with met-mast and Lidar compared to reference PC. . . . 55
8.9 Binned power curves measured with met-mast and spinner anemometers compared to reference PC. . . . 55
8.10 AEP comparison of met-mast and Lidar at different ranges normalized to the guaranteed PC. . . . 56
8.11 Turbine 4 tilt angle plotted against met-mast wind speed . . . 56
8.12 Correlation between met-mast and spinner anemometer wind speed readings at turbine 4. . . . 57
8.13 Correlation between met-mast and spinner anemometer wind direction measurements at turbine 4. . . . 58
8.14 Comparison of YM measurements of spinner anemometers and YM calculations using met-mast and Scada data . . . 58
8.15 Comparison of YM simulations . . . 59
8.16 Distribution of met-mast and spinner anemometer TI measurements at turbine 4 and the correlation between them. . . . 60
8.18 Correlation between met-mast and spinner anemometer TI measurements at turbine 4 including the bin-averaged values and weighted correlation fit. . . . 61
8.19 Binned power curves measured with met-mast and spinner anemometers compared to reference PC. . . . 61
8.20 AEP overestimation of spinner anemometer compared to met-mast with AEP normalized to guaranteed PC. . . . 62
8.21 Correlation between Lidar and spinner anemometer wind speed readings at turbine 4. . . . 62
8.22 Direct comparison of Lidar and spinner anemometers YM measurements . . . 63

9.1 Resulting PCs for Bladed simulations while varying YM. . . . 65
9.2 Simulations of the YM effect on AEP. . . . 66
9.3 Relation between yaw misalignment and power coefficient at turbines R01(top) and R02(bottom) 67
9.4 Average pitch angle per wind speed bin. . . . 68
9.5 Average pitch angle per wind speed bin. . . . 68
9.6 Simulations of the WS effect on ideal yaw error. . . . 69
9.7 Relation between yaw misalignment and power coefficient at turbines R01(top) and R02(bottom) 70
9.8 Sensitivity of phase shift with Boorsma's method using different filters and bin sizes. . . . 71
9.9 Relation between wind speed and maximum power coefficient, phase shift and exponent of cosine fit with Boorsma's method at turbines R01 and R02 . . . 72
9.10 Relation between wind shear exponent and maximum power coefficient, phase shift and exponent of cosine fit with Boorsma's method at turbines R01 and R02 . . . 73

10.1 Wind shear and turbulence conditions at Prinses Alexia with the turbine guaranteed conditions shown by the red box . . . 75
10.2 Number of points per wind speed bin for different TI and WS bins . . . 76

10.3 Simulations of the WS effect on the PC. 77
10.4 Simulations of the WS effect on AEP. 77
10.5 Binned PCs at different wind shear bins 78
10.6 Relative bin power differences at different wind shear bins normalized to the reference PC. . . . 78
10.7 Effect of wind shear on the AEP normalized to the reference PC. 79
10.8 Binned PCs at different turbulence intensity bins 79
10.9 PCs at different turbulence conditions found with Bladed simulations[41]. 80
10.10Relative bin power differences at different turbulence intensity bins normalized to the reference PC. 81
10.11Normalized power difference at different turbulence conditions found with Bladed simulation[41]. 81
10.12Effect of turbulence intensity on the AEP normalized to the reference PC. 82

11.1 Pie chart of the costs concerned with applying a nacelle-based Lidar for YM correction campaign at Prinses Alexia. 86
11.2 Pie chart of the costs concerned with applying spinner anemometers for YM correction campaign at Prinses Alexia. 87
11.3 Development of the accumulated NPV over the lifetime of the project for both the Lidar and the spinner anemometer methods. 88
11.4 Dependency of the NPV on the performance improvement factor (PIF). 89
11.5 Dependency of the normalized IRR and PBT on the performance improvement factor (PIF). . . 90
11.6 Bar chart to show dependency of the NPV on the discount rate. 90
11.7 Calculation sheet for the business case of the Lidar including the input parameter specification. 91
11.8 Calculation sheet for the business case of the spinner anemometers including the input parameter specification. 92

B.1 Proposed dependence of exponent for density correction [2] 105
B.2 Calculated exponents for density correction according to Svenningsen's method. 106

D.1 Topview graphical description of the Lidar measurement principles.(Presented during tele-conferences with Avent Lidar Technologies) 109
D.2 Alternative options for top-view graphical description of the Lidar measurement principles. . . 110
D.3 Topview graphical description of the Lidar measurement principles when using a 5-beam Lidar with LOS2, the central beam. 111

E.1 Correlation of simultaneous power readings from turbines R01 and R02 at Prinses Alexia. 114

F.1 Initial simulation results for turbines R01 and R02 based on the side-by-side method with zero offset in YM. 116
F.2 Simulation results for turbines R01 and R02 based on the side-by-side method with R01 at a YM-offset of +20° 116
F.3 Results of the simulations as the YM for turbine R01 is varied from -20 to +20 degrees while R02 remains unchanged (n=2). 117
F.4 Results of the simulations as the cosine exponent is varied from 2-4. 117

G.1 Bladed modules needed to set wind conditions prior to each power production loading 119
G.2 Bladed module in which calculation parameters for a simulation can be defined 120
G.3 Bladed modules used during post-processing of the power production loading simulations . . . 121
G.4 Reconstructed Fourier Harmonics signal compared to the original simulated electric power signal. 122

H.1 Heatplots for power performance of wind turbines at Prinses Alexia filtered per 0.5 m/s bin ranging from 7 to 9 m/s 123
H.2 Heatplots for power performance of wind turbines at Prinses Alexia filtered per 0.5 m/s bin ranging from 9 to 13 m/s 124

LIST OF TABLES

3.1 Overview of requirements set by the IEC for devices to be used in power performance tests . . . 6

5.1 Specifications of Prinses Alexia turbines . . . 22
5.2 Specifications of met-mast at Prinses Alexia . . . 22
5.3 Weibull parameters and energy content found with different Weibull estimation methods at Prinses Alexia for the period of Feb-July 2015. $V_{mean} = 7.01 m/s$ . . . 23
5.4 Specifications of Norrekaer Enge turbines . . . 24
5.5 Specifications of met-mast at Norrekaer Enge . . . 24
5.6 Weibull parameters and energy content found with different Weibull estimation methods at Norrekaer Enge for the period of Oct. 2014 -April 2015. $V_{mean} = 8.17 m/s$. . . . 26
5.7 Specifications of the Bladed demoa.prj turbine model . . . 28
5.8 Properties to be varied during initial Bladed simulations . . . 30
5.9 Varied load cases during Bladed simulations following the lessons learned in initial simulations. 30

6.1 Specification of significant output signals and corresponding units by the WindIris Lidar[4]. . . 33
6.2 Specification of significant output signals and corresponding units by the spinner anemometer. 36

11.1 Overview of assumptions made for the purpose of the business case. . . . 84
11.2 Summary of economic variables for both business cases using the basic assumptions. . . . 88

A.1 Weibull parameters and energy content found with different Weibull estimation methods at Prinses Alexia for the period of Feb-July 2015. $V_{mean} = 7.01 m/s$ . . . 103

C.1 Influence of different contributions to YM measurement method uncertainty . . . 107

F.1 Overview of assumptions and parameter settings applied during the YM campaign simulations. 115

G.1 Example of Fourier Harmonics module outputs (Harmonic number, Amplitude and phase) of the for load case: v = 10 m/s, WS exponent = 0.4,YM = -2°. . . . 121
G.2 Harmonics comparison of the acquired dynamic PC for the following load case: YM=2° and WS exponent = 0.2. . . . 122

1

INTRODUCTION

Following the goals set by the EU for 2020 to reduce costs of wind energy by 40%, the industry is taking on the challenge to either cut expenses or increase production. This is done, for instance, by making turbines bigger to increase production but also by improving the operational efficiency and decreasing losses through improved wind resource assessment and power performance monitoring.

The current practice of wind resource assessment and Power Curve Verification (PCV) is mostly being done with cup and sonic anemometers mounted on a met-mast[1]. As the wind energy industry keeps growing, wind turbines are becoming bigger. This will cause an increase in costs of future wind resource assessment as the height of met-masts also needs to reach higher altitudes. Also, PCV for offshore wind parks requires a met-mast to be installed on a monopile in the park, a rather costly exercise. In recent years, the wind industry has therefore endeavored into looking for alternative wind measurement devices which will be cheaper and more practical in operation yet accurate enough for wind resource assessment.

Two technologies that are being considered are Lidars, either nacelle-mounted or ground-based, and spinner anemometers. Light Detection and Ranging (Lidar) is a remote sensing technology already used in various industries for nearly 50 years and over the last decade has also become more well-known in the wind energy industry. Spinner anemometers, a DTU Wind Energy invention, is a newer innovation which is still in its' development phase and hence not a lot of research has been performed on this topic. These devices have been experimented with during this thesis, the results of which will be presented in this report.

Besides using novel technologies for wind resource assessment, wind industry partners are also seeking to decrease operational losses by taking a closer look at how turbines function using the gained experience and knowledge in measuring wind conditions. Due to the advances in computational power and accuracy of remote sensing devices, it is possible to investigate how wind conditions like wind shear and turbulence affect the turbine. Another field where a lot of research is being done in is how precise the yaw controller of a turbine functions and what effect this has on the power production. This thesis also reports on the possibility of the afore-mentioned remote sensing devices to measure non-ideal conditions (e.g. wind shear, turbulence and yaw misalignment) and investigates their effects on the power performance.

This report will be structured as follows: First the research objectives as set-up at the beginning of this study will be presented, followed by some theoretical background (Ch. 3) and a brief literature review of the research topics (Ch. 4). In Chapter 5, the methodology applied in this research will be explained, followed by a chapter (Ch. 6) on the steps taken in data validation. This will be followed up by the experimental results of a PCV exercise at wind park Prinses Alexia (Ch. 7), an analysis of the measurement accuracies of the novel devices (Ch. 8), the phenomenon of YM and its effects on a turbine (Ch. 9), and the effects of outer-envelope wind conditions on the PC (Ch. 10). In Chapter 11 a financial case study will be presented to evaluate whether the novel techniques are financially feasible. Finally, the report will end with the conclusions of this research and recommendations for future work in Chapter 12.

2

RESEARCH OBJECTIVES

2.1. RESEARCH OPPORTUNITY

Simultaneous measurement campaigns have been performed by Vattenfall with 3 different techniques (IEC-compliant met-mast, Lidar, and spinner anemometers) at wind park Norrekaer Enge in Denmark. It is therefore interesting to compare the techniques' outputs and determine which of these is the best option for future power performance assessments.

Next to this, power performance tests at two turbines at Prinses Alexia wind park will be performed with an adjacent IEC-compliant met-mast. These measurements can be used to gain experience in the process of PCV and used to analyze the effects of non-ideal conditions on turbine performance.

2.2. RESEARCH QUESTIONS

Considering the requirements and demands connected to an accurate power performance assessment as set by the International Electrotechnical Commission (IEC) [1], the novel devices should be tested on their ability to match measurements from an IEC-compliant met-mast nearby. Also, it will be good to gain experience with these devices and evaluate their economic feasibility, once again compared to a met-mast. Taking the afore-mentioned into consideration leads to the following research questions:

Main research objective:
An experimental study into accuracy of novel techniques in Power Curve (PC) verification.

Sub-questions:

1. How do accuracies in PC verification of novel measurement techniques (Lidar and spinner anemometers) compare to IEC-compliant met-masts? How does this translate to their business cases?
2. How can Yaw Misalignment (YM) be measured accurately with different techniques (IEC-compliant met-mast, Lidar, and spinner anemometers) and how does YM influence the power performance of a Horizontal Axis Wind Turbine (HAWT)?
    (a) Deliberately misalign a turbine in order to find relation with power performance.
3. What is the effect of wind shear on the ideal yaw error of a turbine?
    (a) Perform Bladed simulations of different wind shears to find ideal yaw error
    (b) Perform an analysis of experimental data at Prinses Alexia
4. How do conditions (Turbulence Intensity (TI), Wind Shear (WS), etc.) outside the 'guaranteed PC envelope' influence the PC?

3

THEORETICAL BACKGROUND

In this chapter the theoretical content of several aspects investigated in this thesis will be presented and discussed. First of all, an introduction into the process of power performance measurements and how the standards dictate this process will be touched upon. Next, a deeper look into the calibration and operation of different measurement devices will be taken. Finally, some theoretical background on YM and the effect of wind shear on it will be presented.

3.1. IEC STANDARDS ON POWER PERFORMANCE MEASUREMENTS

Power performance measurements are prone to high uncertainties and errors if no care is taken into cleaning of data for disturbed wind sectors and non-standard conditions. For this reason, the IEC has set up standards which are to be used for certified power performance measurements. These guidelines give a standard procedure to follow during PCV, thereby making a trustworthy comparison possible. In the following section, an explanation of these standards and procedures will be given as described in the IEC 61400-12-1[1].

3.1.1. PREPARATION FOR PERFORMANCE TEST

For an accurate power performance measurement, reliable, accurate wind speed measurements are to be made using an IEC-compliant meteorological mast(met-mast). For these measurements to be accurate, the position of the mast and the wind sectors to be measured are to be chosen wisely, and flow distortion corrections are to be estimated. In this consideration, the distance of the mast to the turbine under surveillance and wind flow altering situations like topographical variations in the site, surrounding trees, buildings and other wind turbines are to be taken into account.

To find an optimum between the blockage effect of a turbine on the met-mast measurements while not handing in too much on the correlation between the measured wind speeds and turbine power, the IEC standards dictate that the met-mast should be positioned between 2-4D, the turbine rotor diameter, while a distance of 2.5D is recommended. For most simple wind energy sites it is best to place the met-mast upwind of the turbine with respect to the prevailing wind direction at the site, as this will deliver more usable measurements for further analysis.

Next, the relevant measurement sectors can be specified. All wind direction sectors where either the turbine under test or the met-mast is in the wake of surrounding obstacles or wind turbines are considered to be disturbed. For each obstacle present in the measurement sector, its individual impact on both the met-mast and turbine readings is to be estimated. This can be done by finding the distance to either the wind turbine under test or the met-mast and the equivalent diameter of the obstacle, be-it a building or other turbine. The IEC standards then give a method to estimate the disturbed sector which is to be disregarded in the power performance measurement. Figure 3.1 shows an example of the requirements to distance and allowed measurement sectors due to the wake of a turbine on the met-mast.

As both sites considered in this thesis are in flat, non-complex territory, the topographical variations are insignificant and thus no site calibration is to be performed in this study. Therefore, this part of the IEC standards will not be explained further in this section.

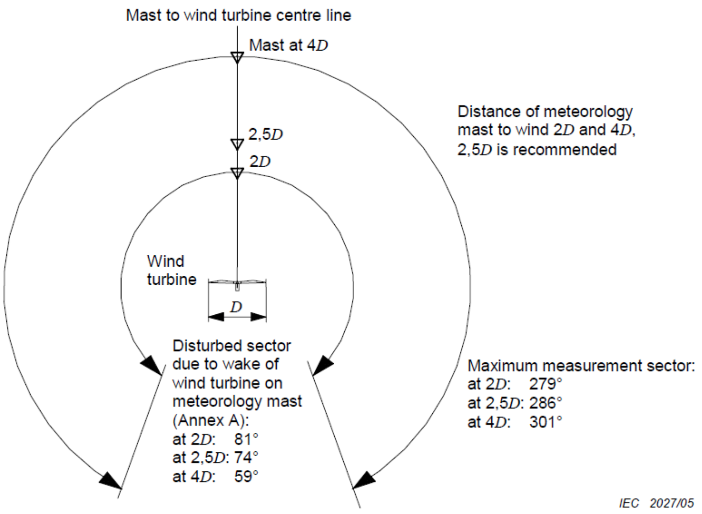
Mast to wind turbine centre line
Mast at 4D
2,5D
2D
Distance of meteorology mast to wind 2D and 4D, 2,5D is recommended
Wind turbine
D
Disturbed sector due to wake of wind turbine on meteorology mast (Annex A):
at 2D: 81°
at 2,5D: 74°
at 4D: 59°
Maximum measurement sector:
at 2D: 279°
at 2,5D: 286°
at 4D: 301°
IEC 2027/05

Figure 3.1: *Requirements to distance and allowed measurement sectors due to wake of a turbine on the met-mast.[1]*

3.1.2. MEASUREMENT DEVICES

The IEC requires the measurement devices to follow certain industry standards. Not only should wind speed, direction and power measurement devices be reliable at an industry level, the environmental conditions and turbine operational signals should also be measured accurately. Table 3.1 gives an overview of these requirements.

Table 3.1: *Overview of requirements set by the IEC for devices to be used in power performance tests*

Measurement quantity	**Device requirements**
Electric power	Class 0.5 or better, meaning a maximal error of 0.5 % at rated power. Device to be mounted between turbine and electrical connection.
Wind speed	Class 1.7A or better, so uncertainty < 0.05 m/s+ 0.005*V. Device to be mounted at ±2.5% from hub-height.
Wind direction	Wind vane mounted on boom. Combined uncertainty less than 5 degrees.
Air temperature	Mounted within 10m of hub height.
Air pressure	Mounted close to hub height.
Turbine signals	Status signals of turbine required. At least data acquisition at 1Hz frequency.

3.1.3. MEASUREMENT PROCEDURE

The objective of a measurement campaign is to acquire good quality data of the turbine in its' normal operational state, therefore it has to be ensured that the turbine status signal is also measured. Wind and power data is to be collected at a minimum sampling rate of 1Hz while other weather conditions and turbine status should be logged at least once a minute. The data acquisition system should then store the measurements in 10 minute averages, thereby giving the mean, minimum, maximum and standard deviation values of the specific time interval.

To ensure that the data used in further analysis corresponds to the turbine during normal operation and conditions, some situations need to be rejected from the database. These situations include external conditions outside the operating range of the wind turbine, turbine not being in operation due to faults or maintenance, failure of the measurement devices and also when wind directions outside the measurement sector as determined earlier are present. The 10-minute data points where one of the above situations occurs should be discarded from the following analysis.

Finally, the length of the measurement period depends on the eventual database. In the data analysis, the binning method is used whereby wind speeds are filtered per 0.5 m/s bin and the corresponding power is averaged. *The selected data sets shall at least cover a wind speed range extending from 1 m/s below cut-in to 1,5 times the wind speed at 85% of the rated power of the wind turbine. Alternatively, the wind speed range shall extend from 1m/s below cut-in to a wind speed at which "AEP-measured" is greater than or equal to 95%*

of "AEP-extrapolated". A complete database is finally depicted as one in which every bin contains at least 30 minutes worth of sampled data, i.e. 3 data points, and the total database includes a minimal of 180 hours of sampled data. If one single bin is found to be incomplete it may be defined by interpolation with two adjacent complete bins.

3.1.4. ANALYSIS PROCEDURE

Density Correction Before the method of binning can be applied, the data sets have to be normalized to sea level air density(ρ_0), 1.225 kg/m^3. Air density is not measured directly but can be calculated using the air temperature, pressure and relative humidity readings in the following equation:

$$\rho_{10min} = \frac{1}{T_{10min}}\left(\frac{B_{10min}}{R_0} - \kappa B_w\left(\frac{1}{R_0} - \frac{1}{R_w}\right)\right) \tag{3.1}$$

where ρ_{10min}, B_{10min}, T_{10min} are the 10min averaged air density, pressure and temperature, respectively. R_0 and R_w are the gas constants of dry air (287,05 J/(kgK)) and water vapor (461,5 J/(kgK)), κ is the relative humidity and B_w the vapor pressure. The vapor pressure is given by the following equation:

$$B_w = 2.05 \cdot 10^{-5} \cdot e^{0.0631846 \cdot T_{10min}} \tag{3.2}$$

As can be seen in the above equation, for low temperatures the second term of the bracket in Eq. 3.1 can be neglected thereby simplifying the equation. For more modern turbines having active power control, the normalization is then applied using the following equation:

$$V_{norm} = V_{10min}\left(\frac{\rho_{10min}}{\rho_0}\right)^{\frac{1}{m}} \tag{3.3}$$

where V_{norm} and V_{10min} are the normalized and measured 10min averaged wind speeds. The IEC standards dictate to use a value of m=3, however Svenningsen [2] found that this method overestimates the Annual Energy Production (AEP) by up to 5% and has proposed a new method of determining this m-value. His approach has been explained in Appendix B as this is the density correction method used in this thesis.

Method of bins In the method of bins, the normalized wind speeds are sorted into bins of 0.5 m/s width after which the mean normalized wind speed and power output is calculated per bin using the following equations:

$$V_i = \frac{1}{N}\sum_{j=1}^{N_i} V_{n,i,j} \tag{3.4}$$

$$P_i = \frac{1}{N}\sum_{j=1}^{N_i} P_{n,i,j} \tag{3.5}$$

where i denotes the specific bin, N_i the number of points in that bin, and P and V the 10min averaged power and wind speed readings. Plotting the binned wind speeds and power, also the measured PC, next to the guaranteed PC of the turbine allows for a first comparison of the turbines' actual performance.

Annual Energy Production The AEP is calculated by multiplying the measured power curve by the wind speed distribution. If the site specific wind distribution has been measured, this may be used instead of the standard Rayleigh wind distribution, for the AEP calculation. An AEP can be calculated for both the measured and the guaranteed PC, thereby making a straight forward comparison possible. The equations used to calculate the AEP are given by:

$$AEP = N_h \sum_{i=1}^{N}[F(V_i) - F(V_{i-1})]\left(\frac{P_{i-1} - P_i}{2}\right) \tag{3.6}$$

Here N_h is the number of hours per year and $F(V)$ represents the cumulative probability distribution function for the wind speed.

3.2. MEASUREMENT TECHNIQUES

In the following sections the working principles and the theory behind the novel measurement devices will be presented, starting with a nacelle-based two-beam Lidar and finishing with a description of the spinner anemometers.

3.2.1. LIDAR

SETUP DETAILS

As the acronym already hints out, a Lidar uses light or laser signals to measure the wind speed. For the case of this thesis, a nacelle-based Lidar was used meaning it is installed atop the nacelle of the turbine and measures at a distance ahead of the rotor. In this section the working principle and exact setup of this device will be elaborated on.

WORKING PRINCIPLE

The underlying principle of a Lidar is the Doppler shift, which is a shift in the wave frequency of a signal caused by an observer moving relative to the source of the signal. A typical everyday example of this physics phenomenon is the changing in the pitch of an ambulance siren as it passes by on street, whereby the person on the street is the observer and the ambulance is the source.

In case of the Lidar, laser signals are sent out in front of the rotor after which they are scattered by aerosols, typically dust, water droplets, pollution etc., in the wind[3]. Now, the Lidar is the stationary observer, while the aerosols, due to their scattering of the signal, are the moving sources of the signals. During this scattering by the moving aerosol particles, the frequency of the signal changes whereby the Doppler shifted frequency is directly proportional to the Line-of-Sight (LOS)- velocity according to the following equation[4]:

$$RWS = \frac{f\lambda_{lid}}{2} \tag{3.7}$$

Here the RWS is the radial, or LOS, wind speed, λ_{lid} is the signal wavelength and f is the Doppler frequency shift. The laser emitters used in these Lidars typically have a wavelength of $1.55\mu m$ and are therefore not dangerous to the human eye. The receivers used in Lidars are very sensitive whereby only one out of every 10^{12} transmitted photons is needed to determine the Doppler frequency shift and thereby the LOS wind speed[5].

A two beam Lidar sends out two laser beams at a separation angle, α, from the rotor axis line. This is done since a single beam only says something about the radial wind speed and nothing about the velocity vector, direction and magnitude, of the aerosol particles in the wind. To find this vector, at least a second beam is necessary. Wagner et al.[6] and later Goossens [7] have given an elaborate explanation of calculations of the actual wind speed and direction for a two-beam nacelle Lidar, of which a short summary will be given using Figure 3.2.

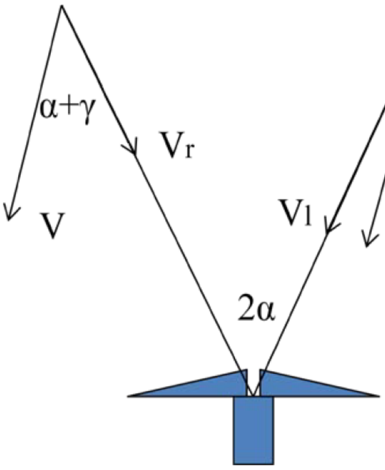

Figure 3.2: *Graphical overview of calculation method of wind vector (V) using a two beam Lidar[6]*

In Figure 3.2, V represents the wind vector, V_l and V_r are the left and right LOS wind speeds facing the turbine, γ the wind direction relative to the Lidar and α once again is the pre-set opening angle. Using the diagram as given in the figure, Wagner[6] and Goossens[7] found the following relations by derivation:

$$\gamma = \arctan\left(\frac{\frac{V_r}{V_l} - 1}{\tan\alpha(\frac{V_r}{V_l} + 1)}\right) \tag{3.8}$$

$$V_r = V\cos(\alpha + \gamma) \tag{3.9}$$

$$V_l = V\cos(\alpha - \gamma) \tag{3.10}$$

so by measuring the LOS wind speeds, the actual wind speed and direction can be calculated.

SETUP REQUIREMENTS

As Lidars are measuring in front of the rotor, it is important that they are configured well before measurement campaigns are started. Aspects to be considered are measurement distance and height, tilt and opening angles, and also the free wind sectors for the pre-set configuration. These aspects will all be treated in the following sections based on procedures suggested by DTU for power performance measurements using a two-beam Lidar[6] .

Tilt angle Ideally, the wind speed to be measured by the Lidar should be at hub-height and actually the IEC dictates that the measurement should be within ±2% of hub-height. As the Lidar is mounted atop the nacelle, it will be measuring above hub-height when the beams are directed horizontally from the device. Besides this, turbines tend to bend backwards due to the wind when in operation. This turbine tilt can be up to 0.5°. As we want to measure the wind speed at the correct height, hub-height, the Lidar will have to be tilted slightly downwards. The optimal Lidar tilt angle depends on several factors and is given by[6]:

$$\beta_{lidar} = \arctan\left(\frac{H}{xD + c}\right) + \beta_{corr} - \beta_{ope} - \beta_{sta} \tag{3.11}$$

Here β_{lidar} represents the tilt angle to be preset to the Lidar during installation, β_{corr} is the tilt correction due to the tilt error found during calibration of the Lidar, β_{ope} is the turbine operational tilt at the predominant wind speed and β_{sta} is the static tilt during installation. The static tilt is often very small and therefore disregarded from the above equation. H represents the height over hub-height while $xD + c$ represents the distance from the Lidar to the point being measured at, where c is the distance from the tower center line to the Lidar optical head. The resulting pretilt angle should be applied to the Lidar during installation to ensure measuring wind speed close to hub-height. Lidars also have inclinometers so the tilt angle can also be registered during measurement campaigns and used to check whether the measurements are indeed taking place at the correct height.

Measurement distance and height To measure the free wind stream in front of the rotor, the IEC has stated that measurements should be performed at a distance of 2-4D from the turbine. At 2.5D in front of the turbine, the turbine blockage effect is minimal while the correlation between the measured wind and the actual wind experienced by the turbine is good. 2.5D is therefore often chosen as the applicable measurement distance in front of the rotor.

Using the measurement distance and the tilt angle of the Lidar, the actual height at which is being measured can be calculated. Figure 3.3 shows a graphic description of the measurement height and it can be calculated using the following equation:

$$z_M = z_{OH} - z_{M_{rel}} = z_{OH} - R\tan(\beta_{lidar}) \tag{3.12}$$

where z_{OH} is the height above ground level of the Lidar optical head[6].

Measurement sectors If Lidar measurements are to be used for PCV, neither of the laser beams should be influenced by wakes of neighboring obstacles or turbines. Sectors in which this does occur should be excluded from the database in the same manner as the IEC dictates for PCV using a met-mast. The IEC gives the following equation to calculate the disturbed sector when using a met-mast[1]:

$$\alpha_d = 1.3\arctan\left(2.5\frac{D_n}{L_n} + 0.15\right) + 10 \tag{3.13}$$

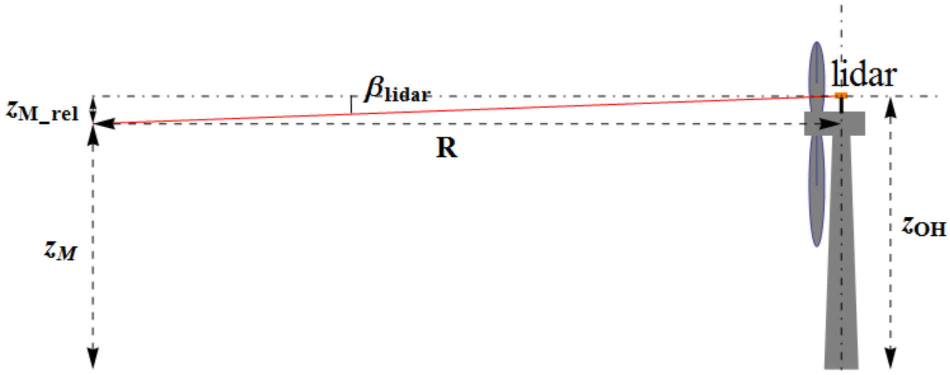

Figure 3.3: *Measurement distance and height of nacelle-based Lidar given the tilt angle and the height of the Lidar optical head[6].*

where D_n and L_n give the rotor diameter of the neighboring turbine or obstacle and the relative distance to it. A met-mast however performs a several vertical point measurements while a two-beam nacelle-mounted Lidar will measure two volumes in the horizontal plane at a distance in front of the turbine. Wagner et al.[6] has therefore advised a slight adjustment to this equation to incorporate using it with a Lidar:

$$\alpha_{Lidar} = 1.3 \arctan\left(2.5\frac{D_n}{L_n - L_b} + 0.15\right) + 10 \tag{3.14}$$

where α_{Lidar} is the width of the disturbed sector to be excluded, D_n is the significant diameter of the neighboring obstacle, L_n is the distance towards the obstacle and L_b is the Lidar measurement range (mostly 2.5D).

3.2.2. SPINNER ANEMOMETERS

As mentioned in the introduction, the second novel wind measurement technique to be compared in this study is the spinner anemometer system developed at DTU. The initial purpose of the device was to detect and eventually correct YM, but more recently studies are also being performed into the applicability in PCV. In the following section, a brief explanation will be given of the working principle of these devices and the necessary steps to be taken during calibration and setup.

WORKING PRINCIPLE

The spinner anemometer system consists of three 1D ultrasonic anemometers, the Metek uSonic-1 anemometers, which are installed on the exterior of the hub cap at azimuth angles of 120° of each other. Sonic anemometers, mainly 3D, have been used in the wind energy industry for a while now although this has always been on the nacelle and behind the turbine rotor. Figures 3.4a and 3.4b give a graphical layout of a typical 1D sonic anemometer and a spinner anemometer system as it would be mounted on the turbine hub cap.

Each sonic anemometer is able to measure the directional wind speeds between its' probes. Due to the perpendicular placing of the anemometers with respect to the spinner, the sonic sensor paths are perpendicular to the rotational velocity component, thereby out-compensating this velocity component. Besides this, comparison of measured and simulated wind speeds have also shown that the influence of the spinner rotation on the measured velocity profiles is minimal and may be ignored. Nonetheless, the spinner anemometer still includes the spinner rotation in its' calculations to be certain[9].

Also, each of the anemometers has a built-in accelerometer with which it can track the sensor's azimuth position relative to the rotor axis. No specific mention was found in reports on spinner anemometers about the working of the accelerometer and how it evades an accumulated error, so-called drift, from occurring. The accelerometer measures acceleration, so, to convert this to the azimuth position, the acceleration has to be integrated twice. When the accelerometer has a slight bias error, this will cause an error in azimuth angle which grows quadratically with time[10]. As no further information was found on this, it is assumed that the accelerometer Romowind has installed in the spinner anemometer has been fixed to avoid this and the azimuth measurements will be correct. Combining the amplitude of the rotation angle and the measured wind speed, the spinner anemometer system can calculate the angle of the wind flow to the rotor (also YM) continuously. How this calculation is done will be explained briefly below.

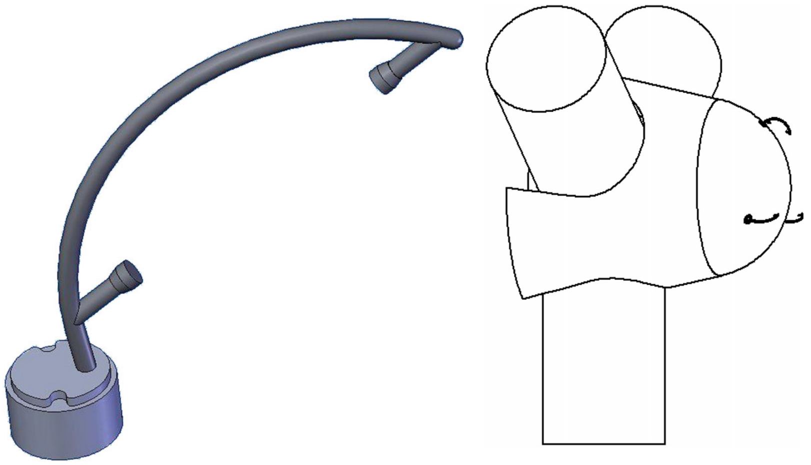

(a) *Typical 1D sonic anemometer*

(b) *Sonic anemometers mounted on hub*

Figure 3.4: *Graphical layout of the spinner anemometer system [8]*

The three sonic anemometers measure wind speed at three positions on the spinner. If the turbine is facing the wind perfectly, an air flow stagnation point forms at the hub nose and the sonic anemometers, if they are placed equidistant from the nose, will measure the same wind speed. Also, the wind speed readings will be constant throughout an entire rotor rotation. *In skew air flow, the stagnation point moves away from the nose. A sonic sensor closer to the stagnation point experiences reduced wind speed, while a sensor further away experiences increased wind speed. This results in a sinusoidal variation in wind speed seen by each sonic sensor during rotation[8].* Figures 3.5a and 3.5b give examples of these sinusoidal variations measured during a wind tunnel test of the system under yawed conditions[11].

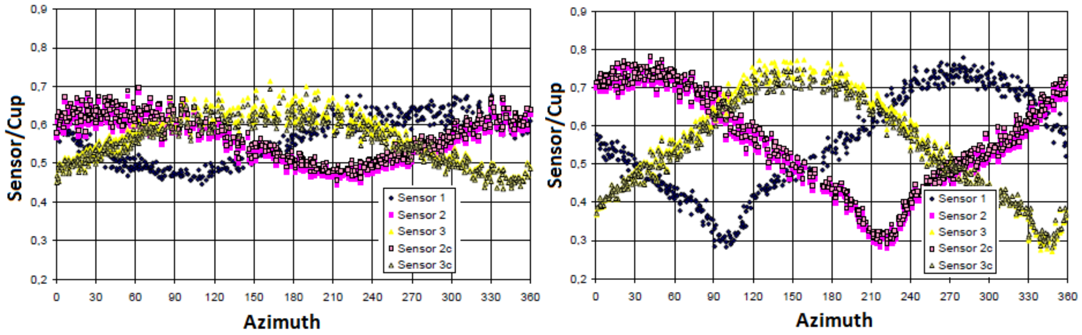

(a) *Output signal of 3 sonic anemometers at a YM of 10°* (b) *Output signal of 3 sonic anemometers at a YM of 20°*

Figure 3.5: *Sinusoidal variations becoming visible in the sonic anemometer wind speed measurements as the turbine is influenced by YM. The index 'c' indicates data has had an internal calibration.[11]*

CALIBRATION AND SETUP

By installing devices on top of the nacelle, the measurements will be influenced by the rotor as is the case with nacelle anemometers. When spinner anemometers are installed on the hub cap however, the turbine also affects the wind flow through rotor blockage and distortion due to the nacelle and blade roots. To compensate for these distortions and to transform the sonic anemometer wind speeds into the horizontal wind speed, yaw misalignment and flow inclination angle at hub-height, a conversion algorithm has been developed by DTU Wind. Pedersen et al. gives an extensive explanation of the algorithm and the methodology applied during calibration in several articles[8][12]. In this section this will be briefly touched upon and the key points for the goal of this thesis will be treated.

The conversion algorithm uses two calibration constants, k_1 and k_2, which are specific to the design of the turbine spinner and blade roots as well as the mounting configuration of the anemometers. The constants are calibrated to convert the measured sonic anemometer wind speed to the free wind conditions at 2.5D, so including blockage effects, ahead of the turbine. How this calibration is done will be explained later on, but first several important relations will be given connecting the spinner anemometer measurements to the required horizontal wind speed and YM at 2.5D.

Spinner anemometer wind speed relations The basic spinner anemometer measurements consist of the three sonic sensor wind speeds V1, V2 and V3, and the rotor azimuth position (ϕ), determined by the accelerometers mounted in each sonic sensor. Figure 3.6 shows how these parameters are related to each other in different coordinate systems complying to the spinner anemometers.

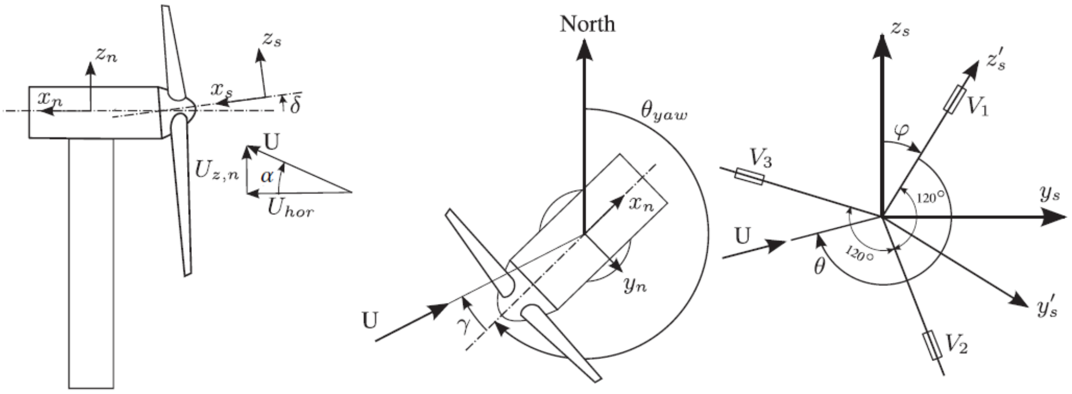

(a) Side view **(b)** Top view **(c)** Front view along the shaft axis

Figure 3.6: *Definition of coordinate systems and variables applicable to the turbine-installed spinner anemometers. The x, y, and z subscripts, s and n, stand for the shaft and nacelle coordinate systems, respectively. The coordinate system with an apostrophe as superscript is the rotating spinner coordinate system. [8]*

Pedersen et al. [8] presents a set of relations which translate these measurements to the vector of the incoming wind speed(U), the inflow angle relative to the axis (α) and the azimuth position of the flow stagnation point on the spinner (θ) in several steps as follows:

$$V_1 = U(k_1 \cos\alpha - k_2 \sin\alpha \cos\theta) \tag{3.15}$$

$$V_2 = U\left(k_1 \cos\alpha - k_2 \sin\alpha \cos\left(\theta - \frac{2\pi}{3}\right)\right) \tag{3.16}$$

$$V_3 = U\left(k_1 \cos\alpha - k_2 \sin\alpha \cos\left(\theta - \frac{4\pi}{3}\right)\right) \tag{3.17}$$

These equations can be rewritten towards:

$$\alpha = \arctan\left(\frac{k_1\sqrt{3(V_1 - V_{ave})^2 + (V_2 - V_3)^2}}{\sqrt{3}k_2 V_{ave}}\right) \tag{3.18}$$

$$U = \frac{V_{ave}}{k_1 \cos\alpha} \tag{3.19}$$

$$\theta = \arctan\left(\frac{V_2 - V_3}{\sqrt{3}(V_1 - V_{ave})}\right) + \pi \tag{3.20}$$

with

$$V_{ave} = \frac{V_1 + V_2 + V_3}{3} \tag{3.21}$$

The equations above can be used to determine the three wind speed components in the fixed nacelle coordinate system as follows:

$$U_x = U(\cos\alpha\cos\delta - \sin\alpha\cos(\phi + \theta)\sin\delta) \tag{3.22}$$

$$U_y = -U\sin\alpha\sin(\phi + \theta) \tag{3.23}$$

$$U_z = -U(\sin\alpha\cos(\phi + \theta)\cos\delta - \cos\alpha\sin\delta) \tag{3.24}$$

with δ representing the shaft tilt angle. Finally, the wind speed components can be used to determine the horizontal wind speed (U_{hor}) and yaw misalignment (γ) with the following equations:

$$U_{hor} = \sqrt{U_x^2 + U_y^2} \tag{3.25}$$

$$\gamma = \arctan\left(\frac{U_y}{U_x}\right) \tag{3.26}$$

The calibration constants, k_1 and k_2 are not directly visible in the above equations but are hidden away in the different wind speed components. In the next section, a brief description will be given of how these constants are determined during calibration.

Calibration procedure The calibration procedure of the spinner anemometer is generally divided into three steps [13] which will be given below:

1. Separate calibration of the individual sonic anemometers performed either as a simple calibration at zero wind speed or in an accredited wind tunnel. The purpose of this calibration step is to find the device offset (at zero wind speed) and the relation between the sonic anemometer readings and the actual wind conditions moving through it.
2. An internal spinner anemometer calibration after installation of the system. The objective of this step is to calibrate the separate sensor paths to each other so as to mimimize mounting errors and non-symmetry of the spinner. In this step, k_1 and k_2 are adjusted for the first time until each sensor measures the same average wind speed over each revolution. This calibration step should be performed at wind speeds higher than 6 m/s in a stable wind direction.
3. Calibration of the turbine type specific constants in order to compensate for the unique spinner, nacelle and blade root geometry of each turbine type. In this step the calibration constants k_1 and k_2 are optimized to make sure that the sonic anemometer readings imitate the free wind conditions affecting the turbine. This step requires the comparison of the spinner anemometer data to either a Lidar or met-mast measuring at 2.5D ahead of the rotor. Finally, the updated calibration constants should be adjusted in the spinner anemometer conversion function.

3.3. YAW MISALIGNMENT

Yaw misalignment (γ) is a phenomenon occurring rather regularly in wind turbines. YM is caused by the turbine not being able to align the nacelle perfectly against the wind and is thereby defined as the difference between the nacelle direction (θ_{nac}) and the actual wind direction (θ_{wind}) acting on the turbine, given by the following equation:

$$\gamma = \theta_{wind} - \theta_{nac} \tag{3.27}$$

Two types of YM are defined; static (or average) and dynamic (fluctuating) YM. Turbines are designed to align with the wind however two main reasons are named for why YM still occurs:

- Yaw controllers and yawing systems generally cannot react fast enough to be able to match the fluctuations in wind direction as this would cause more loads and thus faster degradation of the yaw bearings. This leads to a dynamic YM being induced.
- Wind vane, being the input device to the yaw controller, calibration errors cause the controller to choose the wrong orientation. This generally contributes to the static YM.

The first cause implicates that, unless big improvements in reaction speed of the yawing system occur, a dynamic YM will always remain. The second cause, however, can be compensated effectively if a trusted external device is used to correct the mis-calibration of the wind vane or even used as input device for the yaw controller.

3.3.1. EFFECT OF WIND SHEAR ON IDEAL YAW ERROR

In his research, Goossens[7] found that the produced power seemed to be maximal at a small, positive YM, meaning the ideal yaw error would be unequal to zero. A small positive YM leads to a higher angle of attack (α) in the top of the swept rotor area and a smaller angle of attack at the bottom of the swept area, a higher angle of attack being more favorable. It is suggested that the higher wind speeds at the top of the rotor could cause the more favorable effect to outweigh the unfavorable effect at the bottom of the rotor plane, leading to a small positive ideal yaw error.

In the figures below, the situation described above has been depicted. Figure 3.7a shows a slightly misaligned turbine in a logarithmic wind profile when the rotor blade under investigation is at the top of the rotor.

Figure 3.7b then shows what the influence of the YM is on the airfoil at the top of the swept area, whereby the inflow angle (ϕ) and angle of attack (α) are increased by an angle of $\hat{x}_{YM}$, leading to a higher lift component in the torque.

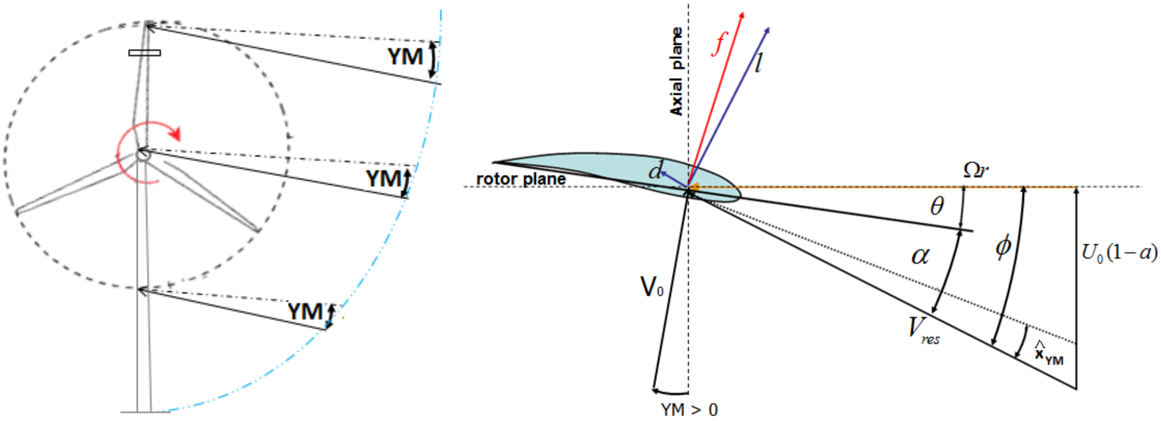

(a) *Misaligned rotor with top blade* (b) *Topview of YM effect on airfoil*

Figure 3.7: *Effect of wind shear on YM at top of rotor plane looking from above.*

The magnitude of the inflow angle change, $\hat{x}_{YM}$, can be calculated using the following trigonometric equation:

$$\hat{x}_{YM} = \arctan\left(\frac{U_0(1-a)}{\Omega r}\right) - \arctan\left(\frac{U_0(1-a)\cos(YM)}{\Omega r - \sin(YM)U_0(1-a)}\right) \tag{3.28}$$

Due to the tip speed ratio, we know that $\Omega r \gg \sin(YM)U_0(1-a)$, meaning this equation can be simplified to:

$$\hat{x}_{YM} = \arctan\left(\frac{U_0(1-a)}{\Omega r}\right) - \arctan\left(\frac{U_0(1-a)\cos(YM)}{\Omega r}\right) \tag{3.29}$$

Whereby, for $YM \neq 0$, $\hat{x}_{YM}$ is positive. The rotor torque on an airfoil can be calculated using the following equation [14]:

$$Q = B\int_{r=0}^{R} dQ = B\int_{r=0}^{R} (l\sin\phi - d\cos\phi)r\,dr \tag{3.30}$$

and, as the power produced is given by the torque multiplied by the angular speed ($P = Q\cdot\Omega$), a higher inflow angle therefore delivers higher power.

Figure 3.8a shows the misaligned turbine with the blade under investigation at the lower part of the swept area. Figure 3.8b shows how the YM decreases the inflow angle and angle of attack, thereby leading to a lower lift and higher drag component of the torque. In effect, this leads to less power at the bottom of the rotor.

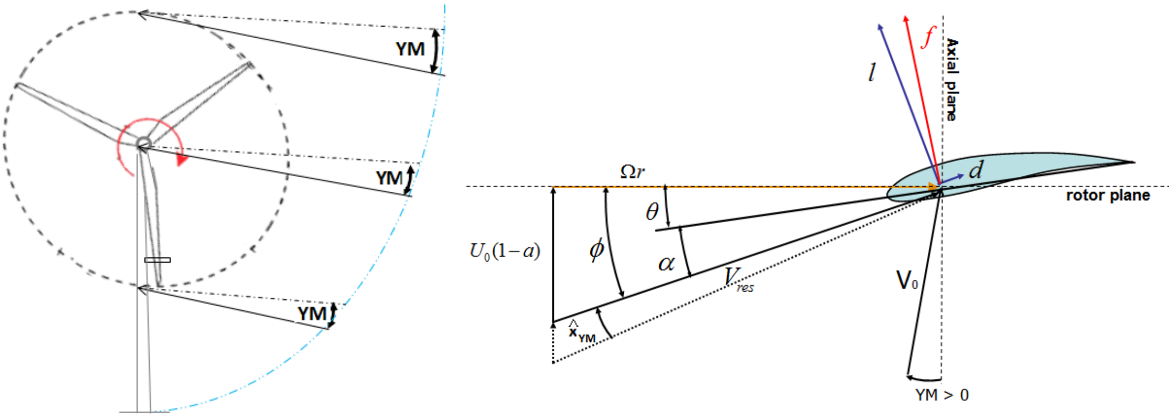

(a) *Misaligned rotor with bottom blade* (b) *Topview of YM effect on airfoil*

Figure 3.8: *Effect of wind shear on YM at bottom of rotor plane looking from above.*

Finally, due to wind shear, it is expected that the favorable conditions at the top of the rotor are reinforced by the higher wind speeds thereby outweighing the lost torque/power at the bottom of the rotor. This would mean that it would be possible to find a relation between the wind shear exponent and the yaw error at which the power produced is maximum.

4

LITERATURE REVIEW

Following the research questions and theoretical background presented in the previous chapters, a literature review has been performed in order to distinguish what research has already been done on the aforementioned topics. In the following sections, a brief overview of the research done so far will be presented.

The literature review will be presented in the same structure and order as the research questions; starting with an overview of the research performed on novel measurement devices, followed by the topic of yaw misalignment and its' effect on power performance and ending with a review of research done on the effects of turbulence and wind shear on the power performance.

4.1. MEASUREMENT DEVICES

The novel measurement techniques to be investigated during this thesis are Lidars and spinner anemometers. Due to its' widespread use in other industries for nearly 50 years, a lot of research has already been done on Lidars' accuracy and applicability in the wind industry. For spinner anemometers, being a newer technology, not a lot of research has been performed on this topic. These devices will be treated separately in the following part.

Lidars The main interests for implementation of Lidars, particularly nacelle-based, in wind energy is as an input of the yaw and pitch control algorithms. As it is able to measure the wind conditions coming towards a turbine, a Lidar's measurement can be used as predictive control input to reduce loads and increase power output. To make this a trustworthy control system, a good accuracy of the Lidar's wind conditions measurements is necessary.

The accuracy of Lidar has been studied in varying circumstances and setups. The most common and trusted way is to compare the Lidar's correlation with an IEC compliant met-mast placed within 2-4D of the Lidar. In a study executed by Feeney et al.[15] at a wind park in South England both a nacelle-based and ground-based Lidar were used to measure wind speeds over the complete rotor and measured a correlation close to unity was found with $R^2 = 0.999$. Also, using the Lidars in PCV did not add extra, significant uncertainty in this study. In a different study, performed by Giyanani at the ECN test site at Wieringermeer, the Netherlands[16], two vertical scanning pulsed Lidars were placed close to a met-mast having both cup and sonic anemometers. Once again the wind speed measurements by the Lidars and cup and sonic anemometers showed correlations close to unity and $R^2 = 0.994$ and $R^2 = 0.997$, respectively. Additionally, wind direction measurements also showed a good correlation.

A different experiment was done at DTU Wind Energy with a Lidar being placed in the rotating spinner[17][18], instead of the hub cap so to say. This experiment was focused on using Lidar to measure yaw misalignment and the wind conditions ahead of the turbine. It was found that these measurements were comparable to met-mast data although more research was necessary into control integration and the effects this would have. Kragh et al.[18] concluded that this approach has a good correlation of yaw error estimation with met-mast data and could therefore be used in a Lidar-based yaw controller. Doubts were however placed on how more complex flow conditions with, for instance, yawed inflow, horizontal wind shear, sloped inflow and vertical wind shear will influence the Lidar velocity measurements. For instance, *a yawed inflow will cause a 1P* *variation in angle of attack and relative airfoil velocity that will induce a 1P variation in the blade root bending moment antisymmetric around the horizontal axis of the turbine. The true axial velocity will in this case be constant in the entire rotor plane, whereas the axial velocity estimated from the LIDAR measurements will have a 1P variation antisymmetric around the vertical axis of the rotor[18].*

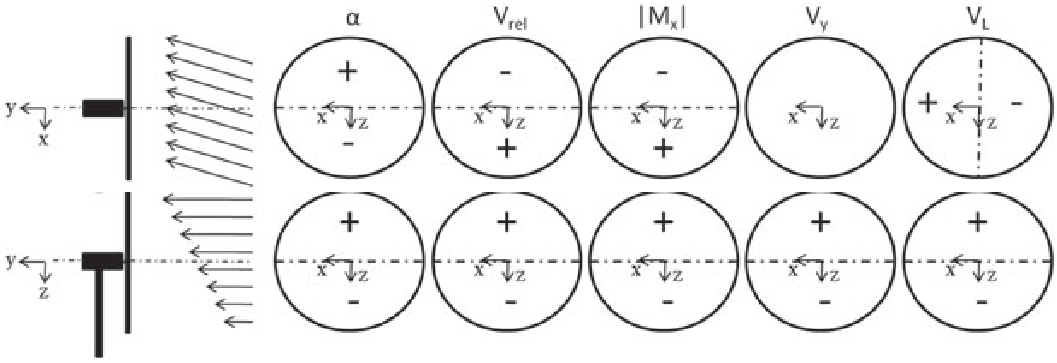

Figure 4.1: *Effects of yawed inflow and wind shear on angle of attack, relative airfoil velocity, blade root moment, axial velocity and velocity measured by Lidar, respectively.[18]*

Wagner is a researcher from DTU who has performed several studies on the application of Lidar in wind resource assessment and power verification. During an experiment at the Danish wind farm Avedore, a nacelle-mounted Lidar was used to measure wind conditions and the readings were compared with an adjacent met-mast[19]. Wagner et al. found that the two-beamed Lidar has problems to measure wind direction accurately in non-uniform horizontal wind conditions, e.g. in the wake of another turbine or the met-mast. The paper proposes a complementary filtering process to filter out these corrupted Lidar measurements. The experiment at Avedore shows very high correlations of Lidar and cup anemometer measurements both at 2D and 2.5D in front of the turbine, hence the measured PCs are very similar too. Lidar seems to have a slightly lower category A uncertainty than met-mast cup anemometers but a higher category B uncertainty, the average combined Lidar uncertainty thus staying slightly above that of the nacelle anemometers. The category A uncertainty is connected to the statistical uncertainty of the quantities being measured whilst category B is related to the instruments, the data acquisition system and the terrain on which measurements are done. Wagner performed an identical experiment at a different site[20] whereby once again good correlations were found. Also, the Lidar was able to measure in free wind sectors whereby the met-mast was in a wake, thus increasing the wind sector which can be measured, one of the advantages of using a Lidar.

Recently, Goossens[7] presented his conclusions on a field-test where a nacelle-mounted Lidar was used to detect wind conditions for the purpose of detecting yaw misalignment. This data was compared to Sonic Detection and Ranging (Sodar) measurements taken nearby. Although Sodar is not yet a standard means of data validation, the measurements show a good correlation close to unity, even though the coefficient of determination is lower than in the previous experiments with met-masts $R^2 = 0.95$. Looking at YM measurements, no correlation was found. This was partially accounted to errors in the accuracy of the Sodar but also named a higher direction inaccuracy of the Lidar than claimed by the manufacturer (4° instead of 0.5°).

Some research has also been done about the possibility of Lidars to measure TI and WS but there is no clear consensus yet whether Lidar can measure these conditions accurately. Wagenaar et al. [21] and Krishnamurthy et al.[22] found that Wind Iris TI measurements compare quite well to met-mast measurements. Slinger et al.[23] used a nacelle-mounted Zephir Lidar to investigate the effects of shear and TI on power curve measurements. It was found that the Lidar can be used to detect TI and shear and even be used to determine the rotor equivalent wind speeds, however no validation device was in the vicinity of the Lidar to make conclusions about the accuracy of the measurements. In comparing Sodar and Lidar TI measurements, Goossens[7] found that no conclusive results on the accuracy could be made either. Finally, whether a Lidar can determine shear depends on the possibility of the instrument to measure at different heights.

Bot has also studied accuracy of two ground-based Lidars in turbulence assessment for ECN as part of the LAWINE project[24]. The results show that the Lidars measure TI in closer agreement with the sonic anemometers than with the cups of the adjacent met-mast. Especially at lower wind speeds (< 4 m/s), this correlation is visible as the cup anemometers measure the lowest TIs. This is explained by the higher response time, due to inertia of the cups, of the cup anemometer to deviations in wind speed. On the other hand, the Lidars measure slightly higher TIs at low wind speeds, which is *probably due to the assumption of a homo-*

geneous velocity field inside the measuring volume, which is a less valid assumption at lower wind speeds. As wind speeds increase, the Lidars measure TIs just below (<0.5%) those by sonic anemometers and just above (<1%) those of the cups. Generally, the Lidars' TI measurements are in between the cup and sonic anemometers, meaning the accuracy compared to the standardized devices is satisfactory.

Finally, research on the possibility of Lidar to measure YM and the benefits of using this as input for yaw controllers can also be found in literature. As mentioned earlier, Kragh et al.[18] found that Lidar measurements of YM have a good correlation with met-mast readings and can therefore be suitable for Lidar-based yaw controlling. In other studies[23] [25], an average YM was measured and statically adjusted in the yaw controller function leading to power production increases of 2 to 5%. Scholbrock et al. [26] found that the nacelle wind vane experienced a bias mainly when the turbine was operating, an occurrence which would disappear when Lidars are to be used as yaw controller input. Byrne et al.[27] looked into the financial benefits to be gained by using Lidar based wind turbine control. Simulations were done using a Monte Carlo tool and it concludes that retrofitting existing turbines would extend lifetimes from 20 to 26 years allowing for a possible decrease of 8% in Cost of Electricity (COE). The uncertainty in loads reduction benefits was however found to be rather high causing a high uncertainty/standard deviation of 3% for the COE-decrease. The simulation weighs the reduced loads on the turbine, the additional O&M and investment costs of the Lidar and the additional wind power which can be harvested.

Spinner Anemometers Spinner anemometers have been invented as an accurate way of correcting YM in turbines. This has resulted in most of the early research being done on the device to be aimed at improving calibration steps and investigating the accuracy of the spinners to measure wind direction and YM. Only recently more focus has gone to the usability in PCV, in other words to measure the wind speed accurately. Nonetheless, little literature is currently available on these devices as they are still in development.

Pedersen et al.[8] tested five different calibration methods for the device using both field-tests and simulations. The preferred method of calibration was chosen to be by yawing the turbine in and out of the wind while in stopped condition. The YM measurement uncertainty remaining after calibration was found to be approx. 10%.

In a field test [28] with a 3D sonic anemometer placed next to the spinner setup, good correlations of wind speeds close to unity were found. This initial result was based on few data points (3 hours of measuring) so cannot be fully relied on. Following this, a full scale test was done on a 3.6MW test turbine for about one year. Here once again a good correlation with the met-mast for both wind speed and direction was achieved. This would mean that, when correctly calibrated, spinner anemometers can be used in yaw control as well as PCV.

The next research step by Pedersen et al. was for a wind park in Denmark, Tjaereborg Enge, consisting of 8 Vestas V80 turbines and a met-mast[29]. In this study it was demonstrated how important both wind-tunnel and in-site calibration is, whereby the spinner anemometers were also compensated for the induction effects. After these corrections, the wind direction and speed measurements were well correlated with those of the met-mast. Besides this, the spinner anemometers were also able to measure flow inclination and TI and once again the TI measurements seem to agree with met-mast albeit with a larger spread than with wind speed and direction scatters.

4.2. YAW MISALIGNMENT

As mentioned in the previous section, several researchers have looked into measuring YM on operational turbines using various measurement devices. Initial studies into the presence of YM were done with an IEC-compliant met-mast placed in the vicinity (2-4D) of the turbine under investigation [30][31] whereby the static YM could be calculated and, if necessary, manually corrected in the yaw controller function. Several studies were performed with Lidars, either nacelle-mounted or ground-based, mostly comparing the acquired YM with adjacent met-mast or sodar readings. Mikkelsen et al.[17], Kragh et al.[18] and Fleming et al.[25] found that the YM-estimation by Lidar compared well to met-mast estimations.

Goossens[7] found the correlation between wind direction, and thereby YM, measurements of the Lidar and Sodar to be non-existent. On one hand, this is dictated to a high uncertainty in Sodar and Scada measurements, whilst, on the other hand, the uncertainty in the Lidar measurements is also estimated to be higher than initially claimed (<0.5°). No conclusive reasons are found for this increased uncertainty as, even in the free stream wind directions, a large spread in YM estimations is found. It is suggested that the dike on which the turbine is situated might have an influence.

Pedersen et al. performed tests with spinner anemometers comparing these with an IEC-compliant metmast placed in the vicinity[28][29]. Correlations of YM estimations between the measurements were found to be good. In a calibration study [8], the spinner anemometers are found to have a YM uncertainty of 10%.

Although it has become clear in many prior studies that YM does indeed occur frequently in wind turbine operation, no clear consensus has yet been presented what the effect of YM is on the power performance of a turbine. Kragh et al.[31] suggest that a perfectly aligned turbine can extract a maximum power from the wind based on the following relation:

$$P_{max} = \frac{1}{2}\rho A_r V_p^3 C_p \tag{4.1}$$

where ρ is the density, A_r the rotor area, V_p is the wind speed perpendicular to the rotor and C_p is the power coefficient. If the turbine is not perfectly aligned, the perpendicular wind speed is reduced to:

$$V_p = V_0 cos(\theta_{YM}) \tag{4.2}$$

where V_0 represents the actual free wind speed and θ_{YM} is the YM angle. This would mean that the extractable power is reduced by a factor $cos^3(\theta_{YM})$. Experimental studies have however found varying cosine exponents, requiring a more generalized equation for the extractable power:

$$P_{max} = \frac{1}{2}\rho A_r V_0^3 cos^n(\theta_{YM}) C_p \tag{4.3}$$

Values for n have been determined experimentally ranging from 1.8 up to 5 in prior studies.[31][32][33]

All the researches are however clear that correcting YM would improve the power performance of a turbine. Kragh et al. found power increase of 1-5 percent for a turbine with high YM [30] and for another turbine no significant power increase due to hardly any misalignment of the turbine[31]. Another reason for the non-significant improvement was dictated to the idea that YM only affects power performance at wind speeds below rated. Fleming et al.[25] performed tests on a turbine with a static YM of 9°, and, by correcting it, was able to increase power capture by 2.4%.

The ultimate way to decrease both dynamic and static YM is seen to be by implementing accurate, high-frequent wind direction measurements into the yawing system. So far such experiments have not been executed, but the effects and possible gains have been modeled. Schlipf et al.[34] modeled the energy to be gained by using a Lidar-based yaw controller whereby it was found that several percentages production increase could be expected varying per turbine and site wind conditions. Nonetheless it is not deemed possible to totally correct YM, as this would need immediate yawing which, in turn, would increase the loads on the turbine and its' yawing mechanism.

Goossens[7] suggested that the higher wind speeds at the top of the rotor might have a different influence on YM than the lower wind speeds at the bottom of the rotor. This would lead to an ideal yaw error unequal to 0° and that a higher wind shear would most probably favor a higher absolute ideal yaw error. To check this, it might therefore be interesting to consider the effect of wind shear on the ideal yaw error. No relevant literature was found on this topic, but an analytical study has been done on the effects of non-uniform velocity distributions on the Betz-Joukowsky limit.[35] By derivation, Chamorro found an analytic correction to the Betz-Joukowsky limit, the maximum efficiency of an ideal rotor, accounting for the non-uniform ABL velocity distributions (i.e. logarithmic wind profiles) on the rotor. The maximum power coefficient is slightly higher for non-uniform Atmospheric Boundary Layer (ABL) velocity distributions than for uniform ones with an increase of 1-2% for a standard turbine depending on the terrain roughness. A similar analytic correction might be applicable for the definition of the ideal yaw error.

4.3. OUTER ENVELOPE CONDITIONS

Several guidelines have been attached to turbine operation and power performance measurements by the IEC standards[36][1], one of which is that measurements with data out of the certified operating range of the turbine should be excluded from the used dataset. Currently, manufacturers deliver turbines which have a guaranteed PC only under certain turbulence intensity and wind shear conditions (typically TI = 10-12% and shear exponent = 0.15-0.2[37]) which were applicable during PC tests. The locations where the turbines are placed do experience wind conditions outside of these certified ones while producing power. It is not yet clear how the outer envelope conditions influence the power performance while turbine operators, like e.g. Vattenfall, would like to increase the accuracy of power performance assessments. The Power Curve Working Group (PCWG) has therefore taken up the task of investigating this and eventually propose adjustments to the certification procedures and guidelines. In the following section, the work on this topic so far will be presented.

The proposed new IEC power performance standard is going to include corrections for both wind shear and turbulence intensity. In an exercise performed by PCWG-members for a dataset from Sweden it was found that the outer conditions do influence the power performance and can cause a decrease in AEP between 0.25-1%[38]. Antoniou et al. on the other hand found that filtering data for low shear, low veer and higher TI increased the AEP by 2% although it is considered that the filtering might have influenced the energy content[39]. This result is therefore not deemed conclusive.

Next, Clerc[40] re-analysed several power performance tests for different turbines and sites in Europe and North America. He found that high TI leads to a higher AEP around cut-in wind speed of the PC while low TI leads to higher AEP around the rated wind speed. Also, this study showed that the proposed IEC TI correction does decrease PC variation compared to the base case and that this can lead to an increase in accuracy in energy prediction.

Villanueva[41] also found that the same kind of behavior of TI on power performance during his MSc Thesis, in which two limited datasets were analyzed and Bladed simulations were performed. He found that wind shear had a less significant influence on the power curve than TI and that compensating for it by applying the equivalent wind speed correction did not lead to a significant improvement, also since the correction brings with it an additional uncertainty. In general, Villanueva found during his research that the change in AEP with shear and TI was minimal and lie within the PC's uncertainty of around 5%, partly because the effects of TI cancel each other out.

Finally, Clifton et al.[42] studied the working of the IEC-proposed turbulence renormalization method, comparing it to the current method of binning used in turbine performance validation. The study concluded that the renormalization method does capture the variation in turbine performance due to turbulence better than the method of binning, whereby it clearly reduces the spread of predicted and observed turbine power data.

5

RESEARCH SETUP

In this chapter the steps taken during this research will be explained. First, a description of the investigated sites and measurement campaigns will be given. This will be followed by the research methodology applied during this thesis and will be closed off with a brief explanation of the analysis tools used in the research.

5.1. SITE DESCRIPTION

During this research period, different measurement campaigns will be performed. In the following section, the sites at which these campaigns will be performed, Prinses Alexia and Norrekaer Enge, will be described.

5.1.1. WIND PARK PRINSES ALEXIA

TEST SITE

Geographical layout This Vattenfall-owned wind park is located in the Dutch Flevopolder close to Zeewolde, the Netherlands (see Fig. 5.1a). It consists of 36 Senvion 3.4M104 wind turbines which have been placed in 3 converging rows. The terrain at this site is mainly farmland partly surrounded by small trees and therefore defined as flat and non-complex. As this region is very favorable for wind energy exploitation, there are a lot of turbines surrounding the wind park. In the section on data validation the implications on the free wind sectors will be explained. Figure 5.1b shows the geographical layout of the wind farm. The turbines being investigated are depicted as R01 and R02 in the layout.

Free wind sector Before analysis can be performed it is important to consider which wind sectors should be discarded from the dataset because of disturbances by nearby obstacles or other turbines. For the case of wind park Prinses Alexia the terrain around the met-mast and turbines R01 and R02 is mostly farm land so the only obstacles to be taken into account in this case are the other turbines in the park. Also, the free wind sector incorporates that both the met-mast and the turbines under investigation should not be in the wake of another turbine within a significant distance of 8D. For instance, for wind directions between 350° and 140° the met-mast is in the wake of one or more of the first 5 turbines in its' vicinity, meaning this measurement sector has to be discarded. On the other hand, R02 is in the wake of R01 for wind directions between 280° and 340° and in the wake of RB-03 for 105° up to 165°. Therefore it was finally chosen to use the range of 165° to 280° as the undisturbed measurement sector. This sector is shown by the red lines given in Figure 5.1b.

Turbine characteristics The park has been operational since September 2013. Table 5.4 displays the characteristics of the turbines at Prinses Alexia as given by the manufacturer. One difference between turbines R01 and R02 is their gearbox, turbine R01 has an Eickhoff gearbox (ratio = 1:87.2) while R02 has a Moventas gearbox (ratio = 1:86.4). This could lead to differences in behavior of the specific turbines.

Measurement devices used As shown in Figure 5.1b, an IEC-compliant met-mast has been installed 222m (2.13D) at 28° from South of turbine R01 and 405m (3.89D) at 100° from South of turbine R02. The met-mast was equipped with MEASNET, wind tunnel calibrated, first class advanced anemometers and wind vanes as

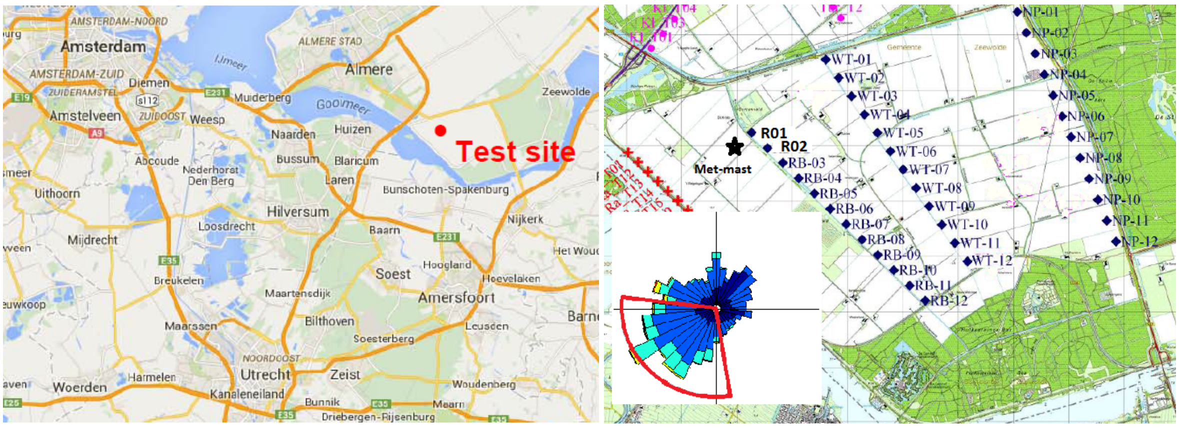
Amsterdam
Almere
Zeewolde
Amstelveen
Weesp
Muiderberg
Huizen
Naarden
Test site
Bussum
Blaricum
Laren
Bunschoten-Spakenburg
Uithoorn
Abcoude
Hilversum
Loosdrecht
Baarn
Nijkerk
Mijdrecht
Breukelen
Soest
Hoogland
Amersfoort
Maarssen
Bilthoven
Leusden
Utrecht
Zeist
Woerden
Harmelen
Woudenberg
Met-mast
R01
R02
WT-01
WT-12
RB-03
RB-12
NP-01
NP-12

(a) *Location in the Netherlands*

(b) *Site layout including free wind sectors*

Figure 5.1: *Graphical description of wind park Prinses Alexia*

Table 5.1: *Specifications of Prinses Alexia turbines*

Manufacturer type	Senvion 3.4M104
Rated Power	3.37 MW
Hub height	98 m
Rotor diameter (D)	104 m
Rated wind speed	13.5 m/s
Cut-in, cut-out wind speed	3.5 m/s, 25 m/s
Minimum and maximum rotor speed	7.1-13.8 rpm
Yaw drive adjusting speed	0.5°/s
Rotor shaft tilt angle	5°
Control	Pitch control with variable speed (MPC293)

well as additional air temperature, pressure and humidity measurement devices. Table 5.2 gives the detailed configuration of the met-mast at Prinses Alexia. Finally, in both turbines under investigation independent power transducers were installed to measure the electrical power output of each turbine simultaneously with the wind conditions.

Table 5.2: *Specifications of met-mast at Prinses Alexia*

Device	**Height [m]**	**Orientation from North**
Wind vane	46.3	134°
Wind vane	96.1	130°
Cup Anemometer	46.4	318°
Cup Anemometer	96	308°
Cup Anemometer	98	308°
Cup Anemometer	98	130°
Raingauge	4	n.a.
Thermometer	96.3	n.a.
Rel. humidity probe	96.3	n.a.
Barometer	95.8	n.a.

MEASUREMENT CAMPAIGN

The met-mast was installed at the end of January 2015 and measurements were performed from 3 February 2015 and are still continuing at the moment of writing. For the purpose of power performance analysis, the data covers the period of 3 Feb.- 7 July 2015. Besides the met-mast and power measurements, additional data necessary for more accurate and thorough analysis was acquired from the turbines' Scada systems for the same period. The signals deemed of interest are the following: turbine availability, yaw angle, blade pitch, rotor speed, generator speed and torque and nacelle anemometer and wind vane readings.

WEATHER CONDITIONS

Over the period of the measurement campaign an average wind speed of 7.07 m/s was measured by the met-mast at hub-height. Figure 5.2a displays the wind distribution at the site Prinses Alexia with Weibull fits according to the methodology described in Appendix A. Table 5.3 displays the Weibull parameters found using the different estimation methods at Prinses Alexia. Taking the goal of energy production by WTGs into consideration, the Weibull distribution found using the WAM (A=7.81 and k=2.09) is thought to be the best fit to the measured wind distribution as the power densities compare best. Looking at the fitted lines in the figure however, it might be considered that the Least Square Estimation method is better. In further calculations the WAM-method is considered to be the most accurate as it considers both the total energy content of the binned distribution as the same total distribution above mean wind speed as the measured distribution.

Table 5.3: *Weibull parameters and energy content found with different Weibull estimation methods at Prinses Alexia for the period of Feb-July 2015.* $V_{mean} = 7.01 m/s$

Method	**Shape (k)**	**Scale (A)**	**Power density (E) [W/m^2]**	**Measured E [W/m^2]**
Least Square Estimation	2.35	7.83	677.44	742.08
Matlab 'wblfit.m'	2.24	7.92	727.24	742.08
Wind Atlas Method	2.09	7.81	742.27	742.08

Figure 5.2b displays the wind rose measured by the met-mast at Prinses Alexia during the measurement campaign. The prevailing wind direction is, as is the case for most of the Netherlands, Southwest. Also, the winds from the Southern to Western directions (bottom-left quadrant of the wind rose) show the higher 10-minute averages.

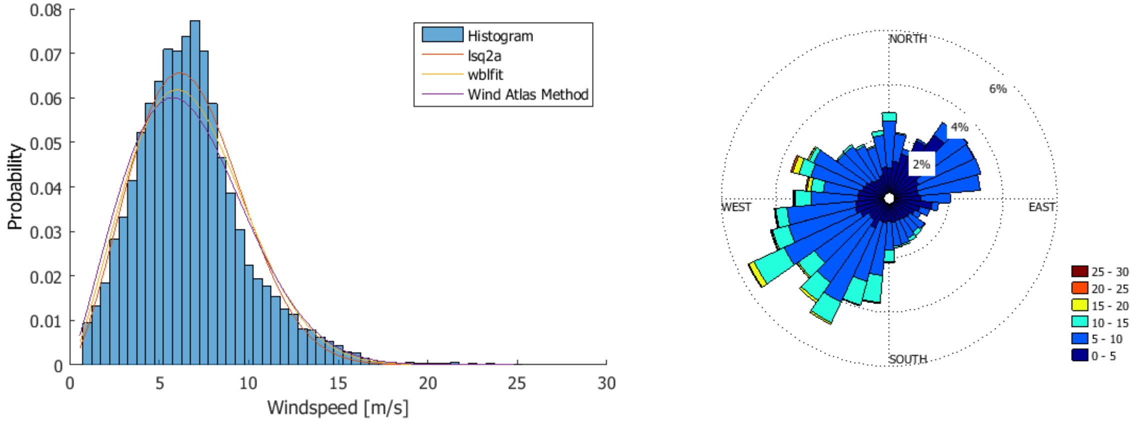

(a) *Wind distribution at Prinses Alexia*

(b) *Wind rose at Prinses Alexia*

Figure 5.2: *Wind conditions at wind park Prinses Alexia for the period of February - October 2015.*

5.1.2. WIND PARK NORREKAER ENGE

TEST SITE

Geographical layout This Vattenfall-owned wind park is located in Northern Denmark(see Fig. 5.3a). It consists of 13 SWT 93 2.3MW Siemens wind turbines which have been placed in a straight line along 75° North with a spacing of 485m. The terrain at this site is defined as flat and non-complex. Figure 5.3b shows the geographical layout of the wind farm.

Free wind sector Before analysis can be performed it is important to consider which wind sectors should be discarded from the dataset because of disturbances by nearby obstacles or other turbines. For the case of wind park Norrekaer Enge the terrain around the met-mast and turbines 4 and 5 is mostly farm land to the South and water to the North. The only obstacles to be taken into account in this case are the other turbines in the park. Also, the free wind sector incorporates that both the met-mast and the turbines under investigation should not be in the wake of another turbine within a significant distance of 8D. For instance, for wind directions between 30° and 95° the met-mast is in the wake of turbine 5 and for the sector between 260° and 330° it is in the wake of turbine 4. Also turbine 4 is in the wake of its adjacent turbines for wind directions between 35° - 95° (turbine 5) and 225° - 285° (turbine 3). These sectors therefore have to be discarded, resulting in a final measurement sector of 95° to 225° and 330° to 30° as shown by the top-left red lines in Figure 5.3b.

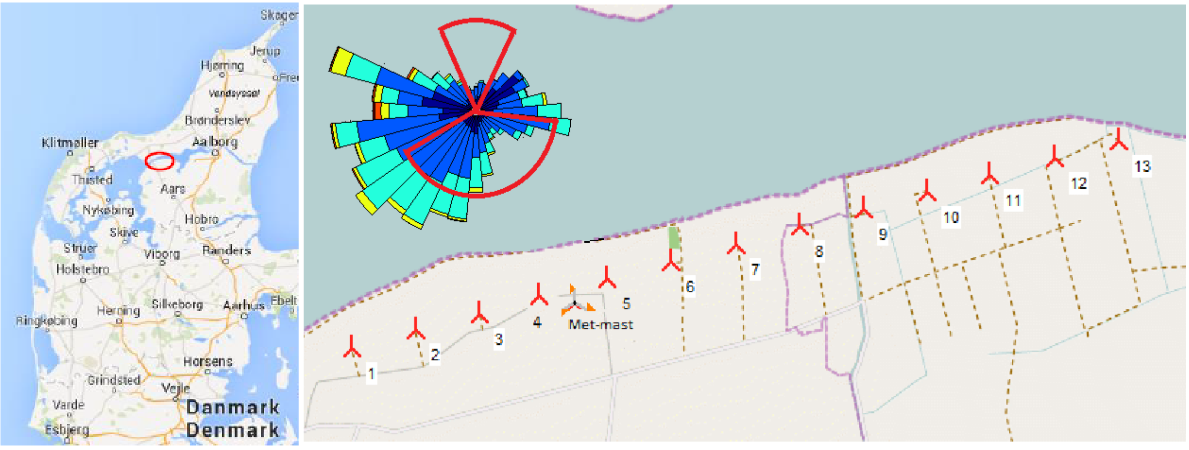
Skagen
Jerup
Hjørring
Frei
Vendsyssel
Brønderslev
Klitmøller
Aalborg
Thisted
Aars
Nykøbing
Skive
Hobro
Struer
Viborg
Randers
Holstebro
Herning
Silkeborg
Aarhus
Ebelt
Ringkøbing
Horsens
Grindsted
Vejle
Varde
Danmark
Esbjerg
Denmark
1
2
3
4
Met-mast
5
6
7
8
9
10
11
12
13

(a) *Location in Denmark* (b) *Layout of wind park with met-mast near T4 and T5 including the free wind sector.*

Figure 5.3: *Geographical description of wind park Norrekaer Enge*

Turbine characteristics The park has been operational since the end of 2009. Table 5.4 displays the characteristics of the turbines at Norrekaer Enge as given by the manufacturer.

Table 5.4: *Specifications of Norrekaer Enge turbines*

Manufacturer type	Siemens SWT 93 2.3MW
Rated Power	2.3MW
Hub height	80m
Rotor diameter (D)	93m
Rated wind speed	13-14 m/s
Cut-in, cut-out wind speed	4 m/s, 25 m/s
Minimum and maximum rotor speed	6-16 rpm
Yaw drive adjusting speed	Unknown
Rotor shaft tilt angle	6°
Control	Pitch regulation with variable speed (WTC 3.0)

Measurement devices used As shown in the layout, an IEC-compliant met-mast was raised and installed by DTU Wind Energy 2.5 rotor diameters (234 m) East-southeast of turbine 4 and three rotor diameters Southwest of wind turbine 5 in October 2014. The met-mast was equipped with MEASNET, wind tunnel calibrated, Class A anemometers and wind vanes. Table 5.5 displays the detailed configuration of the met-mast.

Table 5.5: *Specifications of met-mast at Norrekaer Enge*

Device	**Height [m]**	**Orientation**
Wind vane	33.5	70°N
Wind vane	57.5	70°N
Wind vane	78	70°N
Cup Anemometer	33.5	70°S
Cup Anemometer	57.5	70°S
Cup Anemometer	78	70°S
Cup Anemometer	80	Top
Sonic Anemometer	76	10°S
Rain gauge	2	n.a.
Thermometer	78	n.a.
Rel. humidity probe	78	n.a.
Barometer	78	n.a.

Besides this, a nacelle-based Lidar from AventLidar, the Windiris, was installed on the nacelle of turbine 4, aligned with the nacelle axis, and operated according to the manufacturer's specifications. It was set to measure 234 m (2.5D) in front of the turbine.

Finally, spinner anemometers were installed on all the turbines in the park according to DTU Wind Energy and Romowind standard installation and calibration procedures. The spinner anemometer equipment also determined the nacelle direction as well as the air temperature and pressure enabling calculation of the air density. The power production from the turbines was measured with equipment independent of the Scada system, and this data was also collected by the spinner anemometer monitor equipment. The first set of spinner anemometers were installed on Turbine 4 in August 2014 while the rest of the turbines were equipped in October and November 2015.

MEASUREMENT CAMPAIGN

The Lidar was used only for three months for the period of November 2015 till the end of January 2015, mainly to use as comparison with the spinner anemometers and met-mast at Turbine 4. For the purpose of comparing the three measurement devices, time synchronized wind data was collected in parallel from the nacelle Lidar, the spinner anemometer and the met-mast during study period of 1 November 2014 till 21 January 2015. Also, Scada data, from turbine 4 was gathered over this period. After this test period the Lidar was removed from turbine 4.

The spinner anemometers and met-mast were left in place to perform an analysis on YM of the entire wind park. Measurement data is available from the met-mast and spinner anemometers from their individual installation until 30 April 2015. This is deemed to be a sufficiently representative time period to perform the analyses named earlier.

WEATHER CONDITIONS

Over the period of the measurement campaign an average wind speed of 8.22 m/s was measured by the met-mast at hub-height. Figure 5.4a displays the wind distribution at the site Norrekaer Enge with Weibull fits according to the methodology described in Appendix A. Table 5.4a displays the Weibull parameters found using the different estimation methods at Prinses Alexia. Taking the goal of energy production by a WTG into consideration, the Weibull distribution found using the Wind Atlas Method (WAM) (A=9.21 and k=2.27) is thought to be the best fit to the measured wind distribution as the power densities compare best. In further calculations the WAM-method is considered to be the most accurate as it considers both the total energy content of the binned distribution as the same total distribution above mean wind speed as the measured distribution.

Figure 5.4b displays the wind rose measured by the met-mast at Norrekaer Enge during the measurement campaign. The prevailing wind direction is Southwest. Also, the winds from the more Western directions show higher 10-minute averaged wind speeds.

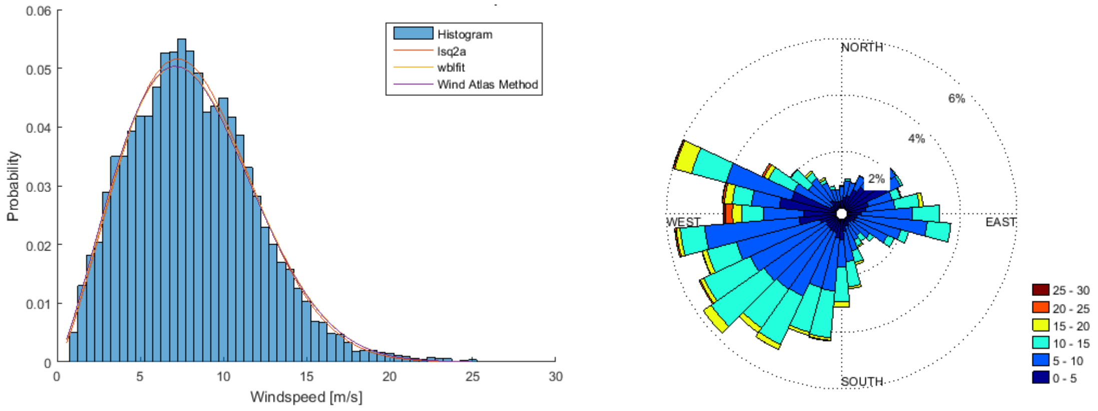

(a) *Wind distribution at Norrekaer Enge*

(b) *Wind rose at Norrekaer Enge*

Figure 5.4: *Wind conditions at wind park Norrekaer Enge over the period October 2014 till April 2015.*

Table 5.6: *Weibull parameters and energy content found with different Weibull estimation methods at Norrekaer Enge for the period of Oct. 2014 -April 2015.* $V_{mean} = 8.17 m/s$.

Method	**Shape (k)**	**Scale (A)**	**Power density (E) [W/m^2]**	**Measured E [W/m^2]**
Least Square Estimation	2.32	9.20	1111.11	1139.23
Matlab 'wblfit.m'	2.28	9.23	1133.96	1139.23
Wind Atlas Method	2.27	9.21	1134.00	1139.23

5.2. RESEARCH METHODOLOGY

The research methodology will be divided over the sub-questions as these need a different approach.

Sub-question 1: Comparison of accuracies of novel techniques to an IEC-complient met-mast
A measurement campaign has been performed by Romowind in cooperation with Vattenfall and DTU since November 2014 and will be continued till November 2015. The campaign includes Lidar, spinner anemometer and met-mast data for the onshore wind farm Norrekaer Enge in Denmark and is performed to investigate the accuracy (and potential benefits) of spinner anemometers compared to Lidars and met-masts.

To answer the first sub-question, a study into the correlation between wind speed, wind direction and TI measurements of a Lidar and the spinner anemometers compared to an IEC compliant met-mast will be performed. The way to determine this accuracy is by applying a linear regression fit to the scattered measurements and quantifying the coefficient of determination(R^2). In the ideal case, the fit should be close to y=x and have an R^2-value close to 1.

Also, a closer look will be taken into regimes where these devices might be less suitable. Literature dictates that spinner anemometers or Lidars might be less accurate in conditions like, for instance, high/low wind speeds, high turbulence or wind shear. Filtering for these different conditions and then performing the same analysis as described above, something can be said about their individual effects on the accuracy of the devices.

Finally, the novel devices' applicability for PCV will be investigated by actually applying the IEC-dictated method to the device measurements. The resulting PCs will be compared to the reference PC as well as the met-mast deducted PC for the same dataset. A more clear comparison will also be obtained by comparing the AEPs resulting from the measured PCs.

Sub-question 2: Accuracy of measuring Yaw Misalignment with different techniques and determining the relation between YM and power performance.
The ability of the aforementioned measurement devices to measure YM corresponds to how accurately the wind direction can be measured. As this will be researched in the first sub-question, it will not be treated deeper here.

The effect of YM on power performance is more complicated to find a good answer for. It can be expected that different models of turbines (and control algorithms) will react differently to YM hence it is good to perform different analysis on several wind turbine models.

The first investigation will be performed by means of Bladed simulations. Incoming yawed conditions will be simulated at different YM angles ranging from -20° to +20° after which the PCs will be calculated. The PCs can be compared directly while the AEPs can be fitted with a cosine relation in order to get an initial estimation of the cosine exponent. A more detailed description of the Bladed simulations will be given further on in this chapter.

A next step will be to take analyze the data available from wind park Prinses Alexia. Boorsma et al. [44] and Wagenaar et al.[21] have proposed a method to analyze the impact of YM on power performance without actively misaligning the turbine. In this case, normal operational data of the turbine in combination with an IEC-compliant met-mast, like for the case of wind park Prinses Alexia, can be used to investigate the effect of YM. The method comprises the following steps:

1. Calculate C_p per 10-min data point by rewriting and then using Eq. 4.1.

2. Filter data for several influential wind speed ranges, like e.g. 7-9 m/s and 9-11 m/s.
3. Bin the measured YM into bins of 0.5° and calculating the average C_p-value for each bin.
4. Fit the function $C_p = C_{pmax} * cos^n(YM - \theta)$ to the YM-averaged C_p-values.

In the equation under step 4, C_{pmax} corresponds to the maximal C_p according to the cosine-fit, n corresponds to the cosine exponent, and θ to the phase shift, i.e. the YM at which C_{pmax} occurs. The cosine function is fitted using the Maltab function *lsqcurvefit*, which varies the input parameters of the wanted cosine fit until the least-squares results for fitted and actual observed data converge. For the purpose of this study, the allowable range of input parameters is set to: 0 to 1 for C_{pmax}, 0 to 6 for n, and -10° to 10° for the phase shift (θ).

Finally an experiment can be performed to investigate the relation between YM and power performance by misaligning a turbine deliberately and measuring power performance. Here a static YM should be inserted into the yaw controller of the turbine for a period of time while the power curve is measured. Ranging the YM from -20 to 20 degrees in steps of 5 degrees should give sufficient data points to determine a relation between the power output and YM. In literature it is found that this relation should be a cosine with an exponent ranging from 2 to 5.

To perform this study there are two possibilities:

1. Do the experiment with a turbine close to a met-mast or Lidar(i.e. at wind park Prinses Alexia)
   (a) Turbine at Prinses Alexia using the installed met-mast.
      - Advantages: Accuracy in YM and power measurements, recent tests at turbines has provided initial knowledge on their performance.
      - Disadvantages: Long measurement time required for IEC-compliant method meaning possible high energy losses and increased loads.

   (b) Turbine at Slufter using a ground-based Lidar.
      - Advantages: Accuracy in YM, Vattenfall owns turbines and Lidar so quick handling is possible, combinable with wind resource assessment for re-powering Slufter, Lidar can be moved to different turbines (varied data).
      - Disadvantages: No density, temperature and accurate power measurements available, loss of energy production in park.
2. Use side-by-side analysis of two adjacent turbines without additional measurement device.
   - Advantages: No instrument installation necessary(easy and cheap solution), VF owns turbines so flexible and quick handling is possible, wide variety of turbines possible. Possibility to determine the shape of the relation of power vs YM but not the ideal YM.
   - Disadvantages: Less accuracy in power performance verification and YM, no T,p, and density measurements.

Eventually, based on the possibilities within Vattenfall and the available time, the choice was made to pursue option 2, the side-by-side analysis. A more detailed description of the YM campaign plan is given in Appendix E.

Sub-question 3: Effect of wind shear on the ideal yaw error

This sub-question is based on the hypothesis that the effect of higher wind speed at the top of the rotor disk might bias a slight YM as this affects the angle of attack of the blade. This would then lead to an ideal yaw error angle not equal to 0. To look into this, the following will be done:

- A comparison with software can be done in the form of Bladed simulations where different wind shears are used to find the change in YM and power performance.
- Filter the Norrekaer Enge and/or Prinses Alexia data, where a met-mast is present, on wind shear, bin the data by shear, analyze YM and find a correlation. Boorsma's method will be adjusted slightly so as to fit a cosine relation to the WS-binned average power coefficients.

Comparing these two exercises should be able to shine light on the relation between YM and wind shear.

Sub-question 4: Outer-envelope weather conditions and their effect on PCs

Currently turbine manufacturers deliver turbines with guaranteed power curves under certain turbulence and shear conditions. Not a lot of research is described in literature about how non-compliant conditions affect the power performance of turbines and hence it is an interesting field to look at for an operator like Vattenfall.

Studying this can be done using both measurement campaigns from Prinses Alexia and Norrekaer Enge, so no additional measurement campaigns are needed for this part. The met-mast measurements will be binned by turbulence intensity and wind shear after which the difference in power performance is calculated. This knowledge could be used in to stimulate future additions to contracts between wind park owners and turbine manufacturers.

5.3. ANALYSIS TOOLS

5.3.1. MATLAB COMPUTATIONS

The wind measurement data is acquired from the different device operators while turbine data is acquired from Vattenfall's Scada systems. Most tools used in the analysis are made in Matlab so as to be able to adapt to new situations and wind parks easily. Parts of the Matlab coding is presented in the Appendices when it is deemed necessary for the completeness of the report.

5.3.2. BLADED SIMULATIONS

To observe the effects of YM on turbine performance and wind shear on the ideal yaw error, the DNVGL wind turbine modeling tool, *GH Bladed*, is used. Bladed is a software package used for turbines performance and loading calculations applicable for preliminary wind turbine design and even certification of turbines. This tool makes it possible to specify turbine parameters and 3D input wind fields, use this to run production loading simulations and eventually post-process these simulations to find the dynamic power curve and AEP of the specific turbine under the tested conditions. With a clear graphical interface, all these results can be made visible for the user.[43]

Initially, the idea was to acquire a Bladed model of the turbine (Senvion 3.4M104) under measurement at Prinses Alexia to make a qualitative comparison with measurement data possible. Sadly this model was not available so it was decided to use the *demoa.prj* readily available to Wind Energy students at the TU Delft. Table 5.7 displays the properties of this specific turbine model.

Table 5.7: *Specifications of the Bladed demoa.prj turbine model*

Rated Power	2 MW
Hub height	61.5 m
Rotor diameter (D)	80 m
Rated wind speed	12 m/s
Cut-in, cut-out wind speed	4 m/s, 25 m/s
Control	Pitch regulation with variable speed

For the purpose of this thesis, the effects of shear on power performance and ideal yaw error can be simulated using this software package. This will be done by varying the wind conditions, being wind speed, shear and wind direction relative to the nacelle (YM) while performing production loading simulations.

To observe the effect of WS on the ideal yaw error, the AEP will be simulated for several YM and WS combinations, so-called load cases, in order to hopefully find a relation between the two parameters. As the Bladed project file consists solely of turbine parameters, the dynamic PC of the turbine needs to be determined for each individual load case before the actual AEP can be calculated. The procedure used to simulate each load case is described fully in Appendix G and can be summarized as follows:

1. The specific load case is set in the 'Wind Conditions' menu of Bladed. Here the shear exponent can be varied under the wind shear tab while the YM can be imitated by changing the wind direction while the yaw controller is switched off.
2. Next, the average, uniform wind speed is varied per simulation run between 4 m/s and 25 m/s. Between cut-in (4 m/s) and rated wind speed (14 m/s) the wind speed is increased in steps of 0.5 m/s, after which a step size of 1 m/s is used up to 16 m/s. Beyond 16 m/s, two more simulations will be run at 20 and 25 m/s so as to acquire a complete PC, which is handy when wanting to calculate the AEP under certain wind speed distributions. In total this would lead to 25 production loading simulations per wind shear and YM situation.
3. Production loading simulations for each wind speed are run in batches per load condition and then stored for post-processing.
4. Using the 'Annual Energy Production' data-processing tool the simulations are used to calculate the

dynamic PC and the AEP of the turbine under the specific load conditions. For the AEP calculation, the Weibull distribution for Prinses Alexia is used.

5. Finally in the 'Data View' menu, the results of the simulations and post-processing can be observed and compared to each other.

During a production loading simulation some transients will be visible in the reaction of the turbine. Figures 5.5a and 5.5b display the outputs of two simulations at an average wind speed of 7 m/s and 10 m/s whereby the transient output can be clearly seen before it 'settles' to oscillate around a constant value. The time after which the transients disappear differs for average wind speeds, wind shear and YM, ranging from 10s to 20s after start of simulation. To be safe, it has therefore been chosen to start writing an output only after 30s. Each production loading simulation will then be simulated for 90s, whereby only the last 60s is written as output.

As can be seen in the figures, the output remains sinusoidal even after the transients have disappeared. In post-processing, a check is done whether the solutions of the AEP-module compares well with the outcome of the harmonics module. More explanation on this check is also given in Appendix G.

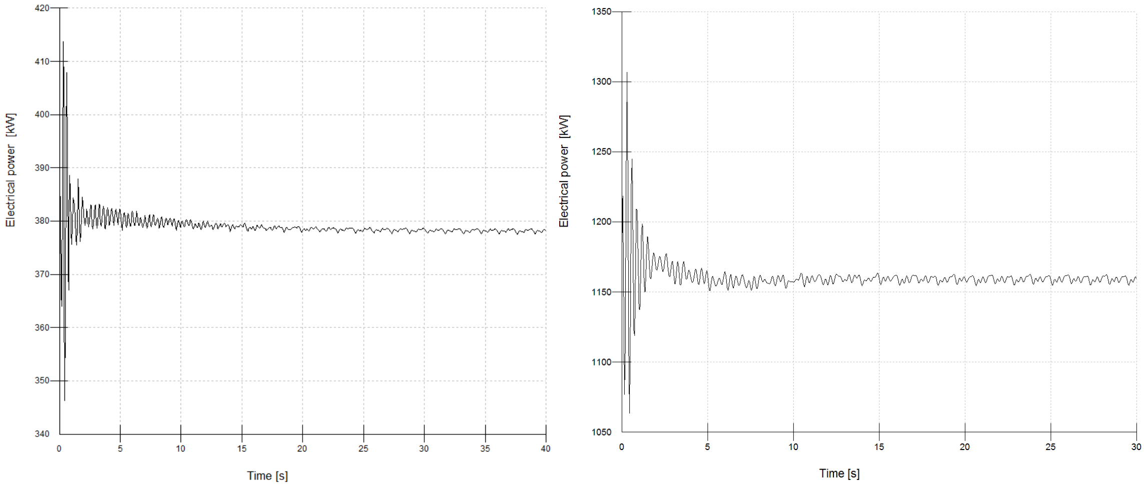

(a) *Bladed electric power for v=7 m/s*

(b) *Bladed electric power for v=10 m/s*

Figure 5.5: *Plots of electric power resulting from Bladed power production loading simulations at different wind speeds.*

The wind shear exponents and YM will be varied per 'load case' whereby firstly a base case will be run with no wind shear and YM. Then the YM will be varied from -20° to 20° in steps of 5° while disregarding wind shear. Next, the wind shear exponent will be varied from 0 to 0.5 in steps of 0.1 while disregarding YM. Figure 5.6 shows the wind profiles the specific turbine would experience with the specific shear exponents.

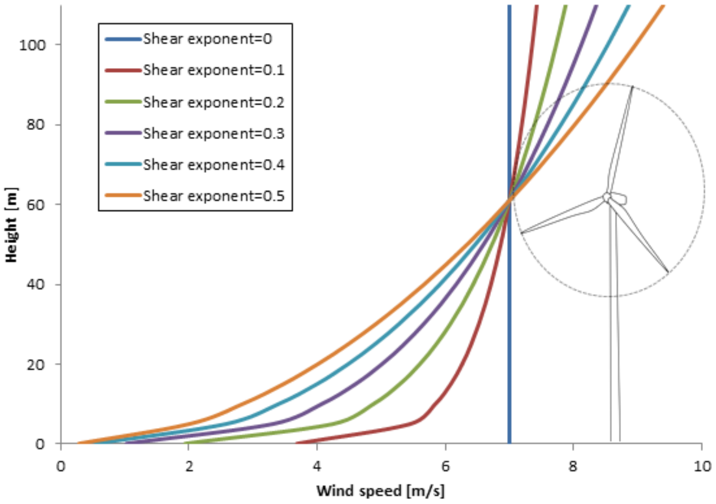

Figure 5.6: *Wind profiles specified by different wind shear exponents*

As it will probably be too time-consuming to run each combination of YM and wind shear, the initial simulations (shown in Table 5.8) will be analyzed and next simulations will be considered in order to test several combinations of YM and wind shear so as to obtain the research goal.

Table 5.8: *Properties to be varied during initial Bladed simulations*

Wind property	Variation range	No. of simulations
Yaw Misalignment	-20°:5°:20°	9
Wind shear exponent	0:0.1:0.5	5
Total		**13 runs**

Based on the insight gained in the initial simulations, the next load cases were performed as displayed in Table 5.9.

Table 5.9: *Varied load cases during Bladed simulations whereby the load cases which have been simulated are represented by '1' and those not simulated by '0'.*

Varied parameters		**YM[°]**															
		-5	**-4**	**-3**	**-2**	**-1**	**-0.5**	**0**	**0.25**	**0.5**	**0.75**	**1**	**1.5**	**2**	**3**	**4**	**5**
WS exponent	**0**	1	0	1	0	1	1	1	1	1	1	1	1	0	1	0	1
	0.1	0	0	0	0	0	0	1	0	0	0	0	0	0	0	0	0
	0.2	1	0	1	0	1	1	1	1	1	1	1	0	0	1	0	1
	0.3	0	0	0	0	0	0	1	0	0	0	0	0	0	0	0	0
	0.4	0	1	0	1	0	1	1	1	1	1	1	1	1	0	0	1
	0.5	0	0	0	0	0	0	1	0	1	1	1	1	1	0	0	0

6

DATA VALIDATION

To be able to perform trustworthy, accurate analyses, one first has to make sure that the used data is unaltered, reliable and traceable. In power performance analysis, this process is referred to as data validation. It includes ensuring that data from different sources is logged (time) simultaneously and in the correct manner, but also filtering-out of influenced, disturbed data during the measurement period. Also, data can be corrected to standard test conditions in order to make a correct comparison to guaranteed performance possible, an example of which is correcting for turbine availability and density. In this chapter, the data validation for both measurement campaigns will be treated.

6.1. PRINSES ALEXIA CAMPAIGN

The first check that should be done is whether the time loggers of the different measurement devices are synchronized. If the different measurements are not taken simultaneously it is not possible to make an accurate comparison. For the campaign at Prinses Alexia, the databases that should be time-matched are the met-mast readings and the turbine Scada system.

Not only should time logs be checked at the beginning of measurements but during several intervals over the campaign as time logging procedures could differ in switching to daylight saving time. For the case of Prinses Alexia this happened on 29 March 2015 at 2:00 AM. Checks were performed for different periods before and after the date and it was concluded that indeed the measurements compare well or at least follow the same trend or pattern.

A good signal to look at in order to compare the time logging of both databases is the wind speed readings from the met-mast and nacelle anemometers of turbines R01 and R02. These should generally follow the same pattern even though they could differ slightly in magnitude due to variation in wind conditions over space, wake losses or measurement accuracies. Figure 6.1 shows an example of a time period where the Scada and mast signals do indeed follow the same trends but do differ a little in magnitude. The graphs in the figure were acquired after shifting the met-mast data ahead by 1 hour, which seemed to be the difference in time logging sequences. This shift was applied over the complete met-mast database.

The next step in data validation is to ensure that disturbed sector measurements are discarded from the dataset. These disturbances are caused by the met-mast measuring in the wake of itself, i.e. one of the anemometers in the wake of the mast, or nearby obstacles like turbines R01 and R02. To look into the shadow caused by the mast itself, the two wind speed signals at hub-height can be compared with each other against the different wind directions. Figure 6.2 shows the ratio between the two wind speed readings. It is clearly visible that the anemometers show big differences in measurements in certain wind directions, as depicted by the spikes in the graph. The main spikes occur at wind directions around 130° and 310° which, when looking at the configuration given in Table 5.2, corresponds to the shadow of the mast itself on either one of the anemometers. Smaller peaks are also visible around angles of 30° and, in less extent, 100°, which are considered to be caused by the wakes of turbines R01 and R02, respectively. The peak due to R02 would be lower since the turbine is further away from the mast and the booms on which the met-mast anemometers are installed are parallel to the direction of R02. The wind sectors around the afore-mentioned wind directions are therefore not accurate and discarded from the dataset in the remainder of the power performance analysis.

Additional filters have been applied to the database for non-numerical inputs, i.e. one of the measurement

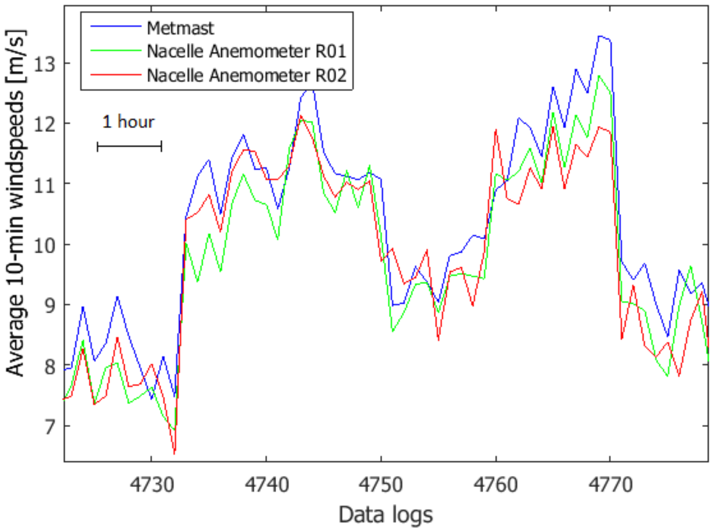

Figure 6.1: *Met-mast and nacelle anemometer readings at Prinses Alexia compared to each other for time-logging validation. Each data log is a 10-minute average value.*

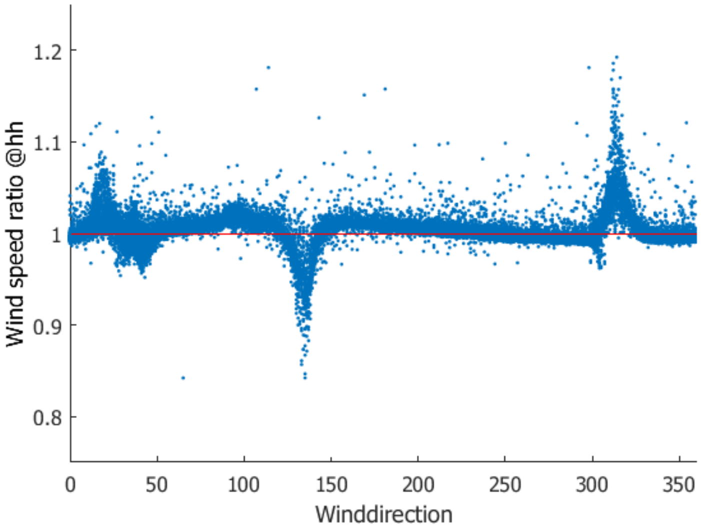

Figure 6.2: *Prinses Alexia: Ratio of two met-mast anemometer readings at 98m per wind direction*

devices has not returned a value over the 10-min period, as well as for the availability of the turbines under investigation according to the requirements by the IEC standards[1]. Figure 6.3 displays a scatter of the average met-mast hub-height wind speed against R01 nacelle anemometer readings before and after filtering and discarding data. It can be seen that the filtered readings significantly improve the correlation between the readings. The fact that the linear regression is not closer to 1 is considered to be caused by the fact that the nacelle anemometer measures wind speeds behind the rotor which have therefore already been influenced and slowed down by the rotor.

6.2. NORREKAER ENGE CAMPAIGNS

The data validation at Norrekaer Enge consists of two additional steps, as two other instruments will be compared to the met-mast in this campaign. In the following section, these steps will be treated for both individual devices, whereby the data is validated against the met-mast in both cases.

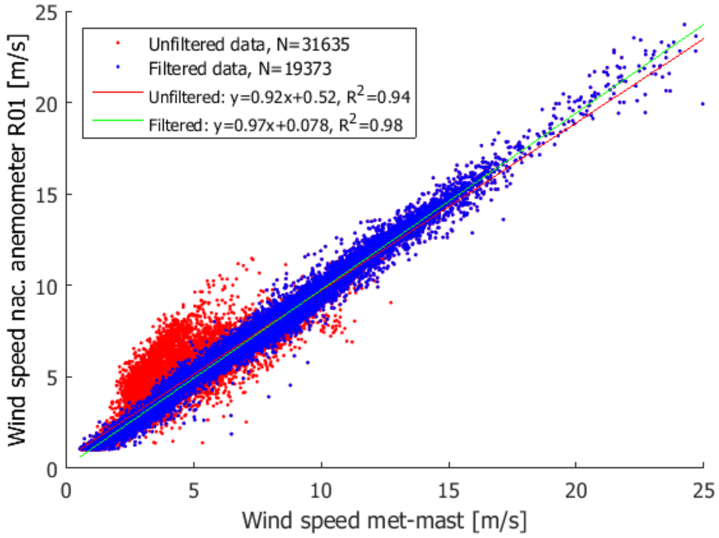

Figure 6.3: *Prinses Alexia: Filtered and unfiltered nacelle anemometer against met-mast readings*

6.2.1. LIDAR VALIDATION

To start with, Table 6.1 gives an overview of all the 10-min averaged signals which are logged by the WindIris in use. Here, the essential signals which are of direct importance for this thesis are the *HWSm*, *Directionm* (also YM), and the *HWS availability*.

Table 6.1: *Specification of significant output signals and corresponding units by the WindIris Lidar[4].*

Signal name	**Unit**	**Description**
Timestamp	[s]	Coordinated Universal Time (UTC)
Range	[m]	Lidar measurement range
HWSm	[m/s]	Average horizontal wind speed
dHWS	[m/s]	Horizontal wind speed deviation
Um	[m/s]	Average wind speed component along Ox axis
Vm	[m/s]	Average wind speed component along Oy axis
Directionm	[°]	Average relative wind direction
RWS0m	[m/s]	Average radial wind speed LOS0
dRWS0	[m/s]	Radial wind speed LOS0 deviation
RWS1m	[m/s]	Average radial wind speed LOS1
dRWS1	[m/s]	Radial wind speed LOS1 deviation
CNR0m	[dB]	Average Carrier-Noise-Ratio LOS0
CNR1m	[dB]	Average Carrier-Noise-Ratio LOS1
Tiltm	[°]	Average tilt angle
dTilt	[°]	Tilt angle deviation
Rollm	[°]	Average roll angle
dRoll	[°]	Roll angle deviation
RWS0 availability	[-]	Data Availability LOS0 $\epsilon[0,1]$
RWS1 availability	[-]	Data Availability LOS1 $\epsilon[0,1]$
HWS availability	[-]	Data Availability HWS $\epsilon[0,1]$

To validate whether these signals are measured properly by the WindIris, an initial check needs to be done to see whether the Lidar is measuring simultaneously to the met-mast and the turbine Scada system. As the Lidar only measures wind speed, from which the wind direction is also derived, the wind speed signal of the met-mast should be compared to the HWS as measured by the Lidar. It was found that the time logger of the met-mast had an offset of 1 hour compared to both the Lidar as the Scada system. This problem was solved by simply subtracting 1 hour from the met-mast timestamps. Figure 6.4 shows a segment of the measurement campaign whereby it can be observed that indeed the signals are time-synchronous after the correction to the timestamps has been applied. It is important to note that caution has to be taken to test the simultaneous measurements at several timespans over the campaign to ensure that daylight saving time or other changes are not affecting either of the devices' time-logging.

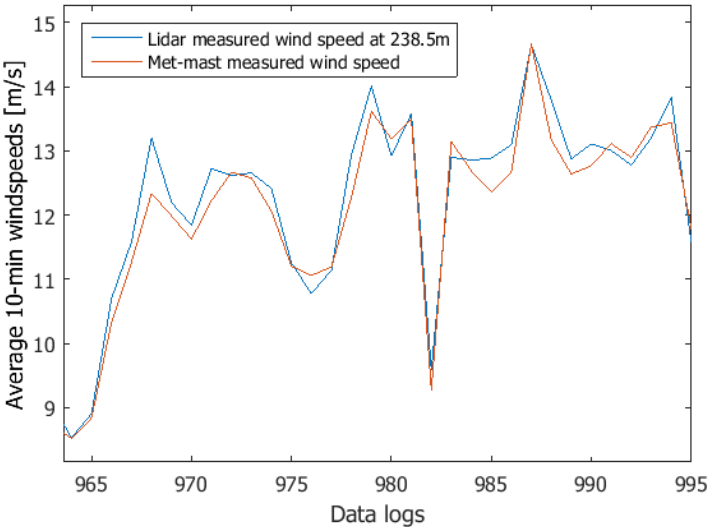

Figure 6.4: *Wind speed validation of Lidar measurements against a met-mast. Each data log is a 10-minute average value.*

To observe how the Lidar is able to cope with wakes of obstacles in the vicinity of turbine 4, its readings were plotted against the wind direction measured by the met-mast. As mentioned in Section 5.1.2, turbine 5 is at 70° for North of turbine 4 while turbine 3 is at 250° from North. If one, or both, of the Lidar beams is directed into the wakes of these obstacles, a distortion is expected to be seen in the measurement. Figure 6.5a shows the ratio between the RWS readings of beam 0 and 1 at different wind directions for the three measurement ranges while Figure 6.5b shows the effect on the YM readings of the wind direction. As can be seen in both figures, the distortion due to the wakes of turbines 3 and 5 are clearly visible at wind directions of 250° and 70°, respectively.

Slightly below the wind direction of 70° LOS0 will be in the wake of turbine 5, thereby measuring a lower wind speed while LOS1 is measuring in free wind. This causes the ratio between the RWSs to drop below 1. As wind direction increases, LOS1 also enters the wake of turbine 5 so the ratio moves back towards 1 and will keep increasing above this as LOS0 moves out of the other side of the wake. Eventually, at a wind direction of about 90° from North, LOS1 will move out of the other side of the wake too and the ratio between the measurements returns to 1 again. The same occurs at the wake of turbine 3.

For the YM calculations an opposite effect of the wakes is seen. When only LOS0 is in the wake of turbine 5, the lower RWS0 induces a positive YM. Falling back to Eq. 3.8, RWS0 is equivalent to V_l and thus the Lidar will translate a lower wind speed at LOS0 as a positive YM, and vice versa. On the other hand, when only LOS1 is in the wake of turbine 5, the Lidar translates this into a negative YM according to Eq. 3.8. It is clear that these peaks and troughs are caused by the wakes of adjacent obstacles and the Lidars' inability to cope with this, therefore the influenced wind sectors should be excluded from the Lidar database during further analysis.

The different measurement ranges have been included in Figures 6.5a and 6.5b as an interesting observation can be made by looking at the different ranges. It can be seen that at shorted measurement ranges, the RWS0 and RWS1, and thereby the YM calculation, are influenced by the wakes of surrounding turbines. This can be attributed to two factors: Firstly, the distance from the origin of the wake to the measurement point by the Lidar is increased, allowing for the wake to recover more and lessen the difference between waked and free wind conditions. Secondly, measuring closer to the rotor means that the actual measurement points of the LOSs in the horizontal plane are less far apart. Since the wake of an adjacent turbine remains equally wide for all the Lidar measurement ranges, the wind sector in which one of the beams is measuring in waked conditions is smaller for shorter Lidar measurement ranges. The decision was made to use the Lidar YM readings at 80m range instead of 238.5m, as this allows for a larger undisturbed wind sector and the wind direction at closer range also corresponds better to the actual wind direction working on the turbine.

Where data validation at Prinses Alexia mainly included time synchronization and disturbed wind sector

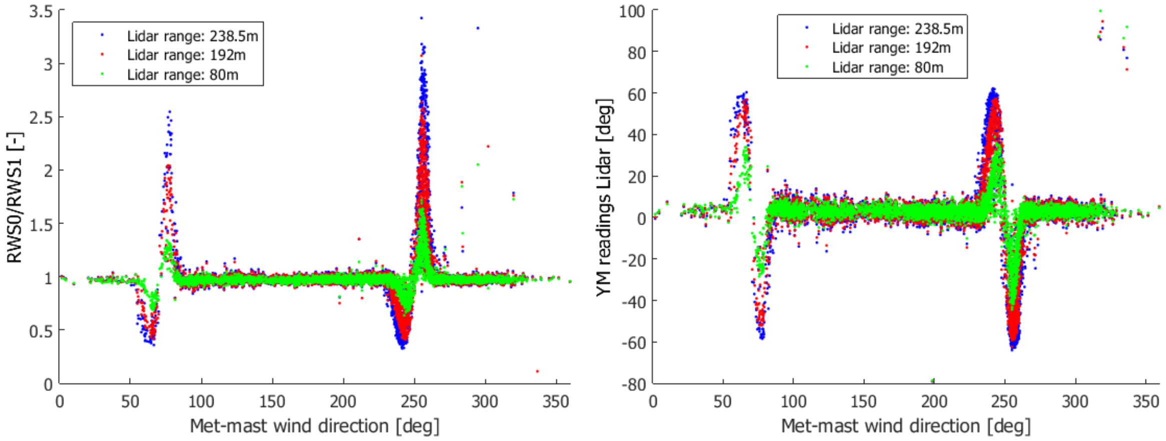

(a) *RWS ratio against wind direction*

(b) *YM against wind direction*

Figure 6.5: *Analysis of the wind sectors as measured by Lidar at different ranges.*

filtering, for the Lidar data validation additional attention has to be paid to the quality and status of the measurement signal. These properties are quantified by the Horizontal Wind Speed (HWS) availability and Carrier-to-Noise Ratio (CNR) and the HWS is actually only logged above a certain CNR. Figure 6.6 reflects this dependency whereby the HWS availability is plotted against the CNR recorded by beam 0. The HWS availability increases steeply above a certain CNR-value, e.g. between -23 and -21 dB, which means that the wind speed is only calculated from the LOSs if the CNR is above this value.

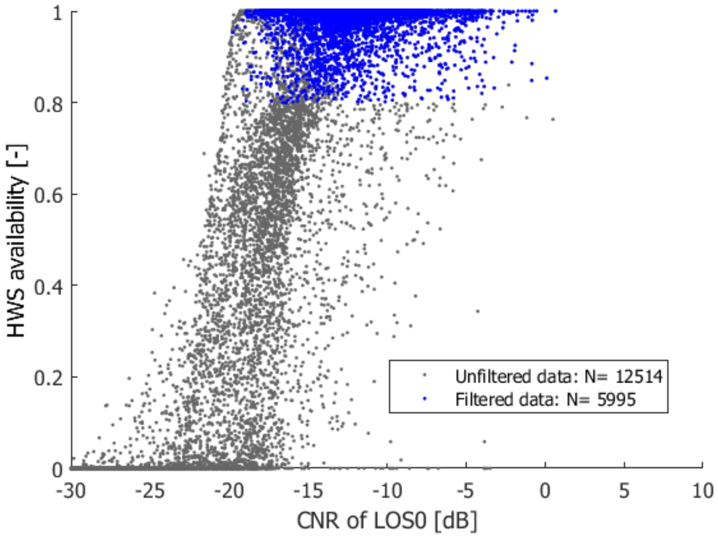

Figure 6.6: *CNR values of LOS0 against the HWS availability before and after the mentioned filters have been applied.*

As the CNR represents the strength of the carrier signal compared to the noise in the measured signal, the CNR can vary over time and space depending on what the Lidar is measuring. For instance, the beams of the Lidar might be blocked by the turbine blades thereby leading to a high magnitude in CNR (<-23dB). Another example could be that one of the beams is measuring in the wake of an obstacle nearby, thereby experiencing a different aerosol scatter and finding a different CNR. Figure 6.7 displays the CNR recordings of both Lidar beams at different ranges. It is observed that beam 0 generally is higher than its equidistant counterpart, which might be caused by occurrences like the ones described above. Filters with thresholds for both CNR and HWS availability were applied at -21dB and 0.8, respectively. By applying these filters, the data points in the rising part of Figure 6.6 can be filtered out as they might add to uncertainties. These values are comparable to values applied in earlier studies[19].

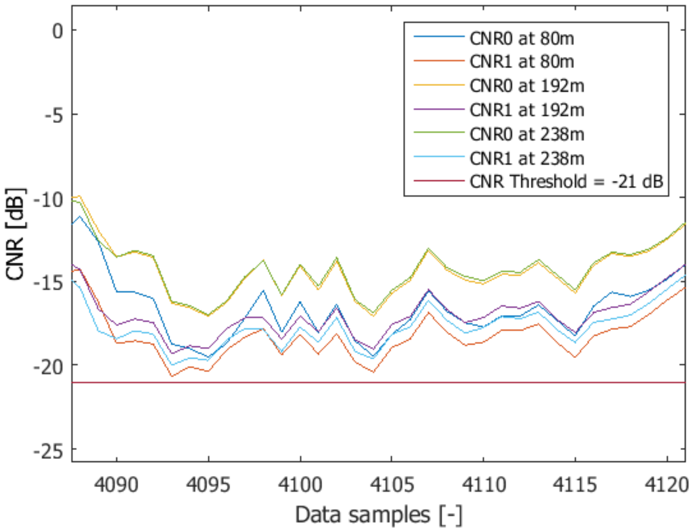

Figure 6.7: *CNR signal of both LOSs at different measurement ranges. Each data log is a 10-minute average value.*

6.2.2. SPINNER ANEMOMETER VALIDATION

The spinner anemometers have a more elaborate list of signals which are logged every 10 minutes. Table 6.2 gives an overview of the signals which are important for the purpose of this thesis. Each of the parameters starting with '*V_Spinner...*' has a log of the mean, maximum, minimum, standard deviation and signal validity values. Also, the signals for a specific sensor, e.g. '*V_SpinnerWindSpeed1,avgVal,f*', are also logged for the other two sensors. These signals are however left out of the table to keep the overview brief.

Table 6.2: *Specification of significant output signals and corresponding units by the spinner anemometer.*

Signal name	**Units**	**Description**
createTime	[s]	UTC +00 time stamp of the 10 min data.
V_SpinnerWindSpeedAvg,avgVal,f	[m/s]	10 min average of uncorrected wind speed
V_SpinnerWindSpeedAvg,sdvVal,f	[m/s]	10 min average of uncorrected Yaw
V_SpinnerYawAngleAvg,avgVal,f	[°]	10 min average of uncorrected YM
V_SpinnerInclineAngAvg,avgVal,f	[°]	10 min average of uncorrected inflow angle.
V_SpinnerWindSpeed1,avgVal,f	[m/s]	Instant free wind speed measured by sensor 1
V_SpinnerSonicTemp1,avgVal,f	[°C]	Instant free temperature measures by sensor 1
V_SpinnerAccelerometer1,avgVal,f	G	Gravitation force measures by sensor 1
V_SpinnerInflowAzimuthAngle,avgVal,f	[°]	Inflow azimuth angle measured by 3 sonic sensors.
V_SpinnerRotorPos,avgVal,f	[°]	Rotor Position
V_SpinnerAngularRotorSpeed,avgVal,f	[°/s]	10 min average angular speed of the rotor.
V_SpinnerYawPosition,avgVal,f	[°]	10 min average values of the nacelle yaw position.
V_SpinnerAirPressure,avgVal,f	[mbar]	10 min average Ambient pressure.
WGDC,TrfGri,PwrAt,cVal,avgVal,f29	[kW]	10 min average Active power
WS_AVG_corr	[m/s]	10 min average wind speed calibrated to 2.5D.
YM_AVG_corr	[°]	10 min average YM angle calibrated for spinner shape
FI_AVG_corr	[°]	10 min average wind speed calibrated for spinner shape
WS_SD_corr	[m/s]	10 min average standard deviation of wind speed.

As the spinner anemometer is able to measure temperature and pressure, the timestamps were checked against met-mast readings using temperature and air density measurements. Simultaneous wind speed measurements are available but the air temperature and density are considered to be less fluctuating over 10 minutes thereby being more suitable to compare to met-mast readings. Like for the Lidar database, an offset between the met-mast and spinner anemometer timestamps of 1 hour was found and compensated for. Figures 6.8 and 6.9 display the temperature and density readings of the met-mast against spinner anemometers in two timespans during the spinner anemometer measurement campaign. Comparing the x-position of the peaks and troughs, it is clear that the time correction of an hour indeed leads to temperature and density signals showing the same trends and patterns.

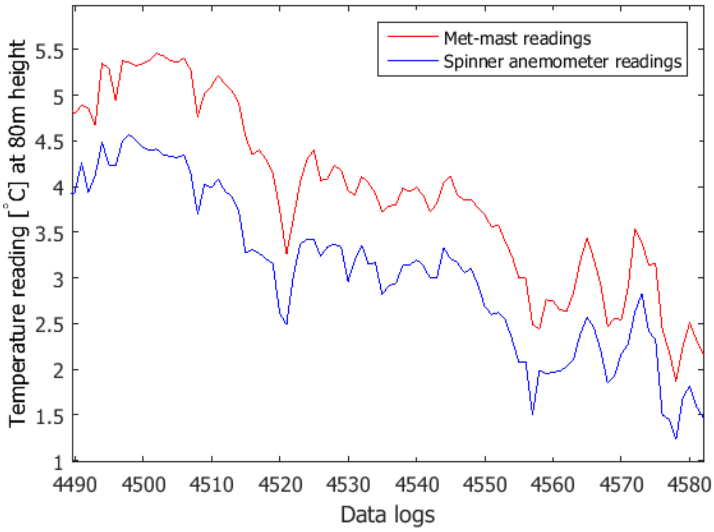

Figure 6.8: *Validation of temperature readings of spinner anemometers against an IEC-compliant met-mast. Each data log is a 10-minute average value.*

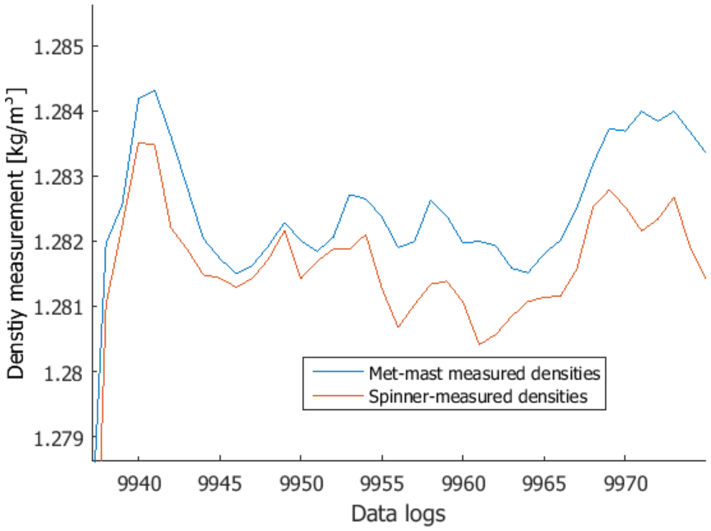

Figure 6.9: *Validation of air density readings of spinner anemometers against an IEC-compliant met-mast. Each data log is a 10-minute average value.*

As with the Lidar database, it is interesting to see what the effect of disturbed wind conditions is on the spinner anemometer measurements. Figure 6.10 shows a scatter plot of YM against the met-mast wind direction. A filter has been applied for wind speeds above 4 m/s to ensure that the turbine is operational and facing the wind. As can be seen, the distortions caused by the adjacent turbine wakes are smaller and less clear than was the case with the Lidar. In fact one may wonder whether the slight peaks caused around the wind directions of 77° and 256° are caused by a measurement error in the spinner anemometer readings or whether this is the actual YM that the turbine is having due to the disturbed wind flow by the turbines upstream. Considering the measurement principle of the spinner anemometer, the latter is the most likely. Nonetheless, the disturbed wind sectors as shown in Figure 5.3b will be discarded in further analysis as the other databases, e.g. met-mast readings, are affected by these waked conditions.

According to the IEC standards on PCV, Romowind installed independent turbine power measurement devices. A final check was therefore performed on how the independent readings compare to the power given by the turbine Scada system. Figure 6.11 shows a scatter plot of these readings including a linear regression fit. The measurements do not match perfectly but the regression fit looks very good with a slope and R^2-value

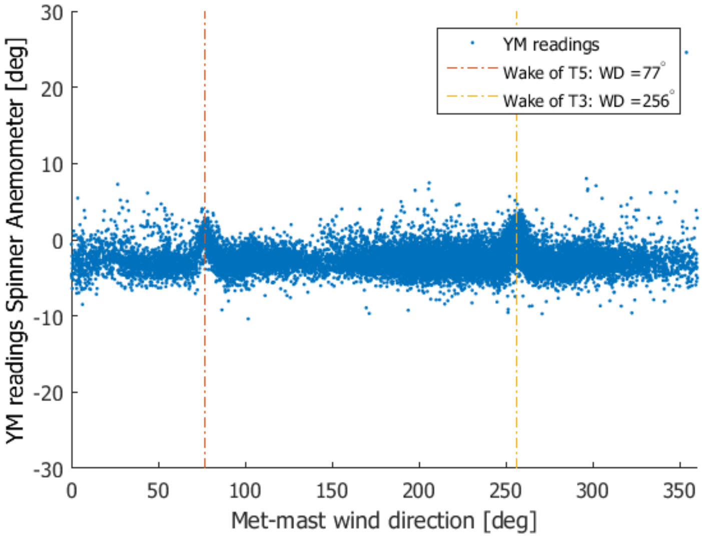

Figure 6.10: *Validation of YM readings of spinner anemometer against the wind direction as measured by met-mast.*

close to unity. As the independent measurement devices have been placed later, they are considered to be more accurate and therefore their readings were used during further analysis.

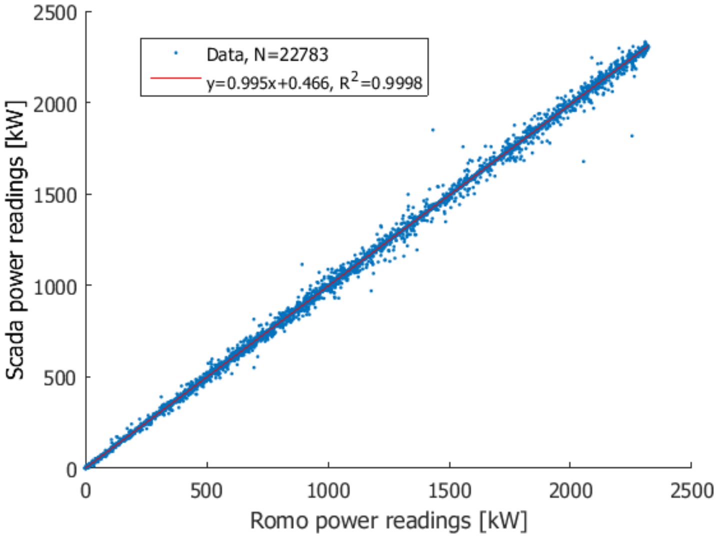

Figure 6.11: *Validation of independent active power readings by Romowind against Vattenfall Scada system.*

ACCELEROMETER VALIDATION

As was described in Section 3.2.2, determining the azimuth position of each sonic anemometer with the use of an accelerometer may be prone to errors. An error bias in the accelerometer could lead to a quadratic increase in azimuth position over time. Sadly, no high frequency data signal of the rotor azimuth is available, thereby making a check into these errors via the azimuth angle impossible. However, both the spinner anemometer and the Scada system have a rotor speed signal, which would also be prone to such an error in the accelerometer readings. To find the rotor speed, the acceleration has to be integrated once. If the accelerometer has an error bias, a linearly accumulating error in rotor speed would occur in the spinner anemometer readings, which should be detectable when compared to the Scada rotor speed signal.

This comparison has been made in Figure 6.12, showing that the rotor speed readings correlate very well. If the spinner anemometer accelerometer would have an error bias, a poor correlation would be seen and probably a correlation gradient much less than 1 as the spinner anemometer rotor speed error would increase over time. It is clear that this is not the case, thereby confirming that indeed the accelerometer installed in the spinner anemometer seems well calibrated.

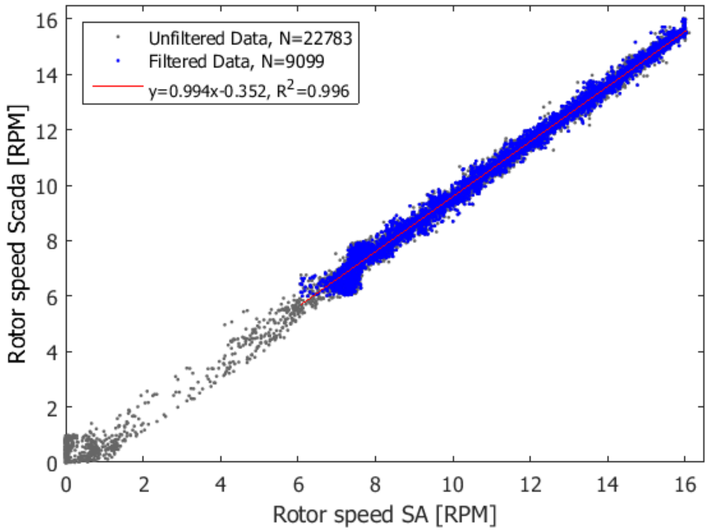

Figure 6.12: *Validation of rotor speed readings by Romowind against Vattenfall Scada system.*

An offset is however visible in the rotor speed readings of the spinner anemometer and the Scada signal. This offset is also visible in the histogram in Figure 6.13, where an average difference of $-0.43 RPM$ is present between the Scada and spinner deducted rotor speed. For the azimuth position readings to be equal between both systems, such a difference would have to be 0 RPM on average, as the rotor speed translates to azimuth position by multiplication with time.

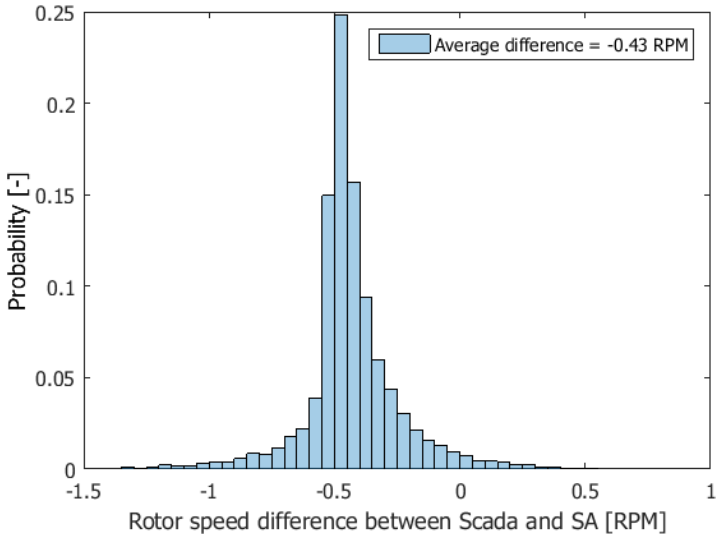

Figure 6.13: *Histogram of rotor speed difference between spinner anemometer and Scada system.*

The validation of the accelerometer is therefore not conclusive. Firstly, the scattered rotor speed readings show a good correlation with each other meaning no accumulating linear error is present. On the other hand, an offset is seen, meaning a difference in azimuth position will build up linearly with time. The offset could however also be caused by a calibration error in the Scada system, which would not affect the spinner anemometer azimuth position and the rest of its' readings. This is considered to be the most likely cause, as no accumulating error is seen in the scattered rotor speeds. As no high-frequency azimuth position or rotor speed data is available for comparison, it will be assumed for the remainder of this thesis that the accelerometers are well-calibrated and not influencing the spinner anemometer measurements.

7

EXERCISE OF POWER CURVE VERIFICATION

As mentioned in the research setup, a power performance test was performed on two turbines, R01 and R02, at wind park Prinses Alexia between February and October 2015, the results of which will be presented in this section. This has been done in order to gain experience and understanding of the process of PCV, a handy step for the rest of this research.

7.1. POWER PERFORMANCE TESTS

To perform power performance tests, the steps set out by the IEC standards as presented in Section 3.1 should be followed. By doing so, the dataset is filtered for availability and undisturbed wind sector of the turbine under investigation after which the wind speeds are also corrected for density.

7.1.1. POWER CURVES

Following the power performance test procedures, the filtered and corrected wind speeds are binned into bins of 0.5 m/s and the corresponding average power produced is calculated. Figures 7.1a and 7.1b display the filtered and unfiltered data for R01 and R02, respectively. Also the binned PCs have been added and can be compared to the reference PC as supplied by the turbine manufacturer. It should be noted here that in case a bin consisted of less than three valid data points, the value of the previous bin was used as mean power. This only occurs at rated power so the influence of this procedure is minimal.

Looking at the binned PCs, turbine R01 seems to always operate below the guaranteed PC, with the biggest difference visible around rated wind speed. Looking at turbine R02 on the other hand, it can be seen that the turbine only under-performs slightly around rated wind speed but generally performs better than the guaranteed PC.

Once again it is interesting to note that the filters applied to this data (availability and free wind sector) show clear yet expected behavior. The data points which have been filtered out are measured when either the met-mast or the turbine under investigation is in the wake of adjacent turbines or other objects. In this case a lower wind speed will be measured than the turbine is experiencing, which explains the clouds of data points above the binned power curve around cut-in wind speed.

7.1.2. ANNUAL ENERGY PRODUCTION

Using the calculated binned PCs, it is possible to calculate the energy a turbine will produce in a year for a specific wind speed distribution. Often wind sites have pre-assessed wind speed distributions, for Prinses Alexia this is a Weibull distribution with k=2 and A=7.9. As explained in Section 5.1.1 and Appendix A, different Weibull distributions were calculated over the measurement period using different methods. Using Equation 3.6, these wind distributions can be used to calculate the AEP of each turbine as well as the AEP calculated using the reference PC. Figure 7.2 displays a bar graph of the AEP of both turbines, R01 and R02, and the reference PC when using five different wind speed distributions; the actual measured, the LSQ estimated, the 'wblfit' calculated, the WAM and the pre-assessed distribution, respectively.

Firstly comparing the different wind speed distributions, the WAM and the LSQ based AEPs are closest to the actual measured distribution. We would expect this for WAM since this method is based on equating the distributed and measured average power density (Table 5.3). The LSQ method however was determined

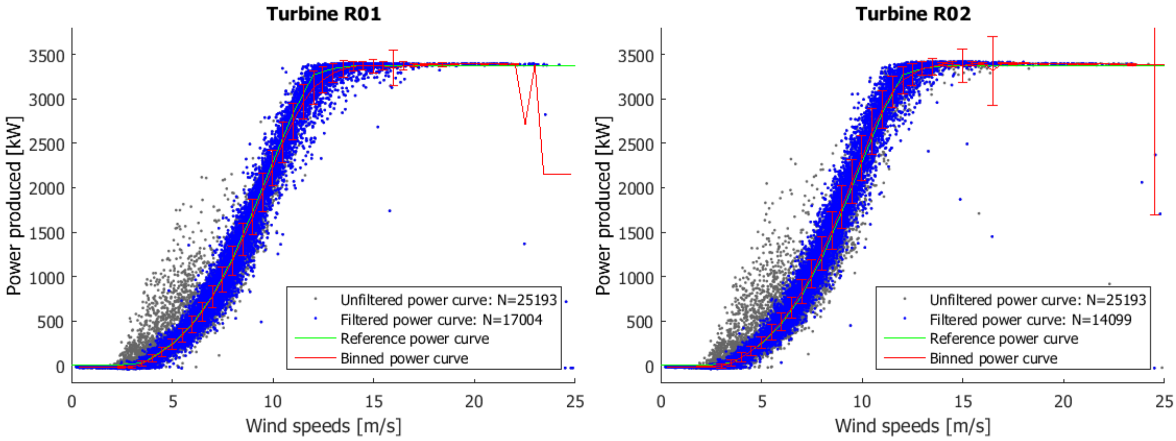

(a) *Measured Power Curve for turbine R01* (b) *Measured Power Curve for turbine R02*

Figure 7.1: *Binned power curves for turbines R01 and R02 compared to reference PC*

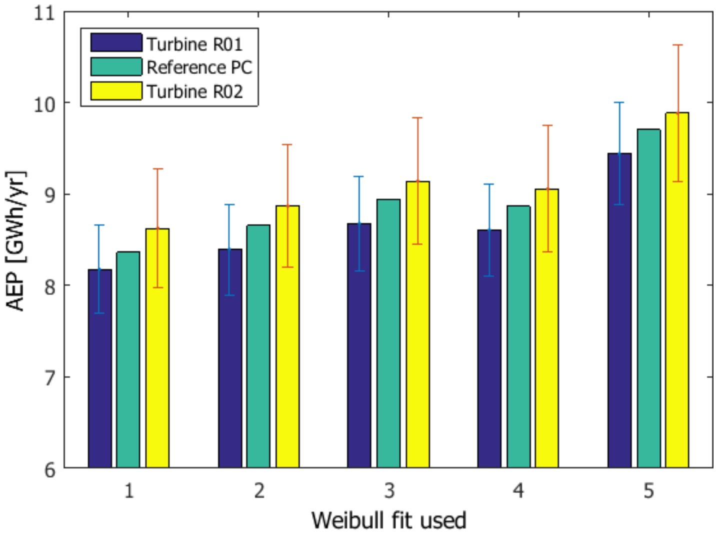

Figure 7.2: *Annual Energy Productions predicted using several wind speed distributions; the measured(1), least square estimated(2), Matlab wblfit(3), Wind Atlas Method(4) and pre-assessed(5) distribution*

to have a much lower power density but follows the actual distribution more closely (see Fig. 5.2a), possibly justifying the LSQ-based AEP to be such a good estimate.

Looking on at the individual turbines compared to the guaranteed PC it is found that turbine R01 delivers 2% less than the guaranteed case and R02 produces 4% more. Besides, there is a 6% difference between the AEPs of both turbines which is a significant difference for two adjacent turbines. Although such a difference with the reference AEP is undesirable, it is well within the guarantees that the turbine manufacturer provides.

7.1.3. PERFORMANCE LOSS FACTORS

Motivated by the 6% difference in AEP, an exploratory study into the bad functioning of R01 and the differences in operation between R01 and R02 was performed.

Yaw Misalignment Taking this research' focus on YM into account, this was the first possible loss factor that was looked into. Filters were applied for wind speed ranges between 4 and 16 m/s, being the most influential range on power loss due to YM, and for the individual turbine free wind sectors. The YM was calculated by subtracting the turbine nacelle direction, as given by the Scada system, from the hub-height wind vane reading of the met-mast. Figure 7.3a displays the YM plotted against wind speed and including the mean YMs of turbines R01 and R02.

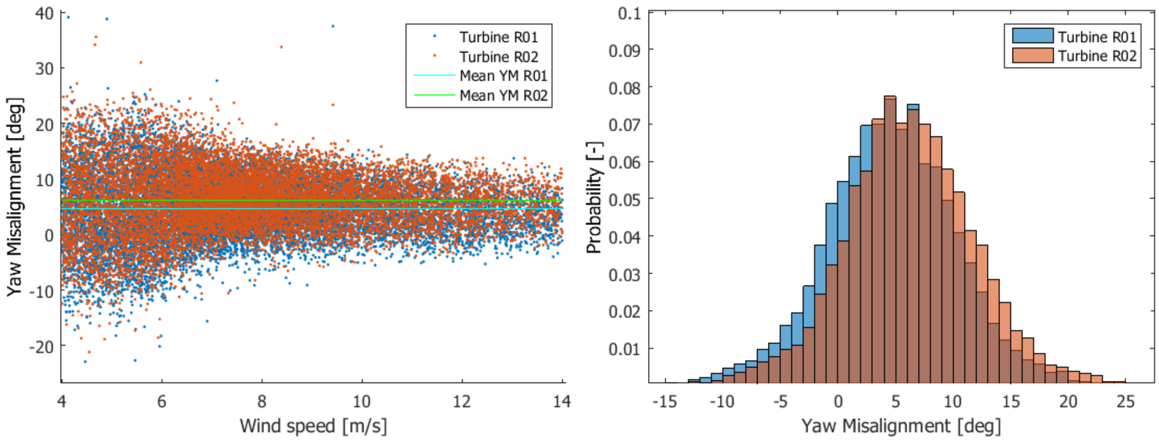

(a) *YM against wind speed including the mean YMs.* (b) *Histogram of YM for R01 and R02*

Figure 7.3: *YM measurements for turbines R01 and R02 using the adjacent met-mast*

As can be seen in the graph, R02 generally has a higher YM than R01. Also, the spread in YM is particularly high at lower wind speeds and decreases as wind speed increases. This can be explained by the fact that at lower wind speeds the turbine might still be starting up and hence takes a while to yaw the turbine in the right direction. This decrease in the spread of YM as wind speed increases is in agreement with earlier studies into the phenomenon of YM. The mean YMs are 4.67° and 6.24° for R01 and R02, respectively.

The distribution of YM at both turbines has also been plotted in a histogram and is given in Figure 7.3b. It can be seen that YM has a normal distribution around its mean value and that both distributions have approximately the same spread. One difference though is that the distribution for R02 is slightly shifted to the right, as can be expected considering the slightly higher mean YM.

In order to get a feeling of what the difference in YM distributions can translate to in terms of power loss, a rough estimation was made of the annual energy loss due to the measured YMs. To start with, the assumption was made that energy loss is dependent on YM by the cos^2-rule (Eq.4.3 with n=2). This is a relation where no general agreement is found on in the wind energy sector but will serve well as a first estimate of the energy loss due to YM. First, the 10-minute average power readings are corrected by this rule to their corresponding YM readings. Next, the adjusted power readings are multiplied by the amount of 10 min periods per year and summed up to give a total annual energy loss. As YM is considered to only influence wind speeds between 4 and 16 m/s for the specific turbines, the annual energy loss is multiplied by the probability of the wind speed being in this range, thereby leading to a more realistic energy loss. Figure 7.4 displays a histogram of the energy loss in kWh corresponding to each YM bin of 0.5° and the probability of it occurring. In the legend of the figure the total annual energy loss has been given and calculated as percentage of the AEP. It would seem like significant gains are possible if YM were to be completely compensated for, however in reality this is not possible due to the fluctuating nature of the wind and the reaction time of a turbine yaw controller.

Concluding on the potential loss due to YM at R01 and R02, as YM is higher for R02 and the fact that a higher YM is expected to give a higher loss, it seems that YM is not the reason for the difference between AEP of R01 and R02. Also, the estimation of energy loss shows that a difference of only 0.6% of AEP can be won between R01 and R02, which is much less than the actaul performance difference of 6%. Nonetheless, it will be interesting to correct this YM and see what effect this has on the power performance.

Pitch angles A next aspect which was looked into was the average pitch angle of the three blades per turbine. Figure 7.5 displays the pitch angles plotted against wind speed whereby it is clear that turbine R02 seems to have a higher pitch than R01 when they experience the same wind speeds. This is deemed peculiar and was initially thought to be a possible explanation for the difference in power performance. However, as the main difference between the binned PCs of R01 and R02 occurs up to rated wind speed, the region where the turbine is torque instead of pitch regulated, the pitch cannot be of such a major influence on the performance.

An exception would be if the pitch angle of turbine R01 is mis-calibrated in both the Scada system as the turbine control system, causing the turbine to think that it's blades are pitched at 0° while they might actually

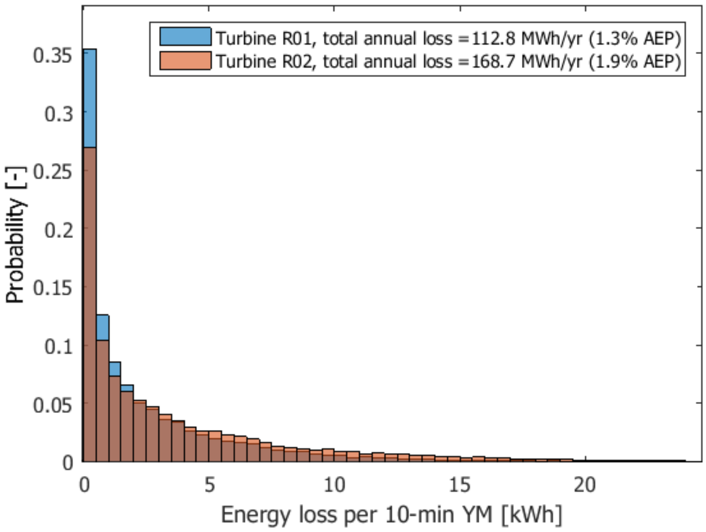

Figure 7.4: *Histogram of the energy loss due to the absolute 10-minute average YM using the* cos^2*-rule.*

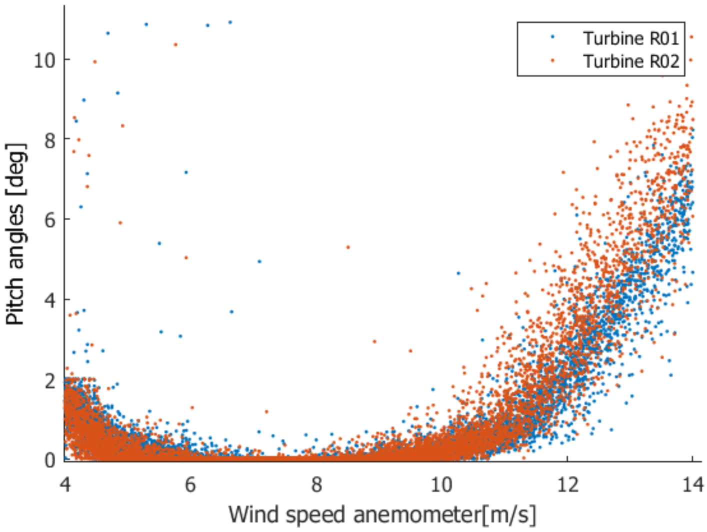

Figure 7.5: *Average pitch angles of turbines R01 and R02 plotted against wind speed*

be at -2° pitch. As this cannot be observed from the database available for this study but only upon visual inspection of the turbine under operation, this explanation is not pursued further in this section.

Generator Torque As generator torque is the input to pitch control, this was the next signal to be investigated. Figure 7.6 shows the generator torque against met-mast wind speed of R01 and R02. The generator torque is a calculated signal found by dividing electrical power by generator speed. As can be seen in the figure, the torque on R02 is slightly higher than R01 in the torque-controlled region, in the same manner as was observed in the binned PCs. As power is linearly related to torque, this difference could explain the difference in AEP between turbines R01 and R02.

Generator and rotor speed The final turbine parameters which were looked into are rotor and generator speed. Figures 7.7a and 7.7b display these signals against met-mast wind speed for turbines R01 and R02. Looking at the rotor speeds there is a clear difference between turbine R01 and R02, whereby it seems that R02 has a slightly up-shifted rotor speed range. The difference between the rotor speeds is approximately 1%. This is considered strange as we are investigating two turbines of the same model and manufacturer.

When comparing this to the generator speed signals, the difference seems to have disappeared. This led to the finding that turbine R02 has a different gearbox (Moventas) than R01 (Eickhoff), with different gear

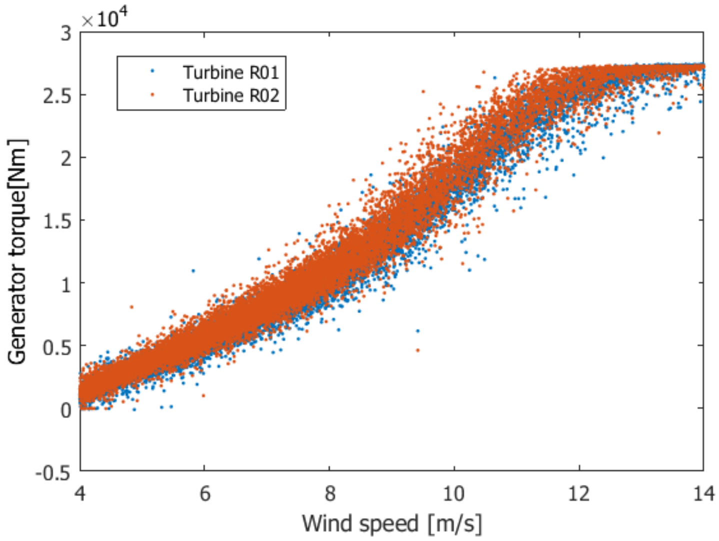

Figure 7.6: *Comparison of generator torque of R01 and R02 against wind speed*

ratios as well ($n_{R01} = 87.2$ and $n_{R02} = 86.4$). Several Moventas gearboxes at Prinses Alexia have been replaced by Vattenfall in the past because of defects, which is also what happened at R01. However, it seems the change in gearbox has not helped to improve the turbine performance and it is expected that the cause lies in the fact that adjustments to the controller function might be necessary with a new gearbox and might not have been applied.

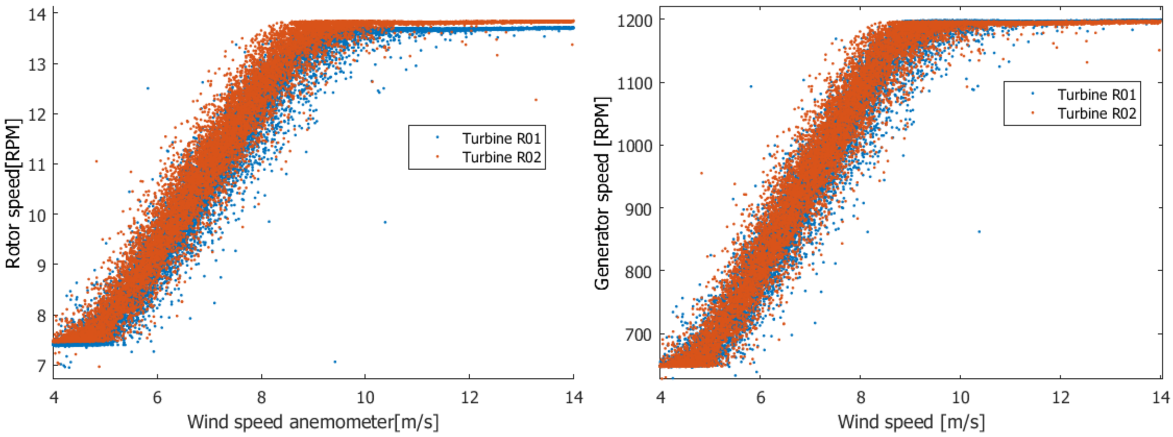

(a) *Rotor speed vs. met-mast wind speed*

(b) *Generator speed vs. met-mast wind speed*

Figure 7.7: *Comparison of rotor and generator speeds of R01 and R02*

Sub-conclusions To conclude on the problems with turbine R01, the eventual fault is thought to be in different gearboxes implemented in these turbines. The loss is occurring in the torque-controlled region of the PC. In this region, the controller will seek the maximum torque(Q_d^{opt}) by holding on to the maximum power coefficient (C_p) and optimal generator speed(ω_g). The controller function is described by the general equation given below:

$$Q_d^{opt} = \frac{\pi \rho R^5 C_p^{opt}}{2\lambda_{opt}^3 G^3} \omega_g^2 \tag{7.1}$$

Here, ρ, R, and G represent the air density, rotor radius and the gearbox ratio, respectively. The optimal power coefficient is controlled by keeping the tip speed ratio (λ) constant around its optimal design value. As can be seen in Figures 7.6 and 7.8, generally the power coefficient, and thereby the torque, for R02 is higher than R01. Also, the optimal λ seems a little higher for R02 than for R01. To my knowledge, the optimal λ is controlled by increasing/decreasing the rotor speed when the wind speed increases/decreases. The rotor speed is generally not the input parameter for the controller, but the generator speed is. This would mean that if the controller function has not been adjusted for a different gearbox ratio, the controller will ask for the same generator speed, but different rotor speed and thus less optimal Labda and C_p. This is seen as a possible explanation for the difference in performance between R01 and R02, although doubts are placed on whether a difference of 1% in gearbox ratio can result in 6% AEP. These conclusions have been presented to the turbine manufacturer, Senvion, who are responsible for further investigations.

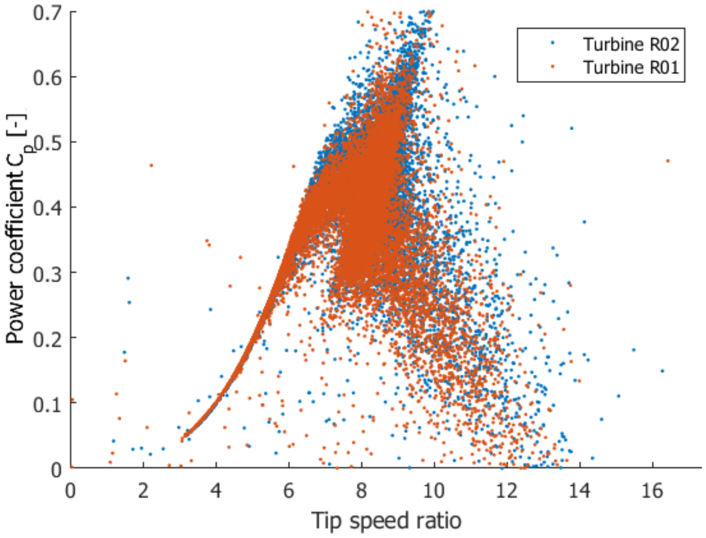

Figure 7.8: *Measured power coefficient of turbines R01 and R02 against tip speed ratio.*

7.2. COMPLETE PARK COMPARISON

Following the above conclusion, a brief investigation was performed into how the other turbines were operating with either of the gearboxes. 9 out of the 36 turbines in the wind park are still equipped with the Moventas gearbox while the rest have all been fitted with the Eickhoff gearbox.

The methodology used to compare performance of the complete park is as follows:

1. Filtering data for wind directions whereby the met-mast has undisturbed wind (180° to 250°).
2. Using each wind speed data point the equivalent guaranteed power is calculated by interpolation of the guaranteed PC.
3. The measured active power is normalized by dividing by the equivalent guaranteed power.
4. Wind speeds are binned into the range where the largest differences between turbines R01 and R02 are visible (8-12 m/s).
5. The normalized data are averaged over the bin and then plotted as a scatter with the x and y coordinates of the turbines and the normalized power as input for the color bar.

Figure 7.9 displays the resulting heatplot of the above method. The goal of the exercise is to see whether the same trend as at R01 is visible at the other turbines which have an Eickhoff gearbox. The turbines which have an Eickhoff gearbox have been named in the figure. As can be seen from the figure this trend is not present although one can doubt whether the applied method makes a good comparison possible since the correlation between the met-mast wind speed and the actual wind speed the turbines experience might be low.

Considering the chosen wind sector, the turbines D01-E06 would be expected to deliver good power but clearly this is not the case. These differences are probably caused by a small forest (trees up to 20m high) to the south of the wind park, causing for increased roughness and less ideal wind conditions than the met-mast measures. Appendix H displays separate heatplots per 0.5 m/s bin over the range of 7 to 13 m/s.

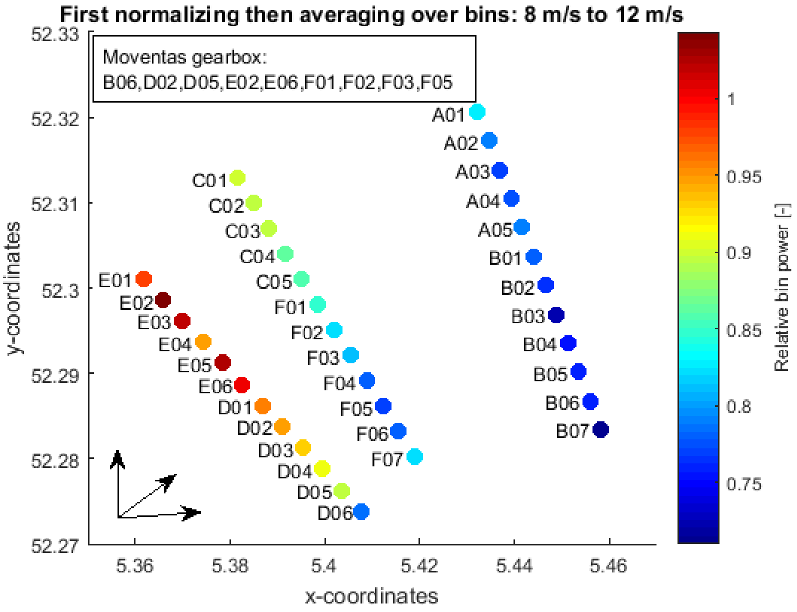

Figure 7.9: *Heatmap displaying power performance of all turbines at Prinses Alexia from February-August 2015.*

8

ACCURACY OF NOVEL DEVICES

In this chapter, the accuracies of the novel measurement techniques are to be investigated in order to partially answer sub-questions 1 and 2 as described in Chapter 2. As the goal of this sub-question is to see whether the novel devices, spinner anemometers and nacelle-based Lidar, can achieve a sufficient accuracy in correlating data with the IEC-standard met-mast, the following sections will be dedicated to comparing correlations of Lidar and spinner anemometer measurements to met-mast readings, respectively. Finally, a direct comparison between the Lidar and spinner anemometer will be made. The campaign at wind park Norrekaer Enge has these three measurement methods installed and measuring simultaneously, making it very well suitable for this comparison.

To be applicable in power performance measurements, the novel devices should be able to measure at least wind speed accurately. In the line of the goals set out by this research, the next comparison to be made is the devices' individual applicability in detecting YM and TI. Finally, the power performance of turbine 4, on which both devices have been installed, will be analyzed using both novel devices, so as to gain insight into the procedures required and eventual bottlenecks.

8.1. NACELLE-BASED LIDAR AGAINST MET-MAST

As described in Section 6.2.1, the Lidar dataset was filtered on data errors, CNR >-21dB, high signal (HWS) availability (>0.8), the free wind sector of turbine 4, and then corrected to density using Eq. B.1.

Following the measurement campaign at Norrekaer Enge, Romowind removed the Lidar from turbine 4 and performed a post-calibration of the Lidar as the tilt readings seemed peculiar. During this post-calibration, performed by Avent Lidar Technology, an error in the inclinometer was discovered of 1.07° in tilt angle and -0.12° in roll angle. Figures 8.1a and 8.1b show the time series of the 10-min averaged inclinometer tilt and roll readings corrected to the post-calibration results. This shows that the Lidar seems to have been measuring at an average of tilt -0.35° and the average turbine roll was indeed close to 0°.

Using Equation 3.11 and assuming the Lidar to be placed at 2.5m above hub-height, the Lidar pretilt angle which should have been set prior to the Lidar upon installation should be -0.4° for correct measurements at a distance of 2.5D ahead of the turbine. This is relatively close to the corrected average tilt angle and therefore in accordance with the IEC standards for PCV[1] which dictate that measurements are to be performed at a height within 2.5% from the turbine hub-height.

Nonetheless, since some uncertainty was present about the height at which the Lidar had been measuring, it was decided to correct the measured data to the actual hub-height. This can be done using the tilt readings of the inclinometer and the wind speed measurements at different heights by the adjacent met-mast. First the wind shear exponent α for each 10-min datapoint is calculated using the following equation:

$$\alpha = \frac{log(\frac{V_{33.5}}{V_{80}})}{log(\frac{33.5m}{80m})} \tag{8.1}$$

With $V_{33.5m}$ and V_{80m} being the met-mast wind speeds at respective heights of 33.5m and 80m.

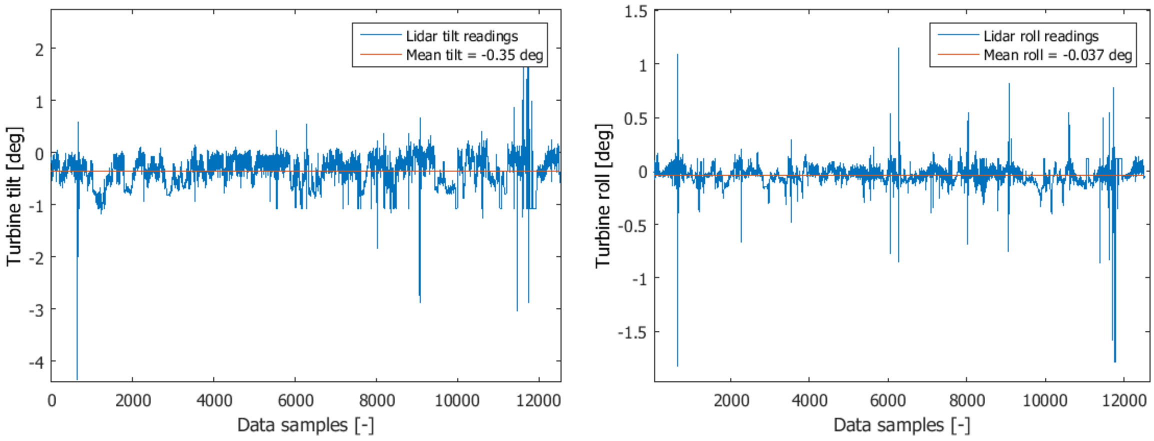

(a) *Tilt measurements* (b) *Roll measurements*

Figure 8.1: *Post-calibration corrected tilt and roll readings as measured by the inclinometer installed on the Lidar.*

Next, the met-mast WS exponents are reused to translate the Lidar wind speed measurements from the 10-min average measuring height to hub-height using the following equations:

$$V_{Lidar80m} = V_{Lidar2.5D}\left(\frac{80m}{h_{lidar}}\right)^{\alpha} \tag{8.2}$$

with $V_{Lidar2.5D}$ being the raw Lidar measured wind speed at 2.5D. Also, h_{Lidar}, the height at which the Lidar is actually measuring, is calculated as follows:

$$h_{Lidar} = 80m + \sin(t) * r_{Lidar} \tag{8.3}$$

where t is the 10-min average tilt reading and r_{lidar} is the Lidar measurement range (either 80, 192 or 238.5m).

Applying this correction it is expected that the wind speed readings should show a better resemblance to the met-mast data than prior to the correction, although such a correction does add to the uncertainty of the Lidar measurement. The correction caused a difference in wind speeds before and after correction of between 0 to -0.2 m/s, with an average of -0.05 m/s, which is a relatively small difference.

8.1.1. WIND SPEED COMPARISON

Next, the accuracy of the nacelle-based WindIris Lidar in measuring wind speed is investigated and compared to the adjacent IEC-compliant met-mast. The Lidar measurements are taken at a range of 238.5m, corresponding to 2.5D in front of the rotor.

Figure 8.2 shows a scatter of both filtered data and unfiltered data, whereby it should be mentioned that the filter between these datasets is merely the wind sector filter. This was done since the data errors and low availability data do not have a significant meaning, while observing the effect of disturbed wind sector on the readings is interesting. As can be seen in the figure, the dataset is halved due to filtering for free wind sector and the Lidar wind speed readings are generally higher than met-mast readings.

A linear regression fit is applied to the filtered wind speed data, showing a good correlation between the measurements. Both the slope of the fit and the R^2-value are close to unity while the offset of the fit is negligible. Allthough this correlation does seem to be good, the Lidar does seem to overestimate the wind speed by 4.6% which is significant, and might be caused by the error or uncertainty concerning the Lidar inclinometer. Earlier studies have shown that Lidars should be able to measure wind speeds accurately[15] [16] [17] [18] [20] [7], hence it seems likely that the inclinometer errors could be the reason for this.

8.1.2. YAW MISALIGNMENT COMPARISON

In the following section, the Lidars' ability to measure YM accurately is investigated. Since the tilt only influences the height at which the Lidar is measuring, it is expected that this should not influence the YM readings. An additional filter is applied to the data for wind speeds between 4 and 16 m/s, the range in which YM could eventually have an impact on power performance. As mentioned earlier, the Lidar installed at Norrekaer

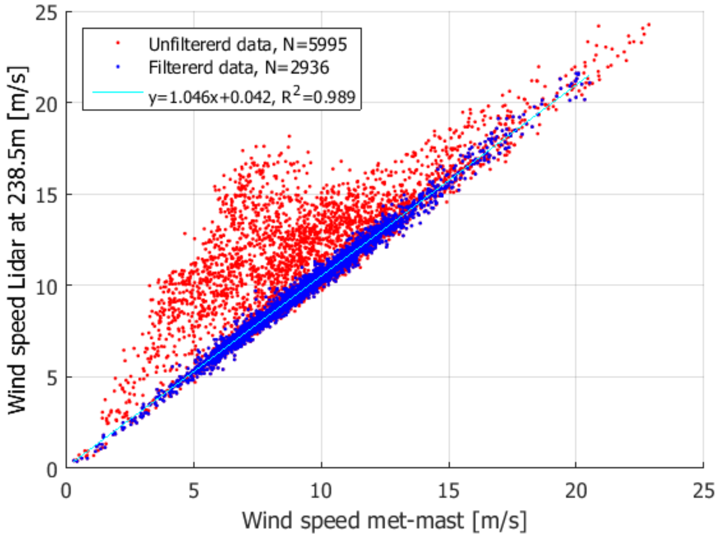

Figure 8.2: *Correlation between met-mast and Lidar wind speed readings measured at 2.5D in front of Turbine 4.*

Enge measures radial wind speeds and thereby also relative wind direction, or YM, at three different ranges, namely 80m, 192m (2D), and 238.5m (2.5D). In earlier studies [7] [17], it has been suggested to measure YM closer to the rotor, i.e. 80m in front of rotor, than the standard 2.5D, as the wind could turn slightly over such a distance. To ensure that the YM being measured is actually correlated as good as possible, it is suggested to measure at around 80m. To investigate whether the distance does indeed influence the YM working on the rotor, the distributions of YM at 80m, 192m and 238.5m has been given in Figure 8.3.

One can note that as the measurement range becomes smaller, so does the spread in actual YM readings, the same trend as was observed in Figures 6.5a and 6.5b. This translates to a lower standard deviation as the range decreases, as given in the legend of the figure. This behavior has also been confirmed by Avent Lidar Technologies and would mean that for the sake of measuring the YM experienced by the turbine, it is best to use the range of 80m.

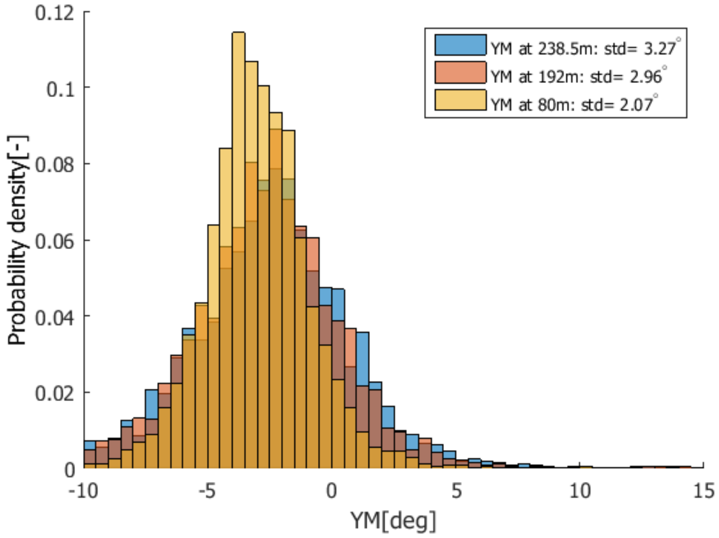

Figure 8.3: *Histogram of Lidar YM measurements at different ranges.*

Next, the YM readings can be compared to the met-mast YM calculations. Figures 8.4a and 8.4b show the YM readings of the Lidar at range 80m scattered against their simultaneous met-mast readings, as well as their individual distributions. No clear correlation is visible between the readings, where the data is solely clouded around the mean YM (-3.03°). Due to this cloud of data points, the linear regression fit cannot give a clear estimation of the behavior either.

Considering the YM distributions, it can be noted that the average YM as measured by the Lidar at 80m seems slightly higher in magnitude than what the met-mast predicts. This could however be caused by the fact that the wind direction has indeed changed as it approaches the wind turbine. Besides this, the spread in YM readings is larger than that of the met-mast distribution. This higher standard deviation, 2.07° against 1.61°, can be seen as a sign of higher uncertainty of the Lidar in determining the YM compared to a met-mast.

Finally, doubts may be placed at whether using a met-mast to measure YM is by itself a thorough method to determine YM since wind direction might change slightly in the distance between met-mast and turbine. Also, an IEC-compliant met-mast will be fitted with well-calibrated wind vanes so their readings may be trusted, but the nacelle direction in the turbine Scada signal could be mis-calibrated. This will then add to the offset in average YM while the total met-mast method standard deviation stays low.

Concluding, standard deviation may not be the best method of evaluating the accuracy of a device. Nonetheless, the difference between the standard deviations is small enough (0.45°) to conclude that a Lidar can measure YM sufficiently accurate to eventually be able to correct the turbine nacelle transfer function.

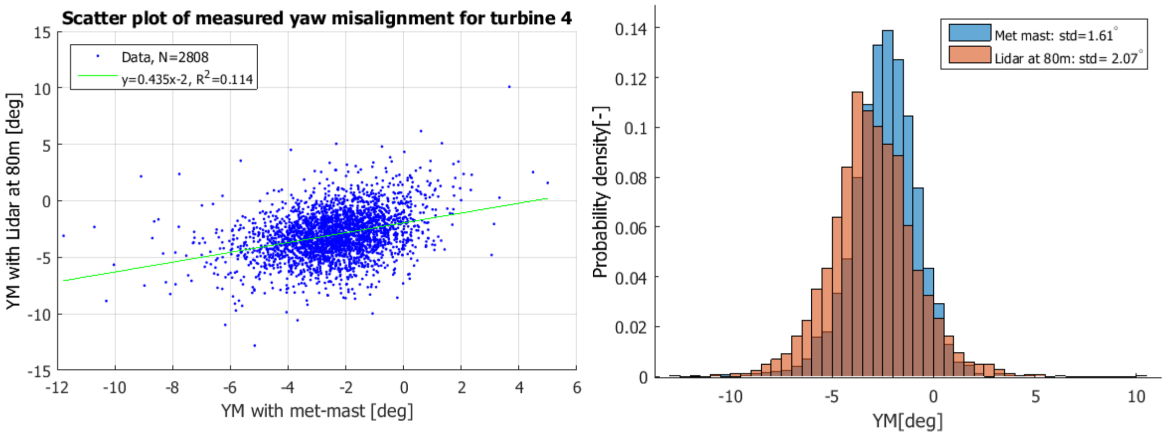

(a) *YM correlation*

(b) *Histogram of YM measurements*

Figure 8.4: *Comparison of Lidar YM measurements at 80m and YM calculations using met-mast and Scada data*

The correlation pattern visible in Fig. 8.4a is similar to the YM correlation found in a previous study by Goossens [7] comparing a Lidar and Sodar to calculate the YM. As no clear correlation could be found, Goossens simulated the measurement campaign using Matlab in order to reconstruct the above-mentioned correlation pattern. This was done by varying the wind direction, mean YM, and accuracy of the measurement devices until the pattern resembled the measured YM scatter, thereby giving an indication of the accuracy of the specific device to measure YM. As the same instrument (WindIris) is used in this study as for Goossens' case, the same methodology has been implemented and slightly optimized for comparison to met-mast, the details of which are explained elaborately in Appendix C. Figures 8.5a and 8.5b display the acquired scatter plot and histogram of the simulated YM.

In the left figure, the dense cloud of points displays a similar pattern to Figure 8.4a, whereby the gradient and R^2 also match the measured fit relatively well. It should be noted that as the simulations use the Matlab random generator the results vary slightly for each run, thereby not allowing for a perfect match in fitting the measured correlation. As the title of Figure 8.5a states, the optimal match between simulated and measured YM correlation was found at accuracies of 1.5° and 2.2° for the met-mast-Scada method and Lidar, respectively.

Looking at the histogram in Figure 8.5b, it is clear that the Lidar has a slightly larger spread compared to the met-mast and true YM distribution, respectively. This seems logical considering the difference in accuracies that the simulations have detected. Comparing the simulated histograms to the measured YMs in Figure 8.4b, it may be seen that the spreads in the simulated case are slightly higher than the measured one for both the met-mast and the Lidar results. This same trend is visible in the YM scatters, where the simulated cloud of points shows slightly larger spread than the measured spread. This could mean that the YM-determination accuracies of both Lidar and met-mast are a little better (lower σ) in reality than the simulations predict.

Goossens[7] found the accuracy of the WindIris to be around 4° in his simulations, which is significantly large than the results in this thesis. Doubts have therefore been placed to whether this simulation method relates to reality, leading to discussions with the Lidar manufacturer (Avent Lidar Technologies). The sug-

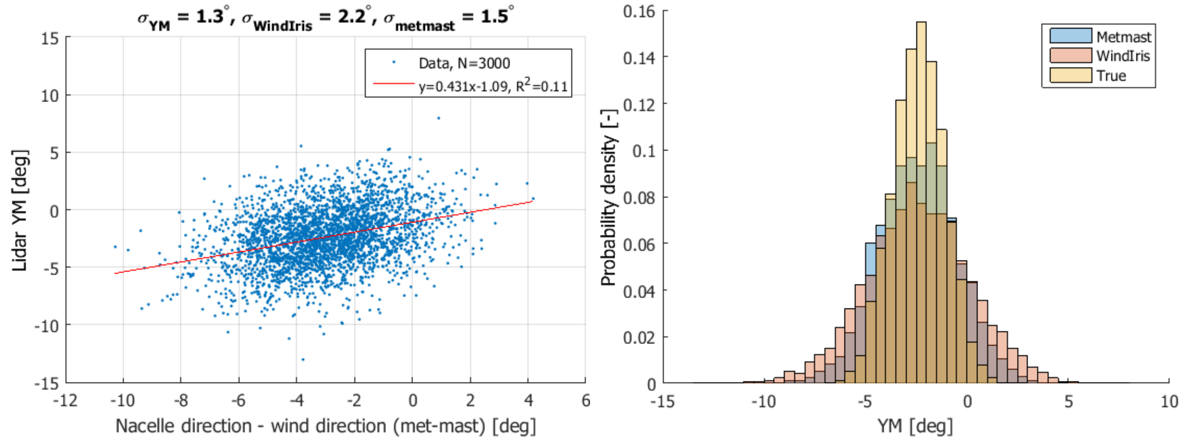

(a) *Simulated YM correlation*

(b) *Histogram of simulated YMs*

Figure 8.5: *Comparison of YM simulations for the Wind Iris Lidar*

gestion was made that wind flow heterogeneity can cause such high inaccuracies for a 2-beam Lidar, which works on the principle of a homogeneous wind flow. These discussions then also led to a concept to incorporate heterogeneity into the Lidar equations, eventually resulting in a proposal for a measurement campaign using a 5-beam Lidar as described in Appendix D. It is expected that if more is known about the impact of heterogeneous flow on Lidar measurements, its' accuracy may be improved even further.

8.1.3. TURBULENCE INTENSITY COMPARISON

Several studies have looked into a Lidars ability to measure TI accurately, resulting in non-conclusive evidence of this being the case [21][22][23][7]. In the following section, a closer look will therefore be taken into how the TI measurements by the met-mast and Lidar compare with respect to each other. Before this comparison can be given though, the calculation of Lidar TI will be explained briefly.

Turbulence intensity is defined as the 10-min average standard deviation of the wind speed divided by the 10-min mean wind speed. The WindIris measures the wind speed by means of two horizontal laser beams at an angle of 15° from the rotor axis. The calculation of the actual TI therefore comprises to calculate the TI of each individual beam and then take the average. The calculation is then given by the following equations:

$$TI_0 = abs\left(\frac{std(RWS0)}{mean(RWS0)}\right); TI_1 = abs\left(\frac{std(RWS1)}{mean(RWS1)}\right); TI_{lidar} = \frac{TI_0 + TI_1}{2} \tag{8.4}$$

with Radial Wind Speed (RWS) being the radial wind speed as measured by beams 0 and 1. It should be noted that the wind speeds used here are at range 2.5D as the IEC standards dictate.

The same correction for the measurement height as was done for the HWS should be applied to the RWSs of beams 0 and 1. It is however not applied to the standard deviations (STD) of the RWSs as these are relative quantities thereby staying approximately the same if measurement height increases. A closer look is therefore taken at the wind speed STD of the Lidar against the met-mast. Figure 8.6a displays the correlation between met-mast and Lidar STD readings. The STD of RWS0 is used in this figure as example but RWS1 gives a similar result. The slope of the STD is lower than 1 for the Lidar while the R^2-value is relatively high. In figure 8.6b, the standard deviations of both LOSs and the met-mast have been averaged per wind speed bin and plotted against wind speed. As can be seen, the Lidar tends to always underestimate the standard deviation compared to a met-mast, meaning it has a low sensitivity to fluctuations in wind speed. This could however also mean that the STD deviation needs a correction for height, however this does not seem logical. For the further TI corrections this has therefore not been applied.

Using the above-mentioned equations and corrections, the TI as measured by the Lidar can be calculated and compared to the met-mast TI readings. Figure 8.7a displays the correlation between the TI measurements while Figure 8.7b gives the TI distribution for both the met-mast and the Lidar.

A logical consequence of the wind speed overestimation by the Lidar is that the TI will be under-estimated for this measurement campaign. Combining this with the lower wind speed standard deviations of the Lidar

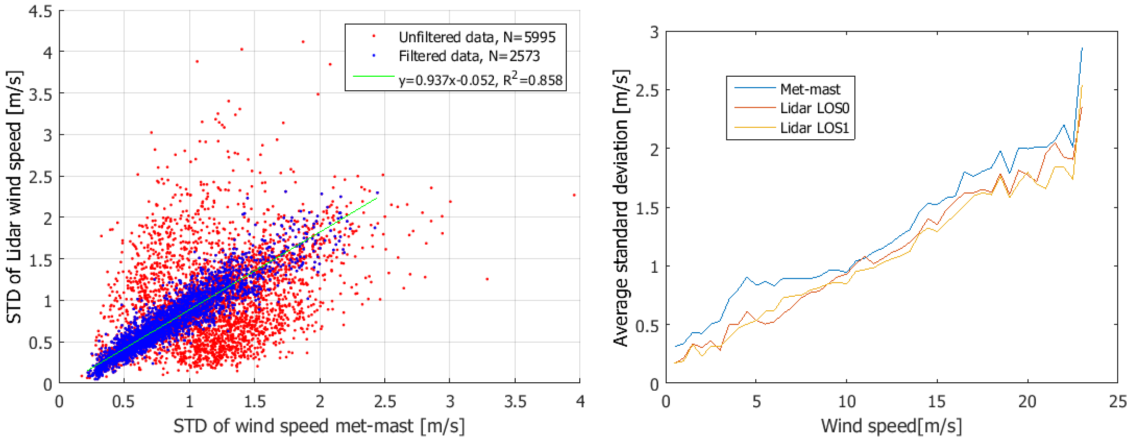

(a) *Correlation between wind speed standard deviations* (b) *Comparison of binned STD measurements*

Figure 8.6: *Correlation between met-mast and Lidar standard deviation measurements at turbine 4 and their binned averages.*

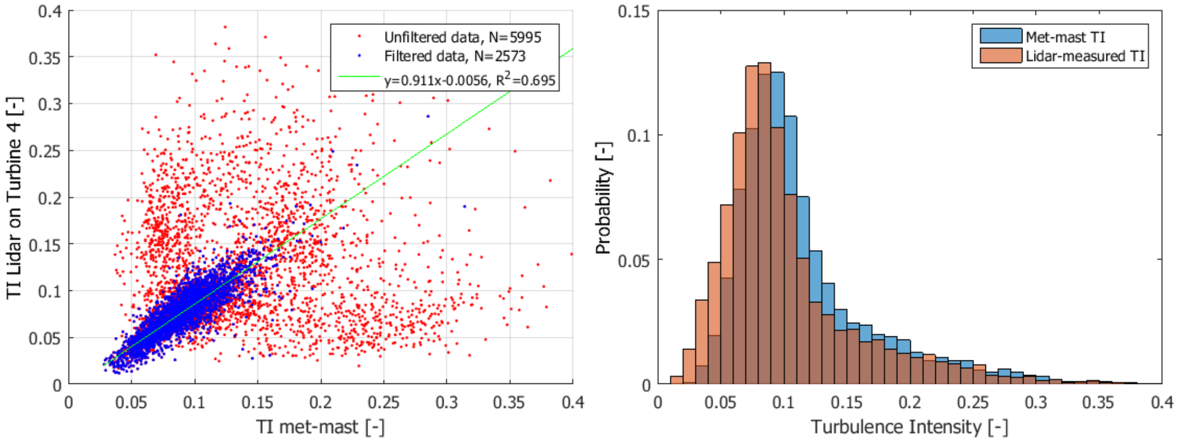

(a) *Correlation between TI measurements* (b) *Histogram of TI measurements*

Figure 8.7: *Distribution of met-mast and Lidar TI measurements at turbine 4 and the correlation between them.*

compared to the met-mast will logically result in the gradient of the regression fit being much lower than 1, as is observed in Figure 8.7a. This is confirmed by the histograms in the right figure, whereby the Lidar distribution is similar to that of the met-mast yet shifted to the left by about 0.01. Also, the R^2-values of the fit is rather low, which is caused by the large scatter of the filtered data points. From this measurement campaign, it might be concluded that the Lidar has difficulty to measure TI accurately, however this may once again be caused by the mis-calibration of the Lidar.

8.1.4. PC VERIFICATION APPLICABILITY

Finally, the applicability of a nacelle-based Lidar in PC verification will be investigated. Ideally, the device should be able to measure wind speeds accurately and with high availability, so as to be a practical device for PC verification. As the IEC advises that the wind should be measured at 2.5D from the rotor in order to minimize blockage effects, the Lidar range of 238.5m is chosen.

Figures 8.8a and 8.8b show the scattered power versus wind speed data for the met-mast and Lidar at 238.5m, respectively. Applying the filters named earlier in Section 8.1 and using the IEC binning method, the binned power curve for each dataset can be calculated. Looking at the filtered data, the Lidar data points seem slightly shifted to the right, which is logical after having concluded that the Lidar over-estimates the wind speed. This also results in the binned PC for the met-mast to be higher than reference PC while the Lidar binned PC is nearly identical to the reference PC.

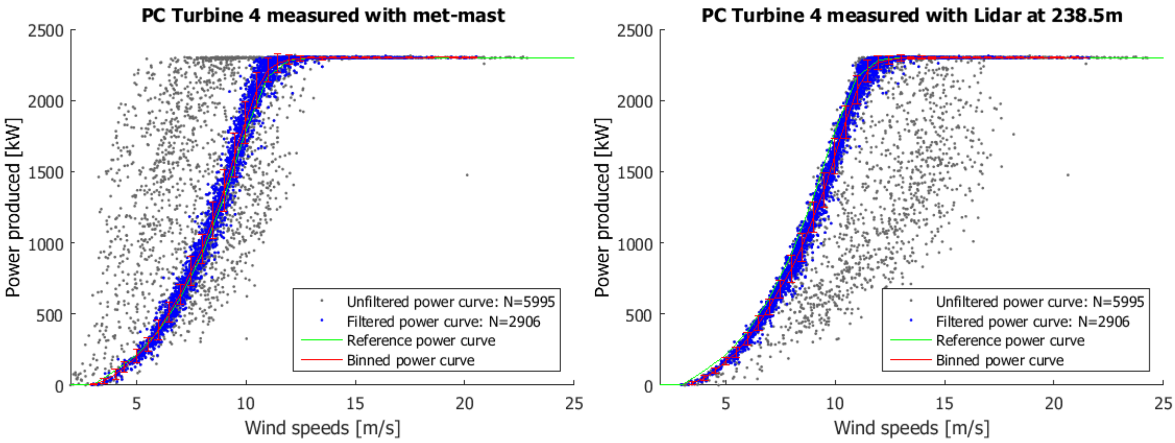

(a) *Met-mast Power Curve* (b) *Lidar Power Curve at 2.5D*

Figure 8.8: *Binned power curves measured with met-mast and Lidar compared to reference PC.*

The unfiltered data has also been included in the plots. Interestingly enough, the disturbed wind sectors show distinct patterns in the resulting wind speeds. For the case of the met-mast, the detected wind speeds are lower than the wind speeds actually working on the turbine, thereby leading to most of the data points lying to the left of the filtered data. This lower wind speed at the met-mast is caused by the wakes, and increased TI, of the neighboring turbines while turbine 4 is actually in an undisturbed wind sector. The Lidar, on the other hand, always over-estimates the wind speed while the turbine is in a disturbed wind sector. This could be caused by the fact that the Lidar beams are set at 15° from the rotor axis, meaning one, or both, beam(s) might be measuring free wind while turbine 4 is in the wake of one of the neighboring turbines.

A closer look was also taken at the PCs as measured by the Lidar at ranges closer to the rotor. Figure 8.9 shows the resulting PCs compared to the met-mast and the reference PC. As is to be expected, decreasing the Lidar measuring range improves the measured PC, moving it further to the left. The PCs for 192m and 238.5m lie very close to each other and the reference PC, while the PC for 80m lies far to the left the rest. This is caused by the rotor blockage effect, whereby the Lidar is measuring a lower wind speed than the actual free wind speed acting on the turbine at ranges closer than 2.5D. Figure 8.10 shows how the binned PCs translate to AEP, normalized to the guaranteed-PC-calculated AEP. For this comparison, the WAM-deducted wind speed distribution was used. As can be expected, measuring at 80m overestimates the AEP (by 3.4%) compared to met-mast-derived AEP. On the other hand, longer Lidar ranges lead to an under-estimation, -5.4% at 2D and -7.0% at 2.5D. These large deviations can be justified by the knowledge that the specific Lidar overestimates the wind speed at these ranges, thereby leading to 'worse' PCs and lower AEPs.

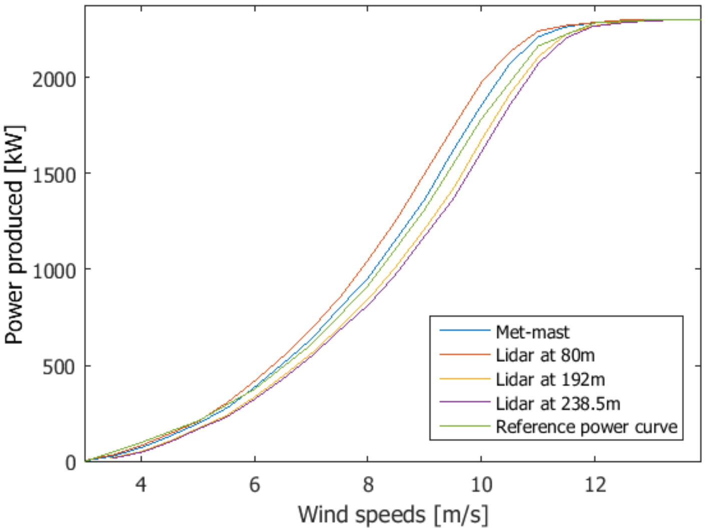

Figure 8.9: *Binned power curves measured with met-mast and spinner anemometers compared to reference PC.*

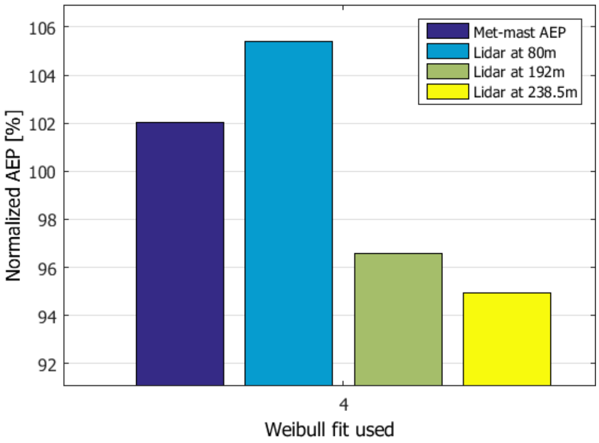

Figure 8.10: *AEP comparison of met-mast and Lidar at different ranges normalized to the guaranteed PC.*

8.1.5. OTHER POSSIBILITIES FOR LIDAR

As was already shown in Section 8.1, the Lidar has an inclinometer installed on it. Using the tilt and roll readings from this inclinometer could be an additional use of the Lidar if data is available in high-frequency(1Hz). In this case one can perform a Fourier Analysis on the signals and try to find the 1P, 2P and 3P frequencies and compare these to the initial design values if available.

Sadly the data supplied during this research was only available on 10-min basis thereby not allowing for such an analysis. Nonetheless, the tilt is plotted against wind speed to see what impact wind speed has on the turbine in Figure 8.11. As can be expected, the data points show a maximum in tilt just before rated wind speed, beyond of which the turbine will start to pitch its blades. At this point C_p and thrust on the rotor are maximized, hence causing the turbine to bend backwards and cause an increase in tilt.

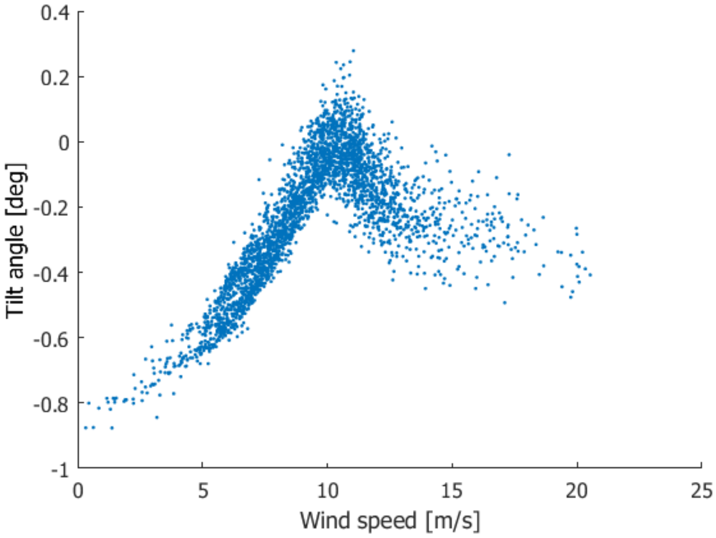

Figure 8.11: *Turbine 4 tilt angle plotted against met-mast wind speed*

8.2. SPINNER ANEMOMETER AGAINST MET-MAST

8.2.1. WIND SPEED COMPARISON

Once again, the first comparison that will be looked at is the wind speed measurements. Figure 8.12 displays the spinner anemometer wind speed readings compared to the adjacent met-mast. The data was filtered for the free wind direction, validity of spinner anemometer measurements and corrected for density using Equation B.1. As can be seen in the figure, both the correlation and the coefficient of determination (R^2) are close to unity. It therefore seems that the spinner anemometer is able to measure wind speeds very accurately after correcting the data with the calibration factor.

A side note must, however, be placed that the calibration of the spinner anemometer was performed using the met-mast, whereas future plans are for the spinner anemometers to actually be calibrated with a nacelle-based Lidar. It is expected that this will cause a decline in correlation and increase in scatter as the general rule is that a calibrated device cannot be more accurate than the device it is calibrated to.

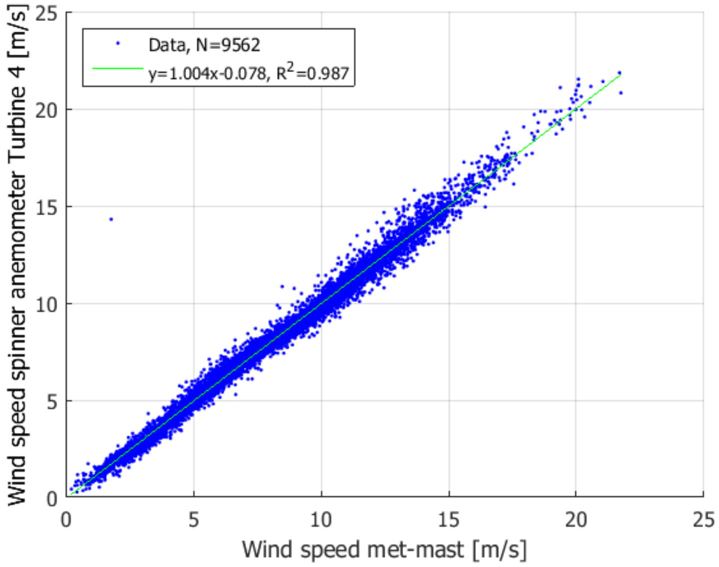

Figure 8.12: *Correlation between met-mast and spinner anemometer wind speed readings at turbine 4.*

8.2.2. WIND DIRECTION COMPARISON

Next, the devices should be able to measure wind direction accurately if it is ever to be used to yaw the turbine. Spinner anemometers actually measure the YM directly and therefore a separate yaw position has to be logged and added to the YM to find the wind direction. Besides the filters used for wind speed comparison, an additional filter is applied for wind speeds between 4 to 16 m/s, outside of which YM is of less influence on the turbine performance. Figure 8.13 displays the correlation between met-mast and spinner anemometer wind direction measurements. Once again a nearly perfect correlation is found with a gradient and R^2-value close to unity.

An offset is also seen of approx. 0.5° which seems to be caused by an offset in the Scada data. This difference also comes back in the YM-histogram (see Figure 8.14b) where the mean YM as detected by the met-mast and spinner anemometers are shown. The offset is positive for spinner anemometers against met-mast when wind direction is compared, while it is negative when YM is compared. For wind direction calculations, the Scada yaw reading is added to the spinner anemometer YM while for YM calculations the Scada yaw readings are subtracted from the met-mast wind direction. This points to the offset cause being the Scada data.

8.2.3. YAW MISALIGNMENT COMPARISON

Considering the good correlation between the wind direction measurements, it is in line of expectation that the spinner anemometer YM measurement will compare well to the YM calculation using the met-mast. Mostly, YM is defined to be the yaw position subtracted from the met-mast wind direction. However, for the case of Norrekaer Enge the met-mast wind direction reading is subtracted from the Scada yaw position, which delivers the equivalent sign of YM compared to the Lidar and spinner anemometer measurements. Applying this calculation method, a comparison can be made between the measured and calculated YMs, as displayed in Figure 8.14a. It can be seen that when applying these methods, the resulting YM is poorly correlated, as was seen for the case of the Lidar.

Figure 8.14b shows the histogram of YMs acquired using the spinner anemometers and met-mast readings. It can be seen that the average YM measured by the spinner anemometers is slightly more negative (0.5°) than when using the met-mast and Scada data, corresponding also to the offset in wind direction correlation of Figure 8.13. Also, the spread of the YM measurements using the spinner anemometers is smaller compared to the met-mast calculations, which would point to a lower measurement uncertainty for the spinner anemometers.

Like for the Lidar, the spinner anemometer correlation pattern visible in Fig. 8.14a is similar to the YM correlation found in a previous study by Goossens [7] comparing a Lidar and Sodar to calculate the YM. As no

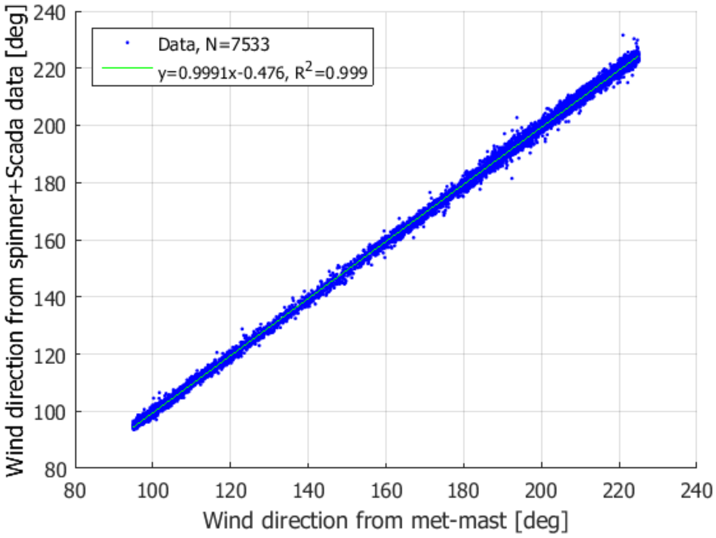

Figure 8.13: *Correlation between met-mast and spinner anemometer wind direction measurements at turbine 4.*

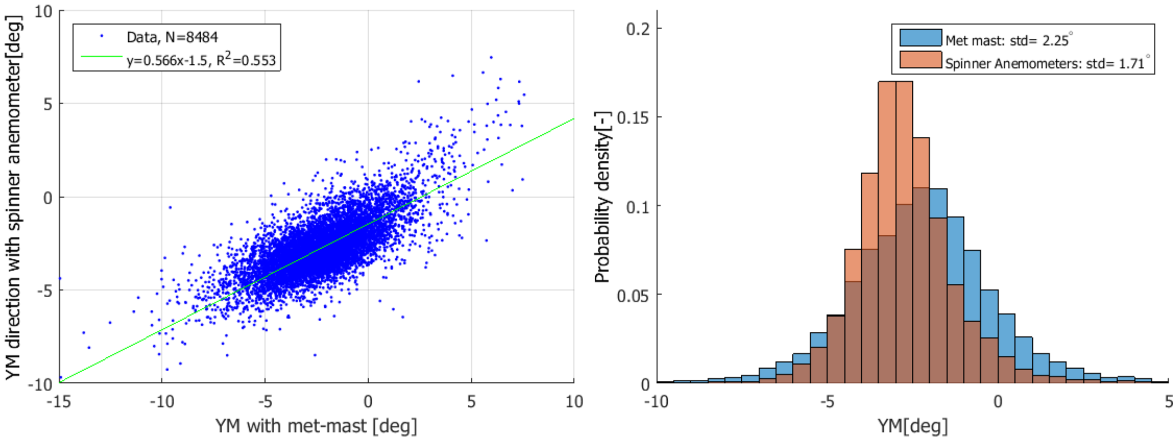

(a) *YM correlation* (b) *Histogram of YM measurements*

Figure 8.14: *Comparison of YM measurements of spinner anemometers and YM calculations using met-mast and Scada data*

clear correlation could be found, Goossens simulated the measurement campaign using Matlab in order to reconstruct the above-mentioned correlation pattern. Similar simulations as were done earlier for the Lidar were performed for the spinner anemometer case, the details of which are explained in Appendix C. Figures 8.15a and 8.15b display the acquired scatter plot and histogram of the simulated YM.

In the left figure, the dense cloud of points displays a similar pattern to Figure 8.14a, whereby the gradient and R^2 also match the measured fit best. It should be noted that as the simulations use the Matlab random generator the results vary slightly for each run, thereby not allowing for a perfect match in fitting the measured correlation. As the title of Figure 8.15a states, the optimal match between simulated and measured YM correlation was found at accuracies of 1.3° and 0.2° for the met-mast-Scada method and spinner anemometers, respectively.

This indicates that the spinner anemometer seems to achieve a very high accuracy in measuring YM while the met-mast method has a higher inaccuracy. It is considered likely that both the Scada data and the distance between met-mast and turbine 4 contribute to the met-mast method uncertainty. The Scada data generally has an accuracy of 0.5° and often it has a bias. A bias will however not increase the uncertainty but only the offset between the different methods. It is assumable that the distance of 2.5D between mast en turbine delivers a larger contribution to the uncertainty as the correlation between wind direction at the mast and turbine decreases with an increase in distance between them.

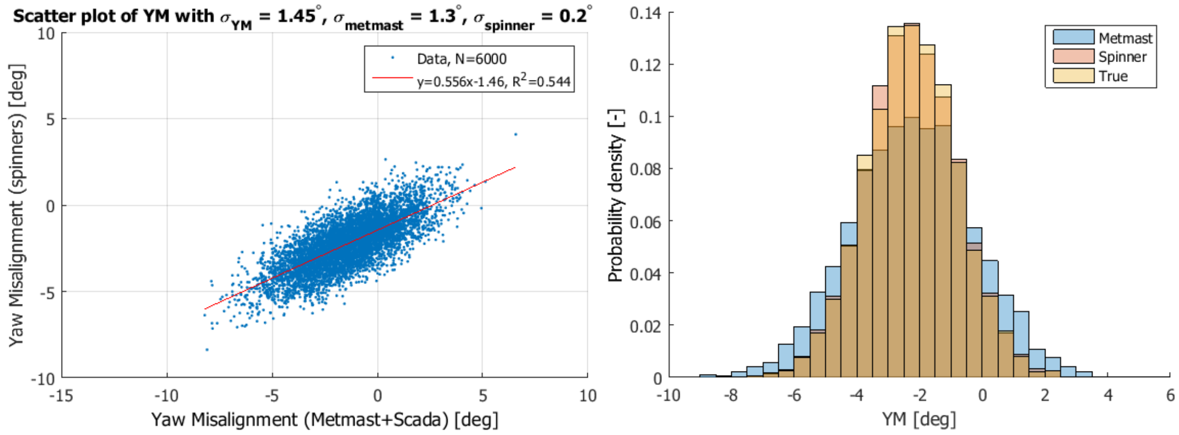

(a) *Simulated YM correlation* (b) *Histogram of simulated YMs*

Figure 8.15: *Comparison of YM simulations*

Looking at the histogram in Figure 8.15b the smaller spread in simulated YM for the case of spinner anemometers compared to met-mast is once again visible, but is also logical considering the difference in accuracies that the simulations have detected. The met-mast simulated YM is no longer shifted compared to the spinner anemometer YM as the same mean YM is used during simulation, which was not the case during measurements. Also the spinner anemometers seem to match the 'true' simulated YM distribution nearly perfectly, made clear by the histograms overlaying each other.

8.2.4. TURBULENCE INTENSITY COMPARISON

The applicability of spinners anemometers in measuring TI has not been proven up till now. As wind is measured very close to the hub, the turbulent wind flow is effected by the hub and therefore doubts are placed to whether this might influence the devices' capability to measure TI accurately.

Figure 8.16a displays the scatter of TI measurements by the met-mast and spinners. An additional filter for TI<0.4 has been applied as the spinner anemometers tend to underestimate TI above this range thereby having a too big influence on the correlation fit. It can be seen that the scatter is much bigger than is visible in the previous figures for wind speed and direction. This results in a low gradient of only 0.79 and low R^2-value of 0.56 which confirms the doubts about the applicability to measure TI that were placed earlier.

Looking at the histogram of the TI measurements in Figure 8.16b, it can be seen that generally the spinner anemometer measures a slightly higher range of TIs and that the spread is also higher. The first observation is considered peculiar as this does not become visible very clearly in neither the previous TI scatter graph nor the correlation fit between the measurements. In fact, the gradient of the linear regression is actually less than 1 meaning the met-mast generally should measure higher TIs.

Considering this strange outcome, further analysis has been performed on the acquired TI measurements. It seems that the dense cloud of data points (0<TI<0.14) is either under-estimated by the linear regression or much more dense at the bottom of the cloud than at the top. To check how the TI readings are spread in the dense cloud of points, the distribution of spinner anemometer readings is observed around a specific met-mast TI value. The data is filtered for met-mast TI values between 0.099 and 0.101, after which the corresponding spinner anemometer readings are plotted in a histogram. Figure 8.17a displays the resulting distribution. The spinner anemometer readings show a slightly higher average TI but more importantly a very large spread around the average. However, it is a normal distribution thereby not justifying the poor correlation found in Figure 8.16a.

So, at low TIs, the correlation fit seems to underestimate the contribution of these values resulting in a mismatch between the fitted line and scattered data. The binning method is therefore applied to the lower TIs (TI<0.14) in order to investigate this. Met-mast TI measurements are binned in bins of 0.001 and the corresponding spinner anemometer TIs are then averaged. Plotting these points and taking the linear regression over the binned averages eventually leads to a good correlation. Figure 8.17b displays the results of this exercise where a regression gradient of 1.03 and a R^2-value close to unity are found. The slope of the averages is slightly higher than the fitted slope for TI < 0.08 but begins to level off beyond this value. This would mean that the spinner anemometers seem to be able to measure low TIs accurately but will underestimate TI at

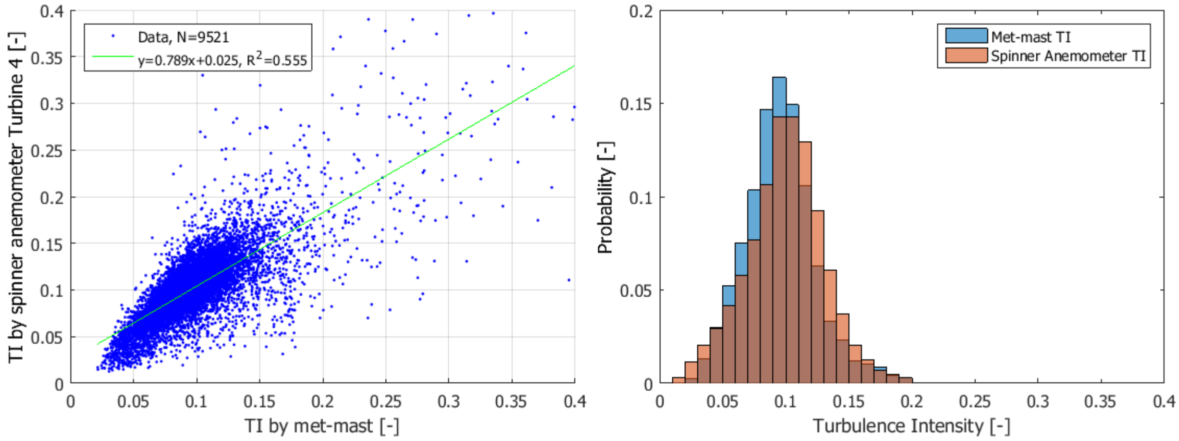

(a) *Correlation between TI measurements*

(b) *Histogram of TI measurements*

Figure 8.16: *Distribution of met-mast and spinner anemometer TI measurements at turbine 4 and the correlation between them.*

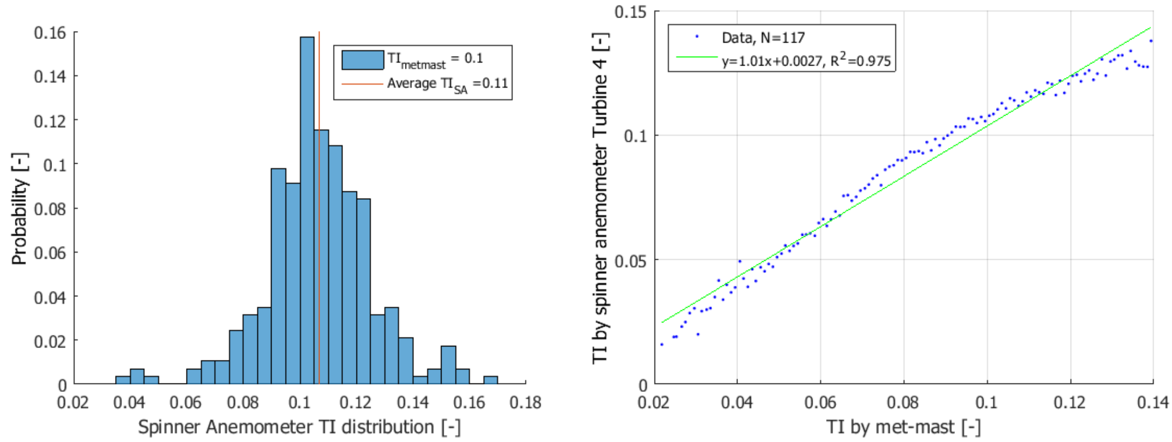

(a) *Distirbution of spinner anemometer readings for met-mast TI around 0.1.*

(b) *Correlation between bin-averaged met-mast and spinner anemometer TI measurements up to TI=0.14 at turbine 4.*

higher turbulent conditions (>0.14).

Using the knowledge acquired in the previous analysis, it was decided to perform a linear regression using a weighted polynomial fit to eventually find a correlation gradient close to unity. A weight factor was added to the lower TI values and increased until a relatively good correlation was finally the result at a weight factor of 10. The weight factor however does not influence the spread of the TI values, resulting in a comparable, and even lower, R^2-value than the original regression fit. Figure 8.18 displays the TI measurements including the weighted linear regression and TI-binned averages. Such a weighted linear regression fit could eventually be used to determine correction factor required to make spinner anemometer TI readings more accurate over the full range of TI occurrences.

8.2.5. PC VERIFICATION APPLICABILITY

The strongest test to see whether a device is applicable for PC verification is by actually applying the IEC-procedure to both datasets. This exercise has been performed for turbine 4 at Norrekaer Enge, the results of which can be seen in Figures 8.19a and 8.19b.

Looking at the unfiltered data, Figure 8.19a shows a large scatter of 'grey' points which represent the disturbed sectors. The points to the left of the reference PC occur when turbine 4 is in free wind but the met-mast is in the wake of the neighboring turbines while the points to the right of the PC occur when turbine is in wake while met-mast is undisturbed. Interestingly enough, the spinner anemometers do not seem to be influenced that much by the disturbed or undisturbed conditions. What can also be seen is that after a filter for the free wind sectors has been applied, the spinner anemometer has a lower scatter compared to

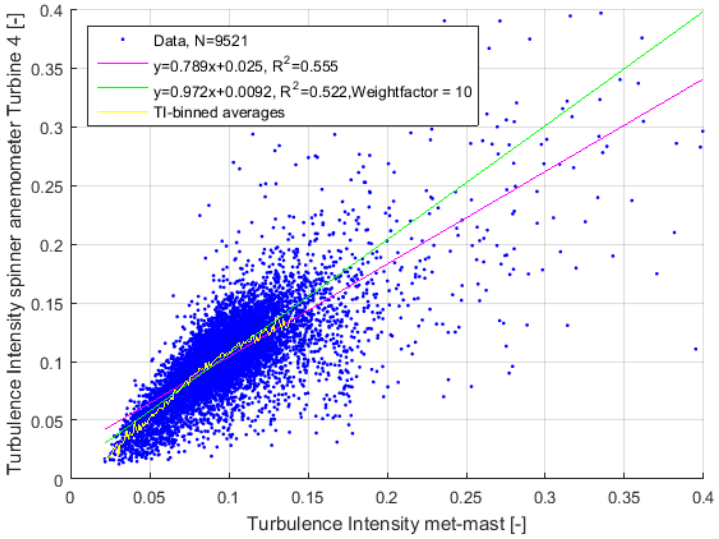

Figure 8.18: *Correlation between met-mast and spinner anemometer TI measurements at turbine 4 including the bin-averaged values and weighted correlation fit.*

the met-mast. This also translates to smaller error bars for the spinner anemometer PC. On the other hand, slightly more outliers to the right of the PC curve are visible.

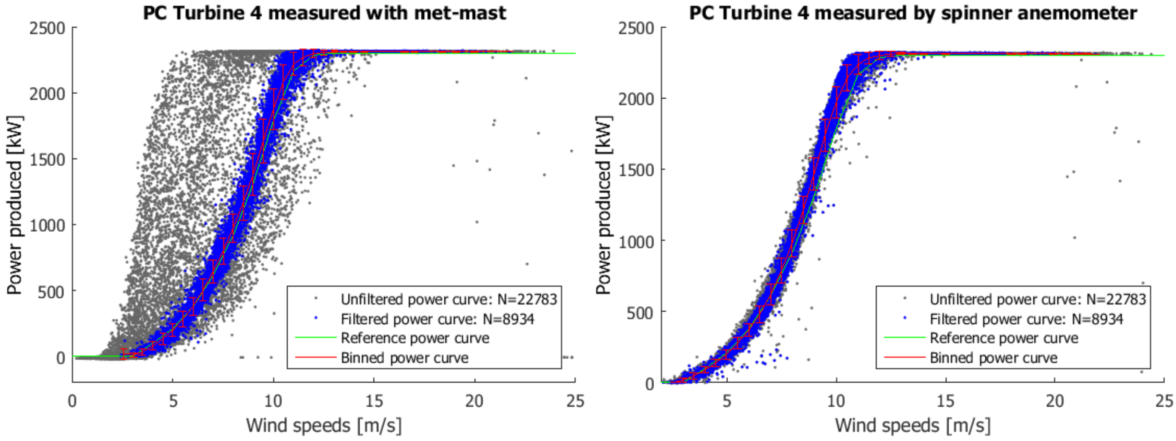

(a) *Met-mast Power Curve*

(b) *Spinner Anemometer Power Curve*

Figure 8.19: *Binned power curves measured with met-mast and spinner anemometers compared to reference PC.*

Comparing the binned PCs, the spinner anemometers seem to overestimate the power curve, probably by underestimating the wind speed slightly. The spinner anemometer deducted PC lies further to the left of the reference PC than the met-mast deducted PC. This has to be a consequence of underestimation of the wind speed since the same power readings are used.

Figure 8.20 shows the normalized AEP of the met-mast and spinner anemometers as a percentage of the guaranteed AEP. The wind speed distribution used in determining these AEPs is the WAM-deducted distribution. It is clear that the spinner anemometer leads to an over-estimation of the AEP of 1.5% compared to the IEC-standardized method using a met-mast.

8.3. DIRECT COMPARISON LIDAR AGAINST SPINNER ANEMOMETER

Romowind's vision, especially for offshore spinner anemometer deployment, is for calibration to be performed by a Lidar as installation of a met-mast will be too costly. Considering the fact that the spinner anemometer will then see the Lidar measurements as the 'true' wind speed and after calibration attempt to copy these measurements, it could be interesting to see how Lidar and spinner anemometer measurements compare after calibration with a met-mast. This comparison will be presented in this section.

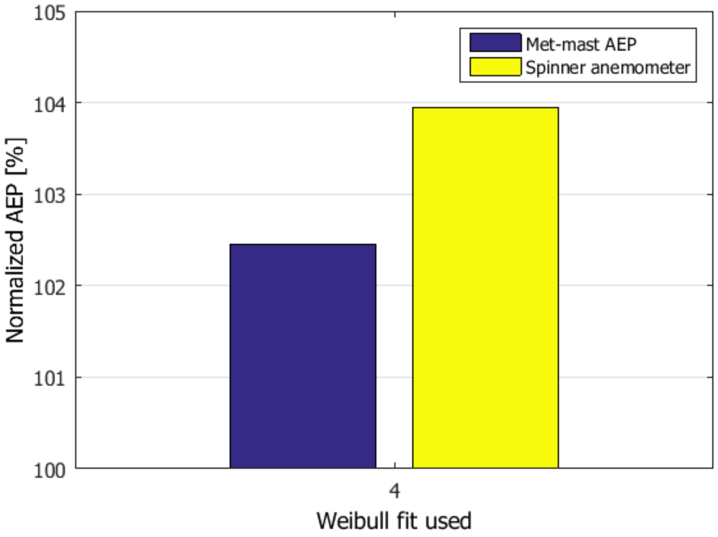

Figure 8.20: *AEP overestimation of spinner anemometer compared to met-mast with AEP normalized to guaranteed PC.*

Wind speed comparison To compare these two devices the appropriate filters have been applied to both databases, including the Lidar HWS availability and CNR thresholds and the spinner anemometer data validity. Following this, the data is also filtered for the free wind sector. Figure 8.21 shows the scatter plot of both the filtered and unfiltered Lidar wind speeds against the spinner anemometer. Just as with the comparison to the met-mast, the unfiltered data displays the same trend in which the Lidar is overestimating wind speed extremely in disturbed conditions. The filtered data show a good correlation with the slope and R^2-value close to unity. The Lidar seems to overestimate the wind speed by 2.9% compared to the spinner anemometers. Against the met-mast, the Lidar showed an overestimation of 3.3% (Figure 8.2), thus, considering the calibration of the spinner anemometer to the met-mast, a comparable overestimation by the Lidar seems logical.

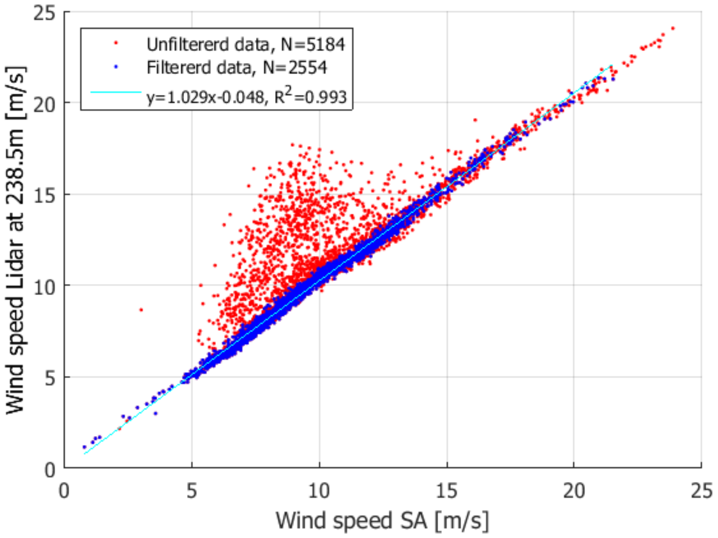

Figure 8.21: *Correlation between Lidar and spinner anemometer wind speed readings at turbine 4.*

YM comparison Next, an additional filter for wind speeds between 4 and 16 m/s is applied after which the YM as measured by the Lidar and the spinner anemometer can be compared directly. In Figure 8.22a the YM readings of both devices are given. Once again the data forms a cloud around the mean YM. The linear regression fit gives a slope close to unity but the cloud of points does result in a very low R^2-value.

Figure 8.22b shows the YM distributions of both devices and including the met-mast. The standard deviations of the distributions have also been included in the legend of the pot. From this, it can be concluded that the spinner anemometer has the lowest STD in YM and thereby uncertainty, which is justifiable considering the spinner anemometer is measuring the difference in wind direction directly at the hub. Wind direction variation than has a smaller contribution to the STD and uncertainty compared to both the met-mast and Lidar.

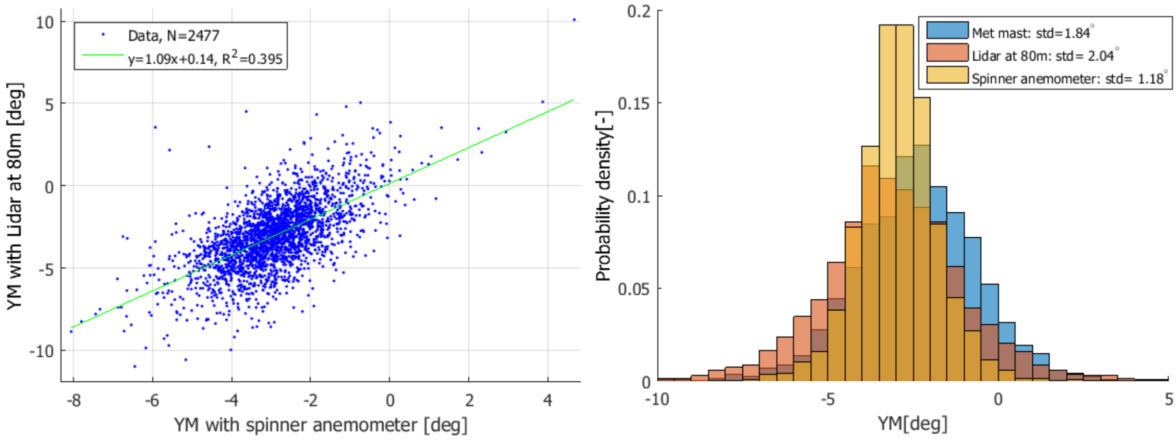

(a) *YM correlation*

(b) *Histogram of YM measurements*

Figure 8.22: *Direct comparison of Lidar and spinner anemometers YM measurements*

9

The Behavior of Yaw Misalignment

9.1. Effect of Yaw Misalignment on turbine

In this section part of the answer to the second sub-question will be investigated, specifically what effects YM has on turbine power performance. Several methods to do this have been suggested in the past, including deliberately misaligning a turbine and measuring the change in power performance[7] and analyzing the relationship between C_p and YM in existing turbine performance measurement databases[21][44]. These methods will be treated later on in this section, but first an exploratory investigation will be performed with Bladed simulations.

9.1.1. Bladed Simulations

As described in Section 5.3.2, simulations were run in Bladed so as to discover the effects of YM and WS on power performance and each other. In the following section the results of the first simulations will be presented.

During the simulations, the YM was varied from -20° to 20° in steps of 5° while the WS exponent (α)was kept constant at 0. Next, power production loading simulations are run for wind speeds between 4 and 25 m/s, the results of which can be used to calculate the dynamic PC and resulting AEP for the specific YM setting. Figure 9.1 shows the effect that the misalignment has on the power curve. Here only the YMs between 0° and 20° are plotted since their negative counterparts are nearly identical. The difference between the PCs for a YM of 0° and 5° is barely visible and hence YM<5° does not seem to have a major impact on the PC. As the YM increases more, however, the PC shifts more to the right. It can also be seen that the gaps between the curves increase as the YM increases, showing a non-gradual or non-linear pattern.

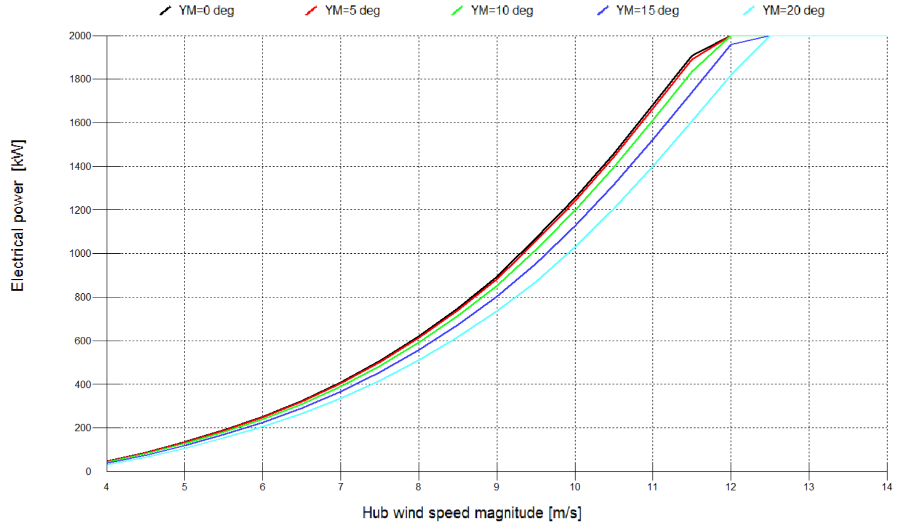

Figure 9.1: *Resulting PCs for Bladed simulations while varying YM.*

A more clear and handy way of judging the effects of YM on power performance is by calculating the AEP for each YM case and normalizing this to the zero-YM case. This has been done for YMs of -20° to 20°, the result of which is shown in Figure 9.2. The plots for $cos(YM)$ and $cos^2(YM)$ have also been added as earlier studies show a possible similar dependency of AEP to YM. Also, during the first simulations the flow inclination angle was set to 8° by mistake, thereby giving different and misleading results. As can be seen in the figure, the simulated YM actually lies below the $cos^2(YM)$-curve meaning the exponent might be slightly higher.

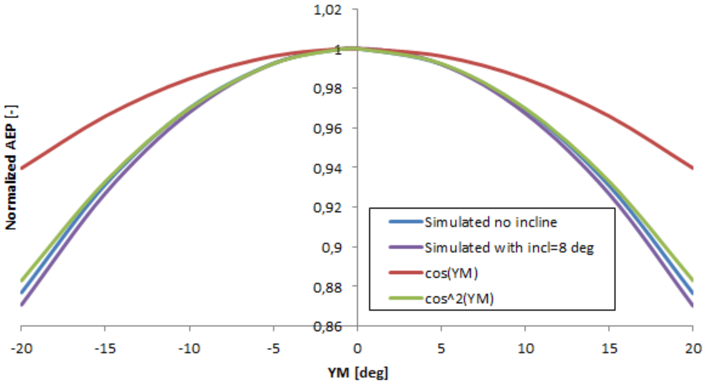

Figure 9.2: *Simulations of the YM effect on AEP.*

Looking at the data itself, it seems that the plot is not perfectly symmetrical around zero-YM, as the normalized AEP at positive counterparts are slightly higher than at their negative counterparts. This would mean that the ideal yaw error of a turbine might actually not be zero, even at a vertically-uniform wind flow. Upon taking a closer look at YM ranges around 0°, it was found that the ideal yaw error lies somewhere between 0° and 0.25° for the no shear case.

This was considered to be peculiar as the theory behind Bladed, BEM theory, is rather straight-forward and does not allow for such a deviation. The settings of the Bladed turbine in use were therefore studied again and a rotor tilt angle of 4° was discovered. This setting simulates a similar effect as wind shear would have on the ideal yaw error, and therefore could be the cause of the non-zero ideal yaw error. Additional simulations were run for the turbine without tilt and several YM settings around 0°, only to find that the ideal yaw error seems to be 0° when no axis tilt or wind shear is applied to the turbine. This confirms that the tilt was indeed the cause for the AEP not being symmetrical around zero YM.

9.1.2. APPLYING BOORSMA'S METHOD ON PRINSES ALEXIA DATA

Boorsma et al. [44] proposed a method to analyze the impact of YM on power performance without actively misaligning the turbine. This method has been explained in Section 5.2 and the results of the implementation will be presented here.

Figures 9.3a-9.3d show an example of this method's results for the case of two influential wind speed ranges (7-9 m/s and 9-11 m/s), whereby the power coefficients corresponding to these ranges are plotted against YM. The scatter in the C_p-values is found to be rather big ranging from 0.1 to 0.8. An additional filter was therefore applied to remove C_p-values below 0.25 and higher than 0.65, which are considered to be surrealistic power performance conditions and thereby corrupting the results of the method. Also, the binned average C_p is only calculated if the YM bin contains at least 5 data points to ensure that single values cannot impact the cosine fit too much. Following this, the YM-binned averages can be calculated and, looking at the figures, they do tend to follow a cosine-shaped pattern. This cosine dependence is especially strong for turbine R01, where exponents of 5 and 2.1 are found.

Whether the method proposed by Boorsma is able to find the relation between C_p and YM is questionable as can be seen in the Figures 9.3a-9.3d. Where the cosine fits sometimes seem to match the averaged C_p rather well, the fit also sometimes shows a cosine with a high exponent while a horizontal line through the average values might look just as good a match. Also, applying this method over the input parameter ranges results in extremely high cosine-exponents (>5) at times, so high even that it seems unlikely and not physically justifiable.

Boorsma et al.[44] already mentioned in his study that the applied method is very sensitive to the chosen wind speed or YM bin size. In the present study, the same trend is seen, adding to the doubts about the re-

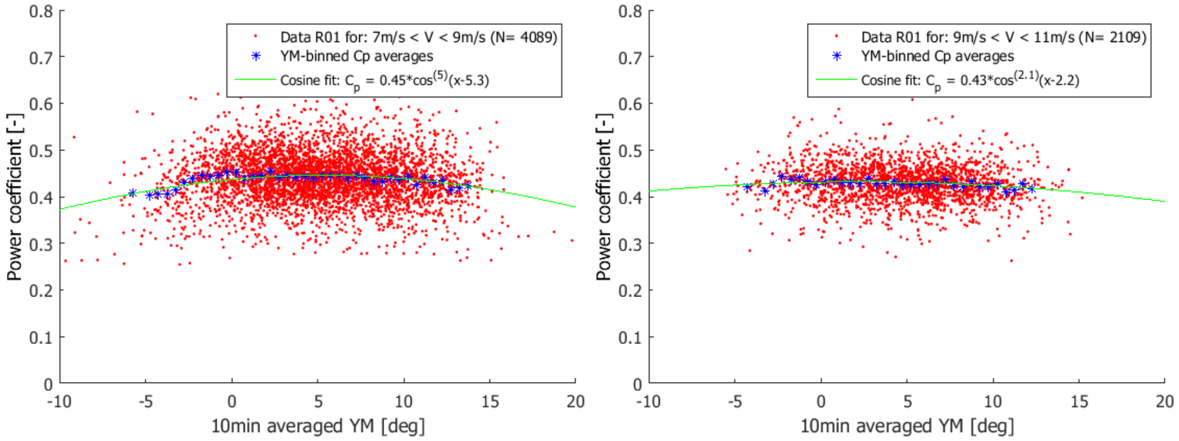

(a) *Wind speed: 7-9 m/s* (b) *Wind speed: 9-11 m/s*

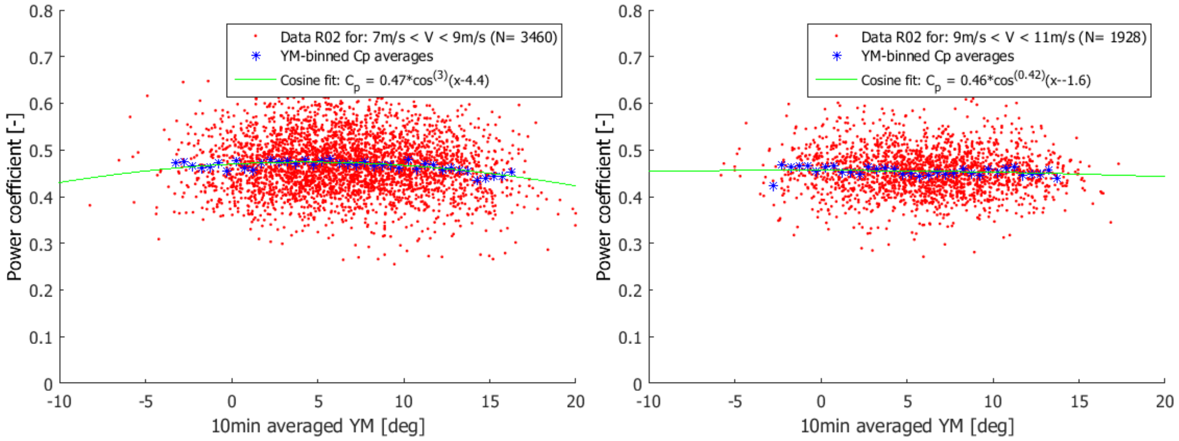

(c) *Wind speed: 7-9 m/s* (d) *Wind speed: 9-11 m/s*

Figure 9.3: *Relation between yaw misalignment and power coefficient at turbines R01(top) and R02(bottom)*

liability of this method. Eventually, it was decided to stick to the same bin sizes and conditions as Boorsma suggested in his study.

Next, the wind speed range is varied over a range of wind speeds (4-14 m/s) in which YM is thought to affect the power performance the most. Boorsma's method is then applied to each wind speed range in order to be able to compare the effect of wind speed on the different fit parameters. Figures 9.9a-9.9c display the resulting plots of the cosine fit magnitude, the phase shift and the exponent, respectively, against the wind speed bin in which this occurs. As mentioned before, a wind speed bin size of 2 m/s is used. For these bins, the average wind speed has been calculated and used in the figures.

Looking at Figure 9.9a, it can be seen that as wind speed increases from 5 m/s towards rated, the maximum C_p increases initially, reaching a maximum around 8 to 9 m/s. As the wind speed comes closer to the rated wind speed(ca. 13 m/s) this value starts to fall rapidly. In the torque-controlled region of the turbine, the region of the PC below rated wind speed, the turbine controller tries to achieve and hold on to the maximum C_p. This is in contradiction with the lower C_p-values found in the figure. Also, one would expect the power coefficient to stay maximal until wind speeds approach rated wind speed, so the outcome of the cosine-fit does seem strange.

To investigate whether this strange behavior is caused by the applied method or rather the controller of the turbine, step 4, the cosine-fitting, was left out of the analysis method. Instead, the maximum C_p-value of each wind speed bin is found and plotted against the average bin wind speed. The reason for doing this is that the cosine-fitting might be pick a lower maximum fitted C_p in order to ensure a better fit, thereby eventually causing for lower C_p-values at lower wind speeds and around rated wind speed. Figure 9.4 displays the maximum C_p-values against the cosine fitted magnitudes for both R01 and R02. As can be seen, the C_p-values acquired without step 4 show similar behavior at low and around rated wind speeds, although the maximum C_p-values are all higher than their relative bin cosine-fitted counterparts. This shows that the applied method assumes a slightly lower fit magnitude than the actual maximum C_p in order to find the best fit. However, it can also be concluded that the analysis method is not the cause of the observed strange behavior.

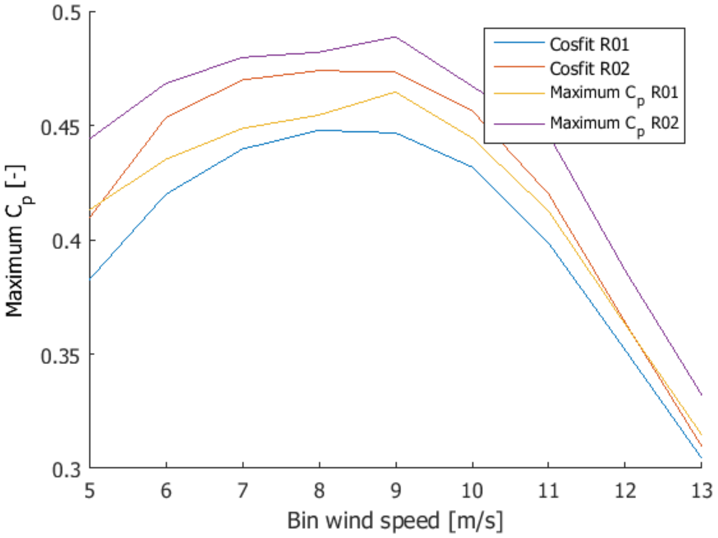

Figure 9.4: *Average pitch angle per wind speed bin.*

As the strange behavior does not seem to be caused by the applied method, the turbine controller is the next logical cause. The controller is able to lower C_p by pitch the turbine blades, hence it is interesting to consider the pitching behavior of the turbines. In Figure 7.5, a scatter plot of the pitch angles against wind speed has already been given. These pitch angles have been binned per wind speed bin and averaged over these bins. Figure 9.5 shows the resulting plots of pitch against binned wind speed. Both plots show that the pitch angle for wind speeds below 6 m/s is not zero, which would be expected. This might be caused by the 10-minute averaging whereby the turbine can be in both stand-still (pitch = 45° or 90°) and starting-up (pitch = 0°) during the corresponding timespan. This would then also explain a lower average C_p over these 10 minute periods. Also, it is observed that both turbines start pitching from wind speed above 9 m/s, further away from the rated wind speed than expected. This is strange behavior by the turbine controller but explains the lower power coefficients at wind speeds above 10 m/s.

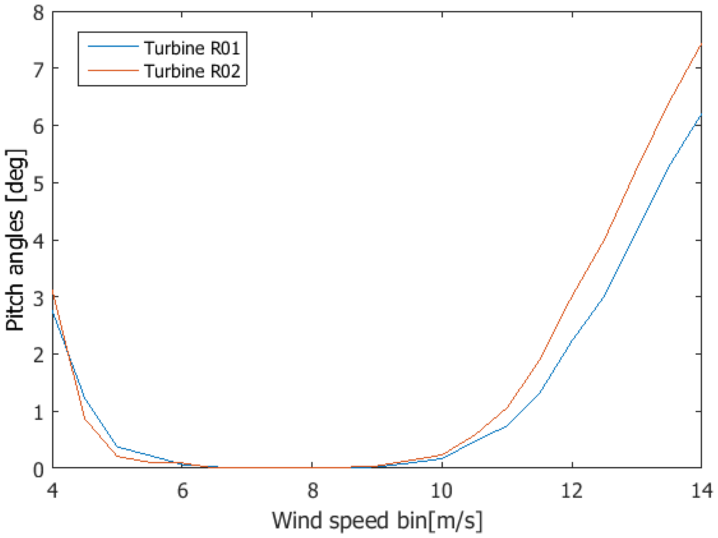

Figure 9.5: *Average pitch angle per wind speed bin.*

Finally, considering Figure 9.9b and 9.9c, no clear conclusion can be made about the behavior of the phase shift and exponent of the cosine fit when a turbine is experiencing YM. At high wind speeds (v>10 m/s), fitted cosine becomes a nearly perfect horizontal line, as can be seen by the low exponent values. The horizontal line als makes the cosine phase shift to be very sensitive to fluctuations, explaining the big phase shifts (>10°) as seen in the figure for turbine R02 for instance. From this it would seem that YM does not have an influence on these specific turbines at wind speeds above 10 m/s.

Deliberate YM campaign As part of this thesis, a deliberate YM campaign has been devised and proposed to Vattenfall to execute at wind park Prinses Alexia. The idea of the campaign is to change the static YM of the turbine by manually biasing the control function and consecutively measuring the power performance of the turbine under test. Sadly, time cut the project short thereby not allowing for the campaign to be executed before submitting this thesis report. Nonetheless, the proposal is presented in Appendix E and when all goes well, it may yet be executed before the end of 2015.

9.2. EFFECT OF WS ON IDEAL YAW ERROR

In the following section, a study will be performed into the hypothesis about the effect of WS on the ideal yaw error as it was posted in Section 3.3.1. This will be done in two forms, first with the help of Bladed simulations, after which the results will be compared to actual turbine production data at Prinses Alexia.

9.2.1. BLADED SIMULATIONS

To investigate the effect of WS on the ideal yaw error, the same Bladed turbine settings and simulation as in the previous section are used. In this case however, the wind shear exponent was varied between 0, 0.2, 0.4 and 0.5 while the YM was changed from -1° to 2° in steps of 0.25° for each WS case. Such a small step size was chosen since this appeared to be the scale in which the ideal yaw error is influenced as WS increases. Once again power production loading runs are performed over the turbine wind speed operational range, after which a dynamic PC and an AEP per WS-YM case can be determined. The ideal yaw error is defined by the point where maximum AEP is achieved, so the goal of this exercise is to find the crest of each WS-unique AEP curve. Figure 9.6 displays the resulting AEP curves for the different WS exponents.

For each WS case it is possible to detect a crest in the AEP curve. More importantly, the YM point at which the crest occurs, the ideal yaw error, increases as the wind shear exponent increases. This is in agreement with the hypothesis as postulated in Section 9.2 whereby a higher wind shear favors the effect of a positive YM on a higher airfoil angle-of-attack at the rotor top, eventually resulting in more power.

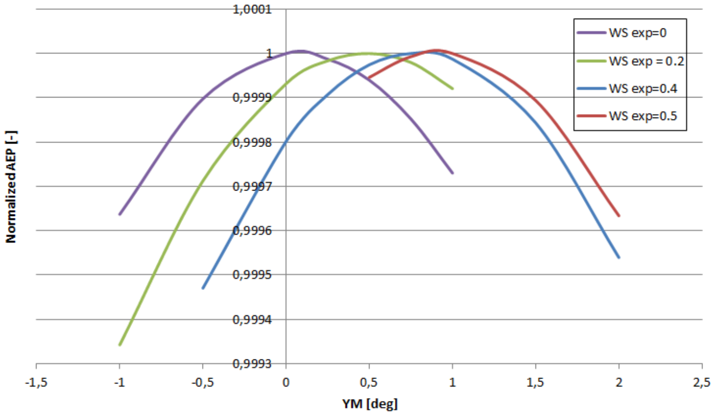

Figure 9.6: *Simulations of the WS effect on ideal yaw error.*

Although this does seem like an important finding in this research study, the actual change in ideal yaw error from ≈ 0° at no wind shear to 1° at a WS exponent of 0.5 is relatively small and might be considered negligible. Wind shear conditions are often within this range meaning an actual impact on turbine performance might be minimal, especially when taking the often higher 'static' YMs observed on operational turbines into consideration.

9.2.2. BOORSMA METHOD WITH WS BINS

Bladed is a software package based on BEM theory, it is therefore difficult to judge whether this shift of the ideal yaw error occurs in practice and not just in theory. Therefore, to compare the simulation findings with reality, a next step is to investigate whether the hypothesis also holds for experimental data at wind park Prinses Alexia.

To perform this investigation, Boorsma's method has been adjusted slightly and applied to the dataset. Instead of applying filters for wind speed bins, the data is filtered for several WS exponent bins ranging between 0.1 and 0.5 with a bin width of 0.2. The WS exponents were calculated making use of the met-mast measurements wind speed measurements at 46.4m and 98m height and applying these different heights to Eq.8.1. The same filters for C_p-range and amount of data points in the YM bin as applied during no WS are applied to the database. The bin WS exponent is calculated by finding the average of WS exponents which lay in the bin. Figures 9.7a and 9.7b show an example of the scattered and the bin-averaged C_p-values including the corresponding cosine fit for both turbines at WS exponents between 0.1 and 0.2.

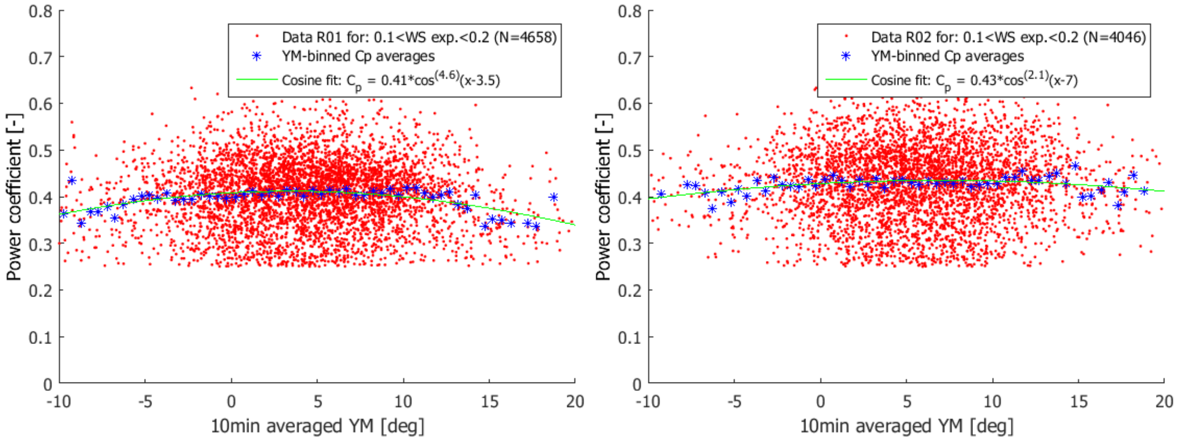

(a) *Turbine R01* (b) *Turbine R02*

Figure 9.7: *Relation between yaw misalignment and power coefficient at turbines R01(top) and R02(bottom)*

Next, the wind shear bins are varied and the cosine fit magnitude, phase shift and exponent are calculated for each bin. Figures 9.10a-9.10c show the resulting plots of the fitting parameters against the bin wind shear exponent.

The results from Figure 9.10b show that indeed as the wind shear exponent increases, so does the fitted cosine phase shift. At a low WS of 0.1, it seems that both turbines favor a phase shift close to their respective average YMs of 4.67° and 6.24° as found in Section 7.1.3. As the WS increases, this favored YM setting of the turbine increases steadily. For both turbines an increase of approximately 2.5° in ideal yaw error is detected when the WS exponent increases from 0.1 to 0.5. During the Bladed simulations, an increase of 1° was found when increasing the WS exponent from 0 to 0.5, significantly smaller than Boorsma's method shows. Nonetheless, it seems that the measurements also confirm the hypothesis that wind shear will cause the turbine to prefer a positive YM. What magnitude this shift in ideal yaw error has cannot be concluded on based on the experiments performed in this study. Also, the question arises what the significance of the average turbine YM as measured earlier in Chapter 7 is. Is this a mis-calibration of the YM related signals or is this model of turbine generally favoring a positive YM, even at vertically homogeneous wind speeds? It seems most likely that the nacelle direction is mis-calibrated, thereby not giving the actual YM of the turbines.

Observing the trend between the cosine exponent and WS exponent in Figure 9.10c, the cosine exponent is rather high(>3.5) for all WS exponents. Literature values for n range between 1 and 5 so one might doubt the validity of these findings. On the other hand, however, the exponent generally does seem to increase as WS increases, meaning YM only becomes more important at higher WS. A higher exponent means that if the turbine is not misaligned at its' ideal yaw error, the performance losses become bigger at deviations from the ideal yaw error. In fact, the combination of high WS exponent and an increased ideal yaw error will probably amplify each other since currently turbine controllers are set to hold an ideal yaw error of 0°. Thus, if the turbine is to align the turbine perfectly while a high wind shear actually demands a higher, positive YM, losses could turn out higher than the cos^2 that many in the wind industry generally hold on to.

SENSITIVITY BOORSMA METHOD

Following the discussion in the previous section on the sensitivity of Boorsma's method, some additional filters were applied to the data to see what their individual impact on the results would be. Boorsma et al.[44] found that the choice of average value and size of the wind speed bin influences the outcome of the analysis. To investigate the significance of the findings concerning the ideal yaw error, a sensitivity analysis is performed. The normal method includes a C_p filter, WS bin size of 0.1 and a YM bin size of 0.5°. The following changes are applied to the method:

- The C_p filter is removed.
- WS bin size is decreased to 0.1.
- YM bin size is increased to 1° and 2°.

Figure 9.8 shows the effect these changes have on the relation between phase shift and WS exponent compared to the 'normal' case for R02. As can be seen, the trend of an increasing phase shift with increasing WS remains visible even if the changes are applied. Only when the WS bin size is halved, the phase shift becomes more fluctuating which seems a logical consequence of the smaller WS averaging. The fact that the changes do not seem to alter the results a lot, gives more trust in the results found on the relation between WS and the ideal yaw error.

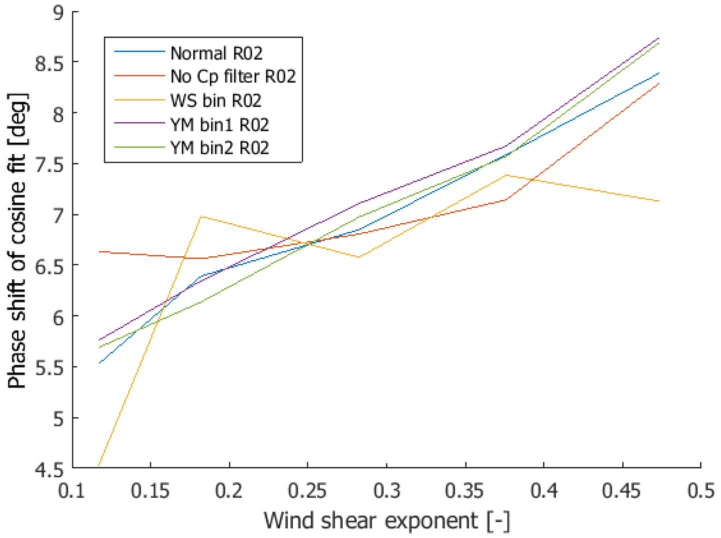

Figure 9.8: *Sensitivity of phase shift with Boorsma's method using different filters and bin sizes.*

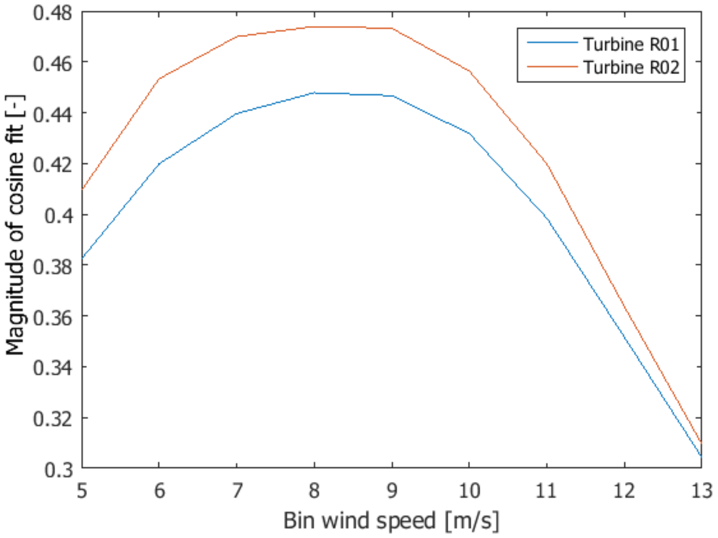

(a) *Effect on power coefficient(C_p)*

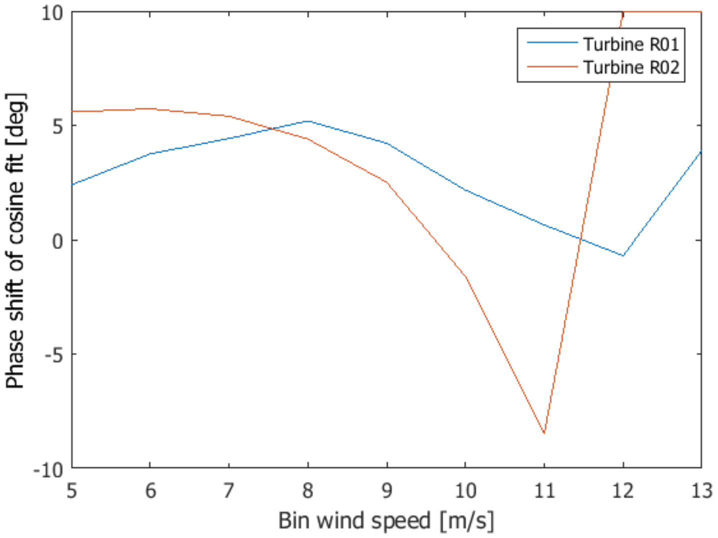

(b) *Effect on phase shift*

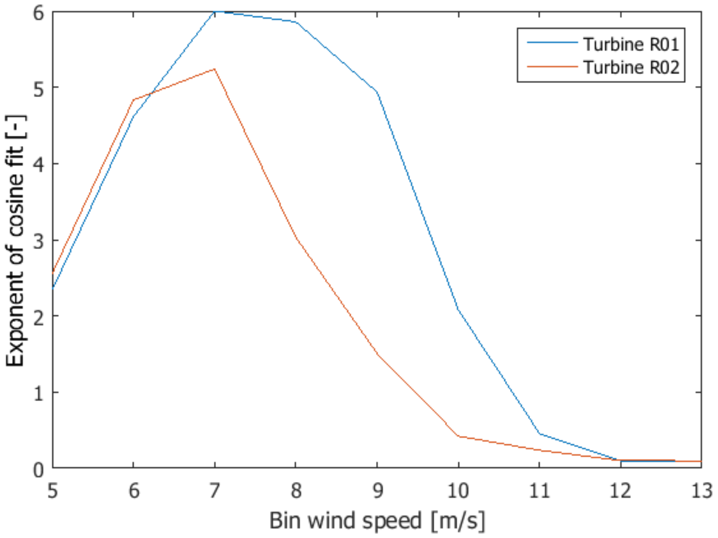

(c) *Effect on cosine exponent*

Figure 9.9: *Relation between wind speed and maximum power coefficient, phase shift and exponent of cosine fit with Boorsma's method at turbines R01 and R02*

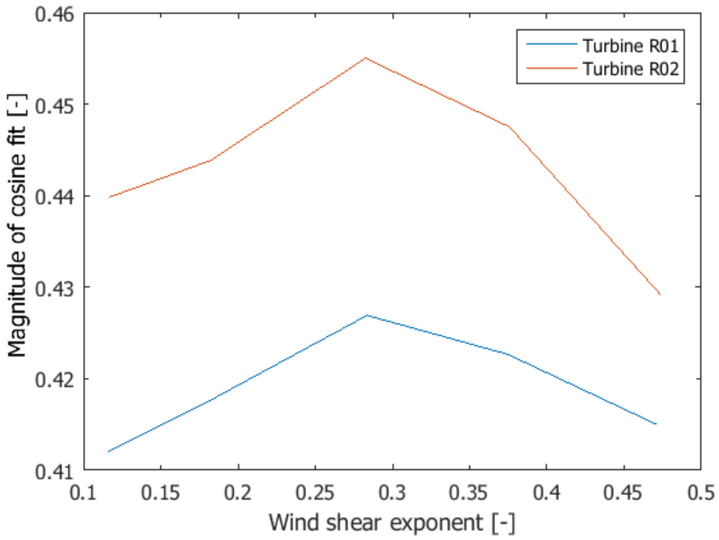

(a) *Effect on power coefficient(C_p)*

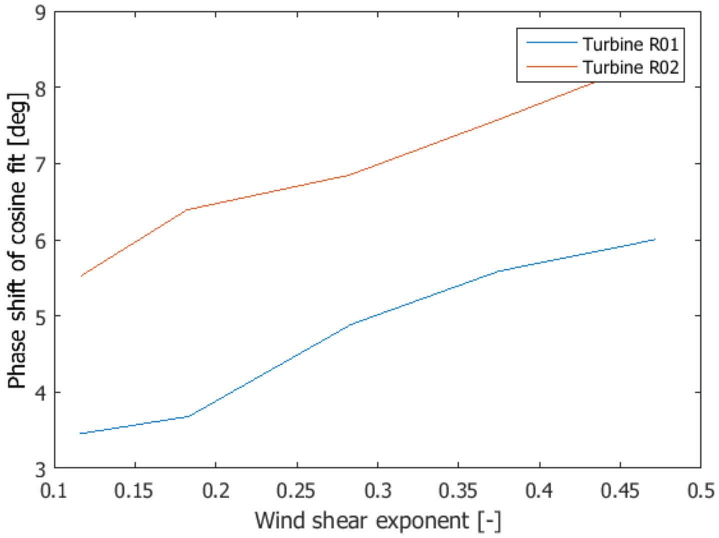

(b) *Effect on phase shift*

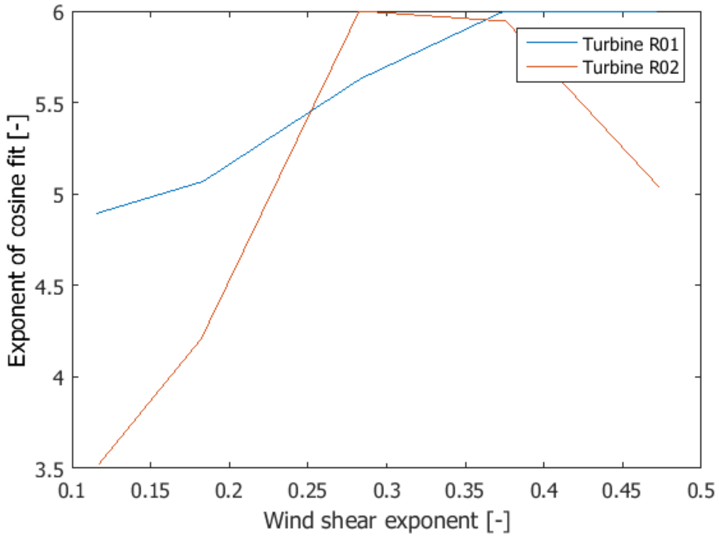

(c) *Effect on cosine exponent*

Figure 9.10: *Relation between wind shear exponent and maximum power coefficient, phase shift and exponent of cosine fit with Boorsma's method at turbines R01 and R02*

10

OUTER ENVELOPE CONDITIONS

10.1. CONDITIONS DURING CAMPAIGN

Following the fourth research objective, a study was done into the presence and effects of 'outer-envelope conditions' over the performed measurement campaign with a met-mast at Prinses Alexia. Figure 10.1 shows the different TI and WS exponent combinations occurring during the campaign. Also, the red box in the figure represents the inner-envelope conditions for the installed turbines, whereby it is clear that there is a great number of data-points (70%) not complying to the guaranteed conditions. It is therefore justifiable to question what effects this will have on the performance of the turbines under test.

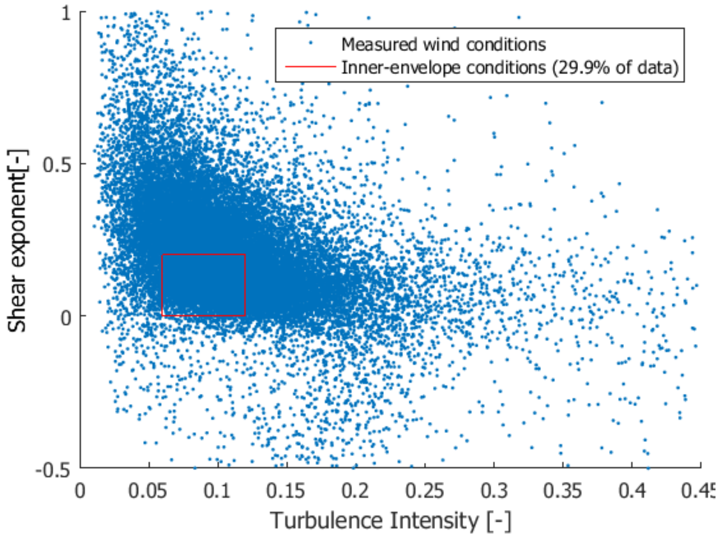

Figure 10.1: *Wind shear and turbulence conditions at Prinses Alexia with the turbine guaranteed conditions shown by the red box*

The methodology applied for this study has been introduced briefly in Section 5.2. It is based on applying the binning method twice, first for a specific WS or TI bin and then a second time for different wind speed bins. The WS exponent is varied from 0 to 0.5 in steps of 0.1 while the TI is varied from 0 to 0.3 in steps of 0.1. In Figures 10.2a-10.2d the resulting number of points per binning method is given for both turbines under investigation. The distribution of number of points differs per turbine since they have different free wind sectors.

It can be seen from the figures that for several TI and WS cases, there are only few, and sometimes no, data points. This is especially the case for very low TIs(<0.05) and TIs above 0.2, but also the higher wind speeds (>10 m/s). A lack of data in a bin would make it impossible to construct a complete PC and calculate the AEP. In this case, the missing bin has to be interpolated using two adjacent wind speed bins. Thankfully, since the measurement campaign was performed over a time period of 8.5 months, enough data was gathered for this to occur only at wind speeds above rated wind speed where the power can be taken to be rated power.

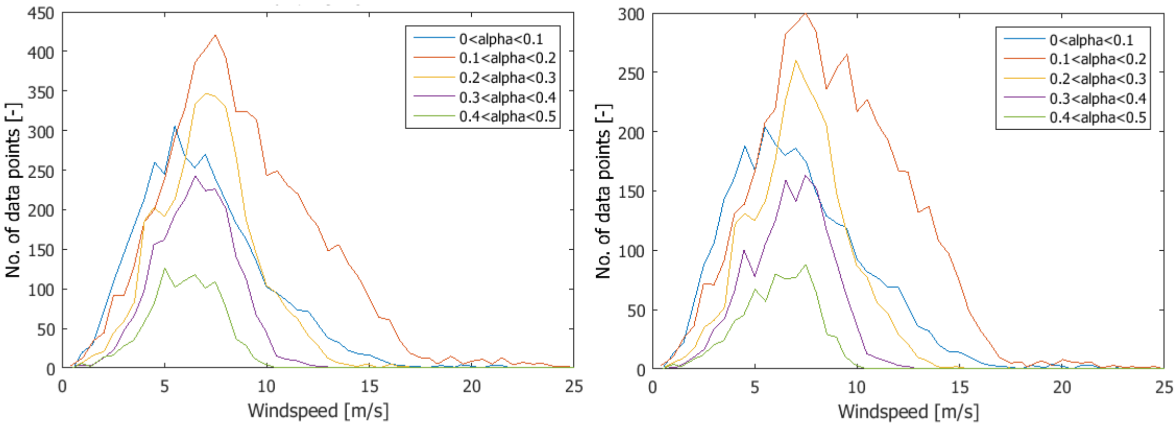

(a) *WS at Turbine R01* (b) *WS at Turbine R02*

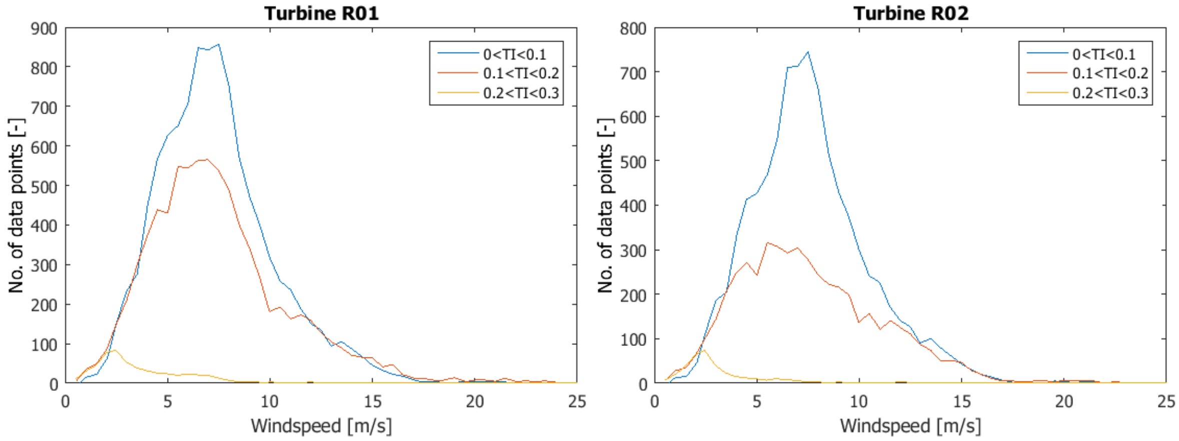

(c) *TI at Turbine R01* (d) *TI at Turbine R02*

Figure 10.2: *Number of points per wind speed bin for different TI and WS bins*

10.2. EFFECT OF WIND SHEAR

Before the effect of WS on turbine performance will be analyzed based on measurements performed at wind park Prinses Alexia, a brief investigation will be done using simulations run in Bladed. Bladed, making use of BEM theory, will be able to give the theoretical relation between power performance and wind shear, after which it will be interesting to compare with the actual measurements at Prinses Alexia.

10.2.1. RESULTS WITH BLADED SIMULATIONS

During the investigation on the effect of WS on the ideal yaw error as described earlier in this report, simulations were also run for different wind shear exponents ranging from 0 to 0.5 while keeping the turbine perfectly aligned. Power curves are generally guaranteed for wind shear exponents lower than 0.2 so the chosen range does sufficiently exceed the guaranteed case. The same method for the simulations was applied whereby first power production loading simulations are run, which are then used to calculate the dynamic PCs and estimated AEP.

Figure 10.3 shows the PCs acquired for the different wind shears. The difference in PCs is hardly distinguishable but, between cut-in and rated wind speed, it can seen that the PCs belonging to higher WSs (WS exponent>0.4) generally lie above the other PCs. This is in agreemeent with an earlier study by Villanueva[41], whereby hardly any effect on the PCs by WS was visible while making use of similar Bladed simulations. It is expected that influence of the higher angle of attack (α) at the top than at the bottom of the rotor is favoured more by the higher wind speeds at the top when high shear exponents are applicable. The larger difference in wind speeds at the top and bottom could then cause a slight increase in power performance. In this case it also makes sense that this only influences the range between cut-in and rated wind speed, as beyond the rated wind speed the aerodynamic efficiency is decreased by pitching the blades.

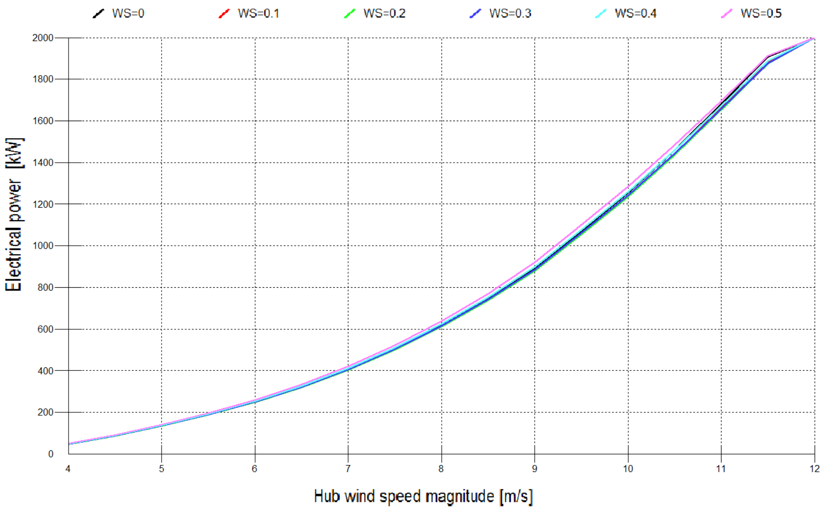

Figure 10.3: *Simulations of the WS effect on the PC.*

Translating the measured PCs to AEP, the effect of WS on the performance of the turbine becomes clearer. Figure 10.4 shows the AEP normalized to zero WS against the shear exponent. As explained earlier in Section 9.1.1, the flow inclination angle was originally set to 8° by mistake thereby leading to lower results which have also been plotted in the figure. Interestingly enough, the simulations dictate that the shear exponent range (<0.2) mostly used for guaranteed PCs actually delivers up to 1% less than the zero WS case. Also, shear exponents above this range (especially >0.4) apparently give higher AEP than guaranteed. This is in agreement with the analysis based on the acquired PCs as shown in Figure 10.3.

In the study performed by Villanueva [41], however, a slight difference was seen in the power performance. The specific study concluded that zero WS delivered the best output, followed by WS exponents of 0.4, 0.1, 0.3 and 0.2, respectively. The simulations in this study limited themselves to a maximum WS exponent of 0.4, so a comparison with 0.5 is not possible. Nonetheless, the results found in this paper do not deviate much from Villanueva's study, where the order of WS exponents related to high to low power performance is 0.4, 0, 0.3, 0.1 and finally 0.2. Since Villanueva did not compare the AEP-outcome directly, it is not known how big the difference between the individual WS settings was in the prior study.

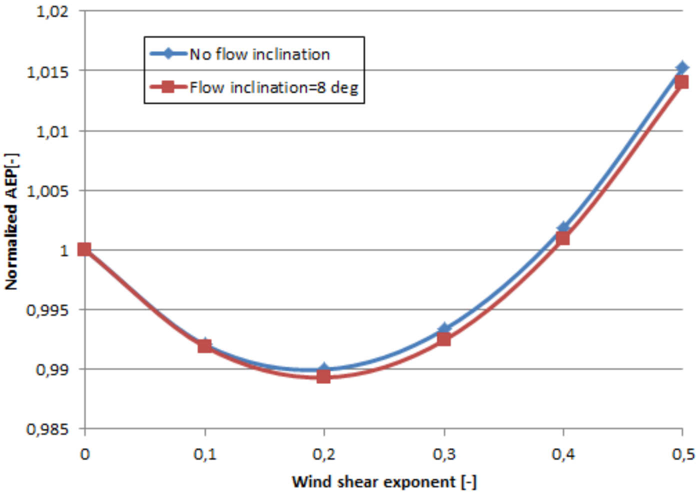

Figure 10.4: *Simulations of the WS effect on AEP.*

10.2.2. RESULTS BASED ON MEASUREMENTS

Using the binning method in combination with filters for different wind shear exponent ranges, power curves for different conditions can be calculated. These PCs for both R01 and R02 at different WS exponents are displayed in Figures 10.5a and 10.5b. Just like in the simulations, hardly any difference is visible in the PCs when WS increases. Only around rated wind speed the PCs are generally lower than the reference PC. This is seen for both turbines R01 and R02.

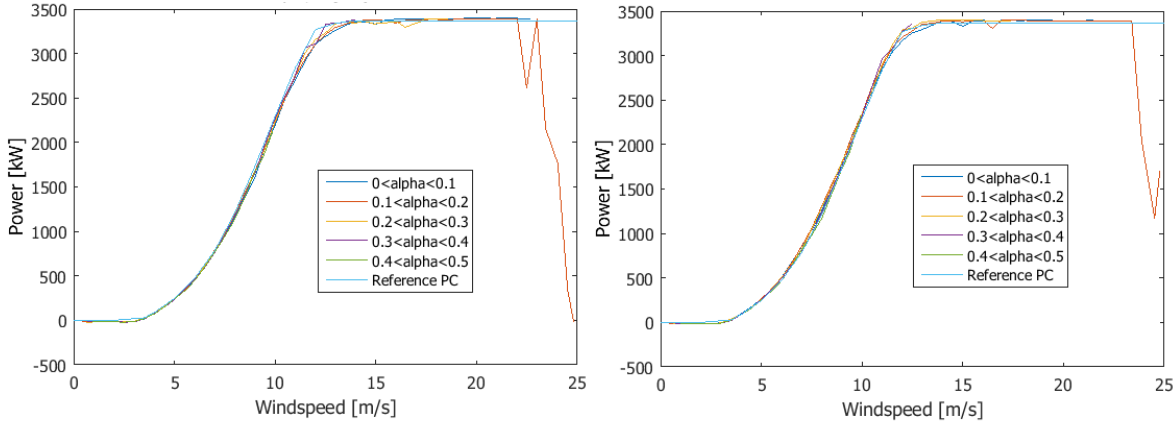

(a) *Binned Power Curves for R01* (b) *Binned Power Curves for R02*

Figure 10.5: *Binned PCs at different wind shear bins*

Because fluctuations are so small compared to the actual magnitude of the power readings, the difference is hardly visible in the PCs. To have a closer look at the differences between the relative PCs, the relative power differences have been normalized to the reference PC. In this case, the average bin wind speed is used to find the corresponding 'reference' power reading by interpolating to the reference PC. Next, the relative power difference is calculated by subtracting the reference PC from the PCs for a specific WS condition and normalizing this with the reference PC. Figures 10.6a and 10.6b show the plots of the normalized power differences compared to the reference PC for the different WS exponent bins.

First of all, a clear difference is seen between R01 and R02, where the readings of R02 are higher than R01. This is in agreement with the findings in Chapter 7 where turbine R02 was found to have better performance than R01. More importantly, it can be seen that at low wind speeds(<8 m/s), lower WS (<0.2) delivers a higher power while at higher wind speeds(>10m/s) the opposite occurs. This is especially visible in the plots for turbine R02 where the blue and red lines are above the rest at low wind speeds but become the lowest as wind speed increases.

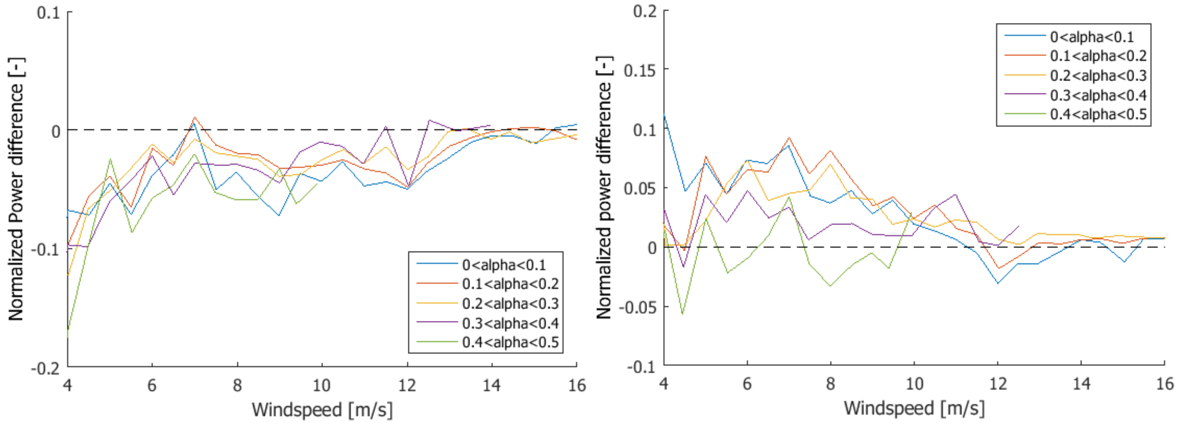

(a) *Relative power differences for R01* (b) *Relative power differences for R02*

Figure 10.6: *Relative bin power differences at different wind shear bins normalized to the reference PC.*

Finally, it is interesting to see how the different PCs translate to AEP calculation. To do so, the acquired WS-binned PCs are multiplied by an appropriate wind speed distribution for the site, in this case the WAM-derived distribution. Figure 10.7 shows the normalized AEPs of both turbines against the corresponding WS exponent. First of all, the difference in power performance between R01 and R02 is clearly visible. Secondly, it can be seen that the AEP reaches its' maximum around a WS exponent of 0.2 and is the lowest for higher WS exponents(>0.4).

This is in contradiction to the results found during the Bladed simulations as shown in Figure 10.4. In the simulations, a minimum AEP is found at a WS exponent of 0.2 and an increase in AEP as WS became bigger.

The difference here might be caused by TI, which was set to zero during the Bladed simulations. As seen in Figure 10.1, a high TI generally occurs at lower WS at wind park Prinses Alexia. Adding to this, Villanueva [41] found that WS has a smaller impact on power performance than TI. The combination of these two could cause the increased power performance seen at low WS to be caused by the high TI related to the low WSs. A way to mitigate the influence of TI, is to isolate the WS filters for TI values within the turbine guaranteed conditions (<0.2) and apply the same methodology. The downside is that a very large dataset is required for both the turbine and met-mast readings to ensure a complete PC.

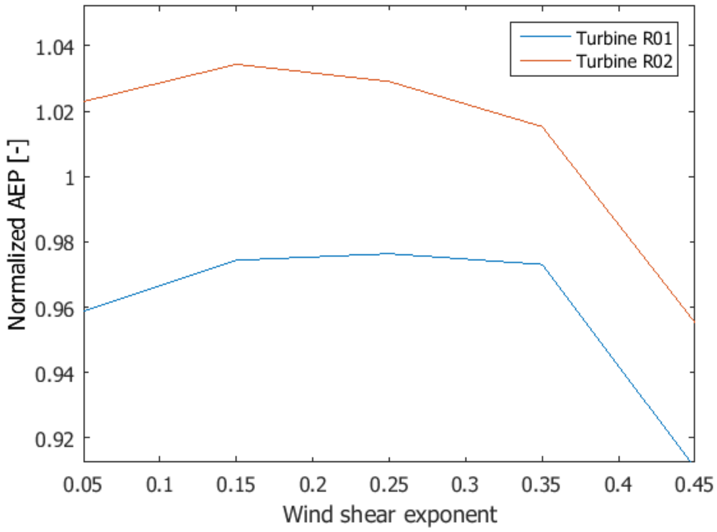

Figure 10.7: *Effect of wind shear on the AEP normalized to the reference PC.*

10.3. EFFECT OF TURBULENCE INTENSITY

In this section, the changes occurring in power performance at varying TI conditions will be investigated. Applying the same methodology as for the WS conditions but then with certain TI bins, TI-binned PCs can be acquired. Figures 10.8a and 10.8b show the binned PCs for the different TI bins. One clear observation in both figures that can be made is that high TI(>0.2) leads to lower power performance around rate wind speed as was found in earlier studies[40][41]. For other wind speeds hardly any conclusive differences are observed, hence a closer look will be taken again at the relative differences between the TI-binned PCs and the reference PC.

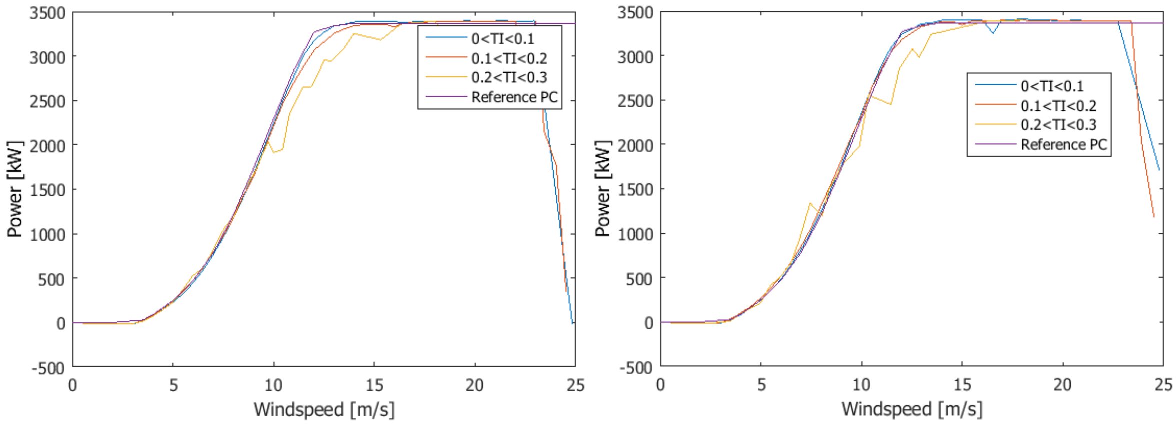

(a) *Binned Power Curves for R01*

(b) *Binned Power Curves for R02*

Figure 10.8: *Binned PCs at different turbulence intensity bins*

In this thesis, Bladed simulations were not run for varying turbulence conditions. Villanueva[41] did, however, perform such a study. In his simulations the TI was varied from 0 to 0.3 in steps of 0.06 while the WS was set to 0. The simulations follow the same procedures as applied in the current research, resulting in dynamic PCs. The comparison of the simulated PCs to the steady PC is shown in Figure 10.9. Similar trends are visible in the simulated PCs as in Figures 10.8a and 10.8b, where high TIs around rated wind speed result in a lower power production. The simulated PCs also show a higher power production for high TIs at low wind speeds(<9 m/s), something which is not clearly observed in the measured PCs at Prinses Alexia.

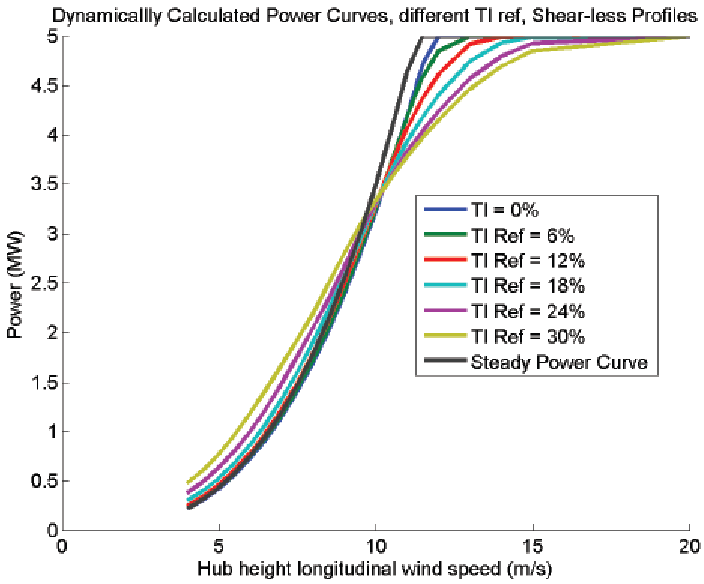

Figure 10.9: *PCs at different turbulence conditions found with Bladed simulations[41].*

Figures 10.10a and 10.10b display the normalized relative differences at different turbulence conditions. The yellow lines in both plots show relatively large deviations which are caused by the lack of data points, thereby being extra sensitive to outliers in the data. Nonetheless, it can be seen that just above cut-in wind speed, high TI favors higher power output compared to the guaranteed PC. As wind speed increases towards rated wind speed, this effect is reversed, where a lower TI corresponds to a higher power output. This transition seems to occur around the wind speed in which the turbine will start to pitch its' blades (around 9 m/s).

A likely explanation for the effects of TI on power performance might be found in the relation between C_p and wind speed as shown in Figure 9.4. TI is defined as the deviation of the wind speed from the mean of the 10-min data point. In the 10 minutes corresponding to the data point, the wind speed will be fluctuating around the average wind speed, above and below, with the magnitude in the order of $TI * v_{mean}$. At low wind speeds (<6 m/s), a deviation above the mean wind speed will contribute more to the average C_p compared to a negative wind speed deviation. As the magnitude of the deviation becomes bigger(higher TI), the influence of higher C_p becomes bigger, thereby eventually biasing a better power performance. After the turbine starts to pitch, the C_p-curve drops rapidly, causing a similar but opposite reaction to occur. Now, higher, positive deviations from the mean wind speed, cause a bigger drop in 10-min average C_p, thereby leading to lower power performance.

Villanueva[41] also plotted the deviations in power produced at different TIs. In this case, the difference between the TI-binned PCs and steady PC is calculated and then normalized to the steady PC. Figure 10.11 shows the resulting plots. For high TI, the power seems to deviate a lot from the steady PC at low wind speeds. These large normalized deviations are mainly caused by the low power readings of the steady PC at these wind speeds, which lead to a large increase during normalization. Such large deviations are not seen for the measured PCs in Figures 10.10a and 10.10b, but the same trend is visible whereby the high TIs lead to higher power at low wind speeds. Also, the trough in power deviation as seen in the measured deviations for high TIs around rated wind speed, appears in the simulated results too. In fact the relative deviation at v=11-12 m/s is approximately -20% for both the measured and simulated PCs during high TI (0.2<TI<0.3). This confirms that indeed the high TI causes power increase at wind speeds just above cut-in and a power decrease around rated wind speed.

Finally, the TI-binned PCs are multiplied by the WAM-deducted wind speed distribution in order to estimate the corresponding AEPs. Figure 10.12 shows the relations between normalized AEP and TI for both

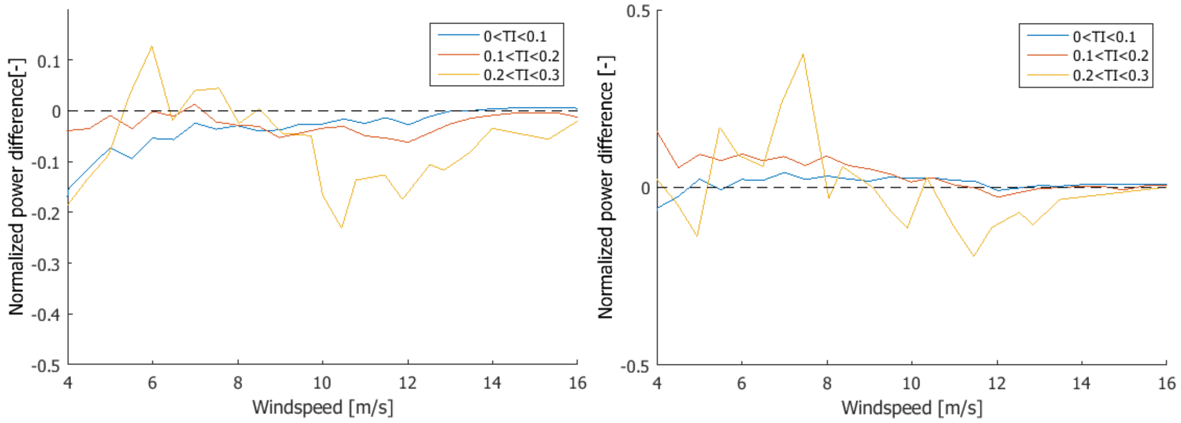

(a) *Relative power differences for R01* (b) *Relative power differences for R02*

Figure 10.10: *Relative bin power differences at different turbulence intensity bins normalized to the reference PC.*

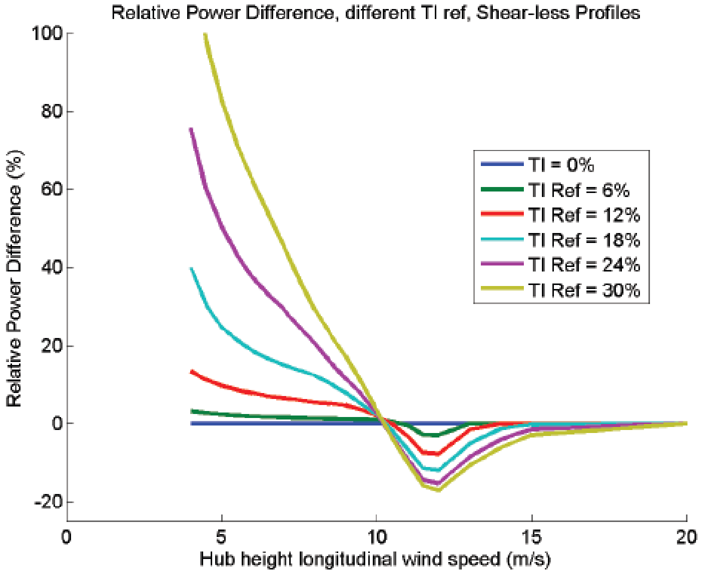

Figure 10.11: *Normalized power difference at different turbulence conditions found with Bladed simulation[41].*

turbines R01 and R02. The relations show an increase in power performance as TI increases up to a TI of 0.2, after which the AEP drops again. At the guaranteed conditions of the turbines (0.06<TI<0.12), it seems the turbines do operate close to their maximum AEP but beyond these conditions the turbine will probably under-perform. This justifies the research that the wind industry is putting into TI-correction of PCs and incorporating this into the new proposed standards.

Returning to the discussion regarding Figure 10.7, whereby it was considered that the deviation in AEP behavior of the simulations and measurements with WS could be caused by TI, it seems that TI could contribute to the behavior but it cannot fully justify the difference in WS behavior. Looking at the magnitude of normalized AEP in the (Fig. 10.4), experiments with WS (Fig. 10.7) and TI (Fig. 10.12), it is seen that the contribution of high turbulence conditions could never fully explain the difference between the simulated and measured AEP-WS relations. This means that no conclusive remarks on the behavior of AEP at varying WS conditions can be made based on the results in these analyses.

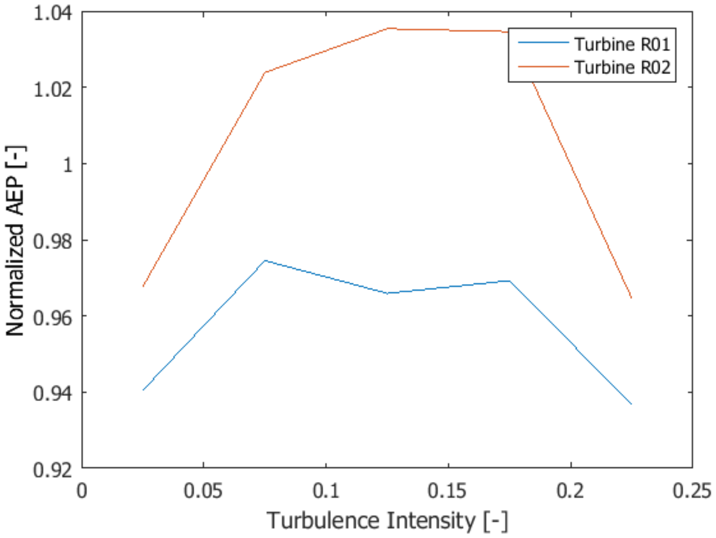

Figure 10.12: *Effect of turbulence intensity on the AEP normalized to the reference PC.*

11

FINANCIAL FEASIBILITY STUDY

In this chapter an attempt will be made to translate the gained knowledge on the novel measurement techniques and the occurrence of YM into prospective business cases. In Chapter 8 the measurement accuracies of the individual devices has been investigated and proven. Next, the goal of this exercise is to see whether the novel instruments will not only be worthy replacements of met-masts in the technical way, but also whether applying these techniques are financially feasible for wind park operators like Vattenfall.

11.1. ANALYSIS METHOD

In this section, a brief overview of the methodology applied to determine the business cases will be given. First the assumptions made in the business cases will be presented and discussed, followed by a short description of the economic factors on which the business cases will be weighed.

11.1.1. ASSUMPTIONS

The first assumption that has been made is to use wind park Prinses Alexia in the business case. This is a relatively new park, having been installed in September 2013, and is therefore expected to stay in operation until September 2033, considering a standard lifetime of 20 years. This means the business case will run from 1 January 2016 till September 2033, resulting in a remaining lifetime of 17.5 years of the park. Implementation of the business case on a new, yet to be constructed, wind park was considered but eventually the choice for Prinses Alexia was made as a lot of knowledge has already been gained on this park and a difference of 2.5 years in lifetime was considered to be of minimal impact on the business case. Besides this, the implementation of novel devices at wind park Prinses Alexia is a current topic of discussion within Vattenfall, making the results of this business case study interesting.

The business case of both devices will depend on the performance improvement possible in a wind park due to correction of the YM on each turbine. Once the measurement device has been installed on the turbine, it will measure the static YM over a period of time, which can then be corrected, either by re-calibrating the wind vane readings or by changing the turbine controller function. Both correction methods are considered to be possible via the turbine Scada system so without having to access the turbine. Although earlier studies have shown that it is possible to detect the static YM in 7-15 days[21], the campaign length necessary to sufficiently determine and correct the turbine YM is assumed to be 2 months. This is a conservative assumption, but also allows for correction of YM in multiple steps, which Romowind have shown to be necessary sometimes. This results in a Lidar being able to correct the YM on 6 turbines in a year, while spinner anemometers will correct all the YM in the first two months as they will be installed on each turbine.

Next, assumptions have to be made about the time-value of money. Essentially, the future cash flows need to be estimated and discounted using the Weighted Average Cost of Capital (WACC) or also the discount rate. This rate incorporates the fact that the money invested in the project cannot earn interest at the bank but also incorporates a risk or uncertainty to the future cash flow of the project. If the uncertainty is higher, the discount rate will also be higher. This is also seen in renewable energy sources, where lesser-developed technologies are related to higher discount rates than more mature technologies. EWEA[45] advises to use a discount rate of 7.5% for wind energy projects. Other literature predicts that discount rates for policy-supported sustainable energy technologies could drop by 2-3% in the next decade and a further 1-2% by 2040 as these technologies develop[46]. For onshore wind energy, the range of discount rates in 2011 was found to 7-10% and expected to drop to 6-8% and 5-8% by 2020 and 2040, respectively. Nonetheless, for the purpose of this study it is chosen to hold on to 7.5%.

A wholesale electricity price of 63.5 €/MWh is assumed for the additional electricity that will be gained due to the YM correction based on information from within Vattenfall. For sake of simplicity, the electricity price is assumed to remain equal over the remaining lifetime of the project. Some studies predict a yearly increase at a rate of 2%, but other sources once again expect a decline in electricity price as more and more renewable energy sources enter the market leading to an over-capacity in the market.

Finally, the turbine availability at Prinses Alexia is assumed to be 98% based on data of 2014. Also, a wind farm wake loss of 5.5% is taken into account based on pre-assessment results in WindPro. Table 11.1 gives a complete overview of the assumptions made on wind park Prinses Alexia based on information gathered internally at Vattenfall.

Table 11.1: *Overview of assumptions made for the purpose of the business case.*

Parameter	**Assumption**
Remaining park lifetime	17.5 years
Number of turbines	36
Campaign time YM correction	2 months
Electricity price	63.5 €/MWh
Discount rate	7.5%
Wind park availability	98%
Wind farm wake loss	5.5%
Pre-assessed wind conditions	A=7.9m/s, k=2
Average wind park YM	4°

11.1.2. METHOD

In this section, the economic variable which will be used to quantify the value of a project with either a Lidar or spinner anemometer will be introduced. A commonly used variable in analyzing the profitability of a project is the Net Present Value (NPV). It represents the summed difference between the present value of benefit inflows and the present value of costs of the project. Here all outgoing and incoming cash flows are corrected to the beginning of the project by the discount rate. The following formula is used to calculate the NPV:

$$NPV = \sum_{t=1}^{T} \left(\frac{C_t}{(1+r)^t} \right) \tag{11.1}$$

whereby C_t represents the net cash flow in the specific year t, r is the discount rate, and T is the total remaining park lifetime. A positive NPV indicates that the project is profitable and therefore the investment may be made. The higher the NPV, the more attractive the investment becomes. As can be seen, the discount rate is related to the NPV inversely and exponentially with time, thus gains at the end of the park lifetime have a smaller impact on the NPV. Also, the chosen discount rate influences the NPV greatly, therefore this rate has to be chosen carefully.

Another variable commonly used in project valuation is the Internal Rate of Return (IRR). The calculation of the IRR is based on the same equation as NPV, but then setting the NPV to zero and solving for the discount rate with which this is reached. Basically, the IRR is therefore the maximal discount rate which is allowable to acquire a profitable project but is also considered to give an estimation of the growth rate of the investment. The advantage to comparing IRR instead of NPV of a project is that it represents a yearly value. If a 5-year investment has the same IRR as a 10-year investment, it might be more interesting to choose for the 5-year investment as after that time the money has grown equally fast as the 10-year investment but you are free to reinvest the money after 5 years.

The final variable which will be looked at is the investment's Payback Time (PBT). Contrary to the NPV and IRR, this variable does not incorporate the time value of money. Rather it quantifies the amount of time necessary for the benefits to equal the pay back the initial costs of the project. The payback time is calculated using the following equation:

$$PBT = \frac{\sum(C)}{B_{in}} \tag{11.2}$$

where C represents the project costs and B_{in} is the annual benefit or cash inflow. An investment with a shorter PBT will be considered a better investment, as companies generally will want to earn their investment back as soon as possible in order to have the money available to make new investments.

11.2. ANALYSIS RESULTS

11.2.1. COSTS

In this section the different costs to be made to perform a YM correction campaign with either a Lidar or spinner anemometer will be presented. Generally, the costs are divided into costs for initial purchasing, installation, Operations and Maintenance (O&M), decommisioning of the device in question as well as costs made for data analysis.

LIDAR

The purchase costs for an Avent WindIris Lidar are estimated to be €130 000 based on indications by Oldbaum Services. It is also possible to rent the device, but considering the fact that 36 turbines have to be corrected it will be cheaper to buy the device. As the Lidar will be used over 6 years at Prinses Alexia, the initial purchase costs are to be written off in the first 6 years, equating a €21 670 per annum. Following the campaign at Prinses Alexia, Vattenfall can move the Lidar to different wind parks to perform the same campaigns there. This added value will however not be taken into account in this feasibility study.

The Lidar installation and decommissioning costs have been acquired from previous operations by Oldbaum Services during the research by Goossens[7]. For both the installation and decommissioning of the Lidar, Oldbaum set up a quotation for €1800 for the hours involved in each of the works, and an additional €1500 for equipment required during the installation. Considering that 6 turbines are to be corrected each year, the sum of installation and decommissioning costs is made 6 times a year. Besides the payments to the installer/decommissioner of the Lidar, potential income is also lost during these operations due to forced stand-still of the turbines. The costs connected to this are calculated by finding the average power output of a turbine at Prinses Alexia and multiplying by the amount of hours the turbine is to be stopped and the electricity price. For the wind conditions at Prinses Alexia, a year-average power output of 1025 kW is found. A turbine stand-still period of 8 hours for each operation is assumed, leading to an energy loss of 8200 kWh per operation. By multiplying this with the electricity price, the potential energy loss is translated to monetary value or lost income.

For the purpose of ensuring that the Lidar is measuring properly, a small cost item is included under O&M. This item incorporates turbine visits necessary to solve eventual problems being detected in the performance of the Lidar. As the Lidar will only be installed for two months on each turbine, it is essential that during this period the Lidar is working as often as possible. It might occur that cables get unplugged[7], thereby requiring a certified technician to climb the turbine and fix the problem. In the quotation by Oldbaum, a price of €750 is quoted for a site visit. To minimize the risks of not measuring during the two months of the campaign, at least one site visit per campaign is assumed, totaling 6 per annum and running till year 6.

The last cost item considered for the Lidar are the costs for data analysis. This is to be performed internally within Vattenfall, by someone from the Wind Resource team. An internal hourly rate of €50 is assumed as costs for the project and that an average of 10 hours are required for data analysis of each turbine. This could be short in the beginning, but, as the employee gains experience and sets up a standardized procedure, it is considered likely that less time will be required to analyze the YM distribution. Per year this totals 60 hours of work and €3 000 in costs for the duration of the first six years.

Figure 11.1 shows a pie chart of the different cost components for the Lidar YM correction campaign. The costs total an amount of €450 000 over the project lifetime.

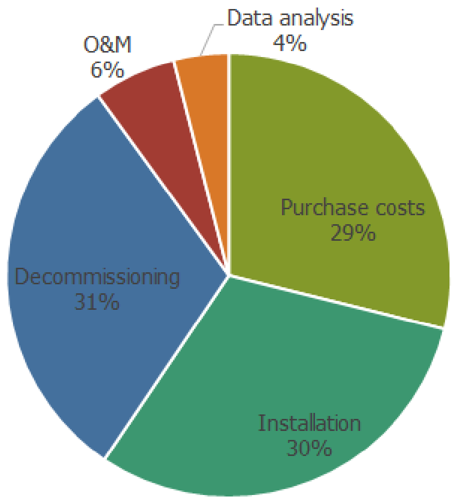

Figure 11.1: *Pie chart of the costs concerned with applying a nacelle-based Lidar for YM correction campaign at Prinses Alexia.*

SPINNER ANEMOMETER

The costs involved with spinner anemometers are simpler to oversee due to the business model which Romowind, the patent-holder and sole manufacturer of this technology, proposes to its' potential clients. The model is based on a combination of a purchase and service agreement. In this case Romowind provide the spinner anemometer at a lower price than their actual price in return for a service agreement of 5 years. Beyond these 5 years, continued service is optional against a yearly fee. For a company that is just starting up this is a logical business model which can ensure a steady cash flow while the company matures.

Romowind have advised to fit every turbine in wind park Prinses Alexia with a spinner anemometer, 35 turbines with the iSpin Monitors basic and 1 turbine with the iSpin Monitor advanced. The advanced device is able to measure air density, thereby making it handy for eventual PC verification by means of the installed iSpins. The purchase costs for the advanced devices are quoted at €11 500 per piece while the basic units are purchased for €5 000. For wind park Prinses Alexia, this would add up to a total purchase cost of €186 500. Like with the Lidar, this amount will be written off over a period of 5 years, thereby spreading the weight of the transaction.

Installation costs for the spinner anemometers are quoted at €1 000 per WTG and will be performed by employees of Romowind. Adding to the installation costs, income will also be lost due to the stopping of the turbines during the installation and calibration of the spinner anemometers. Like with the Lidar, a duration of 8 hours is assumed for the installation to take place. The lost income is calculated by multiplying the average turbine power by the duration of installation and the electricity price.

Within the service agreement provided by Romowind, O&M costs of the system will be carried by Romowind. Besides this, employees from Romowind will be responsible for monitoring of the devices and analyzing the turbines. Quarterly reports will be provided of the YM, flow inclination and rotor wind speed, with which the turbines can be monitored and eventually fixed where necessary. So, the data analysis in this case will be performed by Romowind and the actual YM correcting of the turbines will remain in hands of Vattenfall. The last part is considered such a small part that no additional costs are calculated for this. An advantage of this system is that the turbines will be monitored externally over a period of 5 years. It is however questionable whether any benefits will be achieved after 2-3 months considering YM correction. The O&M costs for the spinner anemometers are €12 000 per month for the entire park, adding up to €144 000 per year over the first 5 years. This is by far the heaviest contribution to the costs.

Finally, the spinner anemometers are considered to be permanently installed on the turbines so no decommissioning is required. However, it is not known what this would imply on the monitoring costs after 5 years. It seems logical that not extending the service agreement after 5 years implies that the spinner anemometers have to be decommissioned. If this is the case, the same costs as during installation will be applicable in year 6. This is however not yet clear.

Figure 11.2 shows a pie chart of the different cost components for a YM correction campaign using spinner anemometer. The costs total an amount of €960 000 over the project lifetime. The monitoring costs account for 75% of the total costs, compared to 19% and 6% for purchase and installation costs, respectively.

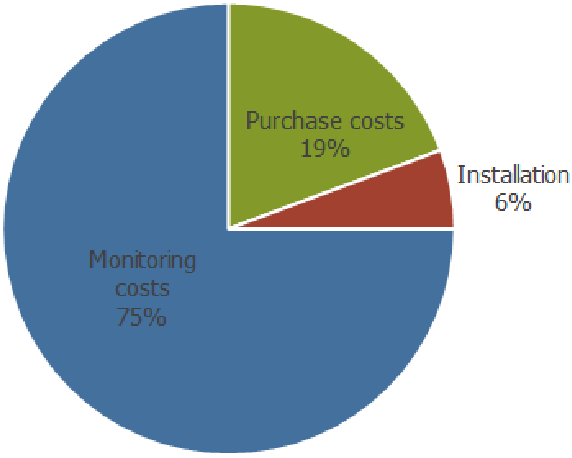

Figure 11.2: *Pie chart of the costs concerned with applying spinner anemometers for YM correction campaign at Prinses Alexia.*

11.2.2. BENEFITS

The benefits of applying the novel devices in a wind park are similar for both devices. By measuring the wind conditions with a Lidar or spinner anemometer, several benefits could be achieved. Correcting for YM, for instance, will not only increase the power output of the turbine but the loads on turbines will also be decreased, thereby allowing for longer turbine lifetime. Besides this, the novel devices could also be used for PC verification as was done in Chapter 7. Following such tests, under-performance of turbines due to component defects could be detected and fixed but also the wind park could increase in value as more becomes known about the wind conditions and turbine performance in the wind park. Load reduction and the benefits of PCV are however difficult to quantify. Therefore, considering the topics investigated in this thesis, the only gain that will be considered here is the additional electricity that could be produced in a wind park due to static YM correction.

As no clear relation between YM and power performance was found in this study, the business case will go by the cos^2-rule. Most earlier studies have shown cosine exponents between 2 and 3 [31][32], so taking the lower bound of this range might be a conservative estimate but will at least result in a less risky business case. The potential gains possible due to YM correction are calculated by applying a *performance improvement factor* to the reference PC below rated power. The Performance Improvement Factor (PIF) is calculated by the equation: PIF=$1 - cos^2(YM_{ave})$, with YM_{ave} being the static YM. An average YM of 4° is considered realistic as given in Table 11.1 and will be assumed for the standard business cases. Both the resulting and reference PC are multiplied by the pre-assessed wind speed distribution at the site (k=2, A=7.9 m/s for Prinses Alexia) to find the energy yield per wind speed bin. Adding over all the wind speed bins and correcting for turbine availability and wind farm wake losses, leads to an estimate of the reference and improved AEP. Subtracting these two from each other leads to the potential annual energy gain, which can be converted to monetary value by multiplying by the wholesale electricity price as given in the earlier assumptions. For an average YM of 4°, a PIF of 0.49% is found which corresponds to an annual energy increase of approximately 36,500 kWh per turbine.

The only small difference between the benefits of the Lidar and that of the spinner anemometers is caused by the fact that one single Lidar is used to correct YM on 36 turbines while a spinner anemometer will be installed on each turbine. This affects the time at which each individual turbine has been corrected for static YM. Taking the YM measurement time of 2 months into consideration, mounting each turbines with a spinner anemometer means all the turbines could be YM corrected two months after installation. When a Lidar is to be used to measure YM, 6 turbines per year can be corrected and a total duration of 6 years will be necessary to correct all 36 turbines in wind park Prinses Alexia. This reduces the benefits of the first 6 years by 93%, 76%, 60%, 43%, 26% and 10%, respectively, compared to the maximum benefits possible per year. For the case of the spinner anemometers, only the first two months after installation will not contribute to the benefit, which corresponds to a decrease of 17% in the first year.

11.2.3. RESULTS

Since no conclusive results were found in this research on the effect of YM on the turbine performance, a business case which is thought to be most realistic was constructed by setting the average correctable YM to 4°. Applying the method and assumptions described above and implementing the costs and benefits of both methods, the selected economic variables can be calculated. Figures 11.7 and 11.8, at the end of this chapter, display the calculation sheets used for the business cases of the Lidar and spinner anemometers, respectively. Figure 11.3 shows the development of the accumulated NPV during the lifetime of the project.

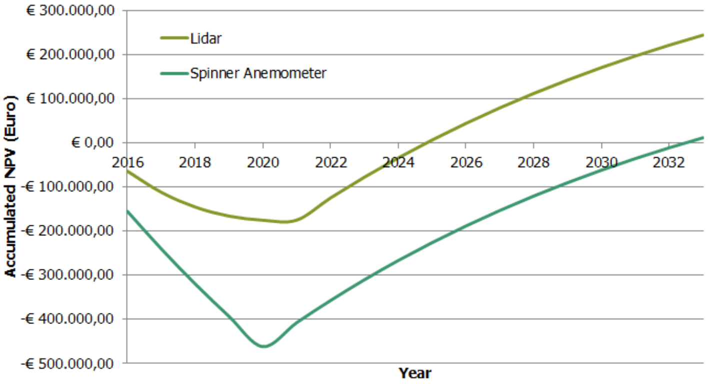

Figure 11.3: *Development of the accumulated NPV over the lifetime of the project for both the Lidar and the spinner anemometer methods.*

As can be seen in the figure, in the first 5-6 years the accumulated NPV is declining due to the writing off of purchase costs and the yearly installation, decommissioning and O&M costs. After these years, the wind park will start to produce only additional income due to improved power performance, thereby causing the accumulated NPV to rise steadily. The figure also shows that the accumulated NPV for the Lidar method reaches a positive value at an earlier stage (2025) compared to the spinner anemometer method(2032). In fact, the spinner anemometer method only just reaches a positive NPV in the last year of operation of the wind park. This big difference between both devices is caused by the yearly monitoring costs which are connected to spinner anemometers, weighing very heavily on the business case. The final observation which can be made is that the plots of the NPVs slowly move towards leveling off. This is caused by the discounting of the cash inflows further in time, thereby making the contribution to the accumulated NPV to shrink each year.

Table 11.2 gives a summary of the important economic variables for both business cases. As mentioned before, these values were found making use of a base case scenario with the following assumptions: $YM_{ave} = 4^{\circ}$, cosine exponent = 2, discount rate is 7.5%. The values for the Lidar YM correction campaign are much better than that for the spinner anemometer campaign, with project NPV being higher, IRR being higher and the PBT being lower. However, both business cases do have a positive NPV, meaning both investments are good. The IRRs for both are also higher than the assumed 7.5%, but in this case choosing for a Lidar might seem less risky. Finally, both investments will pay back within the remaining park lifetime.

Table 11.2: *Summary of economic variables for both business cases using the basic assumptions.*

Variable	**Lidar campaign**	**Spinner Anemometer campaign**
NPV	€243 750	€11 395
IRR	18.5%	7.8%
PBT [yrs]	8.7	11.7

11.2.4. BUSINESS CASE DISCUSSION

In this section the results of the business cases will be discussed in more detailed while a closer look will be taken at the sensitivity of the business cases' outcome to the different assumptions being made.

The big difference between the business cases is that the Lidar is only installed for 2 months on a turbine while the spinner anemometer is permanently installed. The spinner anemometer business case is built on the principle of continuous turbine monitoring while the Lidar business model assumes to be able to correct static YM in 2 months on a turbine. This assumption has been made for the purpose of the feasibility study but doubts may be placed whether this is a correct assumption. Previous experiments by Romowind have shown that static YM has to be compensated for in 2-3 steps. On the other hand, Lidar should be able to determine the YM in 7 days based on the methodology proposed by Wagenaar et al.[21], possibly making this assumption plausible.

A big uncertainty in the business cases is attributed to the PIF. No conclusions could be made during this research about the average turbine YM in the wind park Prinses Alexia or the relation between YM and power performance. Assuming a PIF of 0.49% for the standard business case might therefore be a wild guess and not a realistic value. Some parties in the industry believe a PIF of 2% is possible, however no proof of this has been found so far, and this while the PIF is essential and influences NPV and other economic variables heavily.

For this reason a sensitivity analysis has been performed, varying the PIF between 0.12% and 1.94% by adjusting the average park YM and the cosine exponent while observing how the different variable react to the increase in benefits. Figure 11.4 shows the dependency of the NPVs of both instruments on the PIF. The respective PIFs corresponding to a positive NPV are found to be at PIF>0.29% for the Lidar and at PIF>0.48% for the spinner anemometer. It can be seen that the NPV of the spinner anemometers will increase more rapidly with a higher PIF than the Lidar, thereby being more sensitive to changes in PIF.

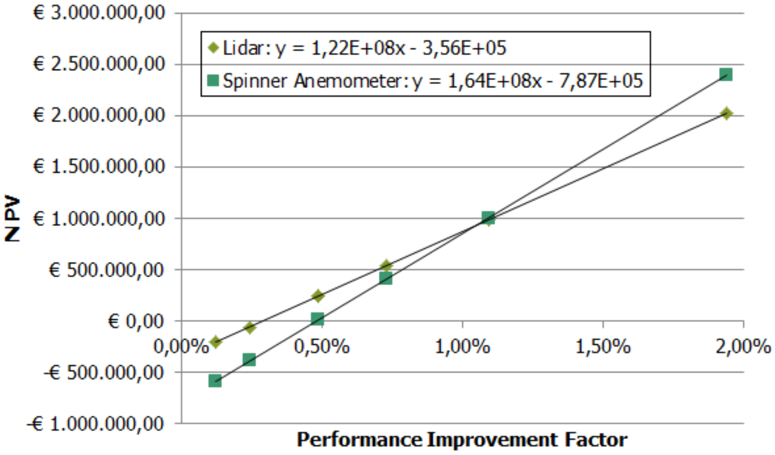

Figure 11.4: *Dependency of the NPV on the performance improvement factor (PIF).*

The behavior of the other economic variables, IRR and PBT, has also been investigated. Figure 11.5 shows the relation between the PIF and the IRR and PBT normalized to the standard business case assumptions. As can be seen in the figure, the IRR for the spinner anemometer increases rapidly with increasing PIF. This increase is so vigorous that, for a PIF of 1.94%, it is not even possible to calculate the IRR as the NPV is never negative during the project. This seems to show that a PIF of 2% is too good to be true. Looking at PBT, it is observed that the Lidar and spinner anemometer show similar decreasing behavior as PIF increases.

The influence of the discount rate on the outcome of the business cases is also interesting. As only the NPV is discounted for time, only the NPV behavior is observed in this section. The discount rate has been varied at 5%, 7.5% and 10%, with 7.5% being the assumption used in the standard business case. Figure 11.6 shows a bar chart with the changing NPVs for the Lidar and spinner anemometer YM correction campaign. As expected, a higher discount rate causes NPV to decline nearly linearly. Since this decline seems similar for both the Lidar and spinner anemometer and the essence of the feasibility study is to compare the two novel techniques, it is considered less essential that the discount rate is absolutely correct. The assumed 7.5% therefore seems to be a good and safe estimation.

A similar consideration is done with the assumption on the constant electricity price over the park lifetime. The electricity gain, and thereby the gained income, in the park is the same for both methods, thus it

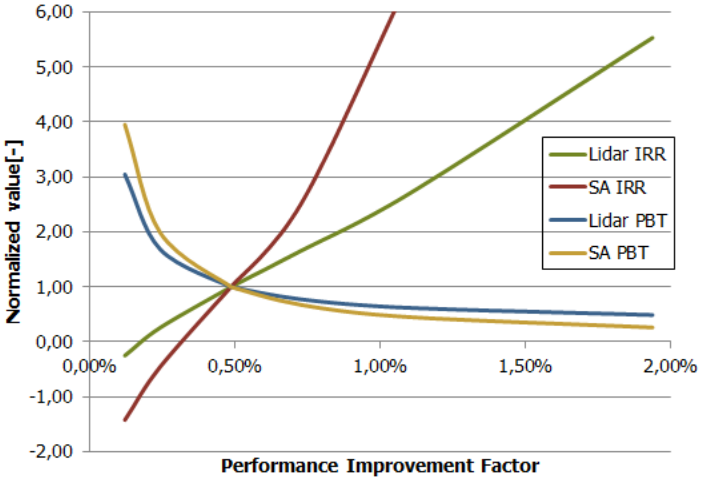

Figure 11.5: *Dependency of the normalized IRR and PBT on the performance improvement factor (PIF).*

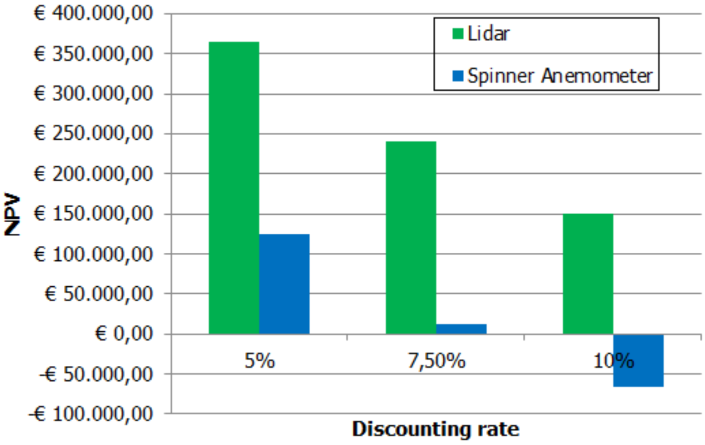

Figure 11.6: *Bar chart to show dependency of the NPV on the discount rate.*

will not impact the difference between the methods severely but rather the actual magnitude of the project NPVs. If the electricity price increases over time, so will the NPVs. Therefore it seems justified to assume a constant electricity price over the project lifetime.

11.3. CONCLUSIONS

To conclude, both investments could turn out good. The high monitoring costs for the spinner anemometers do however weigh heavily on its' business case. Besides this, the assumption is made in this research that after the static YM has been corrected within two months, hardly any additional benefit is possible, this also is not in favor of the spinner anemometer. Considering the high uncertainty involved in the possible gains of a YM correction campaign, it would be advised to choose for a Lidar. If hiccups occur in the project or gains turn out to be lower than initially expected, the Lidar business case has a higher chance of remaining positive.

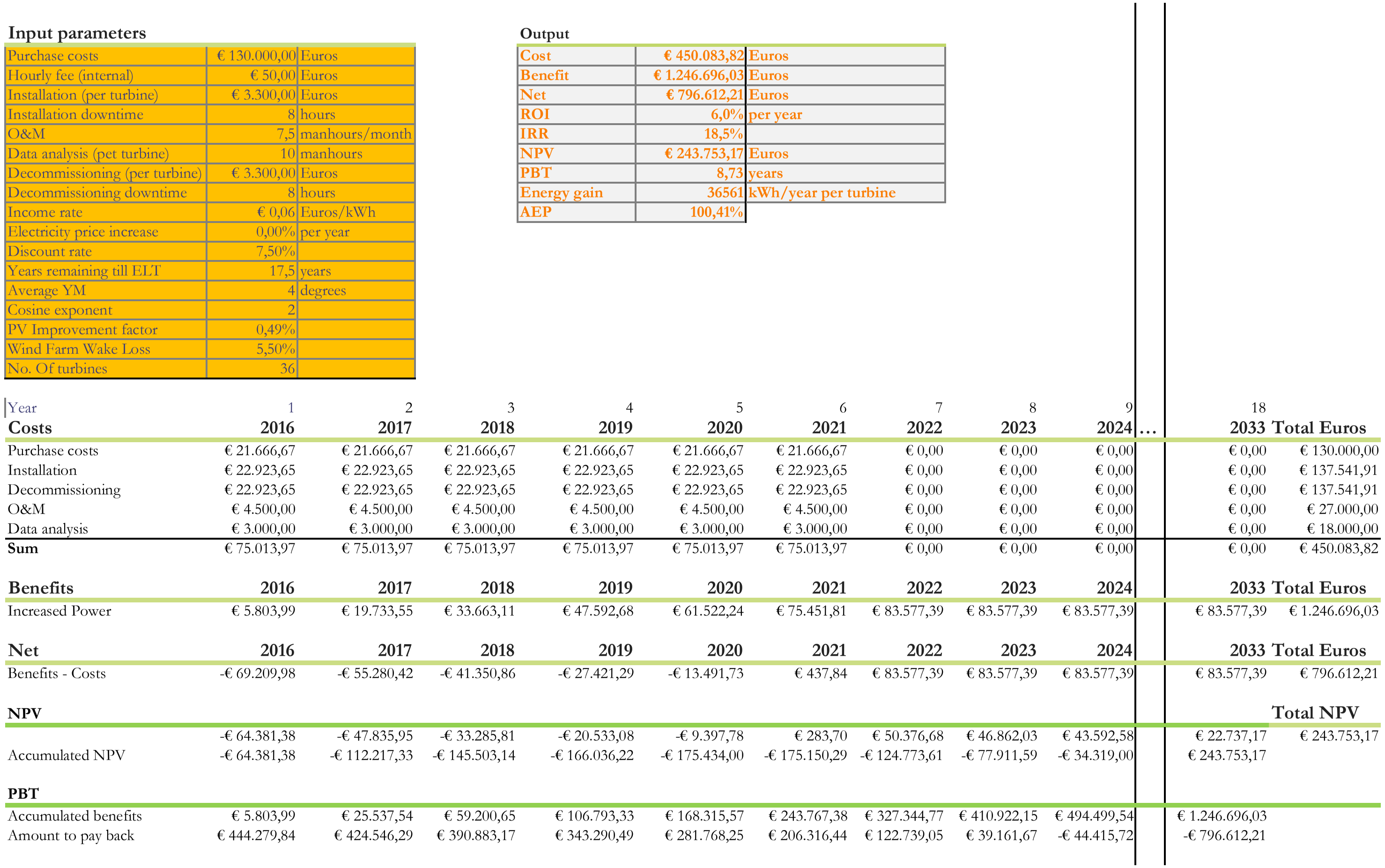

Input parameters

Purchase costs	€ 130.000,00	Euros
Hourly fee (internal)	€ 50,00	Euros
Installation (per turbine)	€ 3.300,00	Euros
Installation downtime	8	hours
O&M	7,5	manhours/month
Data analysis (pet turbine)	10	manhours
Decommissioning (per turbine)	€ 3.300,00	Euros
Decommissioning downtime	8	hours
Income rate	€ 0,06	Euros/kWh
Electricity price increase	0,00%	per year
Discount rate	7,50%	
Years remaining till ELT	17,5	years
Average YM	4	degrees
Cosine exponent	2	
PV Improvement factor	0,49%	
Wind Farm Wake Loss	5,50%	
No. Of turbines	36	

Output

Cost	€ 450.083,82	Euros
Benefit	€ 1.246.696,03	Euros
Net	€ 796.612,21	Euros
ROI	6,0%	per year
IRR	18,5%	
NPV	€ 243.753,17	Euros
PBT	8,73	years
Energy gain	36561	kWh/year per turbine
AEP	100,41%	

Year	1	2	3	4	5	6	7	8	9		18	
Costs	**2016**	**2017**	**2018**	**2019**	**2020**	**2021**	**2022**	**2023**	**2024**	…	**2033**	**Total Euros**
Purchase costs	€ 21.666,67	€ 21.666,67	€ 21.666,67	€ 21.666,67	€ 21.666,67	€ 21.666,67	€ 0,00	€ 0,00	€ 0,00		€ 0,00	€ 130.000,00
Installation	€ 22.923,65	€ 22.923,65	€ 22.923,65	€ 22.923,65	€ 22.923,65	€ 22.923,65	€ 0,00	€ 0,00	€ 0,00		€ 0,00	€ 137.541,91
Decommissioning	€ 22.923,65	€ 22.923,65	€ 22.923,65	€ 22.923,65	€ 22.923,65	€ 22.923,65	€ 0,00	€ 0,00	€ 0,00		€ 0,00	€ 137.541,91
O&M	€ 4.500,00	€ 4.500,00	€ 4.500,00	€ 4.500,00	€ 4.500,00	€ 4.500,00	€ 0,00	€ 0,00	€ 0,00		€ 0,00	€ 27.000,00
Data analysis	€ 3.000,00	€ 3.000,00	€ 3.000,00	€ 3.000,00	€ 3.000,00	€ 3.000,00	€ 0,00	€ 0,00	€ 0,00		€ 0,00	€ 18.000,00
Sum	€ 75.013,97	€ 75.013,97	€ 75.013,97	€ 75.013,97	€ 75.013,97	€ 75.013,97	€ 0,00	€ 0,00	€ 0,00		€ 0,00	€ 450.083,82
Benefits	**2016**	**2017**	**2018**	**2019**	**2020**	**2021**	**2022**	**2023**	**2024**		**2033**	**Total Euros**
Increased Power	€ 5.803,99	€ 19.733,55	€ 33.663,11	€ 47.592,68	€ 61.522,24	€ 75.451,81	€ 83.577,39	€ 83.577,39	€ 83.577,39		€ 83.577,39	€ 1.246.696,03
Net	**2016**	**2017**	**2018**	**2019**	**2020**	**2021**	**2022**	**2023**	**2024**		**2033**	**Total Euros**
Benefits - Costs	-€ 69.209,98	-€ 55.280,42	-€ 41.350,86	-€ 27.421,29	-€ 13.491,73	€ 437,84	€ 83.577,39	€ 83.577,39	€ 83.577,39		€ 83.577,39	€ 796.612,21
NPV												**Total NPV**
	-€ 64.381,38	-€ 47.835,95	-€ 33.285,81	-€ 20.533,08	-€ 9.397,78	€ 283,70	€ 50.376,68	€ 46.862,03	€ 43.592,58		€ 22.737,17	€ 243.753,17
Accumulated NPV	-€ 64.381,38	-€ 112.217,33	-€ 145.503,14	-€ 166.036,22	-€ 175.434,00	-€ 175.150,29	-€ 124.773,61	-€ 77.911,59	-€ 34.319,00		€ 243.753,17	
PBT												
Accumulated benefits	€ 5.803,99	€ 25.537,54	€ 59.200,65	€ 106.793,33	€ 168.315,57	€ 243.767,38	€ 327.344,77	€ 410.922,15	€ 494.499,54		€ 1.246.696,03	
Amount to pay back	€ 444.279,84	€ 424.546,29	€ 390.883,17	€ 343.290,49	€ 281.768,25	€ 206.316,44	€ 122.739,05	€ 39.161,67	-€ 44.415,72		-€ 796.612,21	

Figure 11.7: *Calculation sheet for the business case of the Lidar including the input parameter specification.*

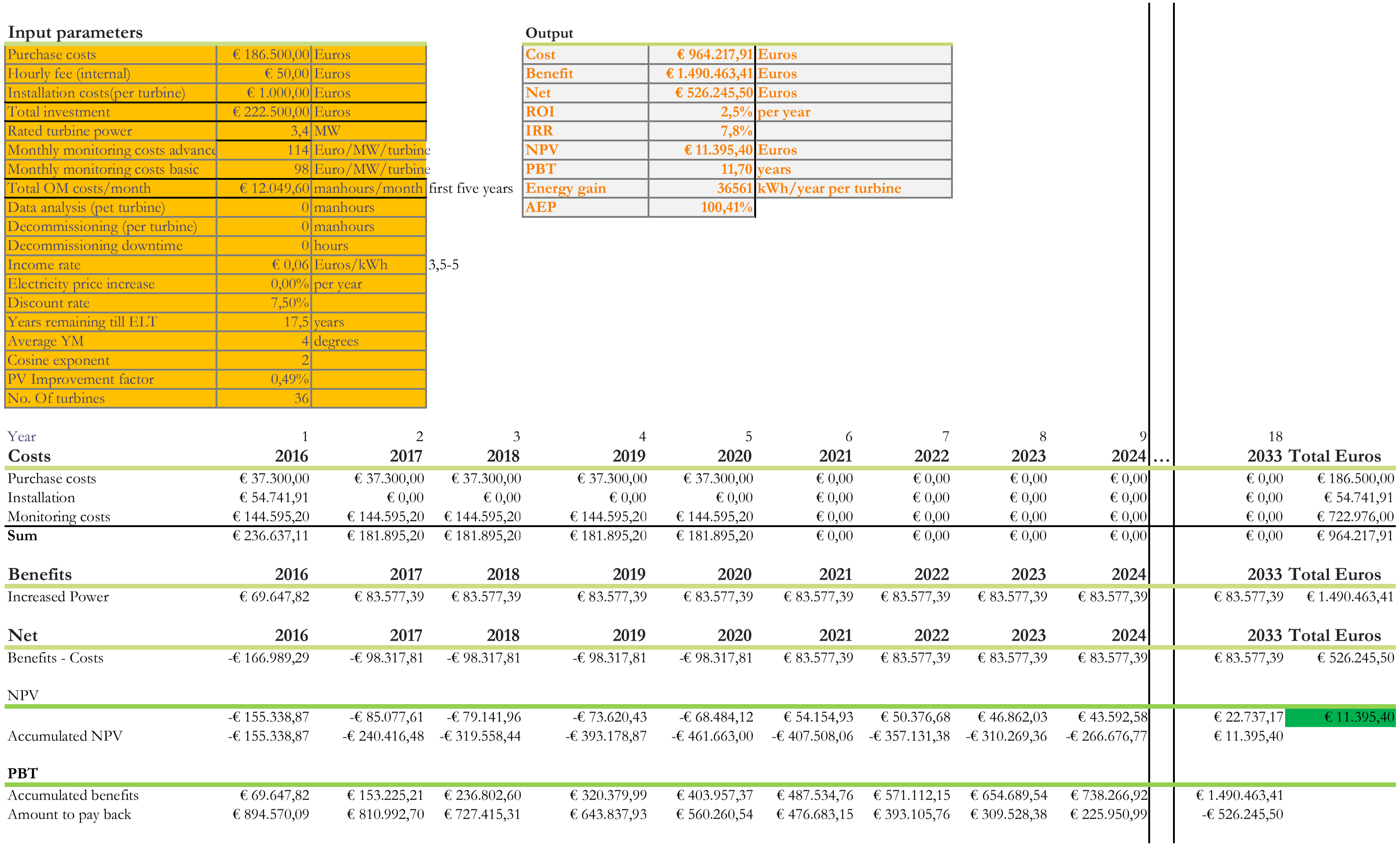

Input parameters

Purchase costs	€ 186.500,00	Euros	
Hourly fee (internal)	€ 50,00	Euros	
Installation costs(per turbine)	€ 1.000,00	Euros	
Total investment	€ 222.500,00	Euros	
Rated turbine power	3,4	MW	
Monthly monitoring costs advance	114	Euro/MW/turbine	
Monthly monitoring costs basic	98	Euro/MW/turbine	
Total OM costs/month	€ 12.049,60	manhours/month	first five years
Data analysis (pet turbine)	0	manhours	
Decommissioning (per turbine)	0	manhours	
Decommissioning downtime	0	hours	
Income rate	€ 0,06	Euros/kWh	3,5-5
Electricity price increase	0,00%	per year	
Discount rate	7,50%		
Years remaining till ELT	17,5	years	
Average YM	4	degrees	
Cosine exponent	2		
PV Improvement factor	0,49%		
No. Of turbines	36		

Output

Cost	**€ 964.217,91**	**Euros**
Benefit	**€ 1.490.463,41**	**Euros**
Net	**€ 526.245,50**	**Euros**
ROI	**2,5%**	**per year**
IRR	**7,8%**	
NPV	**€ 11.395,40**	**Euros**
PBT	**11,70**	**years**
Energy gain	**36561**	**kWh/year per turbine**
AEP	**100,41%**	

Year	1	2	3	4	5	6	7	8	9		18	
Costs	**2016**	**2017**	**2018**	**2019**	**2020**	**2021**	**2022**	**2023**	**2024**	**…**	**2033**	**Total Euros**
Purchase costs	€ 37.300,00	€ 37.300,00	€ 37.300,00	€ 37.300,00	€ 37.300,00	€ 0,00	€ 0,00	€ 0,00	€ 0,00		€ 0,00	€ 186.500,00
Installation	€ 54.741,91	€ 0,00	€ 0,00	€ 0,00	€ 0,00	€ 0,00	€ 0,00	€ 0,00	€ 0,00		€ 0,00	€ 54.741,91
Monitoring costs	€ 144.595,20	€ 144.595,20	€ 144.595,20	€ 144.595,20	€ 144.595,20	€ 0,00	€ 0,00	€ 0,00	€ 0,00		€ 0,00	€ 722.976,00
Sum	€ 236.637,11	€ 181.895,20	€ 181.895,20	€ 181.895,20	€ 181.895,20	€ 0,00	€ 0,00	€ 0,00	€ 0,00		€ 0,00	€ 964.217,91
Benefits	**2016**	**2017**	**2018**	**2019**	**2020**	**2021**	**2022**	**2023**	**2024**		**2033**	**Total Euros**
Increased Power	€ 69.647,82	€ 83.577,39	€ 83.577,39	€ 83.577,39	€ 83.577,39	€ 83.577,39	€ 83.577,39	€ 83.577,39	€ 83.577,39		€ 83.577,39	€ 1.490.463,41
Net	**2016**	**2017**	**2018**	**2019**	**2020**	**2021**	**2022**	**2023**	**2024**		**2033**	**Total Euros**
Benefits - Costs	-€ 166.989,29	-€ 98.317,81	-€ 98.317,81	-€ 98.317,81	-€ 98.317,81	€ 83.577,39	€ 83.577,39	€ 83.577,39	€ 83.577,39		€ 83.577,39	€ 526.245,50
NPV												
	-€ 155.338,87	-€ 85.077,61	-€ 79.141,96	-€ 73.620,43	-€ 68.484,12	€ 54.154,93	€ 50.376,68	€ 46.862,03	€ 43.592,58		€ 22.737,17	€ 11.395,40
Accumulated NPV	-€ 155.338,87	-€ 240.416,48	-€ 319.558,44	-€ 393.178,87	-€ 461.663,00	-€ 407.508,06	-€ 357.131,38	-€ 310.269,36	-€ 266.676,77		€ 11.395,40	
PBT												
Accumulated benefits	€ 69.647,82	€ 153.225,21	€ 236.802,60	€ 320.379,99	€ 403.957,37	€ 487.534,76	€ 571.112,15	€ 654.689,54	€ 738.266,92		€ 1.490.463,41	
Amount to pay back	€ 894.570,09	€ 810.992,70	€ 727.415,31	€ 643.837,93	€ 560.260,54	€ 476.683,15	€ 393.105,76	€ 309.528,38	€ 225.950,99		-€ 526.245,50	

Figure 11.8: *Calculation sheet for the business case of the spinner anemometers including the input parameter specification.*

12

CONCLUSIONS AND RECOMMENDATIONS

This chapter will present the main conclusions of this thesis and several recommendations for future research. The conclusions will be treated on the basis of the research questions as postulated prior to this thesis study, followed by some general conclusions of the performed study.

12.1. REFLECTION ON RESEARCH GOALS

As the underlying principle for the novel measurement techniques presented in this thesis is the procedures involved in PCV, this was the first logical step to undertake in this project. A PCV compliant to the standards set by the IEC was performed on turbines R01 and R02 at wind park Prinses Alexia with the purpose of gaining experience with this procedure. The results of the PCV showed a difference in turbine performance of 6% between turbine R01 and R02, with R01 at 2% below and R02 at 4% above guaranteed performance. A deeper investigation was started into the cause of under-performance, resulting in a hypothesis which was also presented to Vattenfall and the turbine manufacturer Senvion. This hypothesis is still under investigation and no hard conclusions have been made on the turbine under-performance. Generally, the exercise of PCV was a good introduction to the topic of this thesis, thereby providing a good basis for comparison of the novel device applicability for PCV.

For a qualitative PCV, the measurement devices need to be able to measure wind speed, direction and TI accurately. A comparison of subsequent wind speed, YM or wind direction, and TI readings by both the Lidar and spinner anemometer against met-mast has been performed. The spinner anemometer has shown good correlations for wind speeds and direction against the adjacent met-mast as in earlier studies [28], but doubts are placed about the wind speed accuracy of this specific Lidar. Earlier research has shown that both Lidar and spinner anemometers can measure wind speed and direction accurately, hence the current findings on Lidar do not seem to be in agreement with literature this[7][15][16][19][20]. Following peculiar Lidar tilt readings, it was post-calibrated after decommissioning only to find that the inclinometer was indeed mis-calibrated. It is not clear whether the mis-calibration only affected the tilt and roll readings or also the actual wind speed and direction measurements, however it does increase the uncertainty concerning the Lidar measurements. Looking at the Lidar wind speed correlation to met-mast readings, the Lidar seems to be over-estimating wind speeds by 4.6%, which is rather significant compared to earlier studies. Originally, it was thought that this was caused by the high tilt angles, whereby the Lidar was actually measuring at heights up to 10m above hub-height, however this was eventually discarded. It seems likely that if the inclinometer has acquired an error, the same might have occurred for the Lidar wind speed measurements.

Considering YM measurements, however, the Lidar does seem to be able to measure this with sufficient accuracy compared to a met-mast. Also, similar YM distributions and average YMs are found with the three devices. So this research has shown that the spinner anemometers are able to measure wind speed and direction sufficiently accurately to be applied in PCV, while the Lidar campaign is too uncertain for such conclusions to be made.

The measurement campaigns also focused on the capabilities of the novel devices to measure TI. Neither of the devices showed to be capable of measuring TI accurately compared to a met-mast. This is not in agreement with earlier research where both Lidar and spinner anemometer showed good TI correlations with an adjacent met-mast [21][22][23][29]. A possible explanation for the Lidar is thought to be that the large measurement volumes at 2.5D ahead of the rotor could cause a decrease in sensitivity to measure wind fluctuations, explaining the lower standard deviations being measured compared to the met-mast. Considering that the wind speed is also over-estimated, could justify the correlation fit gradient below 1 which is observed. The spinner anemometers seem to be able to measure low TI accurately but have trouble at higher TIs where they under-estimate it.

The devices have also been applied in PCV. The PC found with the spinner anemometer is neater, showing less spread than both the Lidar and the met-mast. Besides this, the spinner anemometer clearly shows to be less affected by disturbed wind conditions. This can be explained by the fact that the spinner anemometers actually measure the wind right in front of the rotor, so a waked condition will influence the measured wind speed and resulting produced power more or less equally. Reflecting the PCs to AEP, it seems the Lidar under-estimates the AEP by 7% compared to the met-mast, a logical consequence of the afore-mentioned wind speed over-estimation. The spinner anemometer, on the other hand, over-estimates it by 1.5% for this data set.

Focussing on occurence and the effects of YM, Bladed simulations were performed and compared to actual measured data. The Bladed results show a deterioration of the PC by a relation close to $(cosine)^2$. The simulations are compared to actual measured data by applying a method proposed by Boorsma[44] whereby a cosine function is fitted to YM-binned average C_p-values. This method resulted in non-conclusive answers with cosine exponents ranging from 1-6 for the influential wind speed range below rated, which is in the range of cosine exponents found in earlier studies [31][32][33]. Boorsma's method was found to be sensitive to the chosen wind speed bin as well as bin width, meaning no conclusions can be made on this. A deliberate YM campaign was proposed but could not be executed in time, resulting only in a proposal which will be discussed in the recommendations for future research. This means that, besides the Bladed simulations, there still is no conclusive evidence for a cosine-relation between YM and power loss, let alone that it is a $\cos^2$-relation. This will have to be left open for future work.

Bladed simulations were also performed to investigate the effect of WS on the ideal yaw error. The simulations show that the ideal yaw error, the YM where maximum power is produced, increases slightly for increasing WS conditions. The change in bias was found to be 1° for an increase in WS exponent from 0 to 0.5. Boorsma's method was slightly adjusted for WS instead of wind speed bins, and applied to measurements at wind park Prinses Alexia in order to compare the simulated results with real data. This analysis shows similar results to the Bladed results, with in fact an increase in ideal yaw error of approximately 2.5° when increasing WS from 0.1 to 0.5. A sensitivity study was performed and it showed that the adjusted Boorsma's method seems less sensitive to the applied filters and WS bins, whereby the behavior of the ideal yaw error remains similar as the input settings are varied. This increases the confidence in the found relation between WS and ideal yaw error. Both the simulations and the measurements seem to confirm the hypothesis as postulated in the theoretical background, meaning a YM of 0° will not always result in the most optimal performance.

Concerning the performance of turbines under non-standard WS and TI conditions, a continuation was performed of the research by Villanueva[41]. Similar Bladed simulations were run for varying WS conditions, the results of which were compared to actual measurements made at wind park Prinses Alexia. The experimental results show that a low WS at lower wind speeds and a high WS at high wind speeds both deliver a slightly higher power performance. The main deviations in power performance occur below rated wind speed though but are not significant.

The effect of TI is clearer, even already in the binned PCs. A high TI delivers higher power performance at wind speeds before the turbine starts to pitch, and, once the turbine starts to pitch, higher TI leads to a loss in power performance. This result is in agreement with the Bladed results presented by Villanueva[41] but also with the preliminary results presented by the PCWG [38][39][40]. The C_p vs. wind speed behavior of the turbines, whereby C_p increases moderately at low wind speeds (<8 m/s) and decreases rapidly at wind speeds around rated (9-13 m/s), is considered to be a possible explanation of the impact of TI at different wind speeds.

Comparing the impact WS directly has on AEP, the experimental data shows exactly the opposite AEP behavior to what the Bladed simulations predicted. The experimental data is not isolated for zero TI, which is the case for the conditions in the Bladed simulations. This could mean that the experimental AEP might be influenced by high TI often corresponding to low WS. Comparing the effect of TI on AEP, however, the contribution of TI is not considered to be significant enough to justify the difference described above. A different effect could thus be influencing the experimental data in the form of other non-ideal conditions.

Finally, the lessons learned about accuracies and application of the novel measurement devices were applied in a financial feasibility study so as to evaluate the business cases of applying either Lidar or spinner anemometers for YM correction. As no conclusive results on possible power performance improvement due to YM correction had been found during this thesis, assumptions had to be made on a realistic power performance improvement factor. Constructing a standard scenario with a PIF=0.49% and r=7.5% at the wind park Prinses Alexia, it was found that using a single Lidar and applying it sequentially to the turbines in wind park is financially more interesting. Both systems give a positive NPV and IRR is higher than the discount rate.

The business cases have shown to be very sensitive to the input parameters, specifically to the PIF. Claims are made by different parties on this that an average PIF of up to 2% is possible when correcting YM, however these claims are not considered proven. The fact that the PIF can change the financial attractiveness so vigorously, means that extra care should be taken at assuming these values. Positive NPVs are reached at PIF>0.29% for the Lidar case and at PIF>0.49% for spinner anemometers. A deliberate YM campaign could help to quantify such a factor and increase certainty in the business case.

12.2. FINAL REMARKS

In conclusion, spinner anemometer have shown a higher measurement accuracy than the Lidar, assuming they have been calibrated properly against a met-mast. Also, the spinner anemometer measurements seem less vulnerable to disturbed wind conditions. Lidar, on the other hand, seems to be the cheaper option due to its' flexibility to be moved from turbine to turbine and its' lower yearly O&M costs.

For onshore wind parks, Lidar will probably be the easiest, cheapest and most accessible manner to perform PCV and YM correction campaigns as described in this thesis. If a YM correction campaign is to be performed on an offshore wind park, however, the sequential moving of the Lidar will cause Lidar costs to rocket and the spinner anemometers are advised in this case. Also, if signals are to be implemented as input for turbine controller, SA is advised due to its low sensitivity to disturbed conditions while having high measurement accuracy.

12.3. RECOMMENDATIONS FOR FUTURE RESEARCH

In this section, several ideas for possible future researches that came to mind in the process of the current research will be given.

Make novel devices more suitable for IEC-compliant PCV: A general recommendation is to put more effort into making the promising novel devices ready, and, more importantly, accepted, for PCV. For a Lidar, for instance, it is recommended to add temperature, pressure and independent power measurements to a campaign. Standard procedures to be applied when measuring PCs with these devices should be set up and then incorporated into the IEC standards. This could save costs for wind energy in the future and should help in achieving the cost reduction goals as set by the EU.

Spinner anemometer calibration with a Lidar: In this research it was observed that spinner anemometers are able to measure wind conditions rather accurately after calibration to a met-mast. Romowind is, however, planning to calibrate their spinner anemometers with a nacelle-based Lidar in the future as it will not be economically feasible to place a met-mast at each wind park. The question arises how the accuracy will be affected by calibration to a device which is not the standard of the industry. This could be tested by performing an experiment with a spinner anemometer installed on a turbine, calibrated to a nacelle-based Lidar, and then compared to an adjacent IEC-compliant met-mast.

Investigate eventual accelerometer bias errors for spinner anemometers: As no conclusive evidence was found that the spinner anemometer readings are not prone to accumulating bias errors in the accelerometer, it is advised to investigate whether this is the case and how this could eventually influence the spinner anemometer wind speed and direction readings. If high frequency (1 Hz) rotor azimuth position measurements of both the spinner anemometer and the turbine Scada system is present, such errors could be evaluated and eventually ruled out.

Effect of heterogeneity on Lidar: Following investigations on the accuracy of Lidar measurements, a discussion started with the manufacturer of the used Lidar, Avent Lidar Technologies, about the effect that heterogeneity has on the measurement accuracy of the Lidar. Whether or not this contribution is to be blamed on the Lidar or the turbulent nature of the wind will not be discussed here, fact is that Lidars work on the principle of homogeneous wind conditions and that this will therefore cause an error in the measurements. A study into the occurrence of heterogeneity and its' effect on Lidar measurements is therefore proposed for future research using a 5-beam Lidar. It is considered possible to quantify heterogeneity and measure it when three beams are present in the horizontal plane. A more elaborate explanation of the proposed plan is given in Appendix D.

Deliberate turbine YM: This research has sadly not delivered conclusive results on the effect of YM on the turbine performance. A proposal has however been made for a short campaign to deliberately misalign a turbine by changing the control function settings manually and measuring the change in power performance due to the YM. A more detailed description of the proposed campaign is given in Appendix E.

Ideal yaw error incorporation in control function: In the Section 9.2 it was found that increasing WS conditions biases the turbine towards a positive ideal yaw error. This change in ideal yaw error has a magnitude in the range of 1° according to simulations and 2.5° according to measurements, which would mean that correcting YM to 0° could result in a non-optimal YM. A study should be done into whether it is feasible to incorporate WS into the yaw controller function and, if so, how this can be done. If WS does not fluctuate too much in 1 minute, the average could be measured and fed into the controller function. Simulations would also have to be run to study how this would impact loads on the turbine and the yaw mechanism.

Isolation of TI and WS in 'outer conditions' analysis: A final recommendation concerns the wind conditions outside of the guaranteed envelope. It would be interesting to isolate WS and TI bins so that they do not effect each other. In this way, a matrix of load cases(WS,TI) can be constructed and the effect on the PC for each individual load case can be measured. To find IEC-compliant and trust-worthy PCs, a very large database is necessary to ensure enough data points for each load case. Such exercises are also performed by the PCWG for presumably different turbine types but it would be interesting to investigate this for one turbine at one specific site. It is expected that such a measurement campaign should have a duration of at least 2 years in length and include an IEC-compliant met-mast.

BIBLIOGRAPHY

[1] IEC, *Iec 61400-12-1,* Wind turbines–Part 12-1: Power performance measurements of electricity producing wind turbines (2005).

[2] L. Svenningsen, *Proposal of an improved power curve correction,* in *European Wind Energy Conference and Exhibition, Warsaw, Poland* (2010) pp. 20–23.

[3] C. J. Karlsson, F. Å. Olsson, D. Letalick, and M. Harris, *All-fiber multifunction continuous-wave coherent laser radar at 1.55 µm for range, speed, vibration, and wind measurements,* Applied optics **39**, 3716 (2000).

[4] *Wind Iris User Manual 1.2.*

[5] D. A. Smith, M. Harris, A. S. Coffey, T. Mikkelsen, H. E. Jørgensen, J. Mann, and R. Danielian, *Wind lidar evaluation at the danish wind test site in høvsøre,* Wind Energy **9**, 87 (2006).

[6] R. Wagner, R. L. Rivera, I. Antoniou, S. Davoust, T. Friis Pedersen, M. Courtney, and B. Diznabi, *Procedure for wind turbine power performance measurement with a two-beam nacelle lidar*, Tech. Rep. (DTU Wind Energy, 2013).

[7] S. Goossens, *Field-test of nacelle-based lidar to explore its applications for Vattenfall as wind park operator*, Master's thesis, TU Delft, Delft University of Technology (2015).

[8] T. Pedersen, G. Demurtas, and F. Zahle, *Calibration of a spinner anemometer for yaw misalignment measurements,* Wind Energy (2014).

[9] T. Pedersen, N. N. Sørensen, and P. Enevoldsen, *Aerodynamics and characteristics of a spinner anemometer,* in *Journal of Physics: Conference Series*, Vol. 75 (IOP Publishing, 2007) p. 012018.

[10] O. J. Woodman, *An introduction to inertial navigation,* University of Cambridge, Computer Laboratory, Tech. Rep. UCAMCL-TR-696 **14**, 15 (2007).

[11] T. Pedersen, N. Sørensen, H. Madsen, R. Møller, M. Courtney, P. Enevoldsen, and P. Egedal, *Spinner anemometry-an innovative wind measurement concept,* EWEC2007 Milan (2007).

[12] T. Pedersen, G. Demurtas, A. Sommer, *et al.*, *Measurement of rotor centre flow direction and turbulence in wind farm environment,* in *Journal of Physics: Conference Series*, Vol. 524 (IOP Publishing, 2014) p. 012167.

[13] G. Demurtas and T. Friis Pedersen, *Summary of the steps involved in the calibration of a Spinner anemometer*, Tech. Rep. (DTU Wind Energy, 2014).

[14] J. F. Manwell, J. G. McGowan, and A. L. Rogers, *Wind energy explained: theory, design and application* (John Wiley & Sons, 2010).

[15] S. Feeney, A. Derrick, A. Oram, I. Campbell, G. Hutton, G. Powles, C. Slinger, M. Harris, J. Medley, and E. B. Des Roziers, *Project cyclops: The way forward in power curve measurements?* EWEA, March (2014).

[16] A. Giyanani, W. Bierbooms, and G. van Bussel, *Analysis of inflow parameters using lidars,* .

[17] T. Mikkelsen, K. H. Hansen, N. Angelou, M. Sjöholm, M. Harris, P. Hadley, R. Scullion, G. Ellis, and G. Vives, *Lidar wind speed measurements from a rotating spinner,* in *2010 European Wind Energy Conference and Exhibition* (2010).

[18] K. A. Kragh, M. H. Hansen, and T. Mikkelsen, *Precision and shortcomings of yaw error estimation using spinner-based light detection and ranging,* Wind Energy **16**, 353 (2013).

[19] R. Wagner and S. Davoust, *Nacelle lidar for power curve measurement-Avedøre campaign*, Tech. Rep. (DTU Wind Energy, 2013).

[20] R. Wagner, T. Pedersen, M. Courtney, I. Antoniou, S. Davoust, and R. Rivera, *Power curve measurement with a nacelle mounted lidar,* Wind Energy **17**, 1441 (2014).

[21] J. Wagenaar, S. Davoust, A. Medawar, G. Coubard-Millet, and K. Boorsma, *Turbine performance validation; the application of nacelle lidar,* Wind Energy **2013**, 2012 (2014).

[22] R. Krishnamurthy, M. Boquet, and M. Machta, *Turbulence intensity measurements for a variety of doppler lidar instruments,* in *2014 European Wind Energy Conference and Exhibition* (2014).

[23] C. Slinger, M. Leak, M. Pitter, and M. Harris, *Relative power curve measurements using turbine mounted, continuous-wave lidar,* Proc. European Wind Energy Association Annual Event (EWEA) (2013).

[24] E. Bot, *Turbulence assessment with ground based lidars,* ECN, report: ECN-E—14-043 (2014).

[25] P. Fleming, A. Scholbrock, A. Jehu, S. Davoust, E. Osler, A. Wright, and A. Clifton, *Field-test results using a nacelle-mounted lidar for improving wind turbine power capture by reducing yaw misalignment,* in *Journal of Physics: Conference Series*, Vol. 524 (IOP Publishing, 2014) p. 012002.

[26] A. Scholbrock, P. Fleming, A. Wright, C. Slinger, J. Medley, and M. Harris, *Field test results from lidar measured yaw control for improved yaw alignment with the nrel controls advanced research turbine,* (2014).

[27] A. Byrne, T. McCoy, K. Briggs, and T. Rogers, *Expected impacts on cost of energy through lidar based wind turbine control,* in *EWEA conference* (2012).

[28] T. Friis Pedersen, N. N. Sørensen, L. Vita, and P. Enevoldsen, *Optimization of Wind Turbine Operation by Use of Spinner Anemometer* (Danmarks Tekniske Universitet, Risø Nationallaboratoriet for Bæredygtig Energi, 2008).

[29] T. F. Pedersen, G. Demurtas, J. Gottschall, J. Højstrup, J. D. Nielsen, W. Christiansen, G. Weich, A. Sommer, and J. R. Kristoffersen, *Improvement of wind farm performance by means of spinner anemometry,* (2013).

[30] K. A. Kragh and P. Fleming, *Rotor speed dependent yaw control of wind turbines based on empirical data,* in *Proceedings of the 50th AIAA Aerospace Sciences Meeting Including the New Horizons Forum and Aerospace Exposition, Nashville, TN, January* (2012) pp. 9–12.

[31] K. A. Kragh and M. H. Hansen, *Potential of power gain with improved yaw alignment,* Wind Energy **18**, 979 (2015).

[32] B. Noura, I. Dobrev, R. Dizene, F. Massouh, and S. Khelladi, *Experimental study of yawed inflow around wind turbine rotor,* Proceedings of the Institution of Mechanical Engineers, Part A: Journal of Power and Energy , 0957650912445015 (2012).

[33] H. A. Madsen, N. N. SOrensen, and S. Schreck, *Yaw aerodynamics analyzed with three codes in comparison with experiment,* in *ASME 2003 Wind Energy Symposium* (American Society of Mechanical Engineers, 2003) pp. 94–103.

[34] D. Schlipf, S. Kapp, J. Anger, O. Bischoff, M. Hofsäß, A. Rettenmeier, and M. Kühn, *Prospects of optimization of energy production by lidar assisted control of wind turbines,* (2011).

[35] L. P. Chamorro and R. A Arndt, *Non-uniform velocity distribution effect on the betz–joukowsky limit,* Wind Energy **16**, 279 (2013).

[36] I. E. Commission *et al.*, *Wind turbine-part 1: Design requirements, iec 61400-1,* International Electrotechnical Commission, Geneva, Switzerland (2005).

[37] P. Stuart, N. Atkinson, and A. Clerc, *Why does t7 underperform? individual turbine performance relative to preconstruction estimates,* in *EWEA Technology Workshop* (2012).

[38] P. Stuart, *Introduction to the power curve working group,* in *EWEA Conference* (2013).

[39] I. Antoniou, P. Enevoldsen, and S. Lind, *Prerequisite to real world power curves,* in *EWEA Conference* (2013).

[40] A. Clerc, *Pcwg validation analysis: Turbulence correction,* in *PCWG workshop* (2014).

[41] H. Villanueva Lopez, *The Illusion of Power Curves: Understanding TI, Shear and Atmospheric Stability in Power Performance*, Master's thesis, TU Delft, Delft University of Technology (2014).

[42] A. Clifton and R. Wagner, *Accounting for the effect of turbulence on wind turbine power curves,* in *Journal of Physics: Conference Series*, Vol. 524 (IOP Publishing, 2014) pp. 12109–12119.

[43] *GH Bladed User Manual 3.81*.

[44] K. Boorsma, *Power and loads for wind turbines in yawed conditions*, Tech. Rep. (ECN-E-12-047, ECN, Petten, The Netherlands, 2012).

[45] S. Krohn, P.-E. Morthorst, and S. Awerbuch, *The economics of wind energy,* .

[46] O. C. Ltd., *Discount rates for low-carbon and renewable generation technologies,* (2011).

[47] J. Wieringa and P. J. Rijkoort, *Windklimaat van nederland*, Tech. Rep. (KNMI (staatsuitgeverij), 1983).

[48] I. Troen and E. Lundtang Petersen, *European wind atlas,* (1989).

A

WIND SPEED DISTRIBUTION

To determine the wind speed distribution at a wind park, e.g. Prinses Alexia, 10 minute averaged values of the wind speeds are used. It is expected that the wind speeds will be Weibull distributed, making it possible to determine the distribution in several different ways. For the acquired data this was accomplished using the Matlab functions 'wblfit' and 'histogram' as well as using least squares estimation and the European Wind Atlas Method, the last two of which will be explained in more detail in this chapter, whereby the data from wind park Prinses Alexia will be used as example.

A.1. LEAST SQUARES ESTIMATION

This method is also referred to as the 'log-log method'. The method is based on changing the cumulative probability distribution function from an exponential to a linear function by taking the logarithmic twice. The cumulative probability distribution function is defined as:

$$F(v) = 1 - \exp^{(-(v/A)^k)} \tag{A.1}$$

whereby k and A are the shape and scale parameters, respectively. Taking the logarithm of this function twice leads to:

$$\ln(-\ln(1 - F(v))) = -k \cdot \ln v + k \cdot \ln A \tag{A.2}$$

which has the form of a linear equation ($y = a \cdot x + b$). Plotting the measured wind speeds in this form and taking the linear fit, one is then able to calculate the Weibull parameters k and A. A linear fit method proposed by Wieringa [47] according to the following relations:

$$k = \frac{m \sum_m (x_i y_i) - \sum_m x_i \sum_m y_i}{m \sum_m (x_i^2) - (\sum_m x_i)^2} \tag{A.3}$$

$$-k \ln(A) = \frac{\sum_m (x_i^2) \sum_m y_i - \sum_m x_i \sum_m (x_i y_i)}{m \sum_m (x_i^2) - (\sum_m x_i)^2} \tag{A.4}$$

This method was compared to the normal polyfit Matlab function and it was found to give the exact same result. For that reason it was decided to further use polyfit as a linear fit tool.

In this research a threshold is also used to filter for wind speeds between 4 and 16 m/s, according to the method proposed by Wieringa [47]. The least squares fit gives a distribution with A=7.89 and k=2.31 at the Prinses Alexia site over the period February 2015 till July 2015.

A.2. EUROPEAN WIND ATLAS METHOD

The European Wind Atlas Method is a method developed at Risø DTU to give an accurate way of estimating the Weibull parameters of a wind speed distribution.[48]. The method is characterized by the combining of the requirements:

1. The total wind energy in both the observed and Weibull fitted distribution are equal.
2. The frequencies of occurrence of wind speeds higher than the observed mean wind speed are the same for both distributions.

These requirements both lead to an equation of the parameters k and A, and when these equations are combined they leave over an equation in k only, which can be solved using a root-finding algorithm.

According to the Wind Atlas Method the first requirement can be described by the available wind power density, which is proportional to the mean cube of the wind speed:

$$E = \frac{1}{2}\rho(\Sigma(v_{bin}^3 \cdot f)) = \frac{1}{2}\rho A^3 \Gamma(1+\frac{3}{k}) \tag{A.5}$$

where E is available power density (W/m^2), ρ is the air density and k and A the Weibull parameters.In this case v_{bin} represents the middle of each wind speed bin. Rewriting the above equation as a function of the scale parameter (A) leads to:

$$A = \left(\frac{(\Sigma(v_{bin}^3 \cdot f))}{\Gamma(1+\frac{3}{k})}\right)^{1/3} \tag{A.6}$$

The second requirement can be converted into equation form using the cumulative Weibull distribution function ($F_(v)$), which gives the probability that the wind speed will be lower than the value v. To find the probability for wind speed to be higher than the value v, the F given in Eq. A.1 should be subtracted from 1. Resorting this equation for A then gives:

$$A = \frac{v}{(-\ln(1-F(v)))^{1/k}} \tag{A.7}$$

Due to the two requirements, the scale parameters calculated with both formulas above should be equal, hence making it possible to find the k where this is the case using a root-finding algorithm. The Matlab code developed to perform the above calculation is shown in the next section. Eventually, the Wind Atlas Method gives a distribution with A=7.81 and k=2.09 at the Prinses Alexia site over the period February 2015 till July 2015. Figure A.1 displays the Weibull distributions as calculated with the three different Weibull estimation methods mentioned in this chapter.

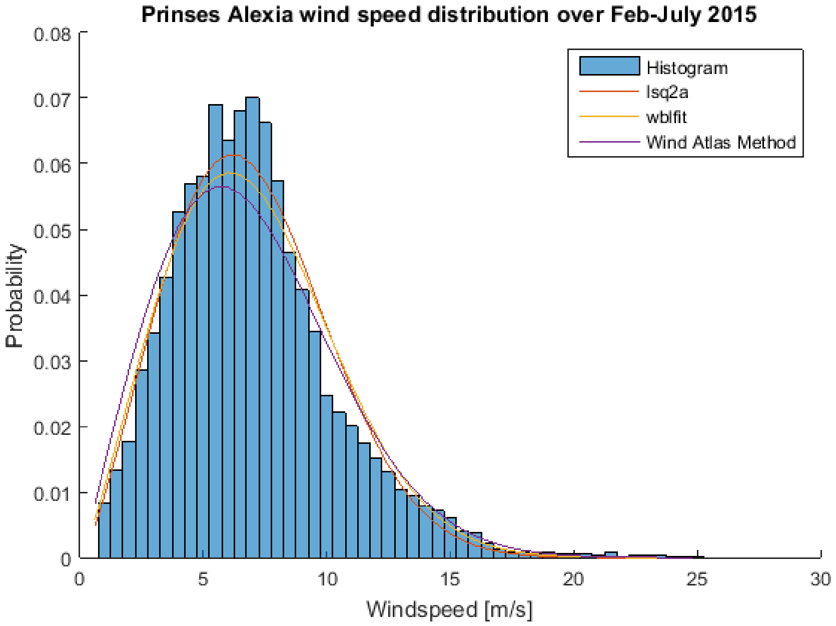

Figure A.1: *Weibull fits of wind speed distribution at Prinses Alexia using the 'wblfit' function, LSQ estimation and the Wind Atlas Method.*

Taking the goal of energy production by WTGs into consideration, the Weibull distribution found using the Wind Atlas Method is thought to be the best fit to the measured wind distribution as the power densities compare best. Looking at the fitted lines in the Figure A.1 however, it might be considered that the Least

Table A.1: *Weibull parameters and energy content found with different Weibull estimation methods at Prinses Alexia for the period of Feb-July 2015.* $V_{mean} = 7.01\,m/s$

Method	**Shape (k)**	**Scale (A)**	**Power density (E) [W/m^2]**	**Measured E [W/m^2]**
Least Square Estimation	2.35	7.83	677.44	742.08
Matlab 'wblfit.m'	2.24	7.92	727.24	742.08
Wind Atlas Method	2.09	7.81	742.27	742.08

Square Estimation method is better. Nonetheless, the WAM-method is considered to be the most accurate as it considers both the total energy content of the binned distribution as the same total distribution above mean wind speed as the measured distribution.

A.3. MATLAB SCRIPTS

This section gives the Matlab codes used to calculate the Weibull parameters of the wind speed distribution.

Firstly, the Least Square Estimator uses the wind measurements and has the possibility to include two threshold values as a minimum and maximum wind speed to consider for the wind speed distribution. This method first finds the cumulative probability distribution and then takes the double logarithm as explained above. Plotting the result and linearly fitting it, one is then able to calculate the Weibull parameters.

```
function [A1 k1]=lsq2a(V,T1,T2)
% syntax: function [sig,alfa]=lsq2a(V,T)
% assume Weibull
% V: stochastic variable
% T1&T2: thresholds

V =sort(V);

N=length(V);
F=[1:N]'/(N+1);
y=log(-log(1-F));
x=log(V);

% apply threshold
Ind=find(V<=T1 | V>=T2);
x(Ind)=[];
y(Ind)=[];
disp(['number of points: ',num2str(length(x))])

p=polyfit(x,y,1);
a=p(1);
b=p(2);

figure
plot(x,y,'*',x,a*x+b);shg;
xlabel('ln(V)')
ylabel('ln(-ln(1-F(v)))')

k1=a;
A1=exp(-b/a);

% figure(12)
% weibullplot(V,'stochastic variable',sig,alfa)
```

The Wind Atlas Method, on the other hand, uses a different approach and calculation. What is needed to calculate the parameters here is the measured 10min averaged wind speeds and the average observed wind speed over the whole period. First the wind speed measurements are sorted into the unit bins and then used to calculate the probability distribution function. Next, the total energy content and the probability that wind speed is higher than the observed average wind speed are calculated.

```
function [F,f,Eb,Fm,Vm]=weibulfit(V,Vm)
% number of bins
c=ceil(max(V));
bins=1:c;
midbins=bins-0.5;
bounds=0:c; %bin boundaries
```

```
f=zeros(1,c);
% select wind speeds for each wind sector and wind class
for i=1:c
    Ind=find(V >= bounds(i) & V < bounds(i+1));
    f(i)=length(Ind);
end

S=sum(f);
f=f./S;

%cumulative distribution
F=cumsum(f);

% calculate energy content per bin, sum up and calculate A2 using eq 8.43 from
% European Wind Atlas
Eb=sum((midbins.^3).*f);
%A3=(Eb/gamma(1+3/k))^(1/3);

%compare with frequencies of occurrence of v>Vm
Fm=interp1(bins,F,Vm,'linear'); %probability that v is lower than Vm

%Using eq 8.41 from European Wind Atlas and rewriting:
%A4=Vm/(-log(1-Fm))^(1/k);
```

These can then be inserted into the m-file below and used to determine A_3 and A_4 using the equations given above. Finally, a root finding algorithm, fzero, can be used to find the value of k for which the difference between A_3 and A_4 is zero.

```
function ck=check(k,Eb,Fm,Vm)
global Eb Fm Vm

% calculate energy content per bin and calculate A2 using eq 8.43 from
% European Wind Atlas
A3=(Eb/gamma(1+3/k))^(1/3);

%compare with frequencies of occurrence of v>Vm
%Using eq 8.41 from European Wind Atlas and rewriting:
A4=Vm/(-log(1-Fm))^(1/k);

% difference must be zero
ck=A3-A4;

%k3=fzero(@check,[0.01 4]); %root finding algorithm
```

B

Density Correction

As named in Chapter 3.1, the IEC standards dictate that the dataset be corrected to a standard reference air density. The procedure proposed by the IEC incorporates that the power available in the wind is always dependent on the wind speed cubed. Svenningsen [2] finds this to however lead to an overestimation of the AEP by up to 5% and has therefore proposed an improved correction method which will be described below.

B.1. Proposed solution

As mentioned in Chapter 3.1, density correction is performed using the following equation:

$$V_{norm} = V_{10min}\left(\frac{\rho_{10min}}{\rho_0}\right)^{\frac{1}{m}} \tag{B.1}$$

where the IEC take m=3. Svenningsen argues that real power curves do not always have a ρu^3 dependency at all wind speeds but only during the sloping part of the power curve. Once rated power has been reached and blade pitch control starts kicking in, the available power is actually lowered to the rated power by making the blades less aerodynamic in the wind. Svenningsen found that the error of the IEC correction overestimated power by up ot 10% close to rated power.

In his method, Svenningsen decided to incorporate the effect of density on the power coefficient curve. He found that up to the peak of the C_p versus wind speed curve the dependence is expected to follow a cubed pattern but beyond the peak the exponent, m, is expected to be less than 3. Analyzing several density specific power curves thoroughly Svenningsen was able to validate a simple and slight adjustment to the IEC method in order to mimic pitch control effects on the PC [2]. He proposes to add a smooth adjustment of m=3 at 7-8 m/s to m=1/1.5 at 12-13 m/s, as displayed in the figure below. Implementing this adjustment to a number of standard air density power curves and comparing this to the density specific PCs delivered by the turbine manufacturers, Svenningsen was able to reduce AEP errors up to +4−5% to ±1% compared to the guaranteed power curve.

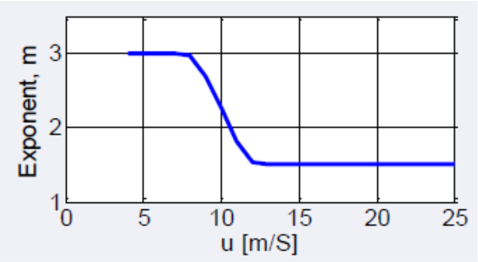

Figure B.1: *Proposed dependence of exponent for density correction [2]*

B.2. Implementation

Svenningsen's method was implemented in the data analysis Matlab script using the following code:

```
%% density correction
rho0=1.225; % standard air density
R0=287.05; % the absolute gas constant of dry air
Rw=461.5; %the absolute gas constant of water vapour
p10mm=100.*mmdata(:,62); %10-min Average air pressure readings from met-mast at 95.8m
T10mm=273.15+mmdata(:,42); %10-min Average Temperature readings from met-mast at 96.3m
Pwmm=2.05E-5.*exp(0.0631846.*T10mm); %vapour pressure
H10mm=mmdata(:,46)./100; %10-min Average Relative Humidity readings from met-mast at 96.3m
rho=(1./T10mm).*((p10mm./R0)-H10mm.*Pwmm.*(1./R0-1./Rw));

%according to IEC standards
%m=3;
%using Hensingtons alternative approach
m = 3-3*heaviside(v80mm - 8)+(-(3/8).*v80mm+6).*heaviside(v80mm-8).*heaviside(12-v80mm)+1.5*heaviside(
    v80mm-12);
V80mmnorm=v80mm.*(rho./rho0).^(1./m); %Normalized wind speed
```

For every 10-min data point, a m-value was calculated and this was in turn used to correct the wind speed to standard air density by means of Equation B.1. Figure B.2 shows an example of the exponent values found during the measurement campaign at Prinses Alexia.

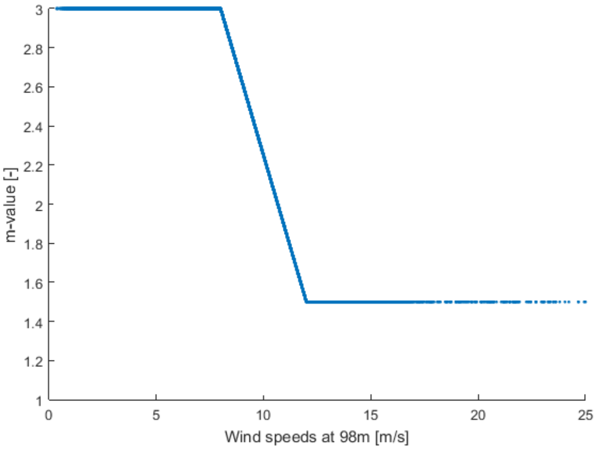

Figure B.2: *Calculated exponents for density correction according to Svenningsen's method.*

C

WIND DIRECTION AND YM SIMULATIONS

Following a non-perfect YM correlation between met-mast and both Lidar and spinner anemometer readings, it was decided to apply a methodology of simulating YM distributions as developed by Goossens [7]. This method simulates wind direction variations and how a turbine and measurement devices would react to these variations. First the wind direction is simulated by using the Matlab random generator *normrnd*. Next, considering that the nacelle responds to the wind direction but likely has a constant (static) and variable (dynamic) misalignment, a signal to depict these two forms of YM is generated, *meanyawmisalignment* and *nacellemisalignmentspread* respectively. Combining these variables with the wind direction signal, the nacelle direction is simulated.

To actually measure the YM at Norrekaer Enge three devices were used, spinner anemometers, a Lidar and a met-mast in combination with Scada data. The spinner anemometers and Lidar measure the YM directly and therefore only their individual accuracies (*spinneraccuracy* for spinner anemometer) influence this signal in the simulations. The met-mast method however acquires an additional uncertainty and *offset* from mis-calibration of the Scada signal.

To be able to find a correlation which matches Figure 8.14a, several input parameters can then be varied. These parameters are:

- *nacellemisalignmentspread*
- *spinneraccuracy* or *lidaraccuracy*
- *metmastaccuracy*
- *offset due to mis-calibration Scada signal*

whereby the met-mast accuracy actually describes the accuracy of the complete method using a met-mast, so including additional uncertainties due to combining Scada and met-mast data. An optimizing solver was added to the method suggested by Goossens so as to vary the input parameters over a specific range automatically and find the best match with the measured YM correlation (slope, offset and R^2-value of the fit) given by *gmeas, offsetmeas and R2meas*. Figure 8.15a shows the acquired best match between simulated and measured YM scatter. The script at the end of this section shows how this is done during the simulations for the specific case of the spinner anemometers.

The source of the uncertainty of each YM measurement method is influenced by several factors, which have been displayed in the table below. Assumptions are made here that the met-mast is positioned at 2.5D, the spinner anemometer is calibrated to this met-mast and the Lidar measures at 2.5D in front of the turbine.

Table C.1: *Influence of different contributions to YM measurement method uncertainty*

Uncertainty contribution	**Met-mast**	**Spinner Anemometer**	**Lidar**
Non-homogeneous wind flow	No influence	No influence	Large influence
Correlation with wind at turbine	Slight influence	No influence	Slight influence
Nacelle flow distortion	No influence	Slight influence	No influence
Calibration next to met-mast	Not applicable	Slight influence	Not applicable
Scada dependency	Slight influence	No influence	No influence

```
function [ind_g, ind_off, ind_R2, ind_opt]=corr2(k1, asp, amm, off, meanYMmm, gmeas, offsetmeas, R2meas)

% This coding is based on earlier work by Goossens and has been adjusted/optimized for the purpose of this
      thesis study.

%range of input parameters inserted into optimization equation
% k1=[1:0.1:3];
% asp=[0.2:0.05:4];
% amm=[0.2:0.05:4];
% off=[-4:0.1:4];

for i=1:length(k1)
    for j=1:length(asp)
        for k=1:length(amm)
            for m=1:length(off)
simlength = 6000;                              % in 10min points
windvariability = 5;                           % in degrees
meanyawmisalignment = meanYMmm;                % in degrees
nacellemisalignmentspread =k1(i);              % in degrees
spinneraccuracy =asp(j);                       % in degrees.
metmastaccuracy = amm(k);                      % in degrees.
offset = off(m);                               % nacelle dir - wind dir constant offset
time = 10*linspace(0,simlength,simlength);     % in minutes
meanwinddirection = linspace(90,20,simlength);
winddirection = normrnd(meanwinddirection,windvariability);
nacelledirection = normrnd(winddirection+meanyawmisalignment,nacellemisalignmentspread);
metmastdirection = normrnd(winddirection,metmastaccuracy);
YM = nacelledirection - winddirection;
YMmetmast = nacelledirection - metmastdirection + offset; %unrounded
YMspinner = normrnd(YM,spinneraccuracy);

xtemp = YMmetmast;
ytemp = YMspinner;
p=polyfit(xtemp,ytemp,1);
ris=ytemp-p(1)*xtemp-p(2);          % residuals
pm = mean(ytemp);
SStot = sum((ytemp-pm).^2);
SSres = sum(ris.^2);
R2 = 1-SSres/SStot;
% difference must be close to zero as possible for optimal situation
c(i,j,k,m)=gmeas-p(1);
d(i,j,k,m)=offsetmeas-p(2);
e(i,j,k,m)=R2meas-R2;
            end
        end
    end
end

MasterM=c.*d.*e;
[M1 ind1]=min(abs(c(:)));
[M2 ind2]=min(abs(d(:)));
[M3 ind3]=min(abs(e(:)));
[M4 ind4]=min(abs(MasterM(:)));
[I1,J1,K1,M1]=ind2sub(size(c),ind1);
[I2,J2,K2,M2]=ind2sub(size(c),ind2);
[I3,J3,K3,M3]=ind2sub(size(c),ind3);
[I4,J4,K4,M4]=ind2sub(size(c),ind4);

ind_g=[I1,J1,K1,M1];           % gradient equalized
ind_off=[I2,J2,K2,M2];         % offset/y-intercept equalized
ind_R2=[I3,J3,K3,M3];          % R2 equalized
ind_opt=[I4,J4,K4,M4];         % combination optimized
```

D

ACCOUNTING FOR HETEROGENEITY

Following simulations to copy the Lidar YM measurements as found by Goossens[7], the WindIris Lidar was found to be able to measure YM at an accuracy of 4°. Upon presenting this to the manufacturer of the Lidar, Avent Lidar Technologies, the remark was made that the effect of heterogeneity on Lidar measurements is not incorporated in the simulations. A discussion may be held on to whether it is the 'fault' of the wind being heterogeneous over the measurement surface or that the underlying Lidar principle is the problem.

The Lidar working principle is based on the idea that the wind conditions between the measurement point of LOS0 and LOS1 are equal. In practice this is however not the case, raising the question as to how this affects Lidar measurements and whether this could be compensated for in the future. With the help of Avent Lidar, a method was developed to quantify the effect of heterogeneity on Lidar measurements. From this quantification, I have proposed a measurement campaign using a 5-beam nacelle-based Lidar with which more insight can be acquired into heterogeneity in wind flow and how a Lidar device could be corrected for it.

D.1. QUANTIFICATION OF HETEROGENEITY IN LIDAR MEASUREMENTS

Several tele-conferences were organized with Vattenfall(Goossens), Avent (Coubard-Millet), ECN (Wagenaar) and the TU Delft (Giyanani) to discuss the effects of heterogeneity on a two-beamed Lidar. During and following these discussions, Coubard-Millet has kindly assisted in working out the influence of heterogeneity on the Lidar by means of the graphical description shown below and the basic Lidar equations as given in the WindIris manual[4].

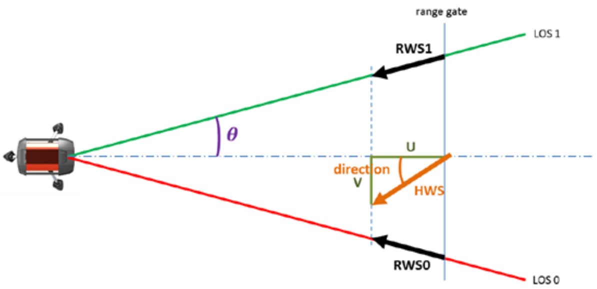

Figure D.1: *Topview graphical description of the Lidar measurement principles.(Presented during tele-conferences with Avent Lidar Technologies)*

The Lidar working principle builds on the idea that the HWS is the same at both LOSs. Wind conditions are however heterogeneous meaning one, or both, of the LOS might be measuring a different wind speed than the actual HWS in the line of the rotor axis. The heterogeneity(X) is therefore quantified as a percentage of the HWS and can then be applied on either one, or both, of the RWS equations. Coubard-Millet proposed to implement heterogeneity only on LOS1, meaning it will measure the HWS plus a deviation due to heterogeneity using the following equations:

In these equations, the YM is assumed to be 0° for simplicity. Rewriting Eq. 3.8 to a the current variables,

Heterogeneity influence	ΔHWS	ΔHWS=X*HWS
LOS0:	HWS0=HWS	RWS0 = HWS*cos(15°)
LOS1:	HWS1=HWS+ΔHWS	RWS1 = (HWS+ΔHWS)*cos(15°)

such a deviation would then influence the direction reading of the Lidar as follows:

$$\alpha = \arctan\left(\frac{V_m}{U_m}\right) = \arctan\left(\frac{RWS0 - RWS1}{(RWS0 + RWS1)\tan(15°)}\right) \tag{D.1}$$

These equations, as given in the WindIris manual[4], can then be combined and simplified to:

$$\alpha_{het} = \arctan\left(\frac{-X}{(2+X)\tan(15°)}\right) \tag{D.2}$$

Whereby α_{het} represents the relative wind direction in heterogeneous conditions and the 15° opening angle (θ) of the Lidar beams.

D.1.1. ALTERNATIVE APPROACHES

Assuming that heterogeneity only affects one Lidar beam (LOS1) implicates that the heterogeneity increases linearly between the LOS measurement points. In this case, however, it would mean that the wind speed representing the HWS would actually be HWS+0.5*ΔHWS. For this reason, two adjustments are considered for the equations as presented by Coubard-Millet which will be explained below.

Option 1: Linear heterogeneity on both beams The first option considers a linear increase in heterogeneity with distance between the LOSs. In this case, however, half of the heterogeneity effect is added to one beam and the other half is subtracted from the second beam. Figure D.2 shows the graphical description of both options, option 1 on the left and option 2 on the right. The wind speed profiles under influence of heterogeneity have been added, whereby the left profile increases linearly with distance to the right.

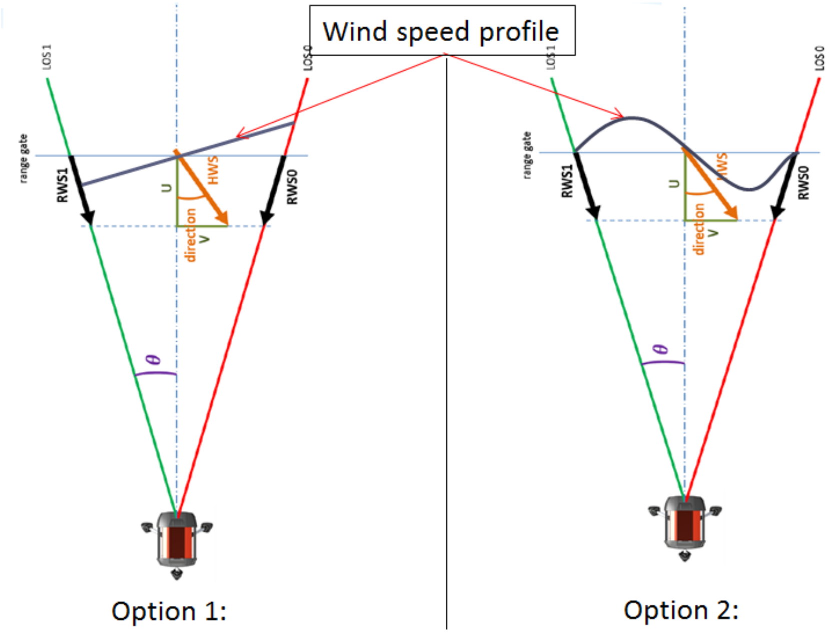

Option 1: Option 2:

Figure D.2: *Alternative options for top-view graphical description of the Lidar measurement principles.*

Applying the ideas for option 1, the equations given earlier in this section can be altered as follows:

LOS0:	HWS0=HWS-ΔHWS	RWS0 = (HWS-ΔHWS)*cos(15°)
LOS1:	HWS1=HWS+ΔHWS	RWS1 = (HWS+ΔHWS)*cos(15°)

Hereby the magnitude of heterogeneity(X) is taken as equal on both LOS0 and LOS1. The Lidar's general equation for wind direction (Eq.D.1) remains unchanged due to this but the simplifying it with the adjusted

RWS0 and RWS1 equations does lead to a different outcome:

$$\alpha_{opt1} = \arctan\left(\frac{-X}{(2 * \tan(15°)}\right) \tag{D.3}$$

Option 2: Non-linear heterogeneity on both beams The second option is that heterogeneity is random, or at least non-linear, over the horizontal distance between the two beams. This seems the most likely scenario in reality considering the turbulent nature of wind. This option requires that a different heterogeneity percentage, both in magnitude and eventually sign, is necessary on each beam. The different heterogeneity factors can be given as X_0 and X_1 for their respective beams and they can be a value between -1 and 1. This option changes the RWS equations to the following form:

Heterogeneity influence:	ΔHWS0=X_0*HWS, ΔHWS1=X_1*HWS	
LOS0:	HWS0=HWS-ΔHWS0	RWS0 = (HWS-ΔHWS0)*cos(15°)
LOS1:	HWS1=HWS+ΔHWS1	RWS1 = (HWS+ΔHWS1)*cos(15°)

Inserting these equations for RWS0 and RWS1 into Equation D.1 results in the following:

$$\alpha_{opt2} = \arctan\left(\frac{-(X_0 + X_1)}{((2 + X_0 + X_1) * \tan(15°)}\right) \tag{D.4}$$

A sharp eye would note that this is the more general form of the equations as Coubard-Millet. If X=X_0+X_1, the same result is acquired for the relative wind direction under heterogeneous conditions.

D.2. PROPOSAL OF HETEROGENEITY MEASUREMENT CAMPAIGN

Following the definition of these three options in which the heterogeneity could influence the YM measurement, an idea came up on how to measure this effect. With a two-beam Lidar, with have 3 unknowns, X, HWS and YM, and only two measurable quantities, RWS0 and RWS1. When using a 5-beam Lidar, however, there would be 3 beams in the horizontal plane, 2 resembling beams 0 and 1 of the 2-beam Lidar and one beam, the central beam, along the rotor axis. This beam will be referred to as RWS2 (see also Fig. D.3).

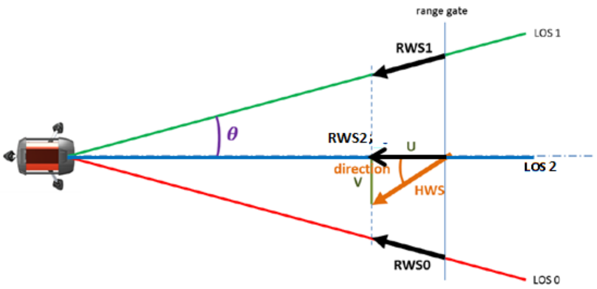

Figure D.3: *Topview graphical description of the Lidar measurement principles when using a 5-beam Lidar with LOS2, the central beam.*

If a 5-beam Lidar is installed on the nacelle of a turbine, two additional comparisons besides RWS0 and RWS1 can be made: RWS0 against RWS2 and RWS1 against RWS2. The HWS and wind direction can be determined using measurements by LOS0 and LOS2, and using measurements of LOS1 and LOS2. Comparing these results, it should be possible to determine the heterogeneity, X, and then eventually the exact HWS and wind direction as measured by LOS2.

Having no experience with the measuring principles of the 5-beam Lidar, it cannot be concluded whether such an experiment could deliver more knowledge on the occurrence of heterogeneity and its' effect on a Lidar. Also, it is considered likely that if heterogeneity changes non-linearly, the additional unknown variable due to two different heterogeneity factors will make the problem unsolvable once again. On the other hand, if heterogeneous behavior is linear on approximation, option 1 could be applied and a solution may be found to the two-beam Lidar's problems to cope with non-homogeneous conditions.

An experiment is therefore proposed at wind park Prinses Alexia. A 5-beam Lidar could be installed on either turbines R01 or R02 which are adjacent to an IEC-compliant met-mast after which a comparative study can be performed. Avent Lidar Technologies is currently developing their own 5-beam Lidar, hence such an experiment would be an opportunity for them to test their novel device against a met-mast. The benefit for Vattenfall would be the gained knowledge and experience with yet another promising remote sensing device.

E

PROPOSAL FAST YM INFLUENCE TEST

In this section a measurement plan is proposed for investigating the effects of YM on power performance without having to do an IEC-compliant PC verification as this would be too time consuming and induce high operational losses and loads at the turbines.

E.1. INTRODUCTION

As Romowind is starting to grow in fame in the wind energy sector, the question is rising within Nuon/Vattenfall whether the spinner anemometers need to be acquired for wind parks in the Netherlands too. This question incorporates not only the accuracy of the device measurements as investigated earlier in this report, but also what the energy and thereby the financial gains of an implementation would be.

Which gains are possible with spinner anemometers? Romowind, and other parties, have based the business case on a certain YM spread that has been measured at different turbines before and the assumption that this YM is related to power loss by $\cos^2$-relation. No conclusive confirmation of this assumption has been found so far which is the reason why the author would like to propose a shortened method to test this at wind park Prinses Alexia.

E.2. THE ANALYSIS METHOD

The method is based on side-by-side analysis whereby the simultaneous behavior of two adjacent turbines is compared before and after adjusting something on one of the turbines. In this case the turbine that remains unchanged is used as reference for the turbine being tested. This methodology is often used in wind turbine performance analysis when there is no met-mast or other type of remote-sensing device available for PCV.

For the case of the Prinses Alexia there is a met-mast close to turbines R01 and R02 but the process of performing a PCV following the IEC standards is very time-consuming. In order to limit the time in which the turbines being tested are misaligned, it is advised to perform a shorter test and do this by a side-by-side comparison of turbines R03 and R02. Since turbine R02 is performing very well it is considered best to do the tests on R03 while using R02 as reference turbine.

Initially, R01 was considered as potential test turbine but this is not possible as tests are still being performed on the turbine by the turbine manufacturer to find an explanation for its' under-performance. If the deliberate YM campaign were to be performed on R01, this would corrupt the results by Senvion. Figure E.1 shows an example of the correlation between simultaneous power readings from turbines R01 and R02 over the period of Feb. to October 2015. It is expected that if this comparison were to be done for turbine R03 against R02, identical results will be found.

The tests to be performed should vary YM on the test turbine from -20° to 20° in steps of 10°. Each YM setting shall be adjusted in the turbine controller and kept that way for a certain amount of time. Eventually the correlation between the power readings of both turbines is expected to change as the YM changes, from which it should be possible to find the relation between power performance and YM.

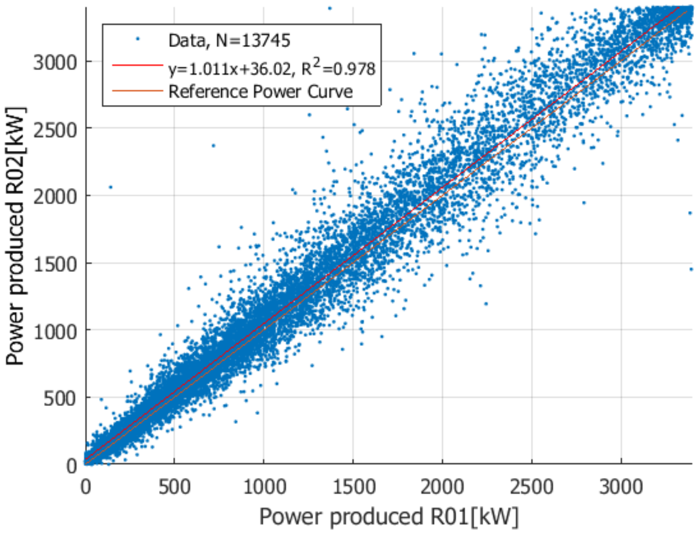

Figure E.1: *Correlation of simultaneous power readings from turbines R01 and R02 at Prinses Alexia.*

E.3. HOW DOES THIS METHOD MAKE THE MEASUREMENT PERIOD SHORTER?

The proposed method makes use of higher-frequency data, using 1-min averages instead of the standard 10-min averages. Most yaw controllers do not react to each quick change in wind direction as this would cause too much wear and tear of the yaw mechanism. A threshold YM is therefore often built in over a longer period of time, say e.g. 2° for a period of 1 minute, and when the turbine surpasses this threshold, the yaw controller will cause the turbine to yaw. Looking at high-frequency Scada data for turbines at Prinses Alexia, no clear yaw response time or threshold value was found. This is yet to be checked with the turbine manufacturers control system. Nonetheless it is expected that by introducing a static YM in the controller, the average YM will change identically thereby making it possible to measure the difference in power production at high-frequency.

Using 1 minute averaged values is thought to be sufficiently long enough to observe characteristics of the YM. By using this timebase up to 10x more data can be gathered in the same amount of time thereby also shortening an eventual measurement campaign time by tenfold. Measuring for 2 days would then deliver 2*24*60=2880 data points per YM. This should be enough data to find a good correlation between the power readings of both turbines. The data necessary for such an analysis are active power, availability and yaw position of each turbine. Additionally, rotor or generator RPM could be handy to filter out certain operational modes. All these signals are available at high-frequency (0.1 - 1Hz) in Vattenfall's Scada system.

Depending on how difficult it is to change the YM bias of the turbine, the YM settings could be varied either every 2-3 hours or every 2 days, as long as the total duration of each YM setting reaches 2 days. The first option, rotating YM settings every 2-3 hours for a total of 8 days, could be handy to ensure measuring during full wind speed spectrum but if the settings are adjusted manually this is not deemed practical. In that case, the following time plan is advised for the execution of a campaign:

Start time	End time	R03 YM setting
Day 1 00:00	Day 3 00:00	-20°
Day 3 00:00	Day 5 00:00	10°
Day 5 00:00	Day 7 00:00	-10°
Day 7 00:00	Day 9 00:00	20°

Matlab simulations have been performed for the power readings of both turbines in order to investigate the possibilities/limitations of the above-mentioned method. By doing this, we hope to discover whether the reaction time of the yaw controller influences the impact of YM and whether this difference is visible at all in the scatter graphs/correlations of two adjactent turbines. The results of these simulations are given in Appendix F.

F

SIMULATIONS OF YM CAMPAIGN USING SIDE-BY-SIDE METHOD

Following proposal for a YM-compensation measurement campaign in Chapter E, some simulations in Matlab were performed prior to starting the campaign so as to determine what effects and trends should be observed in the outcomes. The proposal incorporates a side-by-side analysis of two turbines whereby one is left unchanged as reference turbine while static YM adjustments are being performed on the second, test turbine. Next, the change power-to-power scatters and their correlations will be analyzed. Eventually the goal of this exercise is to determine the effect of YM on the power performance of the turbine. The Matlab coding for this simulation is given at the end of this section.

In order to investigate what trends or changes can be observed during the proposed experiment, the electric power of a turbine is simulated as a function of solely wind speed and YM. In reality this is not the case but as the turbines are adjacent it is expected other influences will be identical for both turbines. The wind speed is considered to vary slightly though for both turbines as wind flow is heterogeneous and varying over the wind farm area. This has been simulated by introducing a different wind speed variability (*windspeed-var*) for both turbines, a measure of the correlation between the wind speeds working on the turbines and the actual wind speed measured by the nearby met-mast. For simplicity, it has been assumed that both power transducers have the same accuracy and therefore do not influence the simulations. Table F.1 displays several key inputs applied during the simulations.

Table F.1: *Overview of assumptions and parameter settings applied during the YM campaign simulations.*

Parameters	**Turbine R01 (test)**	**Turbine R02 (reference)**
Power dependency	f(v_{hub},YM)	f(v_{hub},YM)
Mean YM	4.5°	6°
Wind speed variability	0.2 m/s	0.4 m/s
Wind direction variability	5°	5°
Nacelle misalignment spread	2°	2°
Power ratio rel. to guaranteed PC	0.96	1.02

Using the specifics, like e.g. mean YM and guaranteed PC, of turbines R01 and R02 from Prinses Alexia, it is attempted to initially acquire similar plots to the measured results at Prinses Alexia as shown in Figures 7.3b and E.1. Figures F.1a and F.1b show the simulated plots which do indeed show the same behavior as the aforementioned figures.

Next, the mean or static YM on turbine R01 is varied by -20° to 20° in steps of 2° while the YM on turbine R02 is left unchanged. The effect of YM is calculated through to the wind speed via the $\cos^2$-rule, after which the power reading is interpolated from the guaranteed PC. The turbine power readings for R01 and R02 are multiplied by a factor of 0.96 and 1.02, respectively, which are their individual deviations from the guaranteed PC as measured during earlier experiments (see also Figure 7.2). Figures F.2a and F.2b give an example of the effects of the YM offset, whereby the scatter plots of turbine power and histogram of YM, respectively, at an offset of +20° are shown. It can be seen that the regression fit gradient of the scattered power readings has increased from approx. 1 to 1.23, thereby confirming that turbine R01 is producing less power due to the

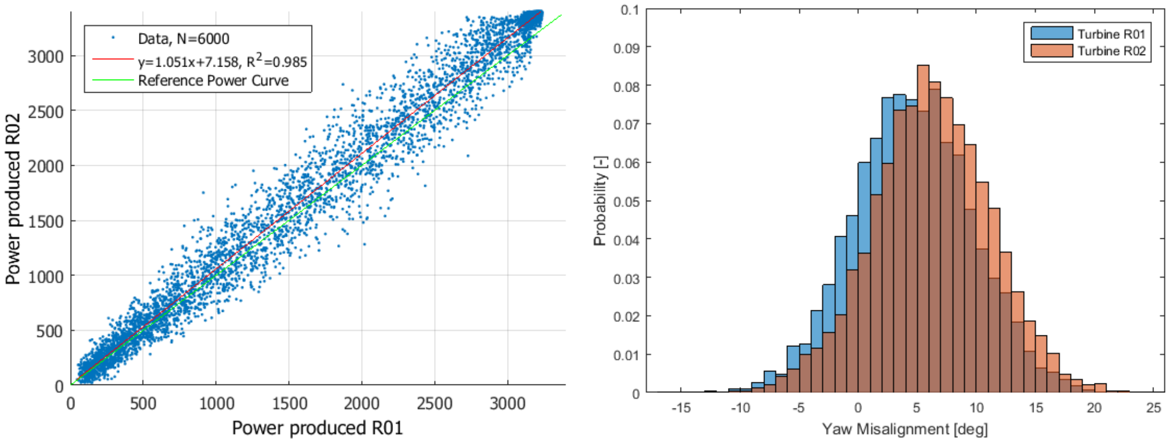

(a) *Simulated power readings R01 and R02*

(b) *Histogram of simulated YM R01 and R02*

Figure F.1: *Initial simulation results for turbines R01 and R02 based on the side-by-side method with zero offset in YM.*

increased YM.

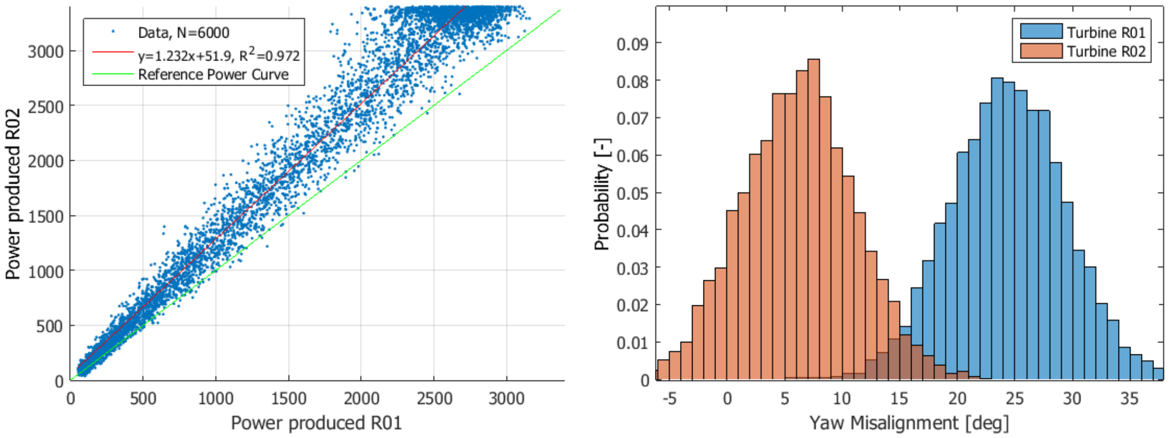

(a) *Simulated power readings R01 and R02*

(b) *Histogram of simulated YM R01 and R02*

Figure F.2: *Simulation results for turbines R01 and R02 based on the side-by-side method with R01 at a YM-offset of +20°*

Initially, it was expected that a conclusion could be made based on the change in correlations between the power readings. There is however no clear relation between the change in gradient and YM. Even though the correlations do change, generally becoming poorer as YM increases in magnitude, there is no clear pattern in this change, neither in correlation gradient nor R^2-value. As the effect of YM is mostly determined in terms of AEP, the energy content of each simulated data point is therefore more interesting to look at. This has been done for the range of simulations named earlier, resulting in a normalized AEP vs YM curve as shown in Figure F.3.

For the case of Figure F.3, a cosine exponent of 2 was assumed. The figure shows that indeed the simulated AEPs match a cos^2-graph nearly perfectly, as can be expected for the calculation method shown in the Matlab script. Furthermore, the graph is shifted to the left by approx. 5° due to the initial mean YM of +4.5° of turbine R01 as given in Table F.1.

The influence of the cosine-exponents on the simulations was also looked into, varying it from 1.5 to 4. Figure F.4 shows the resulting AEP ratio curves, which as could be expected match their individual cosine exponented curves well.

Concluding, initial simulations seem to show that a measurement campaign as proposed in Chapter 8 could indeed provide an answer to the question on what the effect of YM on power performance is. The higher-frequency data than the usual IEC-accepted 10-min should not cause a problem in this either. Doubts

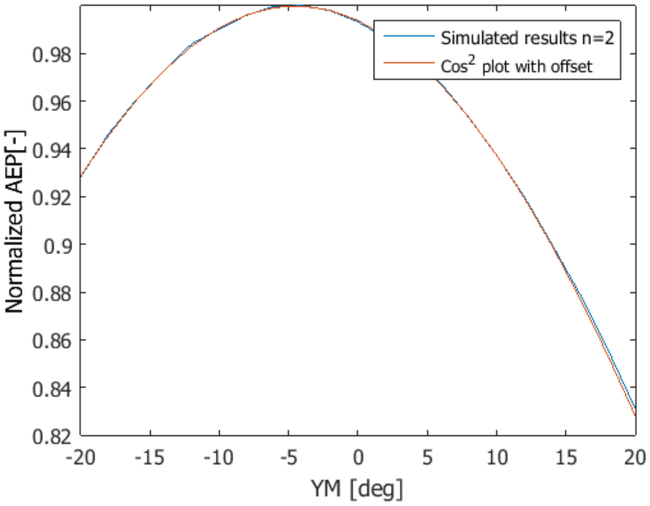

Figure F.3: *Results of the simulations as the YM for turbine R01 is varied from -20 to +20 degrees while R02 remains unchanged (n=2).*

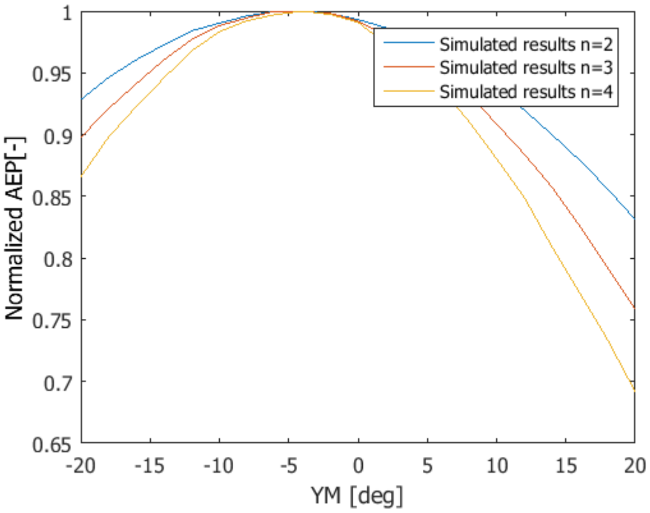

Figure F.4: *Results of the simulations as the cosine exponent is varied from 2-4.*

may however be placed on whether the methodology applied in the simulations is correct, or whether formulating the problem in this way is a self-fulfilling prophecy, i.e. changing the wind speed by $\cos^2(YM)$ automatically incorporates a similar change in power output. However considering the goal of these simulations to give an insight into the behavior of the turbines under test, the simulations are considered practical and useful.

```
clear all
close all

%% PC Turbines at Prinses Alexia
vpc=0:25;
vpc(4)=3.5;
Ppc=[0 0 0 28 87 246 471 783 1209 1733 2293 2839 3269 3340 3370 3370 3370 3370 3370 3370 3370 3370 3370
     3370 3370 3370];

%%
%Definitions
% Turbine 1 is test turbine
% Turbine 2 is reference turbine

% Assumptions:
% 1. Power transducers on both turbines have same accuracy
% 2. Power is influenced solely by windspeed and YM

%Influences
% 1. Windspeed differs for two locations
% 2. Different YM on each turbine


%% input arguments: YM and cosine exponent
n=2;
x=[-20:2:20];

for i=1:length(x)
simlength = 6000;                    % in 1min points
winddirvariability = 5;                 % Variability of the wind direction in degrees (equal for both
     turbines)
windspeedvar1=0.2;                     % Variability of wind speed in m/s
windspeedvar2=0.4;                     % Variability of wind speed in m/s. Higher than for turbine R01 as R02
      is further away from met-mast thereby decreasing the correlation between wind at met-mast and R02.
meanyawmisalignment1 = 4.5+x(i);    % in degrees
meanyawmisalignment2 = 6.2;    % in degrees

nacellemisalignmentspread1 =2; % in degrees (Similar to values found in simulations by Goossens)
nacellemisalignmentspread2 =2; % in degrees

meanwinddirection = linspace(90,20,simlength);
meanwindspeed=linspace(4,16,simlength);
winddirection = normrnd(meanwinddirection,winddirvariability);
windspeed1 = normrnd(meanwindspeed,windspeedvar1);
windspeed2 = normrnd(meanwindspeed,windspeedvar2);
nacelledirection1 = normrnd(winddirection+meanyawmisalignment1,nacellemisalignmentspread1);
nacelledirection2 = normrnd(winddirection+meanyawmisalignment2,nacellemisalignmentspread2);

YM1 = nacelledirection1 - winddirection;
YM2 = nacelledirection2 - winddirection;


v1=windspeed1;
v2=windspeed2;
PT1=0.96*(interp1(vpc,Ppc,v1)).*(cosd(YM1)).^n;
PT2=1.02*(interp1(vpc,Ppc,v2)).*(cosd(YM2)).^n;


E1(i)=sum(PT1.*(1/6))./length(PT1); %average energy per point in kWh
E2(i)=sum(PT2.*(1/6))./length(PT2); %average energy per point in kWh
y(i)=E1(i)/E2(i);
end
```

G

BLADED SIMULATIONS

In this appendix a more elaborate description of the simulation methodology in Bladed will be given including the specific interfaces used in the post-analysis. This method has been touched upon earlier in Section 5.3.2.

G.1. SETTING WIND CONDITIONS

First of all, a short description will be given of how Bladed allows the user to set wind conditions prior to simulations. This is done using different tabs in the 'wind' module, shown in the figures below. In the tab for 'Time varying wind' a constant, non-turbulent wind is set for each power production loading simulation. Non-turbulent wind is chosen by ticking 'No variation' in order to make certain that only the effects of WS and YM are visible in the simulations output, turbulence would not allow for a good analysis in this context. Next, the flow inclination angle is set to 0 as this influences the actual YM and WS. YM can be set by inserting a non-zero value for the wind direction while keeping the yaw controller switched off. This means that the value entered in the 'Wind direction' field is equivalent to the YM.

As simulations are to be done over the full wind speed spectrum of the turbine so as to acquire a complete dynamic PC, a power production loading simulation of each wind speed is to be done for each wind speed value given in Section 5.3.2. This is accomplished by changing the value of wind speed in the tab 'Time varying wind' and consequently running a power production loading simulation. Adding these simulations to a batch and running at once allows for a quicker procedure. Eventually, each load case (individual YM and WS setting) takes a duration of approximately 25 minutes to configure and run.

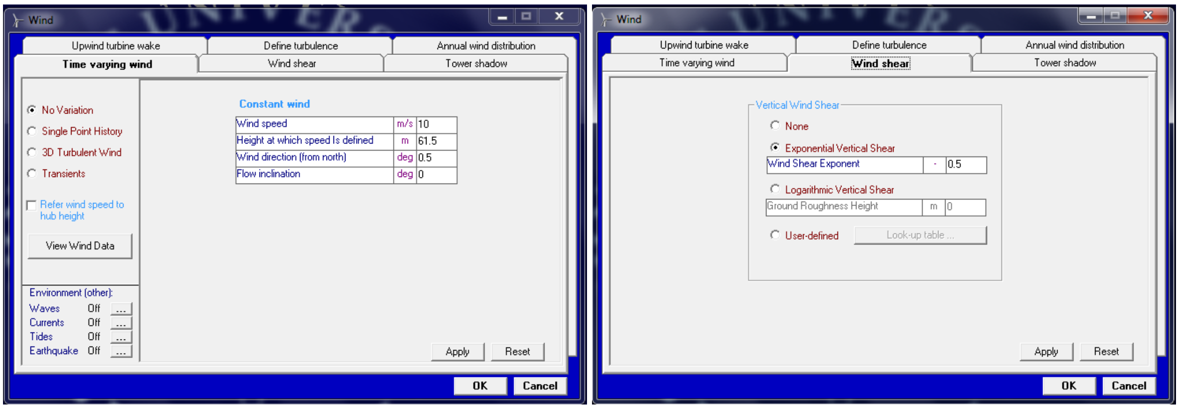
Wind
Upwind turbine wake
Define turbulence
Annual wind distribution
Time varying wind
Wind shear
Tower shadow
View Wind Data
Apply
Reset
OK
Cancel
Wind
Upwind turbine wake
Define turbulence
Annual wind distribution
Time varying wind
Wind shear
Tower shadow
Look-up table ...
Apply
Reset
OK
Cancel

● No Variation
○ Single Point History
○ 3D Turbulent Wind
○ Transients

☐ Refer wind speed to hub height

Environment (other):
Waves Off
Currents Off
Tides Off
Earthquake Off

Constant wind

Wind speed	m/s	10
Height at which speed Is defined	m	61.5
Wind direction (from north)	deg	0.5
Flow inclination	deg	0

Vertical Wind Shear
○ None
● Exponential Vertical Shear
Wind Shear Exponent - 0.5
○ Logarithmic Vertical Shear
Ground Roughness Height m 0
○ User-defined

(a) *Bladed module to set YM and wind speed*

(b) *Bladed module to set wind shear*

Figure G.1: *Bladed modules needed to set wind conditions prior to each power production loading*

Figure G.1b shows the tab in which the wind shear configuration can be set. In these simulations, it was chosen to use an exponential vertical wind profile instead of the logarithmic case. This allows for a more straight-forward analysis since the wind shear exponent gives a clearer ratio of the wind speeds in the profile.

The WS can be changed by varying the value in the 'Wind shear exponent' field according to the desired WS exponents (ranging between 0 and 0.5).

G.2. POWER PRODUCTION LOADING

The power production loading simulations are run using the Bladed calculation module. To make sure that the simulations are run correctly, all necessary input parameters and data requirements should be configured correctly before a simulation is run. Besides this, simulation control parameters should be set under the tab 'Calculation Parameters'. Figure G.2 displays the tab in which calculation parameters for a power production loading simulation are set. As can be seen in the figure, Bladed is set to only start writing output after 30s and a total simulation time of 90s is set, this being in accordance with the description in Section 5.3.2.

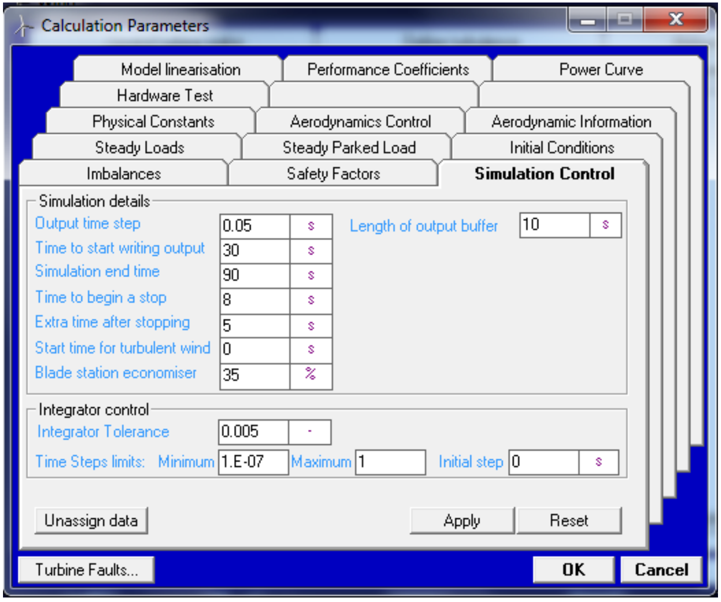

Simulation details
Output time step 0.05 s
Time to start writing output 30 s
Simulation end time 90 s
Time to begin a stop 8 s
Extra time after stopping 5 s
Start time for turbulent wind 0 s
Blade station economiser 35 %
Length of output buffer 10 s

Integrator control
Integrator Tolerance 0.005 -
Time Steps limits: Minimum 1.E-07 Maximum 1 Initial step 0 s

Figure G.2: *Bladed module in which calculation parameters for a simulation can be defined*

G.3. POST PROCESSING

After running power production loading simulations for the complete range of wind speeds for a specific load case, the 'Annual Energy Yield' module can be used to post-process the simulations per load case. This module analyses each loading simulation to find the mean wind speed and electric power and combine these to acquire the dynamic PC for the load case. Next, the PC is used to calculate the AEP based on a predefined annual wind speed distribution. Figure G.3a displays the window with which this step is performed. As can be seen, the wind speed distribution is set to an annual mean wind speed of 7 m/s with a Weibull shape factor of 2.09, identical to the conditions at wind park Prinses Alexia.

As was shown in Figures 5.5a and 5.5b, the output signals of the power production loading simulations keep fluctuating even after the original transients have disappeared. The question therefore arises whether the 'Annual Energy Yield' is able to find an accurate mean power or whether these fluctuations cause errors in the electric power results. To check this, the 'Fourier Harmonics' post-processing is used to evaluate the harmonic nature of each simulation and acquire an amplitude of the main harmonic of the electric power signal. Figure G.3b displays the window with which this post-processing step is done.

The output of the harmonics module is an amplitude and phase shift for each harmonic signal component. The harmonics module finds between 16 (for v>9) up to 29 (for lower v) different harmonic signals in the output signal. Table G.1 gives an example of the output of the Fourier Harmonics analysis of the electric power signal at wind speed of 10 m/s with a WS-exponent of 0.4 and YM of -2°.

The signal can be reconstructed using a harmonic equation and tuned to eventually match the original signal. Figure G.4 shows the result of this reconstruction, whereby the reconstructed signal seems to fit the

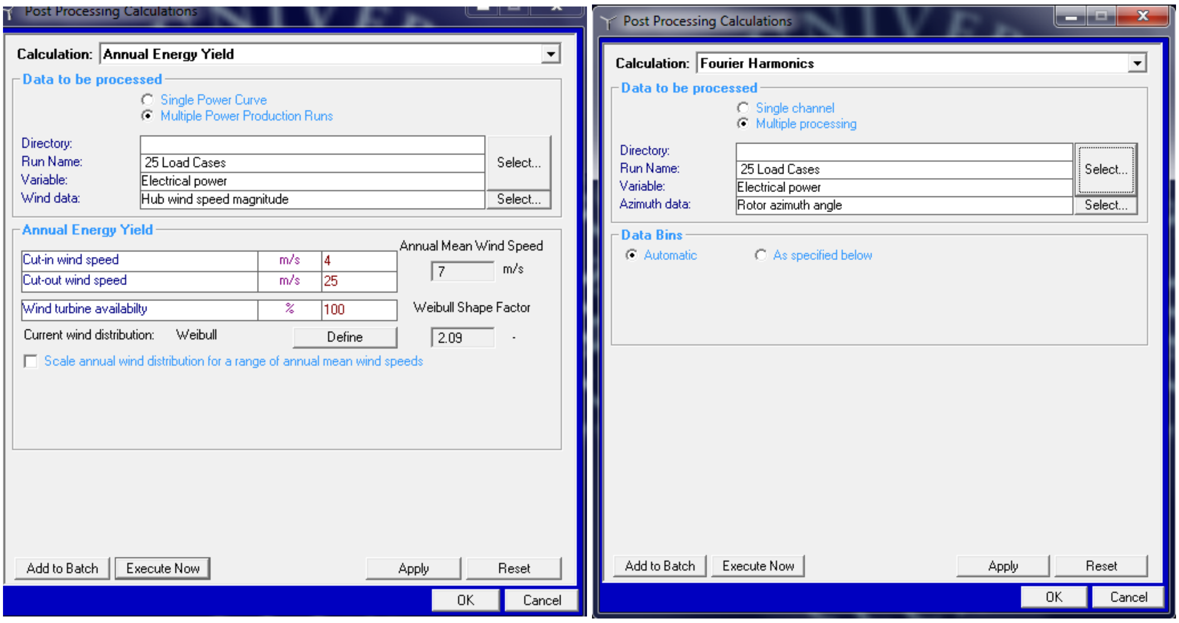
Post Processing Calculations
Data to be processed
Select...
Select...
Annual Energy Yield
Define
Add to Batch
Execute Now
Apply
Reset
OK
Cancel
Post Processing Calculations
Data to be processed
Select...
Select...
Data Bins
Add to Batch
Execute Now
Apply
Reset
OK
Cancel

Calculation: Annual Energy Yield
○ Single Power Curve
● Multiple Power Production Runs
Directory:
Run Name: 25 Load Cases
Variable: Electrical power
Wind data: Hub wind speed magnitude
Cut-in wind speed m/s 4
Cut-out wind speed m/s 25
Wind turbine availabilty % 100
Annual Mean Wind Speed 7 m/s
Weibull Shape Factor 2.09 -
Current wind distribution: Weibull
☐ Scale annual wind distribution for a range of annual mean wind speeds

Calculation: Fourier Harmonics
○ Single channel
● Multiple processing
Directory:
Run Name: 25 Load Cases
Variable: Electrical power
Azimuth data: Rotor azimuth angle
● Automatic ○ As specified below

(a) *Bladed module for AEP calculation*

(b) *Bladed Fourier harmonics module*

Figure G.3: *Bladed modules used during post-processing of the power production loading simulations*

Table G.1: *Example of Fourier Harmonics module outputs (Harmonic number, Amplitude and phase) of the for load case: v = 10 m/s, WS exponent = 0.4, YM = -2°.*

Harm. no. (n)	Amp. (A) [kW]	Phase (ϕ) [rad]	Harm. no. (n)	Amp. (A) [kW]	Phase (ϕ) [rad]
0	1258,85	0	**9**	0,40	6,25
1	0,027	3,13	**10**	0,023	2,08
2	0,032	2,96	**11**	0,026	1,77
3	1,21	1,14	**12**	1,27	4,94
4	0,025	2,70	**13**	0,022	1,91
5	0,024	2,56	**14**	0,019	1,71
6	1,37	4,43	**15**	0,17	3,17
7	0,023	2,33	**16**	0,022	1,45
8	0,025	2,28			

original signal relatively well. This good fit was found at an equation for the Fourier Harmonics signal of:

$$P(t) = \sum_{n=0}^{n_{max}} A_n \cos(2n\pi f t - \phi_n) \tag{G.1}$$

where f is the 1P frequency of the turbine. From this we can conclude that the harmonic number of 0 represents the mean electric power as the frequency of the harmonic is 0*f. The other harmonic numbers represent the 1P, 2P, 3P, etc frequencies of the turbine.

Finally, for the purpose of validating the AEP post-processing module results, the amplitude of the first harmonic (n=0) is compared to the acquired power reading in the dynamic PC in Table G.2 using the load case with YM=2° and WS exponent = 0.2 as example. The two right-most columns calculate the error between the readings and what this is as percentage of the dynamic PC reading. As can be seen in the table, the acquired dynamic PC matches the first harmonic amplitude very well with the average percentual error being below 1-thousandths of a percentage. Such a low deviation is negligible compared to errors in actual power and wind condition measurement devices, thereby confirming that the AEP post-processing tool is able to analyze the dynamic PC (and AEP calculation) accurately enough.

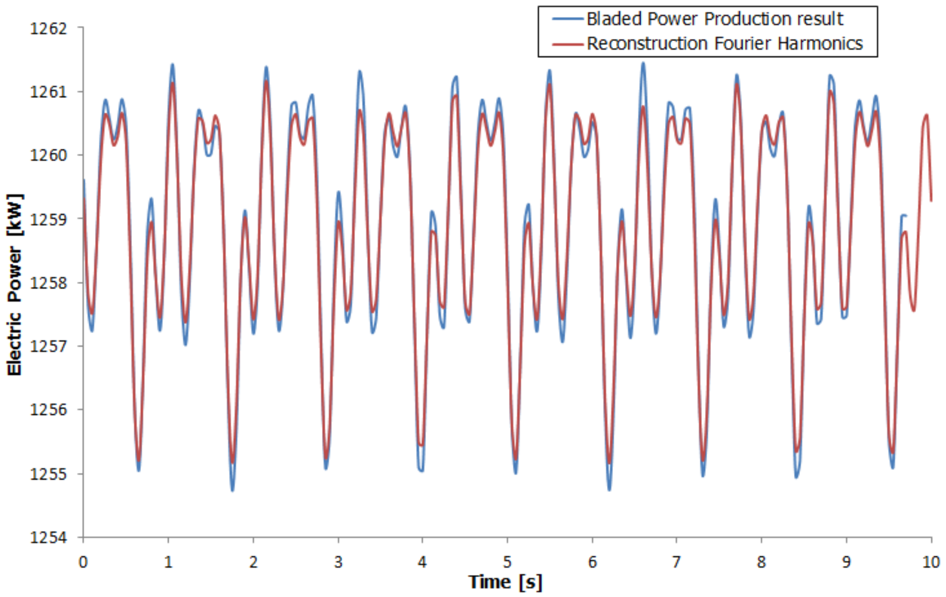

Figure G.4: *Reconstructed Fourier Harmonics signal compared to the original simulated electric power signal.*

Table G.2: *Harmonics comparison of the acquired dynamic PC for the following load case: YM=2° and WS exponent = 0.2.*

AEP post-processing Dynamic PC		Fourier Harmonics		
Wind speed [m/s]	Bin power [kW]	Bin power [kW]	Error [kW]	Percentage [%]
4	48,29	48,29	-0,0024	-5,0E-03
4,5	88,53	88,53	-0,0026	-2,9E-03
5	137,38	137,38	-0,004	-2,9E-03
5,5	191,39	191,39	-0,001	-5,2E-04
6	252,96	252,96	0,001	4,0E-04
6,5	326,06	326,06	0	0,0E+00
7	411,63	411,63	0	0,0E+00
7,5	510,60	510,60	-0,001	-2,0E-04
8	623,90	623,91	-0,002	-3,2E-04
8,5	752,48	752,48	0,003	4,0E-04
9	898,74	898,73	0,01	1,1E-03
9,5	1075,82	1075,81	0,01	9,3E-04
10	1258,87	1258,85	0,02	1,6E-03
10,5	1459,17	1459,16	0,01	6,9E-04
11	1671,66	1671,64	0,02	1,2E-03
11,5	1888,30	1888,28	0,02	1,1E-03
12	2000,07	2000,05	0,02	1,0E-03
12,5	2000,07	2000,05	0,02	1,0E-03
13	2000,07	2000,05	0,02	1,0E-03
13,5	2000,07	2000,05	0,02	1,0E-03
14	2000,07	2000,05	0,02	1,0E-03
15	2000,07	2000,05	0,02	1,0E-03
16	2000,07	2000,04	0,03	1,5E-03
20	2000,07	2000,02	0,05	2,5E-03
25	2000,07	2000,01	0,06	3,0E-03

H

PERFORMANCE HEATPLOTS WIND PARK PRINSES ALEXIA

In this appendix a more detailed overview of all the heatplots filtered per 0.5 m/s bin ranging from 7 to 13 m/s is given as background for Figure 7.9. The plots show relative power performance against the reference PC over the period of Feb.-Aug. 2015.

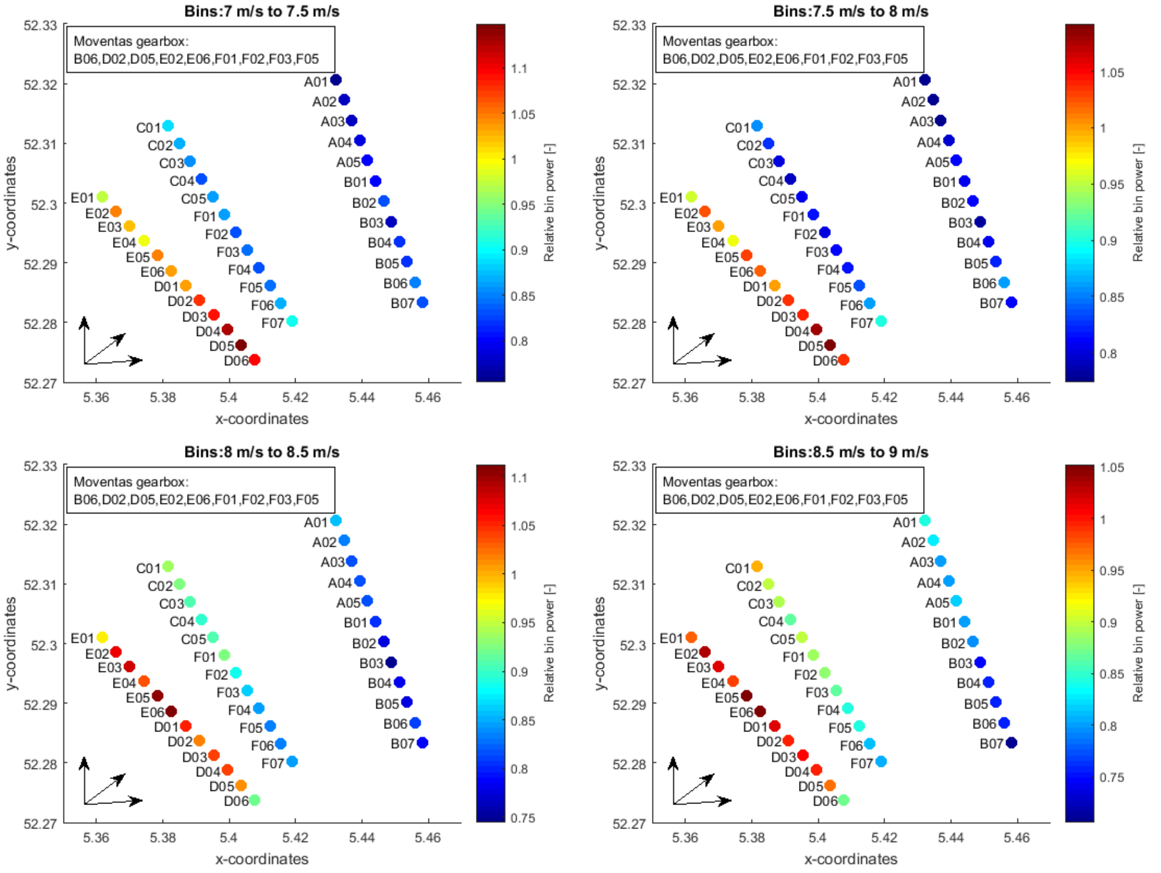

Figure H.1: *Heatplots for power performance of wind turbines at Prinses Alexia filtered per 0.5 m/s bin ranging from 7 to 9 m/s*

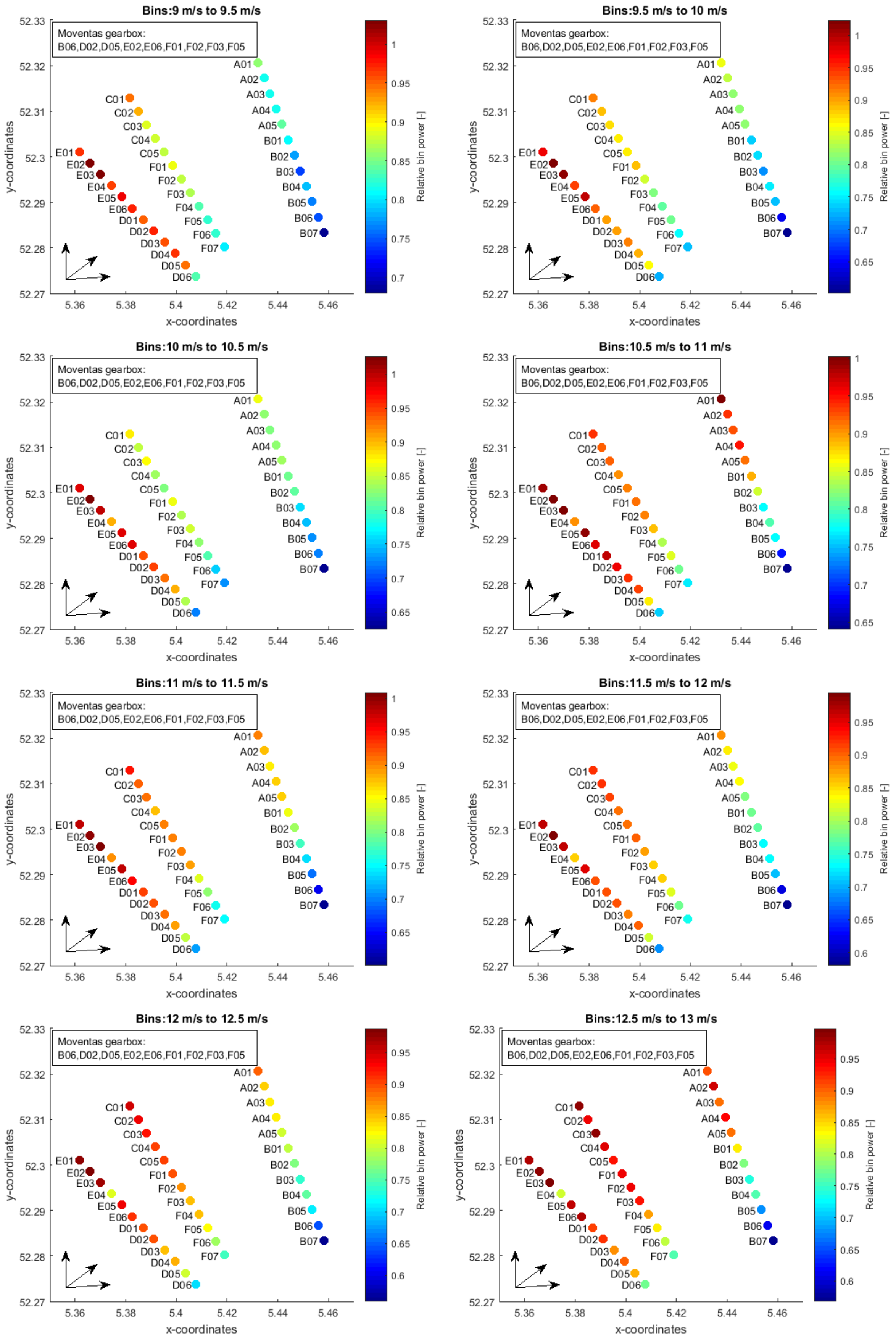

Bins:9 m/s to 9.5 m/s

Bins:9.5 m/s to 10 m/s

Bins:10 m/s to 10.5 m/s

Bins:10.5 m/s to 11 m/s

Bins:11 m/s to 11.5 m/s

Bins:11.5 m/s to 12 m/s

Bins:12 m/s to 12.5 m/s

Bins:12.5 m/s to 13 m/s

Figure H.2: *Heatplots for power performance of wind turbines at Prinses Alexia filtered per 0.5 m/s bin ranging from 9 to 13 m/s*